

Interactions between the Antarctic Ice Sheet and the Solid Earth

van Calcar, C.J.

DOI

[10.4233/uuid:4bca289c-69bd-4b9d-b1b1-6411c07a447f](https://doi.org/10.4233/uuid:4bca289c-69bd-4b9d-b1b1-6411c07a447f)

Publication date

2025

Document Version

Final published version

Citation (APA)

van Calcar, C. J. (2025). *Interactions between the Antarctic Ice Sheet and the Solid Earth*. [Dissertation (TU Delft), Delft University of Technology]. <https://doi.org/10.4233/uuid:4bca289c-69bd-4b9d-b1b1-6411c07a447f>

Important note

To cite this publication, please use the final published version (if applicable).
Please check the document version above.

Copyright

Other than for strictly personal use, it is not permitted to download, forward or distribute the text or part of it, without the consent of the author(s) and/or copyright holder(s), unless the work is under an open content license such as Creative Commons.

Takedown policy

Please contact us and provide details if you believe this document breaches copyrights.
We will remove access to the work immediately and investigate your claim.

Interactions between the Antarctic Ice Sheet and the Solid Earth



Caroline van Galcar

INTERACTIONS BETWEEN THE ANTARCTIC ICE SHEET AND THE SOLID EARTH

INTERACTIONS BETWEEN THE ANTARCTIC ICE SHEET AND THE SOLID EARTH

Proefschrift

ter verkrijging van de graad van doctor
aan de Technische Universiteit Delft,
op gezag van de Rector Magnificus prof.dr.ir. T.H.J.J. van der Hagen,
voorzitter van het College voor Promoties,
in het openbaar te verdedigen op woensdag 28 mei 2025 om 10:00 uur.

door

Caroline VAN CALCAR

Master of Science in Applied Earth Sciences, Delft University of Technology,
The Netherlands,
geboren te Ermelo, Nederland.

Dit proefschrift is goedgekeurd door de promotoren.

Samenstelling promotiecommissie:

Rector Magnificus,	voorzitter
Prof.dr. L.L.A. Vermeersen,	Technische Universiteit Delft, promotor
Prof.dr. R.S.W. Van de Wal,	Universiteit Utrecht, promotor
Dr.ir. W. Van der Wal,	Technische Universiteit Delft, promotor

Onafhankelijke leden:

Dr. S.L. Bradley,	University of Sheffield, Verenigd Koninkrijk
Prof.dr. M. King,	University of Tasmania, Australië
Prof.dr. A. Payne,	University of Liverpool, Verenigd Koninkrijk
Prof.dr. F.C. Vossepoel,	Technische Universiteit Delft, Nederland



Utrecht University



Printed by: Ridderprint, www.ridderprint.nl

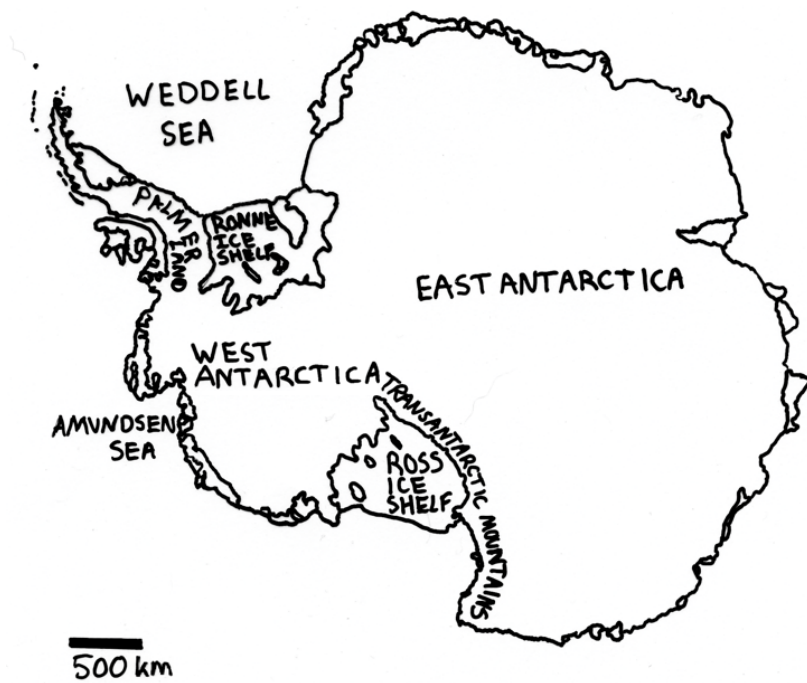
Cover picture: Caroline van Calcar, edited by Arnd Bronkhorst.

Pictures: Liesbeth Bronkhorst, Hans-Gerd Maas, Caroline van Calcar. Edited by Arnd Bronkhorst.

Copyright © 2025 by C.J. van Calcar

ISBN 978-94-6522-337-7

An electronic version of this dissertation is available at
<http://repository.tudelft.nl/>.



CONTENTS

Summary	xi
Samenvatting	xv
1 Introduction	3
1.1 The current state of the Antarctic Ice Sheet	4
1.2 Response of the AIS to changes and feedback in atmosphere, ocean and solid Earth	7
1.3 Glacial isostatic adjustment	11
1.4 Research questions	16
2 Method	19
2.1 Ice sheet models	20
2.2 IMAU-ICE	26
2.3 Glacial isostatic adjustment model	31
2.4 Coupling method	35
3 Simulation of a fully coupled 3D GIA - ice-sheet model for the Antarctic Ice Sheet over a glacial cycle	39
3.1 Introduction	40
3.2 Method	43
3.3 Results and discussion	58
3.4 Conclusions and outlook	62
3.5 Supplemental materials.	64
4 Bedrock uplift reduces Antarctic sea-level contribution over next centuries	75
4.1 Solid Earth and ice sheet stability	76
4.2 Sea-level rise reduction through bedrock uplift	78
4.3 Bedrock uplift delays ice sheet retreat.	79
4.4 Implications for ice sheet projections	83
4.5 Methods	85
4.6 Supplemental materials.	91
5 Approximating ice sheet – bedrock interaction in Antarctic Ice Sheet projections	103
5.1 Introduction	104
5.2 Method	106
5.3 Relation between 3D viscosity and relaxation time	110
5.4 Projections using different approaches to bedrock response	112
5.5 Conclusions and outlook	118
5.6 Supplemental materials.	121

6 Conclusions and Recommendations	129
6.1 Conclusions.	129
6.2 Recommendations	133
Data-statement	155
Acknowledgements	157
Curriculum Vitæ	159
List of Publications	160



Gerlache Strait, Antarctica

SUMMARY

The Antarctic Ice Sheet is a key regulator of the Earth's climate system, containing vast reserves of freshwater that could raise global sea level by 58 meters if fully melted. The stability of the Antarctic Ice Sheet is of global concern, particularly as climate change disrupts ecosystems and human settlements worldwide. Studying the behavior of the Antarctic Ice Sheet is crucial not only to project sea level rise but also to better understand complex interactions between the ice, ocean, and solid Earth systems.

This dissertation focuses on the interactions between the ice and the solid Earth, to understand how these two systems influence each other. It presents the development and application of a coupled 3D Glacial Isostatic Adjustment (GIA) and ice sheet model for Antarctica. GIA is the process by which Earth's surface rebounds or subsides in response to changing ice loads. As ice accumulates, the bedrock depresses; when the ice melts, the Earth slowly rebounds. This bedrock deformation affects ice dynamics because bedrock uplift causes floating ice to become grounded. The Antarctic Ice Sheet mainly loses mass via melt below floating ice shelves that are attached to grounded ice. When floating ice becomes grounded due to GIA, so is less ice shelf area and thus less ice mass loss. GIA therefore has a stabilising feedback on the ice sheet.

Most existing models either oversimplify the Earth's structure as a 1-dimensional model with uniform viscosities for a limited number of layers, or use prescribed representations of ice sheet history instead of a dynamic model, failing to capture the full complexity of the solid Earth-ice system. The model presented in this thesis incorporates lateral variations in mantle viscosity, allowing for a more realistic simulation of how different regions of Antarctica respond to changing ice loads. This advancement is crucial because the Earth's structure beneath West Antarctica is weaker, with lower mantle viscosity, compared to East Antarctica, which is an old craton with a stronger Earth structure. Such regional differences can lead to varying rates of bedrock uplift, and quantifying these is key to accurately projecting future ice sheet behavior. Since mantle viscosity remains uncertain, two different 3D Earth structures are used that are derived based on seismic data and mantle viscosity constraints from literature. One Earth structure is relatively weak to fit a mantle viscosity constraint in the Amundsen Sea Embayment, and one structure is relatively strong to fit mantle viscosity constraints in the Weddell Sea Embayment.

Studying the last glacial cycle is essential for improving projections of future ice sheet behavior and sea-level rise because the physical model can be compared to historical records of how ice sheets have historically responded to natural climate fluctuations. The last glacial cycle, spanning approximately 120,000 years, includes periods of ice growth and retreat in Antarctica, offering valuable insights into the feedback mechanisms between the ice, atmosphere, ocean, and solid Earth during this cycle. By understanding how these systems interacted during past climate shifts, particularly during the Last Glacial Maximum (LGM), between 25,000 and 15,000 years ago, and the sub-

sequent deglaciation, patterns and processes can be identified that are likely to recur under present and future climate change scenarios.

Chapter 3 of this thesis demonstrates that the bedrock elevation at the LGM plays a key role in determining the evolution of the Antarctic Ice Sheet during deglaciation. By simulating an entire glacial cycle using a fully coupled 3D GIA-ice sheet model, it is shown that a weaker Earth structure leads to higher bedrock elevation at the LGM, as the weaker Earth structure allows for uplift during warmer intervals during the glaciation, while a stronger Earth structure continues to subside until LGM. The higher bedrock elevation at the LGM in the weaker structure causes slower ice retreat during deglaciation compared to the stronger structure. This is due to less ice being exposed to ocean water, leading to less ice mass loss and slower bedrock uplift. Surprisingly, while weaker Earth structures typically lead to more uplift, this is not the case here due to the differences in bedrock elevation at the LGM. At present day, the weaker Earth structure leads to a less retreated grounding line and greater ice thickness than the stronger structure.

Previous research has shown the importance of including GIA in ice sheet projections, typically using simplified Earth structures or simplified methods like the elastic lithosphere and relaxed asthenosphere (ELRA) model. However, these approaches often fail to capture the complexity of solid Earth-ice interactions. Chapter 4 demonstrates that a fully coupled 3D GIA-ice sheet model reduces Antarctica's contribution to barystatic sea level rise by 9-23% by 2500, compared to a rigid Earth scenario, depending on the emission scenario and climate models. Additionally, it delays the grounding line retreat by 50-130 years between 2300 and 2500 due to the faster isostatic adjustment enabled by the lower mantle viscosity in West Antarctica.

General circulation models are used to provide atmospheric and oceanic inputs for these projections. To study the effect of spatial differences in ocean warming on GIA, we used the output of one general circulation model where warming mostly occurs in the Weddell Sea and the Ross sea, and another model where warming mostly occurs in the Amundsen Sea and the Ross sea. The study finds that spatial patterns of warming determine the influence on GIA, with stronger impact if warming occurs in areas like the Amundsen Sea where mantle viscosity is low. In a low-emission scenario, warming concentrated in the Amundsen Sea leads to 16% more barystatic sea level rise compared to warming in the Weddell Sea. Including 3D GIA in this scenario reduces barystatic sea level rise by 23%, showing that GIA effects can outweigh uncertainties related to the choice of general circulation model.

GIA has a stronger influence in low-emission scenarios where the slower ice sheet retreat can be stabilised by the bedrock uplift, whereas in high-emission scenarios, the rapid ice sheet retreat makes the rate of bedrock uplift less significant, allowing GIA to slow the retreat but not to prevent a fast collapse of the West Antarctic Ice Sheet. These findings highlight the importance of aggressive mitigation efforts which result in a scenario where GIA's stabilizing effects are relatively enhanced, reduce ice mass loss, and limit long-term sea level rise.

The high computational cost of using a 3D GIA model makes it impractical for ensemble studies that require thousands of simulations, prompting the need for faster, simpler Earth models like ELRA or 1D GIA to approximate bedrock response. Chapter 5 shows that up until 2300, the sea level contribution and ice sheet evolution from these

3D Earth structures can be reasonably approximated by an ELRA model with a uniform relaxation time of 300 years, which is much shorter than used in most existing models. Beyond 2300, a 1D GIA model with an upper mantle viscosity of $10^{19} Pa \cdot s$ and laterally varying relaxation times provides a better approximation. While these simpler models offer useful approximations, the spread in sea level contribution between the two 3D Earth structures is significant, indicating that it is preferable to vary Earth parameters in a simplified model to capture the range of possible 3D GIA responses rather than relying on average results.

The conclusions drawn from this research emphasize the critical role that GIA plays in the evolution of the Antarctic Ice Sheet. The feedback between bedrock uplift and ice dynamics is essential for understanding both past and future changes in the ice sheet, particularly in West Antarctica where the mantle is relatively weak compared to East Antarctica, and where the ice sheet is most vulnerable to climate change. The findings have important implications for future climate projections, as they highlight how sea level rise is overestimated when the effect of GIA is excluded in ice sheet models.

In terms of future research, several model development efforts are recommended. First, there is a need to improve the spatial resolution of both GIA and ice sheet models to better capture local variations in bedrock deformation and ice dynamics. The models presented in this thesis already include extensive observational data from ground-based, airborne, and spaceborne sources; however, their accuracy can be further enhanced by incorporating additional geodetic measurements, such as bedrock uplift and changes in ice thickness. These data would allow for better constraint of uncertain parameters in the models.

The coupled 3D model can be applied to other regions, such as the Greenland and Laurentide ice sheets, to explore how GIA with realistic viscosity variations affects these ice sheets. Lastly, integrating these more advanced models into global climate simulations will help to assess the broader interactions between the ice sheet, the solid Earth, and the ocean-atmosphere system, providing a more comprehensive understanding of future sea level rise.



Iceberg near Elephant Island, Antarctica

SAMENVATTING

De Antarctische ijskap (Antarctic Ice Sheet, AIS) is een belangrijke regulator van het klimaatstelsel van de aarde. De ijskap bevat enorme reserves aan zoet water die de zeespiegel wereldwijd met 58 meter kunnen laten stijgen als de ijskap volledig smelt. De stabiliteit van de Antarctische ijskap is van wereldwijd belang, met name omdat klimaatverandering ecosystemen en menselijke nederzettingen wereldwijd verstoort. Het bestuderen van het gedrag van de Antarctische ijskap is cruciaal, niet alleen om de stijging van de zeespiegel te voorspellen, maar ook om complexe interacties tussen het ijs, de oceaan en de vaste aarde beter te begrijpen.

Dit proefschrift richt zich op de interacties tussen het ijs en de vaste aarde om te begrijpen hoe deze twee systemen elkaar beïnvloeden. De vaste aarde bestaat uit de kern, mantel en korst van de aarde. Het proefschrift presenteert de ontwikkeling en toepassing van een gekoppeld 3D glaciale isostatische aanpassing (GIA) en ijskapmodel voor Antarctica. GIA is het proces waarbij het aardoppervlak daalt of terugveert als reactie op veranderende ijsbelastingen. Naarmate het ijs zich ophoopt, zakt het aardoppervlak in; wanneer het ijs smelt, veert de aarde langzaam terug. Deze vervorming van het gesteente beïnvloedt de ijsdynamiek omdat opheffing van het aardoppervlak ervoor zorgt dat drijvend ijs aan de grond komt en niet meer in contact is met de oceaan. De Antarctische ijskap verliest voornamelijk massa door het smelten van ijs onderaan drijvende ijsplaten. Deze ijsplaten zitten vast aan ijs wat op de vaste ondergrond ligt. Wanneer drijvend ijs aan de grond komt door GIA is er minder ijsoppervlak in contact met water en zal er minder ijs smelten. GIA heeft daarom een stabiliserende feedback op de omvang van de ijskap.

De meeste bestaande modellen vereenvoudigen de structuur van de mantel van de aarde door een 1-dimensionale uniforme viscositeit aan te nemen met een gelimiteerd aantal lagen in de aarde of gebruiken vaststaande representaties van de geschiedenis van de ijskap in plaats van een dynamisch model. In deze modellen kan de volledige complexiteit van het vaste aarde-ijssysteem niet worden meegenomen. Het model dat in dit proefschrift wordt gepresenteerd omvat laterale variaties in de mantelviscositeit, wat een meer realistische simulatie mogelijk maakt van hoe verschillende regio's van Antarctica reageren op veranderende ijsbelastingen. Dit is cruciaal omdat de structuur van de mantel van de aarde onder West-Antarctica zwakker is, met een lagere mantelviscositeit, vergeleken met Oost-Antarctica, wat een oud kraton is met een sterkere aardstructuur. Dergelijke regionale verschillen kunnen leiden tot verschillende snelheden van opheffing van het aardoppervlak en het kwantificeren hiervan is essentieel voor het nauwkeurig projecteren van toekomstig ijskapgedrag. Omdat de mantelviscositeit onzeker is worden twee verschillende 3D-aardstructuren gebruikt die zijn afgeleid op basis van seismische gegevens en mantelviscositeitsbeperkingen uit de literatuur. Eén aardstructuur is relatief zwak om te voldoen aan de bepaalde mantelviscositeit in de Amundsen Sea Embayment, en één structuur is relatief sterk om te voldoen aan de bepaalde man-

telviscositeit in de Weddell Sea Embayment.

Het bestuderen van de laatste glaciële cyclus is essentieel voor het verbeteren van voorspellingen van toekomstig ijskapedrag en zeespiegelstijging, omdat het fysieke model kan worden vergeleken met historische gegevens over hoe ijskappen in het verleden hebben gereageerd op natuurlijke klimaatschommelingen. De laatste glaciële cyclus, die ongeveer 120000 jaar beslaat, omvat periodes van ijsgroei en -terugtrekking in Antarctica, wat waardevolle inzichten biedt in de feedbackmechanismen tussen het ijs, de atmosfeer, de oceaan en de vaste aarde in deze cyclus. Door te begrijpen hoe deze systemen interacteerden tijdens eerdere klimaatveranderingen, met name tijdens het laatste glaciële maximum (LGM) tussen 25000 en 15000 jaar geleden en de daaropvolgende deglaciatie, kunnen patronen en processen worden geïdentificeerd die opnieuw zouden kunnen optreden onder de huidige en toekomstige klimaatveranderingsscenario's.

Hoofdstuk 3 van dit proefschrift toont aan dat de topografie van het aardoppervlak bij het LGM een belangrijke rol speelt bij het bepalen van de evolutie van de Antarctische ijskap tijdens de deglaciatie. Door een complete glaciële cyclus te simuleren met behulp van een volledig gekoppeld 3D GIA-ijskapmodel, wordt aangetoond dat een zwakkere aardstructuur leidt tot een hogere topografie van het aardoppervlak bij het LGM, omdat de zwakkere aardstructuur opheffing toestaat tijdens warmere intervallen tijdens de glaciatie, terwijl een sterkere aardstructuur blijft zakken tot aan het LGM. De hogere topografie van het aardoppervlak bij het LGM in de zwakkere aardstructuur zorgt voor een langzamere terugtrekking van het ijs tijdens de deglaciatie in vergelijking met de sterkere structuur. Dit komt doordat er minder ijs wordt blootgesteld aan oceaanwater, wat leidt tot minder verlies van ijsmassa en een langzamere opheffing van het aardoppervlak. Verassend genoeg leiden zwakkere aardstructuren doorgaans tot meer opheffing, maar dit is hier niet het geval vanwege de verschillen in topografie van het aardoppervlak bij het LGM. Aan het eind van de laatste glaciële cyclus leidt de zwakkere aardstructuur tot een minder teruggetrokken grondlijn en een grotere ijsdikte dan de sterkere aardstructuur.

Uit eerder onderzoek is gebleken hoe belangrijk het is om GIA op te nemen in ijskapprojecties, meestal met behulp van vereenvoudigde aardstructuren of vereenvoudigde methoden zoals het model van de elastische lithosfeer en de vertraagd terugverende asthenosfeer (ELRA). Deze benaderingen slagen er echter vaak niet in om de complexiteit van interacties tussen aarde en ijs vast te leggen. Hoofdstuk 4 laat zien dat een volledig gekoppeld 3D GIA-ijskapmodel de bijdrage van Antarctica aan de barystatische zeespiegelstijging met 9-23% vermindert tegen 2500, vergeleken met een rigide aardstructuur, afhankelijk van het emissiescenario en de toegepaste klimaatmodellen. Bovendien vertraagt GIA de terugtrekking van de grondlijn met 50-130 jaar tussen 2300 en 2500 vanwege de snellere isostatische aanpassing die mogelijk wordt gemaakt door de lagere mantelviscositeit in West-Antarctica.

Klimaatmodellen worden gebruikt om atmosferische en oceanische input te leveren voor deze projecties. Om het effect van ruimtelijke verschillen in oceaanopwarming op GIA te bestuderen, gebruikten we de output van een algemeen klimaatmodel waarbij opwarming vooral plaatsvindt in de Weddellzee en de Rosszee, en een ander model waarbij opwarming vooral plaatsvindt in de Amundsenzee. De studie concludeert dat ruimtelijke patronen van opwarming de invloed op GIA bepalen, met een sterkere impact als opwarming plaatsvindt in gebieden zoals de Amundsenzee waar de mantelvis-

cositeit laag is. In een scenario met lage emissie leidt opwarming in de Amundsenzee tot 16% meer barystatische zeespiegelstijging vergeleken met opwarming in de Weddellzee. De toepassing van 3D GIA in dit scenario vermindert de barystatische zeespiegelstijging met 23%. Het effect van GIA is in dit geval significant groter dan de onzekerheid tussen verschillende circulatiemodellen.

GIA heeft een sterkere invloed in lage-emissiescenario's waarbij de langzamere terugtrekking van de ijskap kan worden gestabiliseerd door de opheffing van het aardoppervlak, terwijl in hoge-emissiescenario's de snelle terugtrekking van de ijskap de snelheid van de opheffing van het aardoppervlak minder significant maakt, waardoor GIA de terugtrekking kan vertragen, maar niet een snelle ineenstorting van de West-Antarctische ijskap kan voorkomen. Deze bevindingen benadrukken het belang van grote mitigatie-inspanningen die resulteren in een scenario waarin de stabiliserende effecten van GIA relatief worden versterkt, het verlies van ijsmassa wordt verminderd en de zeespiegelstijging op de lange termijn wordt beperkt.

De hoge rekenkosten van het gebruik van een 3D GIA-model maken het onpraktisch voor ensemblestudies die duizenden simulaties vereisen, waardoor er behoefte is aan snellere en meer eenvoudige aardmodellen zoals ELRA of 1D GIA om de opheffing van het aardoppervlak te benaderen. Hoofdstuk 5 laat zien dat, tot 2300, de bijdrage van de zeespiegel en de evolutie van de ijskap van deze 3D aardstructuren redelijkerwijs kunnen worden benaderd door een ELRA-model met een uniforme relaxatietijd van 300 jaar, wat veel korter is dan in de meeste bestaande modellen nu toegepast wordt. Na 2300 biedt een 1D GIA-model met een bovenmantelviscositeit van $10^{19} \text{ Pa} \cdot \text{s}$ en lateraal variërende relaxatietijden een betere benadering. Hoewel deze eenvoudigere modellen nuttige benaderingen bieden, is de spreiding in zeeniveaubijdrage tussen de twee 3D-aardstructuren aanzienlijk, wat aangeeft dat het beter is om aardparameters te variëren in een vereenvoudigd model om het bereik van mogelijke 3D GIA-reacties vast te leggen in plaats van te vertrouwen op gemiddelde resultaten.

De conclusies die uit dit onderzoek zijn getrokken, benadrukken de cruciale rol die GIA speelt in de evolutie van de Antarctische ijskap. De feedback tussen opheffing van het aardoppervlak en ijsdynamiek is essentieel voor het begrijpen van zowel eerdere als toekomstige veranderingen in de ijskap, met name in West-Antarctica, waar de mantel relatief zwak is in vergelijking met Oost-Antarctica, en waar de ijskap het meest kwetsbaar is voor klimaatverandering. De bevindingen hebben belangrijke implicaties voor toekomstige klimaatprojecties, omdat ze benadrukken hoe zeespiegelstijging wordt overschat wanneer het effect van GIA wordt uitgesloten in ijskapmodellen.

Wat betreft toekomstig onderzoek worden verschillende modelontwikkelingsinspanningen aanbevolen. Ten eerste is er behoefte aan het verbeteren van de ruimtelijke resolutie van zowel GIA- als ijskapmodellen om lokale variaties in deformatie van het gesteente en de dynamiek van het ijs beter vast te leggen. De modellen die in dit proefschrift worden gepresenteerd bevatten uitgebreide observatiegegevens van grond-, lucht- en ruimtegebaseerde bronnen. Echter, de nauwkeurigheid van de modellen kan verder worden verbeterd door aanvullende geodetische metingen mee te nemen, zoals bodemopheffing en veranderingen in ijsdikte. Het meenemen van deze data maakt het mogelijk om onzekere parameters in de modellen beter te beperken.

Het gekoppelde 3D-model kan worden toegepast op andere regio's, zoals de Groen-

landse en Laurentide-ijskappen, om te onderzoeken hoe GIA met realistische variaties in viscositeit deze ijskappen beïnvloedt. Tot slot zal het integreren van deze geavanceerdere modellen in wereldwijde klimaatsimulaties helpen om de interacties tussen de ijskap, de vaste aarde en het oceaan-atmosfeersysteem te bestuderen, wat bijdraagt aan een vollediger begrip van de toekomstige zeespiegelstijging.



An entrance to Antarctica, Dallmann bay.

1

INTRODUCTION

The Antarctic Ice Sheet (AIS) plays a crucial role in the regulation of the Earth's system. Spanning about 14 million square kilometers, it is the largest ice mass on the planet. The marine-based regions of Antarctica, which are the parts of the AIS situated below sea level, hold sufficient freshwater to raise the global mean sea level (GMSL) by 25 meters (Noble et al., 2020). The South Pole, located 1235 km from the nearest coast, is at an elevation of 2800 meters where temperatures can drop to -50°C (Stammerjohn and Scambos, 2020). The interior of the AIS receives only around 50 mm of water-equivalent snowfall annually, making it a cold desert (Nicola et al., 2023). This snow gradually accumulates, forming ice that flows toward the coast as massive glaciers that extend into the ocean as floating ice shelves.

The AIS significantly influences ocean circulation, atmospheric temperatures, and global sea levels. The melting of ice from Antarctica drives the formation of cold, dense water, which sinks into the surrounding Southern Ocean and fuels global ocean circulation patterns, such as the thermohaline circulation (e.g. Bronselaer et al., 2018; Goosse and Fichefet, 1999). These currents play a vital role in the distribution of heat throughout the planet, thus regulating temperatures and weather patterns. The melting land ice, either from melting or calving of icebergs, adds water to the oceans and could also contribute to sea level rise in case this leads to a negative mass balance of the ice sheet. In recent decades, the warming climate has accelerated Antarctic ice mass loss and sea level rise, raising concerns about present and future coastal flooding and habitat loss (e.g. IPCC, 2023; Rignot et al., 2019). Additionally, the AIS reflects a significant portion of the sun's energy back into space because of its high reflectivity. In case the ice sheet shrinks, less solar radiation is reflected (Jakobs et al., 2021).

A change in the mass of the ice changes the pressure on the Earth's surface, causing the interior of the Earth to deform. When the ice sheet expands during glacial periods, the bedrock beneath subsides under the added weight. Conversely, when the ice sheet melts during the deglaciation phases, the bedrock experiences uplift. This process is called glacial isostatic adjustment (GIA) (e.g. Whitehouse et al., 2019) and plays an important role in vertical deformation in Antarctica (e.g. van der Wal et al., 2023). Bedrock

deformation has a stabilising effect on ice sheet flow because it delays grounded ice becoming afloat in case of ice sheet retreat. Bedrock deformation is therefore one of the feedbacks that control the ice sheet evolution and is a negative feedback, which means that an increase in bedrock deformation can decrease ice sheet melt. The negative feedback from GIA is the focus of this thesis.

Understanding the current state of the Antarctic Ice Sheet is crucial, as its dynamics are intricately tied to past, ongoing and future changes in the Earth's system. Recent observations highlight that accelerated ice mass loss and warming temperatures are significantly altering the ice sheet's structure, impacting not only sea level rise but also the complex feedback mechanisms between the ice, ocean, and atmosphere (Rignot et al., 2019; The IMBIE team, 2018).

1.1. THE CURRENT STATE OF THE ANTARCTIC ICE SHEET

The AIS is composed of two main regions: the East Antarctic Ice Sheet and the West Antarctic Ice Sheet, separated by the Transantarctic Mountains that rise to almost 5 km. Satellite data and in-situ measurements have revealed that the East Antarctic Ice Sheet is grounded mostly above sea level, which can be seen in the lower panel of figure 1.1, where the East Antarctic Ice Sheet is the right-hand side of the ice sheet where the bedrock elevation is mainly above zero (Morlighem et al., 2020). East Antarctica also contains the majority of the ice mass, as can be seen in the middle panel of figure 1.1. The ice is up to 4500 meters thick in the interior of East Antarctica. The West Antarctic Ice Sheet, the left hand side of the ice sheet, is largely grounded below sea level with deep subglacial basins like the Bentley Subglacial Trench at more than 2500 meters below sea level.

Also in terms of ice mass changes, there is a large difference between East and West Antarctica. Since observations started at the beginning of the 21st century, a mass gain has been observed in the interior of Antarctica. However, mass balance estimates, derived from satellite missions like GRACE (Gravity Recovery and Climate Experiment), indicate a net loss of over 150 gigatons per year since the early 2000s due to significant mass loss in West Antarctica (Rignot et al., 2019; The IMBIE team, 2018).

Mass loss in Antarctica occurs mainly via calving of ice bergs and melt at the base of ice shelves (Rignot et al., 2019). These shelves are located in between the orange lines in figure 1.1. Ice streams in Antarctica flow towards these shelves with velocities of up to 10 km per year, as is shown by bright orange streams in the top panel of figure 1.1. The line where the ice sheet transitions from resting on bedrock to floating on the ocean is called the grounding line and is the inner orange line in figure 1.1. The change in position of the grounding line over time is an indicator of the ice sheet's stability. The fastest flowing ice streams, such as Pine Island and Thwaites Glaciers in West Antarctica, have shown grounding line retreat in the order of 1 km per year over the last two decades (Milillo et al., 2019).

Ice shelves can act as a back-stress on grounded ice, called buttressing, holding back the flow of land-based ice from the interior of the AIS. As ice shelves thin or collapse, the grounded glaciers and ice streams behind them are able to accelerate, causing increased ice discharge into the ocean and contributing to sea level rise. The modern analogue of the reduction in buttressing has been observed near Larsen B, where after the collapse

the inland ice flow accelerated (Khazendar et al., 2015; Rignot et al., 2004). Other ice shelves in Antarctica might be vulnerable to this process as well (Miles et al., 2022).

Variations in grounded ice loading over the last glacial cycle and at present day lead to changes in the topography underneath the Antarctic Ice Sheet due to GIA. Global Navigation Satellite System (GNSS) stations on bedrock distributed across Antarctica, provide high-precision, continuous measurements of this vertical movement, with uplift rates varying significantly across the continent (Scheinert et al., 2021). In West Antarctica, where ice loss has been most pronounced, uplift rates have been measured to exceed 40 mm per year at the Amundsen Sea Embayment (Barletta et al., 2018). These GNSS measurements capture instant and short-term deformation due to seasonal snow accumulation and ice mass variations, and long-term deformation from GIA. The spatial variations in long-term uplift rate are not only caused by variations in the load over time and space, but also by spatial variations in the viscosity of the Earth structure.

Quantifying GIA is not only essential for simulating the feedback on the ice dynamics, but also for correcting satellite-derived measurements of ice sheet mass balance, as it directly influences gravity field and surface elevation changes. Furthermore, the uplift measurements help to constrain the mantle viscosity underneath the AIS (e.g. Ivins et al., 2023), a key parameter in GIA models and geodynamic models in general, which in turn refines projections of future ice sheet evolution and global sea-level contributions.

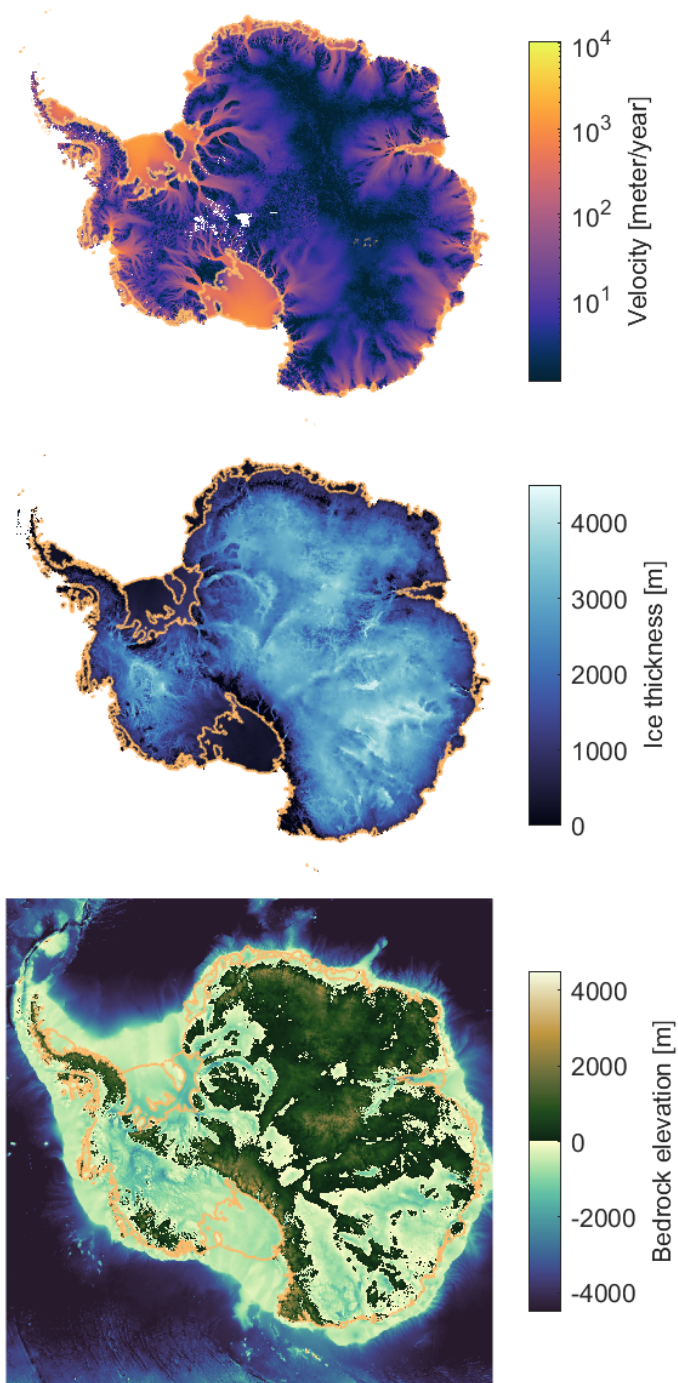


Figure 1.1: The current state of Antarctica as observed by satellite, airborne and in-situ data. The top panel shows the horizontal surface velocity of the ice using inSAR data from Landsat-8, Sentinel-1, and RADARSAT-2 (Mouginot et al., 2017), the middle panel shows the ice thickness, and the lower panel shows the bedrock elevation, both mainly based on airborne radio-echo sounding, satellite interferometry and seismic data (Morlighem et al., 2020).

1.2. RESPONSE OF THE AIS TO CHANGES AND FEEDBACK IN ATMOSPHERE, OCEAN AND SOLID EARTH

Direct observations of the Antarctic Ice Sheet cover only the last centuries while the response of ice sheets to climate shifts is a long-term process. It is therefore important to study the paleo time scales as this understanding is also needed to simulate current ice sheet processes. Paleo-records also provide valuable insights into past ice sheet and climate changes, particularly during the last glacial cycle starting 120000 years ago, when sea levels shifted by about 120 meters (Gowan et al., 2021; Simms et al., 2019) and global temperatures dropped by 4–6 degrees Celsius (Annan et al., 2022; Tierney et al., 2020). Studying the last glacial cycle reveals important feedbacks of the AIS with the atmosphere, ocean and solid Earth (Noble et al., 2020), which are shown in figure 1.2 and discussed in this section.

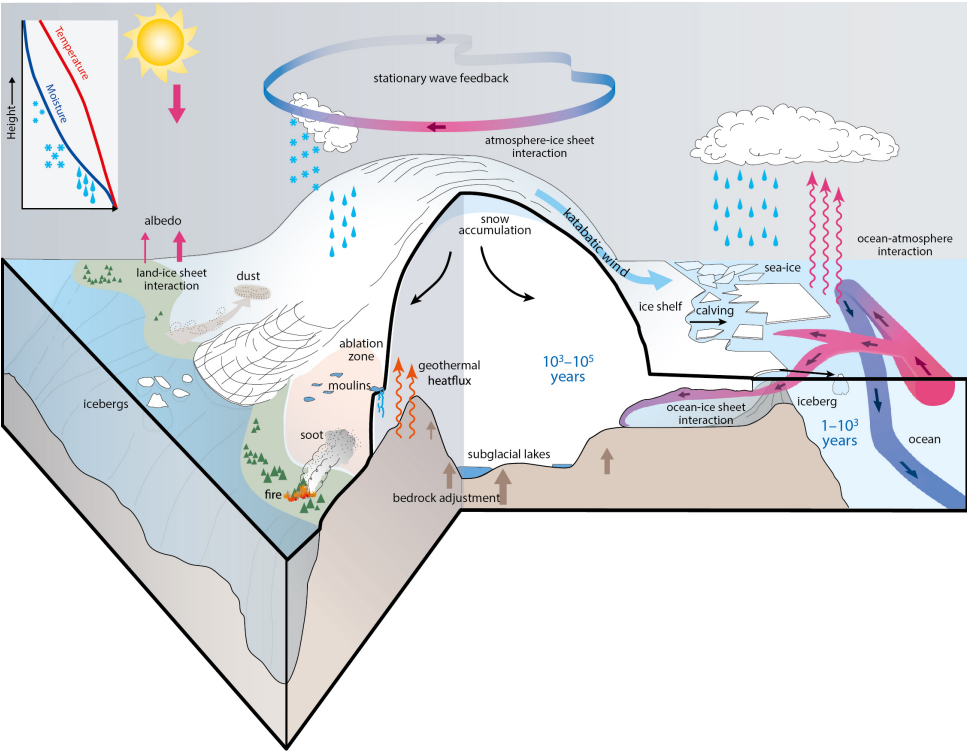


Figure 1.2: Ice sheet interactions. This figure is adopted from Stocker et al. (2013).

ATMOSPHERIC FEEDBACK

During the last glacial cycle, the AIS underwent significant changes driven largely by orbital forcing and atmospheric feedbacks (Löffverström et al., 2014). Orbital forcing, particularly changes in Earth’s axial tilt, eccentricity, and precession, determines the

amount and spatial and temporal distribution of solar radiation reaching the planet, driving glacial and interglacial cycles via complex feedback mechanisms that involve the land-ocean distribution and seasonal variations. During glacial periods, colder temperatures allowed the AIS to grow. At the peak of the last glaciation, the Last Glacial Maximum, around 20000 years ago, the ice sheet was considerably larger and thicker than it is today. The planet enters a deglaciation phase starting roughly 15000 years ago when warmer atmospheric and ocean temperatures caused by increased solar radiation led to ice sheet retreat and thinning, contributing to global sea level rise.

Atmospheric feedbacks, such as the ice-albedo effect, amplified these changes in ice sheets (Stap et al., 2017): as ice melted, the exposed darker ocean and land surfaces absorbed more solar radiation which accelerated warming. Additionally, changes in atmospheric carbon dioxide concentrations, which increased during interglacial periods due to ocean-atmosphere interactions, further enhanced warming. Also the melt-elevation feedback, which is the interaction between surface melt and atmospheric temperature gradients, has a substantial impact on the ice sheet. As ice melts, the surface elevation of the ice sheet decreases, moving the ice sheet surface to lower altitudes where atmospheric temperatures are generally higher because air temperature increases by several degrees per kilometer of descent (Hahn et al., 2020). Thus, this elevation loss subjects the ice to warmer temperatures, which enhances surface melting, further lowering the elevation. Additionally, as the ice sheet thins, the change in surface elevation may also affect local air circulation patterns, which can influence temperature distribution and further intensify the feedback loop. The melt-elevation feedback thus amplifies the rate of ice sheet thinning contributing to more rapid ice mass loss over time.

The surface elevation of the AIS also significantly impacts local precipitation (Tewari et al., 2021). When the AIS decreases in height, the atmosphere becomes warmer and wetter, leading to more precipitation and increased snow accumulation. Conversely, if the AIS height increases, the atmosphere cools and dries out, resulting in less precipitation. While increased precipitation from a thinner AIS can help stabilize its surface elevation, this is often more than offset by rising surface temperatures, and the combined effect of melt and precipitation is destabilizing (Kittel et al., 2021). Additionally, changes in AIS elevation affect the atmospheric circulation by influencing local surface winds and the jet around the Antarctic continent.

The future evolution of the AIS will be strongly influenced by ongoing and projected greenhouse gas emissions. As atmospheric concentrations of CO₂ and other greenhouse gases continue to rise due to human activities, the resulting warming of the Earth's climate will accelerate ice sheet melting and destabilization, particularly in the vulnerable regions of West Antarctica (IPCC, 2023). If global temperatures continue to rise in line with high-emissions scenarios, such as those outlined in the IPCC's shared socioeconomic pathway (SSP)5-8.5, significant portions of the West AIS could collapse within the coming centuries (IPCC, 2023). This could lead to a multi-meter rise in global sea levels over the next centuries. Conversely, under a more moderate emission scenario SSP2-4.5, or the strong mitigation scenario SSP1-2.6 where global emissions are substantially reduced, the rate of ice loss from Antarctica may be slowed, limiting sea level rise. However, even under lower-emission pathways, continued ice loss is expected, as the AIS is already responding to the climate warming that has occurred to date.

The present thesis explores the effect of GIA on the Antarctic ice sheet evolution over the last glacial cycle, and under the SSP1-2.6 and SSP5-8.5 scenarios to explore the full uncertainty range. It is assumed the middle scenario falls within the uncertainty range.

OCEAN FEEDBACK

The evolution of the AIS and the surrounding ocean are tightly interconnected through several feedback mechanisms, which play a critical role in influencing both ice dynamics and ocean circulation patterns. One of the key feedbacks between the AIS and the ocean involves the interaction between warm ocean water and ice shelves, which can lead to enhanced ice shelf melting resulting in ice mass loss, and changes in ocean properties (Jenkins et al., 2018).

Warm ocean currents originating from the deep Southern Ocean flow underneath the floating ice shelves that fringe much of the Antarctic coastline. These warm waters melt the base of the ice shelves, thinning them and reducing their buttressing capacity. When warm ocean water reaches the grounding line, it can melt the ice at its base, causing the grounding line to retreat inland. This retreat can expose more of the ice sheet to ocean water, accelerating ice loss. In some cases, this can lead to a feedback known as marine ice sheet instability in areas where the bedrock slopes downward inland, allowing more warm water to intrude further under the ice sheet and enhance melting (Joughin and Alley, 2011; Mercer, 1978; Schoof, 2007). Parts of the AIS and its ice streams lie on a reversed bedrock slope (Figure 1.1). When an ice sheet on a reverse-sloped bed loses its buttressing, the flow of ice increases. This can cause acceleration of the retreat which continues until the grounding line reaches forward-sloped or flat bedrock, or until the buttressing ice shelf regrows. Grounding lines on reverse slopes are conditionally unstable, and their retreat is influenced in a complex way by factors such as ice flow, bedrock shape, and the surface mass balance.

In the coming centuries, ice mass loss in Antarctica will mainly occur in areas where warm ocean currents are melting ice shelves from below, such as the Amundsen Sea Embayment where the retreating Pine Island and Thwaites Glaciers are located. Feedback processes, such as the marine ice sheet instability which has potential to occur in West Antarctica, could accelerate ice loss beyond current projections.

As ice melts and calving increase, large amounts of freshwater are released into the surrounding ocean. This freshwater influx reduces the salinity and density of the surface waters around Antarctica, which can disrupt local ocean circulation patterns, including the formation of Antarctic Bottom Water. This is a dense water mass that sinks and drives global thermohaline circulation, influencing ocean heat transport and climate worldwide. Changes in freshwater input from the AIS can slow down or alter these circulation patterns, potentially reducing the ocean's ability to transport heat and regulate global climate. Meltwater also affects sea ice formation because the reduced salinity leads to an increase in the freezing temperature. This might influence precipitation patterns as the uptake of moisture depends on the presence of sea ice.

A change in sea level also influences ice sheet growth and melt. An increase in sea level near the ice sheet slows ice sheet growth by causing the grounding line to retreat, thereby expanding the ice shelf area exposed to sub-shelf melting (De Boer et al., 2014; Gomez et al., 2010, 2015, 2018; Konrad et al., 2015). Additionally, higher sea levels may

accelerate calving rates, as more ice at the ice shelf front comes into contact with ocean water (Fig. 1.5). Conversely, a drop in sea level near the ice sheet reduces both sub-shelf melting and calving rates because less ice interacts with the ocean. Finally, variations in sea level can alter the depth of the ice shelf base, potentially exposing it to ocean waters of different temperatures. These temperature changes can affect sub-shelf melting, which is tested for and further explained in Chapter 4 of this thesis.

SOLID EARTH FEEDBACK

The interactions between the solid Earth and the AIS involve several processes that shape both the ice and the underlying land, which are shown in figure 1.3. Erosion and deposition continuously reshape the landscape, while basal heat flux influences the thermal dynamics of the ice sheet. Glacial isostatic adjustment influences both the local geometry and global sea levels. Together, these processes govern the complex relationship between the ice and the Earth beneath it.

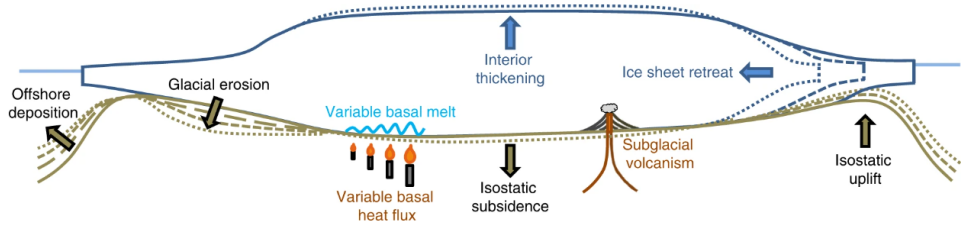


Figure 1.3: Interactions between the solid Earth and the ice sheet. This figure is adopted from Whitehouse et al. (2019).

Erosion occurs as the AIS moves across the bedrock beneath it (Livingstone et al., 2012). The pressure of the ice cause it to scrape and grind against the Earth's surface, leading to the removal of material. This process is known as abrasion, where the ice, often carrying rocks and sediment, smooths and polishes the underlying bedrock. Deposition is the counterpart to erosion, where the ice sheet deposits the material it has eroded and transported. As the ice melts, it releases sediment in the form of glacial till, which is an unsorted mixture of rock, clay, and other particles. This deposited material builds up, forming features such as moraines and drumlins beneath the ice. Erosion and deposition under the ice sheet carves out valleys and fjords, reshaping the landscape beneath the ice. The landscape is an important factor determining the velocity and direction of ice flow.

The basal heat flux refers to the transfer of heat from the Earth's interior to the base of the ice sheet. This heat, originating from deep layers within Earth's interior, can lead to melting at the ice sheet's base (Reading et al., 2022). The amount of heat reaching the ice base controls the temperature which determines the basal melt rates and thereby the friction between ice and bedrock which influences the flow of the ice. Areas of increased basal heat flux can create areas of subglacial lakes and rivers, which further affect the movement and dynamics of the ice.

GIA plays a critical role in shaping the evolution of ice sheets (Whitehouse, 2018). Understanding GIA is thus essential to project how ice sheets like Antarctica will evolve

in a warming climate and to accurately project sea-level rise. GIA will be discussed in detail in the next section.

1.3. GLACIAL ISOSTATIC ADJUSTMENT

Solid Earth deformation due to ice and ocean mass changes is governed by the principles of rheology, which describes how Earth's materials respond to applied stresses both elastically and viscously (Ivins et al., 2023; Sabadini et al., 2016). The deformation of the Earth due to ice load changes depends on the material properties of both the lithosphere and the mantle.

The lithosphere responds elastically to stress, meaning that it deforms immediately when a load is applied and fully recovers when the load is removed. The thickness and stiffness of the lithosphere play an important role in determining the magnitude and wavelength of this elastic response. A thicker lithosphere tends to deform less under the same ice load compared to a thinner one.

The mantle, in contrast, can be considered to behave viscoelastically, meaning that on short timescales, the mantle deforms elastically, but over longer timescales, it flows like a fluid, with the flow rate governed by its viscosity. Viscosity is a key parameter that controls how quickly or slowly the mantle can adjust to the changing stresses imposed by ice loading and unloading. Higher viscosity in the mantle leads to slower isostatic adjustment, while lower viscosity allows for more rapid flow and quicker recovery of the surface after changes in loading.

The viscosity of the mantle beneath Antarctica is spatially variable due to differences in the geological characteristics of the lithosphere and underlying mantle across the continent (Kaufmann et al., 2005; van der Wal et al., 2023). There are two main geologic regions in Antarctica: East Antarctica and West Antarctica. East Antarctica is geologically older and more stable, with a thick, cold, and rigid lithosphere. The upper mantle underneath East Antarctica is more viscous, meaning it resists flow more effectively. In contrast, West Antarctica is younger and geologically more active, with a thinner lithosphere and a hotter, more deformable upper mantle. This region has lower mantle viscosity, allowing for faster mantle flow and isostatic adjustment in response to ice mass changes. These variations in mantle viscosity are controlled by factors like temperature, mantle composition, and stresses, leading to significant spatial heterogeneity across Antarctica but also on a regional scale.

The interaction between the elastic lithosphere and the viscous mantle governs the timescales and spatial patterns of GIA. On a post-Last Glacial Maximum scale, which occurred between 25000 and 15000 years ago, GIA has significantly influenced the landscape as the ice sheet began to retreat, governed by adjustments in bedrock elevation over thousands of years. This long-term process continues to shape the region today, with ongoing adjustments in response to the melting ice. In recent decades, GIA has been observed at shorter timescales (Barletta et al., 2018; Nield et al., 2014). Regions vulnerable to climate change, such as the Amundsen Sea Embayment happen to overlay a relatively weak Earth structure with a low mantle viscosity. There, the impact of GIA is therefore significant over decadal to centennial time scales (Book et al., 2022). GIA is therefore a crucial factor in understanding historical, contemporary and future shifts in Antarctica's ice dynamics.

Ice mass changes can be measured using gravimetry data from the GRACE and GRACE-FO satellite missions which detects mass changes at a spatial resolution of about 300 km by measuring changes in gravity. However, these measurements contain both ice loss and GIA signals. To separate the signals, the GIA component is computed by GIA models which assume a certain mantle viscosity. The mantle viscosity can be constrained using measurements of vertical bedrock deformation in Antarctica by GNSS stations mounted on bedrock. These models have proven essential in explaining high uplift rates in regions such as the Amundsen Sea sector, where a low-viscosity mantle leads to significant bedrock rebound (e.g. Barletta et al., 2018).

The bedrock uplift directly leads to a drop in sea level, causing the sea level to vary not only temporally, but also spatially. Furthermore, the sea level varies spatially due to the self-gravitating effect of the ice sheet. As an ice sheet grows during a glaciation phase, the increased gravitation of the ice mass attracts the sea level, which rises nearby the ice sheet and drops far from the ice sheet (e.g. Farrell and Clark, 1976). As the ice sheet melts, the opposite occurs and the decrease in gravitational attraction of the ice causes the sea level to drop close to the ice sheet, while it rises far from the ice sheet. The total change in regional sea level over time thus depends on vertical bedrock deformation and on the self-gravitating effect of the ice sheet.

Around 21000 years ago, the barystatic sea level was about 130 meter lower than it is at present day, but for example in Canada, the sea level was about 450 meter higher than at present day because of the presense of the Laurentide Ice Sheet (Fig. 1.4) (Lambeck et al., 2014). Furthermore, the sea level is projected to drop by 200 meters close to the West Antarctic Ice Sheet in the coming 500 years in case of a high emission scenario due to ice mass loss from the AIS, whereas the AIS contribution to barystatic sea level (the global mean sea level) is 6 meters in that same scenario (Gomez et al., 2024). This sea level change included vertical bedrock deformation and the effect of self-gravitation of the AIS.

The change in sea level impacts bedrock deformation since the change in ocean mass also acts as a surface load on the Earth. However, in Antarctica the change in sea level is relatively small compared to the change in ice thickness, which can be up to 2 km over the coming 500 years and over the last deglaciation. In this thesis, the change in ocean loading is taken into account at locations where ice was melting or growing by computing the change in ice above flotation, which is then applied as loading on the Earth surface. Outside of these locations, the load of the change in ocean mass is neglected, which slightly decreases the bedrock response to changes in loading.

The Earth's rotation influences sea level by causing a redistribution of water (Wu and Peltier, 1984). This rotational effect causes sea levels to be higher at the equator and lower at the poles with a difference of 2 meters over a glacial cycle (Martinec and Hagedoorn, 2014). Additionally, changes in the Earth's rotation can be caused by the redistribution of mass. These changes, known as rotational feedback, can also result in regional variations in sea level. However, the rotational feedback is neglected in this thesis since the effect of rotation is much smaller than the effect of a change in ice loading.

Finally, the bedrock deformation causes more deformation by itself due to the self-gravity of the Earth itself. The sensitivity tests presented in Chapter 3 and 4 show that the effect of self-gravitation of the Earth on bedrock deformation is much smaller than

the effect of ice loading on the bedrock deformation. The magnitude of localized stress caused by ice loading far exceeds the localized impact of the Earth’s self-gravitation. Ice loading directly deforms the Earth’s lithosphere and mantle beneath the ice, while the self-gravitation effect is distributed globally and contributes relatively little to the deformation in comparison.

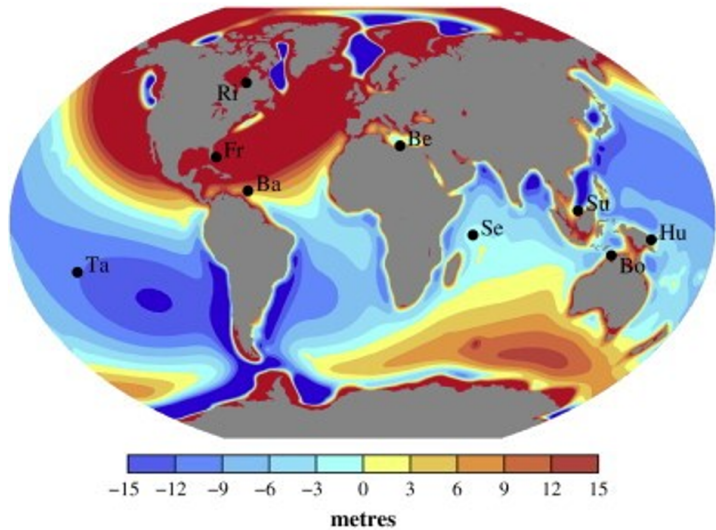


Figure 1.4: Difference between the barystatic sea level change and the regional sea level change. Note that the dark red and blue colors indicate regions with a difference greater than 15 meters. The letters in the figure refer to different locations: Tahiti (Ta), Freeport (Fe), Richmond Gulf (Ri), Barbados (Ba), Benghazi (Be), Seychelles (Se), Sunda Shelf (Su), Bonaparte Gulf (Bo) and Huon Peninsula (Hu). This figure is adopted from Milne and Mitrovica (2008).

FEEDBACK ON ICE DYNAMICS

As the bedrock rebounds, it influences the evolution of the ice sheet in multiple ways (Figure 1.5).

First, and most importantly, when bedrock uplift occurs, floating ice can become grounded, causing the grounding line to retreat less. This dynamic interaction between the rising land and the overlying ice reduces the initial perturbation and therefore increases the stability and acts as a negative feedback in the ice sheet evolution. The effect of self-gravitation of the ice sheet on the ocean is also a negative feedback. In this thesis, the effect of bedrock deformation on ice sheet dynamics is always taken into account, whereas the effect of self-gravitation of the ice sheet on the sea level is neglected. To test the importance of self-gravity of the ice sheet on the sea level compared to the effect of bedrock deformation on sea level, a sensitivity test is performed and described in Chapter 4 of this thesis.

Second, the surface elevation of the ice increases when bedrock elevation increases. The ice surface is then in a colder atmosphere, which could increase snowfall and reduce

melt.

Third, GIA influences the bedrock slope within the West Antarctic Ice Sheet. Uplift associated with GIA can lead to the flattening of reverse bed slopes, promoting glacier advancement and enhancing the stability of the ice sheet (Adhikari et al., 2014). Over the past deglaciation, GIA has been suggested to alter bed slopes by 0.25–0.4 m/km (Whitehouse et al., 2019). A reversed bed slope can even become a forward bed slope, depending on the location (Konrad et al., 2015). The shape of the bedrock affects ice dynamics as variations in slope impact ice velocity and flow direction.

Last, bedrock deformation also influences the shape of the cavities below the ice shelves and the depth of the continental ridge, and thereby the temperatures below the ice shelves which regulate the melt of ice shelves (Kreuzer et al., 2023).

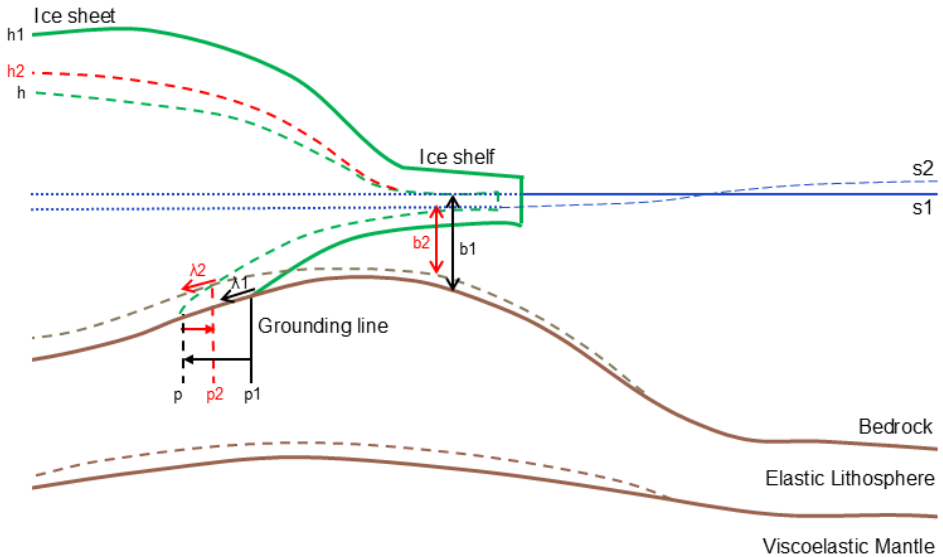


Figure 1.5: The effect of bedrock uplift on the ice sheet. This figure is adopted from van Calcar et al. (2024).

MODELLING THE GIA FEEDBACK

GIA is modelled by solving the momentum equation, which, for this purpose, describes how surface loads induce forces within the Earth, and cause deformation over time. Central to this process is the buoyancy force, driven by density contrasts between the crust and the underlying mantle and to a lesser extent by density contrasts below. As ice sheets melt and the surface load decreases, the mantle's buoyancy force pushes the crust upward. The density of the crust and the mantle control this upward movement. GIA models need to include the rigidity to simulate its instant elastic response, and the viscosity to simulate the delayed viscoelastic deformation of the mantle. GIA models are also used to compute the regionally varying sea level over paleo timescales and for future sea level change projections by solving the sea level equation (e.g. De Boer et al., 2017; Yousefi et al., 2022).

Traditionally, GIA has been studied with a focus on the last glacial cycle, which spans the past approximately 120000 years, using a prescribed ice sheet history (e.g. Blank et al., 2021; Geruo et al., 2013; Gomez et al., 2013; Hay et al., 2017; Kaufmann et al., 2005; Nield et al., 2014, 2018; Powell et al., 2021; van der Wal et al., 2015; Whitehouse et al., 2012; Yousefi et al., 2022). Over these long time scales, GIA leads to sea level changes up to hundreds of meters, and solid earth deformation which significantly influences the glacial cycle (Abe-Ouchi et al., 2013; Oerlemans, 1980). This type of modelling is used to constrain the local mantle viscosity by conducting many simulations with different Earth structures and possible ice sheet histories to obtain present day uplift or gravity rates, or paleo sea levels that match observations.

A reconstruction of the ice sheet history (hereafter referred to as prescribed ice sheet history) provides a representation of the growth and retreat of ice sheets, allowing to compute the crustal response and mantle flow directly. This approach assumes that the ice sheet's behavior over time is well-documented and generally does not use available information about ice sheet dynamics. Such reconstructions are used in GIA models to simulate sea level change self-consistently by means of the Sea Level Equation (e.g. Spada and Melini, 2019; Yousefi et al., 2022). While this method has been useful in some regions and globally, it does not capture the feedback between ice dynamics and bedrock deformation, which is critical for future projections (Kachuck et al., 2020; Pollard et al., 2017).

To project sea level rise, ice dynamical models are employed to simulate the movement and evolution of ice sheets in response to climate change. However, GIA has often been excluded from these models or treated in a simplified manner (Bulthuis et al., 2019; Coulon et al., 2024; DeConto et al., 2021). One of the methods used to incorporate GIA in such projections is the Elastic Lithosphere Relaxing Asthenosphere (ELRA) model (Le Meur and Huybrechts, 1996). The ELRA model assumes that the Earth's lithosphere behaves elastically while the asthenosphere (the shallow and more fluid part below the lithosphere) relaxes viscously under the load of ice. Though it provides a basic framework for calculating the crustal response to changing ice mass, it is limited by its assumption of a uniform and idealized Earth structure, making it unsuitable for complex variations.

Another approach to include GIA has been the use of 1D GIA models, which simplify the Earth's structure by assuming radial symmetry (Golledge et al., 2019; Gomez et al., 2015; Konrad et al., 2015; Rodehacke et al., 2020). These models can vary lithospheric thickness and mantle viscosity but do so in only one dimension, treating the Earth's layers as uniform. While 1D models are computationally efficient and useful for global-scale projections, they lack the ability to account for lateral heterogeneity—geological variations in Earth's properties across different regions, such as exist in Antarctica, and they are not as fast as ELRA models.

3D GIA models incorporate lateral variations in Earth's structure, such as changes in crustal thickness and mantle viscosity, and several have been applied to study Antarctica (Geruo et al., 2013; Hay et al., 2017; Kaufmann et al., 2005; Powell et al., 2021; van der Wal et al., 2015; Yousefi et al., 2022). These 3D models allow for a more realistic representation of how different regions of the Earth's lithosphere and mantle respond to ice mass changes. While 3D GIA models offer significant improvements over 1D models, they have mainly been applied in studies using a prescribed ice sheet history. This means

that while the Earth's response is modelled in three dimensions, the ice sheet's behavior is prescribed which does not account for the dynamic feedback between ice mass loss and GIA, which could significantly impact projections of ice sheet retreat and sea-level rise.

To fully understand the role of GIA during glacial cycles and in future projections, a coupled 3D GIA-ice sheet model is necessary. In such a coupled model, the ice sheet, solid Earth and sea level evolve together, allowing for feedbacks at different timescales between the systems.

Besides the studies presented in this thesis, there exist only two other studies on the last glacial cycle using a coupled 3D GIA - ice sheet model (Albrecht et al., 2024; Gomez et al., 2018), and one other study on projections of the AIS (Gomez et al., 2024). These studies use a different coupling scheme than the scheme developed for this thesis, and they make use of different ice sheet and GIA models. In this thesis, we present a new coupled 3D GIA - ice sheet model which allows us to study the GIA feedback on glacial time scales, as well as the coming centennials. The main difference between this model and other coupled 3D GIA - ice sheet models is the input for the Earth's rheology. The mantle viscosity in the model presented here depends on the stress resulting from changes in ice loading, the mantle temperature derived from seismic measurements, and on the water content and grain size. In contrast, other coupled models use a prescribed viscosity as input for the GIA model that is independent on the loading and static in time.

The 3D GIA model presented in this thesis will be a computationally expensive model, making it impractical for ensemble studies, where thousands of simulations are required to explore the uncertainties of sea level rise projections. Therefore we also use the results of the coupled model to study if and how simpler bedrock deformation and GIA models with a faster computation time can be used.

1.4. RESEARCH QUESTIONS

While prescribed ice sheet histories and simplified GIA models (like ELRA or 1D GIA) have been widely used in the past, they fail to capture the full complexity of interactions between the ice sheets and the Earth's crust. Investigating the last glacial cycle with a newly developed coupled 3D GIA - ice sheet model allows to understand the feedback in detail. This leads to the first research question, answered in Chapter 3:

1. How does a 3D mantle structure affect the Antarctic Ice Sheet over a glacial cycle?

Subsequently, the ice dynamical component was replaced by the latest state-of-the-art model, and the coupled model was applied to address the second research question, answered in Chapter 4:

2. How does a 3D mantle structure affect the Antarctic Ice sheet over the next centuries?

The long computation time of coupled ice sheet - 3D GIA models creates the need for approximations of the bedrock response for a 3D Earth structure using methods that are already incorporated in other ice sheet models. This leads to the final research question, answered in Chapter 5:

3. How can the bedrock response for a 3D Earth be approximated in ice sheet models?

This thesis concludes with Chapter 6, which reflects on the contributions of the study to the field of ice sheet dynamics and GIA, discusses the limitations of the approach taken in this thesis, and suggests directions for future investigations.



Antarctic Peninsula

2

METHOD

For this dissertation, a coupled 3D GIA - ice sheet model has been developed using two different ice sheet models. To simulate the last glacial cycle, the 3D GIA model is coupled to the ice sheet model ANICE (De Boer et al., 2013) and the results are presented in Chapter 3. To conduct projections, the same GIA model was coupled to the newer ice sheet model IMAU-ICE (Berends et al., 2022), of which the results are presented in Chapter 4. In Chapter 5, the sea level rise resulting from a coupled 3D GIA - ice sheet model is approximated using the ELRA model and a 1D GIA model coupled to IMAU-ICE.

The general physics behind both ice sheet models is the same and is discussed in section 2.1 of this chapter. Since this is the first time Antarctic projections are conducted with IMAU-ICE, a detailed description of relevant features of IMAU-ICE is provided in section 2.2. The GIA model and the coupling method are discussed in sections 2.3 and 2.4.

2.1. ICE SHEET MODELS

The ice sheet models IMAU-ICE (Berends et al., 2022) and ANICE (De Boer et al., 2013) use a combination of the shallow ice and the shallow shelf approximations (SIA and SSA, respectively) to solve the balance of membrane, basal and driving stresses (Bueler and Brown, 2009; Lipscomb et al., 2019). Using the SIA, there is no sliding and the driving force of gravity is balanced by vertical shearing within the ice. The SIA is solved in ANICE and IMAU-ICE using the following equations:

$$\frac{\partial}{\partial z} \left(\eta \frac{\partial u}{\partial z} \right) = \rho g \frac{\partial h}{\partial x} \quad (2.1a)$$

$$\frac{\partial}{\partial z} \left(\eta \frac{\partial v}{\partial z} \right) = \rho g \frac{\partial h}{\partial y}, \quad (2.1b)$$

where η is the effective viscosity, u and v are the components of the horizontal velocity, ρ is the density of ice, g is the gravitational acceleration, and $\frac{\partial h}{\partial x}$ and $\frac{\partial h}{\partial y}$ are horizontal derivative of the ice surface elevation.

In the SSA, the driving stress is balanced by the basal shear stress, and the membrane stresses caused by horizontal stretching and shearing of the ice, while vertical shearing is neglected. The SSA deployed in IMAU-ICE is described by the following set of equations:

$$\frac{\partial}{\partial x} [2\bar{\eta}H(2\bar{u}_x + \bar{v}_y)] + \frac{\partial}{\partial y} [\bar{\eta}H(\bar{u}_y + \bar{v}_x)] - \rho g H \frac{\partial h}{\partial x} = \tau_{b,x} \quad (2.2a)$$

$$\frac{\partial}{\partial y} [\bar{\eta}H(2\bar{v}_y + \bar{u}_x)] + \frac{\partial}{\partial x} [2\bar{\eta}H(\bar{v}_x + \bar{u}_y)] - \rho g H \frac{\partial h}{\partial y} = \tau_{b,y} \quad (2.2b)$$

The terms between square brackets are the membrane stresses from longitudinal stretching and lateral shearing with $\bar{\eta}$ as the vertically averaged effective viscosity, \bar{u} and \bar{v} as the vertically averaged horizontal velocities and H as the ice thickness. $\tau_{b,x}$ and $\tau_{b,y}$ are the basal shear stress components which are dependent on friction and basal hydrology parameters.

In ANICE, the gradients in the effective viscosity are neglected and the new vertically averaged viscosity $\bar{\mu}$ is equal to $\bar{\eta}H$. As is described in Berends et al. (2021), the equations to solve the SSA are simplified to:

$$4 \frac{\partial^2 \bar{u}}{\partial x^2} + \frac{\partial^2 \bar{u}}{\partial y^2} + 3 \frac{\partial^2 \bar{v}}{\partial xy} - \frac{\tau_{b,x}}{\bar{\mu}} = \frac{\rho g H \frac{\partial h}{\partial x}}{\bar{\mu}} \quad (2.3a)$$

$$4 \frac{\partial^2 \bar{v}}{\partial y^2} + \frac{\partial^2 \bar{v}}{\partial x^2} + 3 \frac{\partial^2 \bar{u}}{\partial xy} - \frac{\tau_{b,y}}{\bar{\mu}} = \frac{\rho g H \frac{\partial h}{\partial y}}{\bar{\mu}} \quad (2.3b)$$

To solve the SIA and SSA, the basal friction and the grounding line position should be computed. The basal friction is computed using regularised Coulomb law, as explained in the following section "Sliding", which is followed by a section explaining the determination of the grounding line position. Afterwards, the solution to the SSA is discussed, and how basal and surface mass balance are solved to compute the ice sheet evolution.

2.1.1. SLIDING

The velocity components \bar{u} and \bar{v} consist of a deformational and a sliding component. In this paragraph we describe the sliding component. Sliding at the base of the Antarctic Ice Sheet occurs when the ice moves over a layer of water or sediment, reducing friction between the ice and the bedrock. This process is influenced by the presence of meltwater, allowing the ice to slide more easily. Basal sliding plays a critical role in the ice sheet dynamics, particularly in regions like West Antarctica, where much of the ice is grounded below sea level. The rate of sliding is affected by factors such as bedrock topography, subglacial water pressure, and the roughness of the ice-bed interface. Faster sliding can lead to accelerated ice flow.

In IMAU-ICE, multiple sliding laws are implemented to compute a basal friction coefficient (β), of which each law has advantages and disadvantages (Joughin et al., 2019). In this thesis, we use the newest implemented regularised Coulomb law by Zoet and Iverson (2020), which is based on experiments of ice flow over water saturated till and thus takes into account slip over both hard and soft beds:

$$\beta = N \cdot \tan(\phi) \cdot u^{\frac{1}{p-1}} (u + u_t)^{\frac{-1}{p}}, \quad (2.4)$$

where u is the horizontal velocity, and u_t and p are a uniform transition velocity and slip exponent, respectively.

The variable N is the effective pressure, which is the overburden pressure minus the pore water pressure. The overburden pressure can be described as $\rho g H$. There are different approximations to compute the pore water pressure. In this thesis, the newest approach proposed by Martin et al. (2011) is used, in which the pore water pressure is dependent on the ice thickness and scales with the bedrock topography and the sea level. The pore pressure increases with ice thickness and decreases with bedrock topography. The effective pressure is by default assumed to be 4% of the overburden pressure at sea level. The effective pressure then increases with bedrock elevation up to where the elevation equals 1000 m. Above that, the effective pressure equals the overburden pressure.

The variable ϕ is the till friction angle that approximates the bed roughness. There exist different parameterisations, for example Martin et al. (2011), where the angle is dependent on the bed topography. However, in this thesis a fixed friction field from a calibration procedure was used, as explained in section 2.2.2.

As ANICE is an older ice sheet model than IMAU-ICE, β is computed following another version of the regularised Coulomb law from Bueler and Brown (2009)):

$$\beta = N \cdot \tan(\phi) \cdot u^{\left(\frac{p-1}{u_{threshold}^p}\right)}, \quad (2.5)$$

where the plastic parameter p is set to 0.3 and the scaling velocity $u_{threshold}$ is set to $100 \frac{m}{s}$. N and ϕ are determined in the same way as in IMAU-ICE.

2.1.2. GROUNDING LINE POSITION

The basal friction applies only to grounded ice and the sub-shelf basal melt is only applied to floating ice. For this reason, we need to calculate the position of the grounding line which separates floating and grounded ice. To do so, the flotation function is solved,

which determines whether ice is grounded or floating, and provides a floating function (f). A grounding line parameterisation is used to define the grounding line position in regions where ice transitions from grounded to floating, following Leguy et al. (2021). In here, the floating function is computed at the center of each grid cell as follows:

$$f = -b - \frac{\rho_i}{\rho_o} H, \quad (2.6)$$

where b is the bedrock elevation, H the ice thickness, ρ_i the density of ice and ρ_o the density of ocean water. The floating function equals zero at the grounding line, is negative for grounded ice and when positive, the function equals the water depth between the ice shelf base and the seafloor.

In ANICE, the basal friction coefficient is multiplied with the grounding fraction, which is 1 if the cell centre is grounded and zero if the cell centre is floating. In IMAU-ICE, the basal friction coefficient is multiplied with a grounded fraction (ϕ_g). An interpolation process calculates the grounded fraction (ϕ_g) at the cell vertices by estimating how much of the surrounding grid box of the staggered grid is grounded ($f < 0$) using a bilinear interpolation scheme. The grid box of the staggered grid has its corners at the center of the grid cells of the main grid. Within the grid box, f is a bilinear function of x and y :

$$f(x, y) = a + bx + cy + dxy, \quad (2.7)$$

where x and y are scaled between 0 and 1. The southwest corner is at (0,0) and the northeast corner is at (1,1). a, b, c and d equal:

$$\begin{aligned} a &= f^{SW}, \\ b &= f^{SE} - f^{SW}, \\ c &= f^{NW} - f^{SW}, \\ d &= f^{NE} + f^{SW} - f^{NW} - f^{SE}, \end{aligned} \quad (2.8)$$

At the grounding line, $f(x, y)$ equals zero and y can be written as an explicit function of x . The grounded fraction at a vertex is then computed using an integral that can be solved analytically:

$$\phi_g = \int_0^{x_0} y(x) dx = \frac{(bc - ad) \ln|1 - \frac{ad}{bc}| + ad}{d^2} \quad (2.9)$$

Depending on the flotation condition, the grounded fraction varies smoothly between 0 (fully floating) and 1 (fully grounded). The grounded fraction is then applied to adjust the basal friction at grid vertices, ensuring that friction changes smoothly across the grounding line. This interpolation method ensures that the grounding line migration is handled accurately, even at coarser grid resolutions, improving the overall performance and stability of the simulations.

2.1.3. ICE VELOCITIES

Knowing the basal friction and the grounding line position we can solve the equations for the SSA (Equation 2.2a and 2.2b). The Shallow Shelf Approximation (SSA) requires an

iterative procedure because the ice viscosity is nonlinear and dependent on the strain rate (the rate of deformation of the ice) (Robinson et al., 2020). The effective strain rate ($\dot{\epsilon}$) is the second invariant of the strain rate tensor ($\dot{\epsilon}_{i,j}$). The strain rate tensor components are computed as follows:

$$\dot{\epsilon}_{i,j} = \frac{1}{2} \left(\frac{\partial u_i}{\partial x_j} + \frac{\partial u_j}{\partial x_i} \right), i, j = 1, 2, 3 \quad (2.10a)$$

$$\dot{\epsilon} = \left(\frac{1}{2} \dot{\epsilon}_{i,j} \dot{\epsilon}_{i,j} \right)^{\frac{1}{2}} \quad (2.10b)$$

The viscosity of the ice is a function of the strain rate through Glen's flow law, where the viscosity (η) decreases as the strain rate increases (i.e., ice deforms more easily when it's flowing faster):

$$\eta = \frac{1}{2} A^{-\frac{1}{n}} \dot{\epsilon}^{\frac{1-n}{2n}}, \quad (2.11)$$

where A is the flow factor, which is a function of the ice temperature according to an Arrhenius relationship (Huybrechts, 1996), and n is 3 in Glen's flow law.

Since the strain rate depends on the velocity field, and the velocity field depends on viscosity, there is a coupling between the two. Thus, to solve for the velocities, the model starts with a given initial viscosity, compute the velocity field, and then update the viscosity based on the newly calculated strain rate. This process is repeated iteratively until the viscosity and velocity fields converge to a consistent solution. The iterative procedure to compute ice velocities is adopted from Robinson et al. (2020).

To compute the velocities, first the gravitational driving stress (τ_d) in horizontal directions is computed using

$$\tau_{d,x} = -\rho_i g H \frac{\partial h}{\partial x} \quad (2.12a)$$

$$\tau_{d,y} = -\rho_i g H \frac{\partial h}{\partial y} \quad (2.12b)$$

Here, ρ_i is the density of ice, g is the gravitational acceleration, H is the ice thickness, and $\frac{\partial h}{\partial x}$ and $\frac{\partial h}{\partial y}$ are the surface slopes in x and y direction, respectively.

After this step the following iterative procedure is used to solve the effective viscosity, effective basal friction and ice velocities:

1. Calculate the total effective strain rate ($\dot{\epsilon}$) using equations 2.2a and 2.2b.
2. Calculate the effective viscosity (η) using equation 2.11.
3. Compute the product of the effective viscosity and the ice thickness.
4. Calculate the basal friction coefficient (β) using equation 2.4. The velocity components u and v are needed to compute β . The first iteration of the first time step starts with u and v equal to 0 everywhere, and the first iteration of each subsequent time step uses the final velocity from the previous time step.

5. At grid cells at the grounding line, apply the subgrid grounded fraction (Φ_g as computed using equation 2.9) to the basal friction coefficient β following $\beta_1 = \beta \cdot \Phi_g^m$, where m is a constant equal to 2, and β_1 is the corrected basal friction coefficient (Berends et al., 2022).
6. While the SSA equations involve nonlinear viscosity (because viscosity depends on the strain rate), the system is treated as linear for a given viscosity field as computed in step 2. After discretizing using finite differences on a staggered grid (as explained in detail in Berends et al. (2022)), a linear system of equations is formed: $A\mathbf{u} = \mathbf{b}$. The coefficient matrix A is derived from the discretization of the stress divergence terms (which include the viscosity and ice thickness). The right hand side, \mathbf{b} , is a vector representing the driving stress from the ice surface slope and basal drag terms and equals $\frac{-\tau_d \cdot \Delta^2}{N}$. \mathbf{u} is the vector of the unknown velocities \bar{u} and \bar{v} .
7. Check if the iteration has converged to a stable solution using the L^2 error norm:

$$\delta_{u,v} = \frac{2\sqrt{\sum(u_1 - u_0)^2 + \sum(v_1 - v_0)^2}}{\sqrt{\sum(u_1 + u_0)^2 + \sum(v_1 + v_0)^2}}, \quad (2.13)$$

where u_1 and v_1 are the velocities for the current iteration, and u_0 and v_0 are the velocities from the previous iteration. The sum is taken over all grid cells with nonzero velocity. In this thesis, the typical convergence limit ($\delta_{u,v}$) of 10^{-2} is used (Robinson et al., 2020).

2.1.4. SURFACE MASS BALANCE

Besides velocities, we also need the surface mass balance (SMB) and basal mass balance (BMB) in order to calculate the evolution of the ice sheet in time. The surface mass balance is computed with IMAU-ITM using the yearly mean atmospheric temperature and monthly precipitation as input. The precipitation and atmospheric temperature at present day is taken from ERA5 (Uppala et al., 2005). For the last glacial cycle, the precipitation is assumed equal to present day, and the time dependent spatially averaged atmospheric temperature is provided by De Boer et al. (2014). For projections, precipitation ratios and atmospheric temperature anomalies until the year 2300 result from two CMIP6 models, CESM2-WACCM and IPSL-CM6A-LR, and is provided by Coulon et al. (2024). To use this data for this thesis, an extra option was added to IMAU-ICE to read precipitation ratios and atmospheric temperature anomalies, interpolate to the correct time step and apply them to the present day precipitation and temperature from ERA5.

Ablation (A) is computed according to Bintanja et al. (2002):

$$A = \frac{4(T - T_f) + 0.513(1 - \alpha)Q_t - 88}{100} \quad (2.14)$$

where T_f is the melting temperature of ice (273.16 K), Q_t is the incoming shortwave radiation at the top of the atmosphere (in $\frac{W}{m^2}$) taken from Laskar et al. (2004) and α is the surface albedo. The albedo of ice-covered areas depends on the depth of the firn layer

and the melt of the previous year. The depth of the firn layer is computed using the snow-fall and can be maximum 10 meters thick. The coefficients in Equation 2.14 are derived by Bintanja et al. (2002) by calibrating model simulations of Antarctica to mass balance observations for the present-day climate.

Snowfall is computed using the precipitation multiplied by the snow fraction. This fraction is computed according to Ohmura et al. (1999) and depends on the atmospheric temperature. The part of precipitation that doesn't fall as snow, is considered as rainfall. Part of the rainfall refreezes, the amount of which is calculated according to Huybrechts and De Wolde (1999) based on the amount of water that refreezes on top of the snow-pack, and liquid water.

Finally, the SMB is computed as follows:

$$SMB = Snowfall + Refreezing - Ablation \quad (2.15)$$

This simplistic SMB parameterisation performs well for Greenland (Fettweis et al., 2020) and has the advantage that it can be used for glacial time scales because the incoming shortwave radiation at the top of the atmosphere follows from the Milankovitch theory. For the application on Antarctica, the SMB parameterisation has been tuned such that the modeled surface mass balance matched the observed surface mass balance (De Boer et al., 2014).

2.1.5. BASAL MASS BALANCE AND CALVING

The basal melt is computed by a quadratic temperature-depth dependent parameterization (Favier et al., 2019). In there, first the temperature and freezing point are derived at the base of the ice shelf based on provided temperature and salinity profiles. Next, the ocean freezing point is subtracted from the ocean temperature to obtain the difference in temperature available for melt. Last, the BMB is computed as follows:

$$BMB = \gamma_T \left(\frac{\rho_{SW} c_{po}}{\rho_i L_i} \right)^2 (T_o - T_f)^2, \quad (2.16)$$

where γ_T is the calibrated heat exchange velocity, ρ_{SW} the density of ocean water, ρ_i the density of ice, c_{po} the specific heat capacity of the ocean mixed layer, and L_i the latent heat of fusion of ice. The ocean temperature at present day is determined using a calibration process to an equilibrium state of the ice sheet, as explained in section 2.2.2. The salinity at present day is taken from the WOA which is extrapolated to the sub-shelf cavities (Zweng et al., 2019). The ocean temperature anomalies and salinity anomalies for projections until the year 2300 result from the same two CMIP6 models as the atmospheric temperature anomalies and precipitation ratios, CESM2-WACCM and IPSL-CM6A-LR, and is also provided by Coulon et al. (2024).

Leguy et al. (2021) defined three different parameterisations to determine sub-shelf melt at the grounding line, which are all applied in the ice sheet models ANICE and IMAU-ICE. In this thesis, the floatation condition melt parameterisation (FCMP) is used. Here, melt is applied to the full grid cell if the center of the grid cell is floating. Other parameterisations are the partial melt parameterisation, which uses a bilinear interpolation

scheme to determine the floating function of the grid cell to which the melt is proportional, and the non-melt parameterisation which assumes no melt at grounding line grid cells.

2

Calving is governed by a simple rule that initiates calving when the ice thickness exceeds a threshold, which is set to the commonly used value of 200 meters (Wilner et al., 2023).

2.1.6. TIME STEPPING

Both ANICE and IMAU-ICE use an adaptive time step for the ice-dynamical solver (Brends et al., 2022; De Boer et al., 2014). ANICE uses separate steps for the SIA (which is mostly diffusive) and the SSA (which is mostly advective), while IMAU-ICE always solves both simultaneously. In ANICE, the other model components (thermodynamics, surface/basal mass balance, climate forcing) are solved synchronously (i.e. in every ice-dynamical time step), while in IMAU-ICE these have their own, separate time steps. In the simulations presented in this thesis, we used 1 year time steps for the thermodynamic, SMB and bedrock modules, and 3 month time steps for the climate, ocean and BMB modules. To define the time step for the ice-dynamical solver in IMAU-ICE, two critical time steps are computed, namely the critical time step for advective ice flow and the critical time step based on the truncation error in ice thickness (Cheng et al., 2019; Robinson et al., 2020).

The critical time step for advective ice flow is calculated as follows:

$$\Delta t_{n+1} = \frac{\Delta x}{\bar{u} + \bar{v}}, \quad (2.17)$$

where Δx is the spatial resolution of the model (16 km), and \bar{u} and \bar{v} the vertically averaged horizontal velocities in two directions as before. The label $n + 1$ indicates the next time step.

The length of the critical time step based on the truncation error in ice thickness (χ) is calculated as follows:

$$\Delta t_{n+1} = \left(\frac{\epsilon}{\chi^{n+1}} \right)^{(k_l + k_p)} \left(\frac{\epsilon}{\chi^n} \right)^{-k_p} \Delta t_n, \quad (2.18)$$

where ϵ is the target tolerance, and $k_l = \frac{2}{10}$ and $k_p = \frac{1}{10}$ are control parameters. This time step and the necessary parameters is computed in the predictor-corrector method, which is explained in detail in section 2.2.

The time step for the ice dynamical solver is the smallest time step between the time step based on the advective ice flow and the time step based on the truncation error.

2.2. IMAU-ICE

In this section, IMAU-ICE is discussed in detail in terms of the general setup, the velocity and ice thickness computations, calibration, sea level, and bedrock since the adjustments to these modules only apply to IMAU-ICE and not to ANICE.

2.2.1. MODEL SETUP

To couple IMAU-ICE to the 3D GIA model, IMAU-ICE is required to restart every 5 years. For this purpose, the model was restructured such that the model restarts properly. To do so, the order in which modules are called for at each time step was adjusted compared to IMAU-ICE version 2.0 from Berends et al. (2022). The new order is shown in figure 2.1 and explained in detail below.

During initialisation of IMAU-ICE at a certain start time, all the input data fields are read, the SMB and BMB are computed, the ice temperature and velocities are read from a data file or a restart file, and the bedrock deformation is computed. Next, the length of the first time step is determined as described in the timestepping section. Last, the ice thickness at the end of the first time step is computed based on the mass transport equation. The ice thickness in the model is not updated yet, that is done during the time step and not in the initialisation. This initialisation process is shown in figure 2.1.

At each time step, several modules of IMAU-ICE are called for, in the order as shown in figure 2.1. First, the model checks which modules should be run at this specific time step, as described earlier in the timestepping section. Then, the geometry is updated based on the ice thickness that is computed at the previous time step. Then, SMB, BMB, and the temperature of the ice are computed. Last, the ice velocities and the new ice thickness and ice extent at the end of the time step are computed. The main steps of each time step, and the steps of the initialisation are shown in figure 2.1.

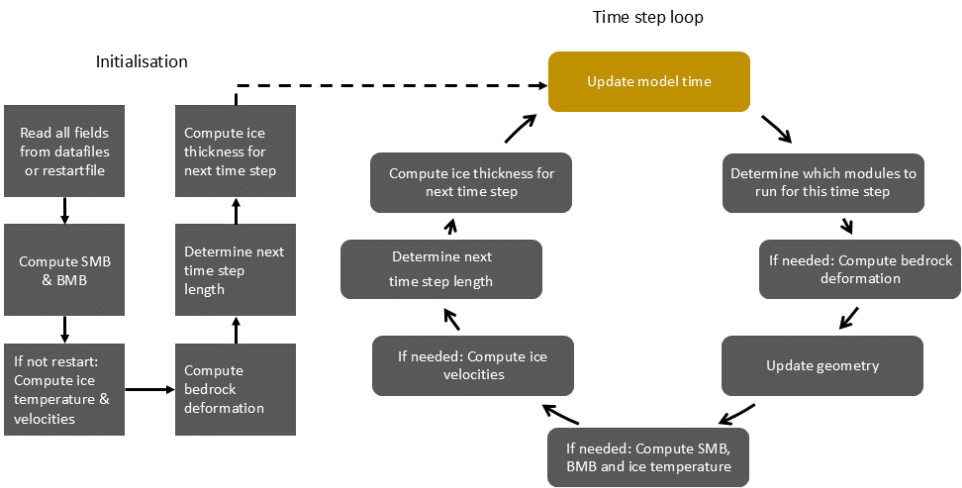


Figure 2.1: Flowchart of the time steps within IMAU-ICE. Each time step consists of one loop and the next time step starts at the yellow block called "Update model time". The ice velocities are computed following the iterative process as discussed in section 2.1.3.

The step "Compute ice velocities" in figure 2.1 is conducted in IMAU-ICE using the predictor-corrector method. This method significantly improves the accuracy of the solution compared to the forward Euler method (Robinson et al., 2020), which was used in ANICE (De Boer et al., 2013).

Following the predictor-corrector method, the ice thickness is first predicted using

the velocities from the previous time step. Then, the velocities are computed based on the predicted ice thickness, and the ice thickness is computed again starting from the ice thickness of the previous time step. The procedure contains the following steps:

2

1. Compute the predicted ice thickness as follows:

$$H_{n+1}^* = H_n + \Delta t_n [\nu_1 f(H_n, \bar{u}_n) + \nu_2 f(H_{n-1}, \bar{u}_{n-1})], \quad (2.19)$$

where H_{n+1}^* is the predicted ice thickness, Δt is the timestep, $\nu_1 = 1 + \frac{\zeta_t}{2}$, $\nu_2 = -\frac{\zeta_t}{2}$ and $\zeta_t = \frac{\Delta t_n}{\Delta t_{n-1}}$.

2. Set the previous ice thickness to the current ice thickness, and the current ice thickness to the predicted ice thickness. Compute the new surface elevation using the ice thickness change and bedrock elevation change over the time step. Then, compute the change in surface elevation over the time step and the new grounding line position.
3. Solve the velocities following the iterative procedure between viscosity and velocities as discussed in the section "ice velocities".
4. Calculate the change in ice thickness based on the new velocities, the surface elevation change as computed in step 2, and the surface and basal mass balances.
5. Set the current ice thickness to the ice thickness of the previous time step, and update surface elevation and grounding line position.
6. Calculate the corrected ice thickness (H_{n+1}) as follows:

$$H_{n+1} = H_n + \frac{\Delta t_n}{2} [f(H_{n+1}^*, \bar{u}_{n+1}) + f(H_n, \bar{u}_n)], \quad (2.20)$$

7. Calculate the applied ice thickness rate of change, which is dependent on the corrected ice thickness, the current ice thickness and the critical time step.
8. Determine the truncation error as follows:

$$\tau_{n+1} = \frac{\zeta_t (H_{n+1} - H_{n+1}^*)}{(3\zeta_t + 3)\Delta t_n}. \quad (2.21)$$

The truncation error is then used to determine the new velocity time step as described in the timestepping section above.

2.2.2. CALIBRATION

Two large uncertainties in the ice sheet model are the friction at the base of grounded ice and the ocean temperature at the base of ice shelves. For this reason, a calibration method was developed where the observed surface velocities are compared with the surface velocity from the modeled 3D velocity field. During the calibration time of 10000 years, the ocean temperature and friction parameter are tuned at each time step to obtain a 3D ice velocity field in equilibrium with the observed ice surface elevation and bedrock

elevation. By tuning these parameters, the velocity field is changed until the modeled ice thickness matches the observed ice thickness. This final velocity field of the calibration will serve as the present-day (initial) velocity field for the projections.

The inversion procedure of the friction parameter was developed by Berends et al. (2022). When modeled ice thickness at a certain location is thicker than the observed ice thickness, the friction parameter is decreased such that the velocities can increase which will lead to decreased ice thickness. Conversely, when modeled ice thickness at a certain location is thinner than the observed ice thickness, the friction parameter is increased such that the velocities will decrease which will lead to increased ice thickness.

The inversion procedure of the ocean temperature, occurring at the same time as the friction inversion, was developed for this thesis. During the calibration, the model inverts for an anomaly to the extrapolated ocean temperature provided by the World Ocean Atlas (WOA) (Zweng et al., 2019) and iterates until the ice thickness is in equilibrium and as close to the observed ice thickness at present day as possible (Morlighem et al., 2020).

To obtain an ice sheet in equilibrium at present day conditions, a 13000 year calibration is performed. The inversion of the ocean temperature is done by changing an anomaly to the extrapolated ocean temperatures from the WOA. This anomaly is increased when the modeled ice is too thick compared to the observed ice thickness from Bedmachine version 3 (Morlighem et al., 2020) such that more sub-shelf melt will occur and velocities will increase such that the ice thins. Conversely, the anomaly to the ocean temperature is decreased when the modeled ice is thinner than the observed ice thickness.

To apply this concept in the model, first the ice thickness difference with respect to the observations (ΔH) is computed.

$$\Delta H = H - H_{obs}, \quad (2.22)$$

where H is the modeled ice thickness and H_{obs} the observed ice thickness from Bedmachine version 3 (Morlighem et al., 2020). Then, two regularisation terms (θ_1 and θ_2) are computed as follows:

$$\theta_1 = \frac{\Delta H \cdot \tau}{H_0}, \quad (2.23a)$$

$$\theta_2 = \frac{2 \frac{dH}{dt}}{H_0}, \quad (2.23b)$$

where τ is the time scale for regularisation and H_0 is the ice thickness scale for regularisation. Both parameters are set to 100.

After each model time step, the ocean temperature is increased by a certain temperature anomaly, indicated by ΔT . In the model, this anomaly to the ocean temperature is not computed directly, but instead an adjustment to the anomaly is computed using the above mentioned regularisation terms (θ_1 and θ_2). This adjustment to the anomaly is the change of temperature over the model time step and is indicated by $\frac{d\Delta T}{dt}$. The adjustment to the anomaly is computed as follows:

$$\frac{d\Delta T}{dt} = \theta_1 + \theta_2 \quad (2.24)$$

The adjustment to the ocean temperature anomaly is extrapolated beyond the ice shelves. Then, a Gaussian smoothing filter is applied to the anomaly.

Finally, the adjustment is applied to the ocean temperature anomaly itself as follows:

2

$$\Delta T_i = \Delta T_{i-1} + \frac{d\Delta T}{dt} \cdot dt \quad (2.25)$$

where ΔT_i is the ocean temperature anomaly of the current time step, and ΔT_{i-1} the ocean temperature anomaly of the previous time step.

The ocean temperature that is used to compute the sub-shelf basal melt is simply computed by adding the anomaly to the ocean temperature itself.

In the first 100 years of the calibration, the grounding line is fixed to prevent a fast discharge of grounded ice due to warm ocean water, which leads to an overestimation of the basal melt rates inducing a too strong shock to the model. After 8000 years of inverting for the friction angle and the ocean temperature anomaly, the friction angle is kept fixed. After 10000 years of calibration, also the ocean temperature anomaly is kept fixed. The last 3000 years of the simulation shows that an equilibrium state has been reached and the difference of the modeled ice thickness and observed ice thickness is mostly insignificant except for small regions with maximum 500 meter difference (details are shown in section 4.5).

2.2.3. SEA LEVEL

Both ice sheet models ANICE and IMAU-ICE contain a bedrock elevation, an ice surface elevation and a sea level. The change in sea level due to bedrock deformation is included by altering the bedrock elevation. This will change the grounding line position and the ice above floatation, and therefore also the sea level.

The change in sea level due to the self-gravitation of the ice sheet is included by altering the sea level parameter directly. The scalar containing the global mean sea level in IMAU-ICE was used as the spatial variable containing the sea level. To study the effect of a regionally changing sea level on the ice sheet, IMAU-ICE is adjusted to apply a regional varying sea level from an external file when the option "geoid" is chosen. When using this option, the sea level is not a spatial uniform field like for the global mean sea level, but instead a spatially varying field. The geoid is computed by the GIA model, as explained in section 2.3.1.

2.2.4. BEDROCK

The surface topography, bedrock topography and ice thickness are taken from Bedmachine version 3 (Morlighem et al., 2020), which used data from airborne ice penetrating radar measurements and satellite interferometry, stereophotogrammetry, radar and altimetry. The bedrock elevation is defined with respect to global mean sea level and affects ice dynamics directly in several ways:

- The water depth is defined as the negative bedrock elevation and determines, together with the ice thickness, whether a column of ice on a grid cell of IMAU-ICE is floating, grounded, or partially grounded. The ice is determined to be floating when the ice thickness is smaller than the water depth times the density of sea water divided by the density of ice. The thickness above floatation is the ice thickness

minus the water depth times the same density ratio. The grounded fraction of a grid cell, which ultimately determines where the grounding line is exactly positioned, is then computed using the thickness above floatation of the neighbouring cells, as is explained in the grounding line position section above.

- The bedrock elevation determines, together with the ice thickness, the modeled surface elevation (S) of the ice sheet. The surface mass balance is dependent on the surface elevation via the surface temperature (T), which is computed as follows: $T = T_{obs} + (S - S_{obs}) \cdot \lambda$, where λ is the lapse rate of -0.01 K/m . T_{obs} is the observed surface elevation temperature at the observed surface elevation S_{obs} , which can also be replaced by a given surface temperature and surface elevation computed by an earth system model.
- The gravitational driving stress determining the ice velocities is dependent on the bedrock slope, which is the horizontal derivative of the bedrock elevation.
- In some parameterisations, such as Martin et al. (2011) which is used in this thesis, the bedrock elevation determines the pore water pressure at the base of the grounded ice sheet as described in point 4 of the velocity procedure in section 2.2.1.
- In one parameterisation of sub-shelf basal melt, which is used in the ice sheet model ANICE of Chapter 3, the sub-shelf basal melt is scaled by the water depth between the bathymetry and the base of the ice shelf, which is in turn dependent on the surface elevation (as discussed in the first bullet). However, the sub-shelf basal melt parameterisation of chapters 4 and 5 is not dependent on the water depth.

The bedrock deformation was computed in IMAU-ICE using the Elastic Lithosphere Relaxed Asthenosphere (ELRA) model. This model simplifies the Earth's response to surface loading by considering the lithosphere as an elastic plate and the asthenosphere as a viscous layer that relaxes over time. The equation governing the time-dependent bedrock deformation in the ELRA model is:

$$\frac{db(i, j)}{dt} = \frac{w(i, j) - b(i, j)}{\tau}, \quad (2.26)$$

where $\frac{db}{dt}$ is the bedrock elevation change over time, w is the equilibrium profile from the elastic lithosphere, b the current bedrock elevation, i, j the grid coordinates, and τ the relaxation time. The details of the ELRA model are described in section 5.2.

For this thesis, IMAU-ICE was extended to apply a spatially varying relaxation time in the ELRA model. The option is called LVELRA. Furthermore, the option was added to use a prescribed bedrock deformation over time. For this, an externally computed bedrock deformation is applied to the bedrock elevation linearly over time. This option is called "external GIA" and relies on GIA calculated with an external model as described in the following section.

2.3. GLACIAL ISOSTATIC ADJUSTMENT MODEL

To couple a GIA model to an ice sheet model, the GIA model has to save all the variables after each time step and write the surface deformation to a file. To run a time step,

the model needs to restart from the previous time step. For this thesis, the GIA model from Blank et al. (2021) was restructured and a restart option was added. The coupling method, the models, and the changes made to the models are discussed in detail in section 3.2.

2.3.1. MODEL SETUP

The Earth's mantle behaves elastically over short timescales but exhibits viscous flow over longer timescales. For a spherical, self-gravitating, incompressible Earth, the governing equations of motion after linearization are (Wu and Peltier, 1982):

$$\vec{\nabla} \cdot \vec{\bar{\tau}} - \vec{\nabla} (\vec{u} \cdot \rho_0 g_0 \hat{r}) - \rho_0 \vec{\nabla} \Phi_1 = 0. \quad (2.27)$$

Here, $\vec{\bar{\tau}}$ is the stress tensor, \vec{u} is the displacement vector, and \hat{r} is a unit vector in the radial direction. The variables ρ, g, Φ are density, gravitational acceleration and gravitational potential, respectively. The subscript zero denotes the hydrostatic background state, while subscript one refers to the perturbed state. The first term in equation 2.27 represents the internal stresses within the Earth. The second term describes the advection of pre-stress in the Earth, which is caused by the initial gravitational field. This stress, the hydrostatic background stress, is carried by the material in motion and acts as the restoring force that maintains balance in response to surface changes, known as isostasy. The third term accounts for the effect of self-gravitation where the redistribution of mass due to deformation alters the gravity field and its potential.

Compressibility cannot directly be implemented in spherical models based on Abaqus (Reusen et al., 2023). Implementing compressibility would therefore require additional code which increases the computation time (Huang et al., 2023). The effect of compressibility on vertical deformation is small and can be partly compensated by adjusting the rigidity of the model (Tanaka et al., 2011). Therefore, in this thesis the Earth is assumed to be incompressible, meaning that there is no internal buoyancy, and changes in the gravitational potential do not need to be computed with Poisson's equation. Instead, the perturbed gravitational potential Φ is a function of the radial displacements and the surface load, and can be solved using the following Laplace equation (Wu, 2004):

$$\frac{\partial^2}{\partial r^2} \Phi_{l,m} + \frac{2}{r} \frac{\partial}{\partial r} \Phi_{l,m} - \frac{l(l+1)}{r^2} \Phi_{l,m} = 0, \quad (2.28)$$

where r is the Earth's radius. The Laplace equation is solved by applying boundary conditions assuming density varies radially but not laterally (Wu and Peltier, 1982). The perturbed gravitational potential is computed for each layer of the GIA model. In this section, only the computation of the perturbed gravitational potential at the surface is described. Including the boundary conditions for the surface of the Earth, the solution to the Laplace equation is:

$$\Phi_{l,m} = \frac{4\pi G}{2l+1} r [\sigma_{l,m} + \rho_0(r) U_{l,m}(r)] + \frac{4\pi G}{2l+1} \sum_{k=0}^{N-1} r_k U_{l,n}(r_k) (\rho_k - \rho_{k+1}) \left(\frac{r_k}{r} \right)^{l+1} \quad (2.29)$$

where $\sigma_{l,m}$ and $U_{l,m}$ are the coefficients of the spherical harmonic decomposition of the surface load and radial displacements, respectively, N is the total number of layers, G the

gravitational constant ($6.67430 \cdot 10^{-11} m^3 kg^{-1} s^{-2}$), ρ_0 the density at the surface, ρ_k the density of the k^{th} layer, r the distance from the Earth's center to the surface ($6371 \cdot 10^6 m$), r_k the distance from the Earth's center to the outer radius of the k^{th} layer.

Equation 2.29 computes the perturbed gravitational potential due to changes in ice and ocean loading (σ), and due to the displacement itself (U). The changes in ice and ocean loading can be computed by the sea level equation:

$$S = N - U, \quad (2.30)$$

where S is the change in sea level, N the change in geoid and U the radial displacement. The sea level equation can be solved globally including migrating shorelines but solving that is computationally expensive and requires to compute the ice sheet evolution globally (Mitrovica and Milne, 2003), whereas we only compute the Antarctic Ice Sheet evolution in this thesis. Furthermore, the changes in ocean loading are significantly smaller than the changes in ice loading (as discussed in sections 3.2 and 4.5). Therefore, the ocean loading is not taken into account as a loading on the GIA model, and only the ice loading is applied.

The sea level determines, together with the bedrock elevation, whether ice is floating or grounded, as discussed in section 2.2.4. The projections presented in this dissertation use a fixed sea level in time but tests are conducted to study the effect of a spatial- and time-varying sea level in the ice sheet model. To obtain this varying sea level, the GIA model was used to compute the change in geoid. The geoid is the equipotential surface of the Earth's gravity field that best approximates regional sea level.

The geoid height (N) depends on the difference between the gravitational potential at a given point (V) and the reference potential surface (V_0), and can be computed as follows:

$$N = \frac{V - V_0}{g}, \quad (2.31)$$

where g is the average gravitational acceleration near the Earth's surface ($9.81 m/s^2$). The spherical harmonic coefficients computed with equation 2.29 are converted to the spatial domain such that the perturbed gravitational potential can be used to compute the geoid according to equation 2.31. The geoid is then applied in the ice sheet model as described in section 2.2.

The equations of motion can be solved by the finite element software Abaqus after applying a stress transformation (Wu, 2004). The finite element method is coupled to the Laplace equation using an iterative scheme. This is typically done by, first, computing the displacement using the FE method over all time steps and then computing the gravitational potential over all time steps. The gravitational potential is added as an additional loading, after which the radial displacements at all timesteps can be computed based on the updated loading (Wu, 2004). This method requires the surface loading for the full simulation time to be known. However, in this thesis, the loading is computed by the ice sheet model and depends on the radial displacements computed by the GIA model. Therefore, the iterations between the FE model and the Laplace equation are applied at each time step, instead of over the full simulation period.

The change in gravitational potential due to deformation itself is hereafter referred to as the effect of self gravitation of the Earth on solid Earth deformation. Chapters 3 and 4 include a sensitivity study on the effect of self gravitation of the Earth over a glacial cycle and projections, respectively. We found that the effect of including self gravitation of the Earth is relatively small, whereas the computation time doubles. Therefore, the coupling between the FE method and the Laplace equation has been excluded in the main results of this thesis.

2.3.2. RHEOLOGY

The model calculates the displacement of each element after placing a certain load on the Earth's surface for a period of time which requires input of the so-called constitutive equation that relates stress and strain through material parameters. The material of the mantle is viscoelastic and the strain rate is computed using equation 2.32 (van der Wal et al., 2013; Blank et al., 2021).

$$\Delta\epsilon_{ij} = \frac{3}{2}(B_{diff} + B_{disl}\tilde{q}^{n-1})q_{ij}\Delta t \quad (2.32)$$

$\Delta\epsilon_{ij}$ is the strain, B_{diff} and B_{disl} are the spatially variable diffusion and dislocation parameters respectively, \tilde{q} is the Von Mises stress which is assumed to be 0.1 MPa (Ivins et al., 2023), n is the stress exponent, taken to be 3.5, consistent with Hirth and Kohlstedt (2003), q_{ij} is the deviatoric stress tensor, and Δt is a variable time increment for the numerical integration within Abaqus during the coupling time step that is computed for a specified accuracy. With this method, the model does not require average mantle viscosity and lithospheric thickness as input parameters as many other methods do (see overview in Ivins et al. (2023)). The diffusion and dislocation parameters in equations 5.2a and 5.2b depend on the grain size of the mantle, the water content, the pressure and the temperature. Pressure is calculated based on the densities in the earth model and temperatures is derived from seismic observations. The material parameter grain size and water content can also be used in and constrained by geologic observations (e.g. Martin and van der Wal (2023)), and other geodynamic models. However, the formulation results in viscosity values that are not well constrained, therefore calibration of the model is necessary in areas where GIA is relatively well known.

To create 3D rheologies, a seismic model is used to convert seismic velocity anomalies to dislocation and diffusion parameters, which then determine the deformation in the mantle for given ice loading. The seismic model was adjusted to include high resolution seismic information over Antarctica combined with global seismic model. How different 3D structures are obtained using this new seismic model is described in detail in sections 3.2 and 4.5.

The mantle viscosity in Antarctica varies radially and laterally with several of orders of magnitude (van der Wal et al., 2023). The variation is largest between East and West Antarctica, but varies significantly within West Antarctica as well. Here we constrain the mantle viscosity by the viscosity values obtained in Palmer Land in the Antarctic Peninsula, in the Weddell Sea Embayment and in the Amundsen Sea Embayment (Wolstencroft et al., 2015; Bradley et al., 2015; Barletta et al., 2018). These values are used to fit grain size and water content, as described in detail in section 4.5.

The model has a high resolution area over Antarctica. With a global resolution of 200 km and an Antarctic resolution of 30 km, the model contains about 290,000 elements. Each element get assigned a density and Youngs modulus, dependent on the layer that the element is in. Between 35 and 670 km depth, the elements get assigned a dislocation and diffusion parameter. All elements in the top 35 km get assigned a viscosity of $10^{44} Pa \cdot s$, which is purely to force this layer to respond elastic. Certain elements in the upper mantle also respond elastic but that is not prescribed and instead determined by the assigned diffusion and dislocation parameter, and the applied stress by changes in surface laoding. Elements in the lower mantle gets assigned a constant viscosity of $5 \cdot 10^{21} Pa \cdot s$.

2.4. COUPLING METHOD

In this dissertation, the GIA model is coupled to two different ice sheet models: ANICE for Chapter 3, and IMAU-ICE for chapters 4 and 5. Section 3.2 describes in detail the coupling method for a glacial cycle, and section 4.5 describes in detail the coupling method for a projection. In all three chapters the same concept is used for the coupling, which is described further in this section.

A simulation is initialised by running the ice sheet model over the first coupling time step using the ELRA model. Now, the initialisation has finished and the simulation of

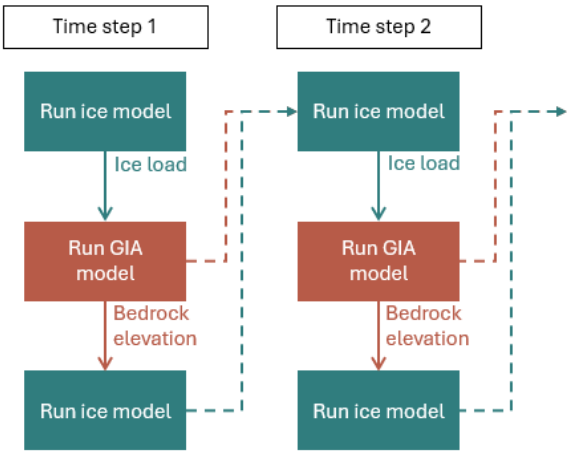


Figure 2.2: Concept of the coupling method.

the first coupling time step starts by running the ice sheet model while applying the bedrock deformation that resulted from the initialisation. This step is shown by the first blue block of the conceptual diagram in figure 2.2. The resulting change in ice load over the first coupling time step is then passed to the GIA model which computes the bedrock deformation over the first coupling time step. Last, this bedrock deformation is passed back to the ice sheet model, which is again run over the first coupling time step. Hereafter, the ice sheet configuration at the end of the first coupling time step is used as starting point for the second coupling time step, together with the last computed bedrock defor-

mation. This is indicated by the dashed blue and red lines in figure 2.2. For the second coupling time step, first the ice sheet model is run, then the GIA model, and finally the ice sheet model, after which the model moves on to the third time step, and so on.

The change in surface loading over a time step, given by the ice sheet model, is applied linearly over a time step in the GIA model. Moreover, the bedrock deformation resulting from the GIA model is applied linearly to the bedrock elevation in the ice sheet model. The time step should therefore be short enough such that the linear approximation is valid. Tests to determine the coupling time step and the number of iterations within one coupling time step are described in section 3.2 for the last glacial cycle, and section 4.5 for the projections. The tests show that for a small enough time step length, the model converges after 1 iteration. Therefore, figure 2.2 shows the application of 1 iteration. A coupling time step of 5000 years was chosen for the glaciation phase of the last glacial cycle, 500 years for the deglaciation phase, and 5 years for projections.



King George Island, Antarctica

3

SIMULATION OF A FULLY COUPLED 3D GIA - ICE-SHEET MODEL FOR THE ANTARCTIC ICE SHEET OVER A GLACIAL CYCLE

ABSTRACT

Glacial Isostatic Adjustment (GIA) has a stabilizing effect on the evolution of the Antarctic Ice Sheet by reducing the grounding line migration following ice melt. The timescale and strength of this feedback depend on the spatially varying viscosity of the Earth's mantle. Most studies assume a relatively long laterally homogeneous response time of the bedrock. However, the mantle viscosity is spatially variable with a high mantle viscosity beneath East Antarctica, and a low mantle viscosity beneath West Antarctica. For this study, we have developed a new method to couple a 3D GIA model and an ice-sheet model to study the interaction between the Solid Earth and the Antarctic Ice Sheet during the last glacial cycle. In this method, the ice sheet model and GIA model exchange ice thickness and bedrock elevation during a fully coupled transient experiment. The feedback effect is taken into account with a high temporal resolution where the coupling time steps between the ice-sheet and GIA model are 5000 yr over the glaciation phase and vary between 500 and 1000 yr over the deglaciation phase of the last glacial cycle. During each coupling time step, the bedrock elevation is adjusted every ice-sheet model time step and the deformation is computed for a linearly changing ice load. We applied the method using the ice-sheet model ANICE and a 3D GIA finite element model. We used results from a regional seismic model for Antarctica embedded in the global seismic model SMEAN2 to determine

Published as: van Calcar, C.J., van de Wal, R.S.W., Blank, B., de Boer, B., and van der Wal, W.: Simulation of a fully coupled 3D glacial isostatic adjustment – ice sheet model for the Antarctic Ice Sheet over a glacial cycle. *Geoscientific Model Development*, 16, 5473–5492, 2023. Minor corrections are included in this thesis.

the patterns in the mantle viscosity. The results of simulations over the Last Glacial Cycle show that differences in mantle viscosity of an order of magnitude can lead to differences in grounding line position up to 700 km and to differences in ice thickness in the order of 2 km at present day near the Ross Embayment. These results underline and quantify the importance of including local GIA feedback effects in ice-sheet models when simulating the Antarctic Ice Sheet evolution over the Last Glacial Cycle.

3.1. INTRODUCTION

The stability of the Antarctic Ice Sheet (AIS) is largely controlled by the bedrock profile (Pattyn and Morlighem, 2020). The bedrock elevation and slope vary in time due to Glacial Isostatic Adjustment (GIA), which is the response of the solid Earth to a changing ice load. Accurate GIA simulations are needed when analyzing the past and future ice sheet dynamics and stability (e.g. Pan et al., 2021; Gomez et al., 2010). At present, the AIS loses mass in areas where the basal melt increases and the grounding line retreats (Meredith et al., 2019). Fig. 3.1 shows schematically how GIA affects grounding line migration when the ice sheet retreats. Initially, before the on-set of ice shelf melting, the ice sheet and bedrock topography are represented by the solid grey and brown lines, respectively. The initial position of the grounding line is indicated by p1. Thinning of the ice shelves by increased basal melting, represented by the dashed grey line, leads to a retreat of the grounding line to position p2. Due to a decreasing ice thickness, and thus a decreasing ice load, the Earth's surface experiences a direct instantaneous elastic uplift and a delayed uplift of the viscoelastic mantle of the Earth, represented by the dashed brown line. The uplift of the bedrock causes a local shoaling of water, decreased ice flux towards the ice shelf, and an outward movement of the grounding line to position p3 (Fig. 3.1). As a consequence, the GIA feedback slows down retreat of the grounding line and acts as a negative feedback (Larour et al., 2019; Konrad et al., 2015; Adhikari et al., 2014; Gomez et al., 2012).

There exist other GIA feedbacks on the ice sheet evolution apart from the direct effect on the grounding line via the bedrock elevation. First, the local sea level decreases due to the diminishing gravitational attraction of the ice on the surrounding water in case the ice sheet melts (e.g. De Boer et al., 2017; Gomez et al., 2015). As a consequence, a decrease in sea level reduces the load of the ocean on the bedrock and in turn enhances uplift from GIA, although to a smaller degree than the loss of grounded ice. Second, GIA could steepen or flatten the bed slope dependent on the local topography. A flattened bed slope decreases the rate of basal sliding and ice deformation and therefore decreases the ice flux and ice velocity towards the shelves (Adhikari et al., 2014). Finally, GIA stabilizes the ice sheet as it reduces the surface elevation change of the ice sheet caused by surface melt in a warming climate. The reduced lowering of the surface elevation thereby suppresses melt rates (Van Den Berg et al., 2008).

Several types of models have been developed to include GIA in ice-sheet models. A widely used approach to take changes in bedrock topography into account is by using an Elastic Lithosphere Relaxing Asthenosphere (ELRA) model (Le Meur and Huybrechts, 1996). This is a two-layer model that contains a local elastic layer and an asthenosphere that relaxes with a single constant relaxation time. This simplified model is computationally cheap and provides a first-order estimate of bedrock changes (e.g. Pelletier et al.,

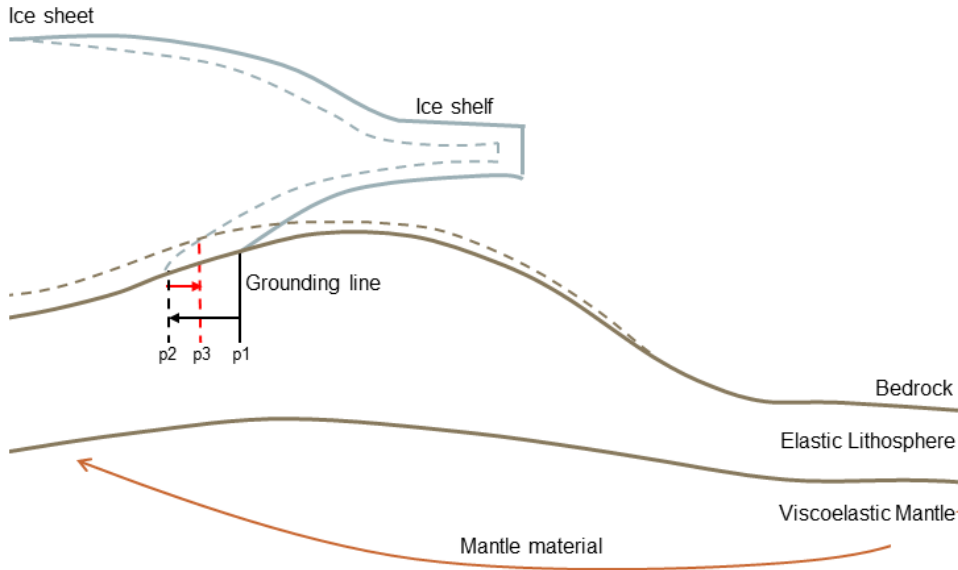


Figure 3.1: Schematic figure of GIA feedback on grounding line migration. The solid light grey and upper brown lines represent the initial ice sheet/shelf and bedrock elevation respectively before retreat of the grounding line. The lower solid brown line separates the elastic lithosphere and the viscoelastic mantle. p1 is the grounding line position corresponding to the initial steady state. The dashed light grey line represents the ice sheet/shelf after retreat, the dashed black line is the perturbed mantle elevation, and the dashed brown is the new bedrock surface. p2 is the grounding line position after retreat without GIA effects. P3 is the grounding line position after the GIA response. The change in sea level is not applied as load on the GIA model and only the global mean sea level is prescribed as forcing on the ice-sheet model. The sea level is for this reason not shown in this figure.

2022; De Boer et al., 2017; Pattyn, 2017). However, the ELRA approach assumes a homogeneous flat Earth while the actual Earth properties vary radially and laterally. To partly overcome these limitations, Coulon et al. (2021) included regions with different relaxation times in the ELRA model to capture the main patterns of spatial variability in the relaxation time scale. Still, ELRA neglects the effect of self-gravitation, the size dependency of the Earth's response to ice loading, and the fact that larger ice sheets respond to deeper Earth characteristics and smaller ice sheets respond to shallower Earth characteristics (Wu and Peltier, 1982).

The solid earth response is mainly determined by the thickness of the elastic lithosphere and the viscosity of the mantle. ELRA models have been improved by coupling the lithosphere with a viscous half-space, where mantle viscosity can be used as input parameter instead of the relaxation time (Albrecht et al., 2020; Bueler et al., 2007). Another approach to compute GIA is self-gravitating visco-elastic (SGVE) spherical Earth models. They compute the response to global ice sheet thickness changes with radially varying Earth models, labeled 1D GIA models, that account for gravity field perturbations. Most 1D GIA studies also account for relative sea level change by solving the sea level equation (DeConto et al., 2021; Pollard et al., 2017; Konrad et al., 2015; De Boer et al., 2014;

Nield et al., 2014; Gomez et al., 2013; Whitehouse et al., 2012). For Antarctica, these 1D GIA models commonly use an Earth structure with an upper mantle viscosity of 10^{20} - 10^{21} Pa·s and a lithosphere of approximately 100 km thick which is close to the Antarctic average (Gomez et al., 2018; Geruo et al., 2013). The present-day ice surface elevation resulting from a coupled 1D GIA – ice-sheet model with a mantle viscosity of 10^{21} Pa s can be achieved with reasonable accuracy by the ELRA approach with a relaxation time of 3000 yr, but deformation through time differs and it is not known how well other viscosities can be approximated (Pollard et al., 2017; Van Den Berg et al., 2008; Le Meur and Huybrechts, 1996).

However, even 1D GIA models are oversimplified for realistic Antarctic conditions, as it can be derived from seismic data that the viscosity of the mantle under the AIS varies laterally with six orders of magnitude with much lower viscosities approximately 10^{18} Pa·s in West Antarctica than the generally assumed global average mantle viscosity (Hay et al., 2017; van der Wal et al., 2015; Ivins et al. 2021). In these low viscosity regions, the Earth's mantle approaches isostatic equilibrium one to two orders of magnitude faster than the timescale of 3000 yr that is commonly used in the application of ELRA models (Whitehouse et al., 2019; Barletta et al., 2018). This can only be overcome by 3D GIA models which have been developed to simulate GIA using a lateral variable rheology in Antarctica (Yousefi et al., 2022; Blank et al., 2021; Powell et al., 2021; Nield et al., 2018; Hay et al., 2017; van der Wal et al., 2015; A et al., 2013; Geruo et al., 2013; Kaufmann et al., 2005), but those approaches so far neglected the GIA feedback on the ice sheet evolution because they use a predefined ice sheet history.

Whitehouse (2018) emphasises the importance of coupled 3D GIA – ice-sheet models to study regions with a low mantle viscosity and there are ongoing efforts to develop an efficient coupling method on a high temporal resolution using a 1D GIA model (Han et al., 2021). Coupled GIA – ice-sheet models need an iterative method to include the GIA feedback since ice-sheet models need bedrock deformation as input to compute the ice thickness and GIA models need ice thickness as input. We define a coupling time step as the time period over which the ice sheet model and GIA model exchange ice thickness and bedrock elevation during a fully coupled transient experiment. There are coupled 1D GIA – ice-sheet models that use short coupling time steps of tens of years but those models simulate projections and hence consider a much shorter time scale than the glacial cycle (DeConto et al., 2021; Konrad et al., 2015). The only model that couples 3D GIA with ice dynamics is developed by Gomez et al. (2018), who show significant differences in ice thickness of up to 1 km in the Antarctic Peninsula and the Ross Embayment when a 3D Earth rheology was used instead of a 1D rheology. From this model it can be concluded that uplift is typically underestimated in West Antarctica and overestimated in East Antarctica when using lateral homogenous Earth structures in ELRA or 1D GIA models (Nield et al., 2018). Gomez et al. (2018) apply the following iteration method to simulate the AIS evolution from 40 kyr to present-day. First, the 3D GIA model computes bedrock elevation changes relative to the geoid at time steps of 200 yr for the entire 40 kyr using ice thickness changes from a previous coupled 1D GIA simulation. These bedrock elevation changes are corrected at each time step for the difference between the simulated present-day bedrock topography and the observed present-day topography. The corrected bedrock elevation changes are passed to the ice-sheet model to recompute the ice

thickness history for the entire period of 40 kyr till present-day with time steps of 200 yr. Finally, the new ice thickness history is passed to the 3D GIA model and the process is repeated until the ice and bedrock elevation histories converge. Typically, only four iterations are needed. However, both models are still simulated over the entire period of 40 kyr with a fixed ice or bedrock elevation history as input. As a consequence the coupling time step between ice sheet model and 3D GIA model is 40 kyr. Yet, for example in the Amundsen Sea embayment in West Antarctica, GIA occurs on decadal to centennial timescales (Barletta et al., 2018). Present-day GIA estimations and the evolution of the ice sheet could therefore be improved by including the 3D GIA feedback in a coupled model at coupling time steps shorter than 40 kyr.

This study presents a method to fully couple an ice-sheet model and a 3D GIA model on century to millennial timescales from 120 ka onwards. The method simulates the 3D GIA feedback by iterating an ice-sheet model and a 3D GIA model at every single coupling time step. The method is applied using the ice-sheet model ANICE (De Boer et al., 2013), and a 3D GIA finite element (FE) model (Blank et al., 2021), where the coupling time steps are 5000 yr over the glaciation phase and vary between 500 and 1000 yr over the deglaciation phase of the last glacial cycle. The GIA model computes deformation due to ice loading and does not solve the sea level equation, but the viscoelastic model does account for the effect of self-gravitation of the mantle deformation when a 1D Earth structure is used. To decrease computational time, the GIA model excludes the effect of self-gravitation when a 3D Earth structure is used which is explained in section 3.2.2. Global Mean Sea Level (GMSL) from the northern hemisphere ice-sheets is prescribed in the ice-sheet model. The ice-sheet model is applied to Antarctica to assess the impact of the stabilizing GIA effect on the AIS evolution over the last glacial cycle using 1D and 3D Earth structures.

We assess whether widely used 1D Earth structures, for example those used by Pollard et al. (2017), yield similar stability characteristics for ice sheet evolution caused by bedrock uplift, in comparison to 3D Earth structures during the deglaciation phase. The developed coupled model can be applied to different regions and the coupling method could be applied to different ice-sheet models and GIA models. The model has potential to improve GIA estimates, and hence corrections for ongoing GIA to geodetic data (e.g. Scheinert et al., 2021). This method cannot only be applied to improve glacial-interglacial ice sheet histories, but also for future projections of the AIS evolution.

3.2. METHOD

The coupling method that we present in this chapter can be applied to any ice-sheet and GIA model, as long as the models have the possibility to restart at certain time steps. We applied the coupling method to the ice sheet model ANICE and the 3D GIA model, which are introduced first in this section 3.2.1 and 3.2.2. The coupling method alternates between the ice-sheet model and the GIA model, where the ice-sheet model uses the bedrock deformation computed by the GIA model and the GIA model uses the changes in ice thickness computed by the ice-sheet model. The interpolations that are necessary to feed the ice-sheet model output to the GIA model and the GIA model output to the ice-sheet model are discussed in section 3.5. Finally, we describe the coupling method in section 3.2.3. The models are coupled at a coupling time step that varies during a

glacial cycle. During the glaciation phase, the coupling time step is 5000 yr and during the deglaciation phase, the coupling time step is 1000 and 500 yr. The effect of the size of the coupling time step is discussed in section 3.2.3. At intermediate time steps the ice-sheet model uses a linear interpolation of the bedrock changes and the GIA model uses a linear interpolation of the ice thickness changes.

3.2.1. ICE-SHEET MODEL: ANICE

The ice-sheet model ANICE is a global 3D ice-sheet model allowing to simulate the AIS, Greenland ice sheet, Eurasian ice sheet and North American ice sheet separately or simultaneously (de Boer et al., 2013). Each ice sheet can be simulated on different equidistant grids. The horizontal resolution is 20 km for Greenland and 40 km for the other regions. The temporal resolution of ANICE is 1 yr, hereafter referred to as the ANICE time step. ANICE has been used for a variety of experiments (Berends et al., 2018, 2019; Bradley et al., 2018; De Boer et al., 2013, 2017; Maris et al., 2014). For this study, ANICE is used to simulate the Antarctic Ice Sheet evolution with a resolution of 40x40 km. Atmospheric temperature and GMSL act as the main forcing for the ice-sheet model, as is shown in Fig. 3.10, and are the result of previous ice volume reconstructions using ANICE and benthic isotopes forcing (De Boer et al., 2013). The accumulation for the ice sheet is computed using present-day monthly precipitation from ERA40, which are temporally extrapolated as a function of the free atmospheric temperature (Bintanja and van de Wal, 2008; Bintanja et al., 2005). A time and latitude dependent surface temperature-albedo-insolation parameterization is used to calculate ablation (Berends et al. 2018). Insolation changes are based on the solution by Laskar et al. (2004). The Shallow Shelf Approximation (SSA) (Bueler and Brown, 2009) is used to solve mechanical equations to determine sliding and velocities of ice shelves, and the Shallow Ice Approximation (SIA) is used to compute velocities of grounded ice (Morland, 1987; Morland and Johnson, 1980). Basal sliding follows a Weertman friction law where friction is controlled by bedrock elevation. The position of the grounding line and GMSL determine whether ice is grounded or floating, thus whether the ice experiences sub-shelf melt or not. A combination of the glacial-interglacial parametrization by Pollard and DeConto (2009) to scale the global mean ocean temperature beneath the shelf, and the ocean temperature-based formulation by Martin et al. (2011) are used to compute sub-shelf melt. This parameterisation assumes a linear relation between sub-shelf melt and ocean temperature. Changes in ocean circulation are not taken into account.

Besides the effect of GMSL, there is an effect from regional sea-level variations as well. Although the effect of the northern hemisphere ice sheets on GMSL is significant, the effect of the AIS itself is most important for regional sea level (Gomez et al., 2020). At regions where grounded ice melts, such as the Ross and the Filchner-Ronne embayments during the deglaciation phase, the near field sea level is reduced due to the decreasing gravitational attraction between the ice sheet and the ocean. De Boer et al. (2014) studied the differences between using ANICE with a gravitationally self-consistent sea-level, and with global mean sea level. At last glacial maximum, the ice volume of the AIS is lower when including regional sea level because the increased regional sea level due to increased gravitational attraction of the growing ice sheet leads to a small reduction in grounded ice. During the deglaciation, the differences in ice volume are small. The spa-

tial variation caused by Northern Hemisphere ice volume changes over a glacial cycle is smaller than the spatial variation in regional sea level by Antarctic changes and is therefore considered a second order effect. The regional sea level variation is not yet included in this model.

The standard version of ANICE uses the ELRA method to compute bedrock elevation changes using a uniform relaxation time that is usually taken to be 3000 yr. For this study, ANICE is adjusted to use the bedrock deformation computed by a GIA model instead of computing the bedrock deformation using the ELRA method (see section 3.2.3 for explanation of the chosen coupling time steps). The initial topography at 120 ka is taken from ALBMAP (Le Brocq et al., 2010). Within one coupling time step, the bedrock elevation is updated in ANICE at time steps of 1 yr using linear interpolation of the deformation computed by the GIA model:

$$b_t = b_{t0} + \frac{\Delta b}{\Delta t_{coupling}} \cdot \Delta t_{ANICE}, \quad (3.1)$$

where b_t refers to the updated bedrock elevation at the ANICE time step, b_{t0} refers to the bedrock elevation at the beginning of the coupling time step, $\frac{\Delta b}{\Delta t_{coupling}}$ refers to the total deformation of one coupling time step computed by the GIA model divided by the length of the coupling time step in years, and Δt_{ANICE} refers to the ANICE time step of 1 yr. Linear interpolation introduces inaccuracy of the true GIA deformation which generally follows an exponential curve. As a consequence, the total deformation at the end of the coupling time step is the same, but the deformation would be slightly underestimated at the beginning of the coupling time step. This effect is higher at regions with a lower viscosity of the Earth's mantle due to the increased nonlinearity of the Earth's response compared to higher viscosity regions. The effect of this approximation can be reduced by reducing the length of the coupling time step as is shown in section 3.2.3.

3.2.2. GIA MODEL

The GIA Finite Element (FE) model from Blank et al. (2021) is used, which is based on the commercial Finite Element Method (FEM) software ABAQUS following Wu (2004). It computes bedrock changes for surface loading on a compressible spherical Earth with a composite and Maxwell rheology. The Poisson's ratio is assumed to be 0.28. The effect of density variations required for full compressibility is not included. Each element of the model gets assigned a dislocation and diffusion parameter from which the mantle viscosity can be computed based on, among others, the applied stress from surface loading. Section 3.2.2 discusses how these parameters, and the viscosity are computed. The FEM approach allows for discretization and computation of stresses and the resulting deformation in the Earth using a modified stiffness equation and Laplace's equation (Wu, 2004). The ice loading is applied to the GIA FE model at each coupling time step. When running the GIA FE model, each coupling time step is divided in increments for numerical integration inside the finite element model. The size of each subsequent increment is determined based on how fast the computation of the deformation converges. In this study, each coupling time step is divided into approximately 30 increments so that the nonlinear solution path can be followed sufficiently accurate. The advantage of this FEM approach based on ABAQUS is its flexibility as its grid size and rheology can

be adjusted. Furthermore, FE models operate in the time domain so the program can be stopped at each time step and all information about the state of stress is stored, contrary to SGVE models which operate in the Laplace domain for which the entire ice history has to be available to compute the next time step (e.g. de Boer et al., 2014), introducing complication if the coupled evolution is addressed. Because of the solution in the temporal domain FE models can exchange information with the ice-sheet model at every required time step. This advantage allows, for example, to simulate the glaciation phase of the last glacial cycle once on a high spatial and temporal resolution and to use the state of the Earth at the end of the glaciation phase as a starting point for different experiments of the deglaciation phase where, for example, the coupling step size or the forcing of the ice-sheet model is adjusted. The restart option also allows for simulation of projections where the model is restarted from an initialized GIA FE - ice-sheet model.

The adopted 3D GIA FE model from Blank et al. (2021) used a prescribed ice load history for all time steps in the GIA FE model and iterates several times over the past 120000 yr to include self-gravitation (Wu, 2004). However, restarting with a different ice load at each coupling time step is necessary to include the GIA-feedback on the ice dynamics. For this reason adjustments to the GIA FE model have been made, to be able to continue the GIA FE model with a new ice load after each coupling time step using the RESTART option in ABAQUS. When simulating the 1D Earth structures, two iterations of the GIA FE model are performed over each coupling time step to include self-gravitation before moving on to the next time step. When simulating the 3D Earth structures, only one iteration of the GIA FE model is performed over each coupling time step to decrease the simulation time with 50%. The difference between including and excluding the effect of self-gravitation is less than 10% of the total deformation as shown in Fig. 3.11. For future studies, the same iteration over each coupling time step could be used to solve the sea level equation (Wu, 2004; Blank et al., 2021) and rotational feedback (Weerdesteijn et al., 2019).

The applied changes in ice loading are relative to the present-day ice load, as it is assumed that the Earth was in isostatic equilibrium with present-day ice loading at the beginning of the last glacial cycle. The ice load is computed at each time step by computing grounded ice thickness above flotation, taking into account the relative sea level change, as described in Simon et al. (2010). The ice load is computed by ANICE using:

$$H_{AF} = H - \max(0, (SL - b) \cdot \frac{\rho_w}{\rho_i}) \quad (3.2)$$

where H_{AF} refers to the ice thickness above flotation of grounded ice, H to the ice thickness of grounded ice, SL to the sea level relative to present day sea level, b to the bedrock elevation relative to present day sea level, and ρ_w and ρ_i to the density of water and ice respectively. The change in ice load is applied as a linear change on the GIA FE model during each coupling time step. This is an approximation of the true ice dynamics over the coupling time step, of which the ice dynamic equations are solved on much shorter timescales (1 yr) than the coupling time steps and are nonlinear. The determination of the chosen coupling time steps of 5000, 1000 and 500 yr is described in section 3.2.3.

Not only ice loading causes deformation, but also ocean loading due to temporal variations in sea level. We conducted a test where we prescribed a spatially variable global

ice and ocean loading caused by other ice mass changes, taken from Whitehouse et al. (2012), in addition to loading from the Antarctic ice-sheet model. From the results of the test, we conclude that the effect of global ocean and ice loading on deformation could be important on the scale of individual glaciers in Antarctica, but the load of global ice and ocean loading from other ice mass changes was negligible compared to the ice load variations on the scale of the AIS. Including global loading in the GIA FE model increases the computation time because a load is applied to every surface element globally instead of only on the surface elements where there is a change in grounded ice in Antarctica. Thus, loading due to other ice masses, spatially variable ocean loading, and loading due to variations in Earth's rotation, are not considered with the aim of reducing computational burden, as this paper focuses on the direct effect of mantle viscosity.

MODEL SETUP AND RESOLUTION

In the GIA model adopted for this study, referred to as the GIA FE model (Blank et al., 2021; Hu et al., 2017), a different mantle viscosity can be assigned to each element which allows for the use of 3D Earth structures (van der Wal et al., 2015). Other parameters (such as density and Young's modulus) are taken constant in layers that represent the core, lower and upper mantle and the elastic lithosphere. The horizontal grid has a higher resolution over Antarctica, which is visible in Fig. 3.2. Sensitivity tests for the grid size are conducted for the trade-off of accuracy versus the computation time. For these tests, the GIA FE model is loaded with a parabolic ice cap for 1000 yr using four different spatial resolutions, respectively: 70, 55, 30 and 15 kilometers. The details of the test are described in Fig. 3.12 in the supplementary materials. The tests show that using a horizontal resolution of 15 by 15 kilometers instead of 30 by 30 kilometers decreases the deformation with 0.01 percent over 1000 yr and increases the computation time of the GIA FE model by approximately 30 percent to 15 minutes (Fig. 3.12). A coarser resolution of 55x55 km does not notably reduce the computation time. Therefore, a resolution of approximately 30 by 30 km is chosen at the surface in Antarctica from 62 degrees latitude to the south pole, and 200 by 200 km elsewhere in the GIA FE model. Since the grid lies on a sphere, the elements are not equal, but their size approaches the given resolution. The resolution in the lower mantle and core are double as coarse as the lithosphere and the upper mantle. The chosen resolution results in approximately 300,000 elements divided over several layers, where the lithosphere and upper mantle have double the elements of the lower mantle and the core. The FE model is divided in eight layers for the 1D simulations and nine layers for the 3D simulations to represent the upper and lower mantle so that the elements in each layer lie at the same depth (see Table 3.1 for detailed parameters of the layers). The bottom of the upper mantle is connected to the lower resolution lower mantle with the use of so-called tie constraints. Fig. 3.2 shows an example of a change in a deformed sphere due to ice unloading at East Antarctica and ice loading at West Antarctica, with a relatively high-resolution in and around Antarctica and lower resolution in the far-field.

Following the 5-layer model used in Spada et al. (2011), one value for density, Young's modulus and, in the case of a 1D model, a viscosity is assigned to each layer, as is shown in Table 3.1. In case of a 3D Earth structure, the elastic top layer is fixed till 35 km depth as this is the thinnest lithosphere found in West Antarctica (Pappa et al., 2019), and a 3D rheological model with specific dislocation and diffusion creep parameters is assigned

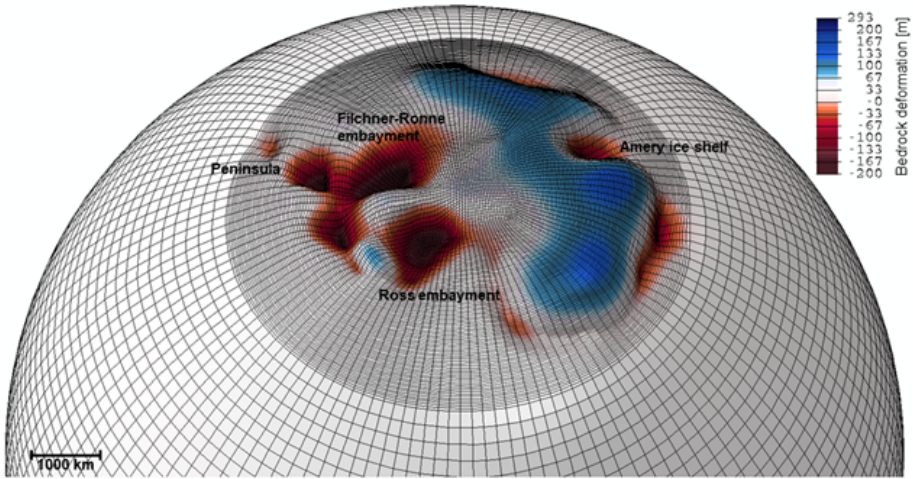


Figure 3.2: Example of the deformed Earth simulated by the GIA FE model at 115 ka. The grid has a higher resolution area of 30 by 30 km at latitudes until -60 degrees, and a lower resolution area of 200 by 200 km above -60 degrees latitude. The ice sheet is mainly growing in West Antarctica, causing subsidence, and slightly decreasing in East Antarctica which causes uplift.

to each element between 35 and 670 km depth, as is described in section 3.2.2. The effective lithospheric thickness is therefore spatially variable and follows from the effective mantle viscosity. If the viscosity in a region is so high that viscous deformation in one of the top layers is negligible over the entire cycle, the region can be considered to be part of the lithosphere (e.g. van der Wal et al., 2013; Nield et al., 2018). This will lead to a thicker effective lithosphere than 35 km in most of Antarctica. Thus, the second model layer partly consists of lithosphere and partly of upper mantle and is called the shallow upper mantle in Table 3.1. In the 1D model, the lithosphere is prescribed as 100 km thick which is similar to the lithospheric thickness used in Gomez et al. (2018). The chosen viscosities of $5 \cdot 10^{21}$ and 10^{21} Pa·s for the mantle between 420 and 2891 km depth, are shown in Table 3.1, and consistent with GIA based inferences of radial viscosity (Lambeck et al., 2014; Lau et al., 2016). The core is included in the model only through boundary conditions to provide a buoyancy force on the mantle (Wu et al., 2004). The complete overview of the parameter set up is shown in Table 3.1.

Table 3.1: Material properties of the GIA FE model. The top of upper mantle 2 is at 100 km depth for the 1D simulation and at 35 km for the 3D simulation.

Earth layer	Depth [km]	Number of layers	Density [kg/m ³]	Young's modulus [Pa]	Viscosity [Pa · s]
Top layer	0 - 35 ^(3D) /100 ^(1D)	1	3037	$0.50605 \cdot 10^{11}$	$1 \cdot 10^{44}$
Upper mantle	35 ^(3D) /100 ^(1D) – 420	3/4	3438	$0.70363 \cdot 10^{11}$	1D/3D variable
Transition zone	420 - 670	2	3871	$1.05490 \cdot 10^{11}$	$1 \cdot 10^{21}$
Lower mantle	670 - 2891	2	4978	$2.28340 \cdot 10^{11}$	$5 \cdot 10^{21}$
Core	2891 - 6371	1	10750	$1 \cdot 10^{-20}$	0

RHEOLOGY AND SEISMIC MODELS

The deformation as a result of the applied ice load depend on the rheological model that is used by the GIA FE model. Rheological models describe the relation between stress and strain. The 1D version of the GIA FE model uses a linear Maxwell rheology at all depths, whereas the 3D version uses a composite rheology following van der Wal et al. (2010) at depths between 30 and 420 km (see Table 3.1). The composite rheology combines two deformation mechanisms, diffusion and dislocation creep such that the strain computed in ABAQUS is:

$$\Delta \epsilon_{ij} = \frac{3}{2} (B_{diff} + B_{disl} \tilde{q}^{n-1}) q_{ij} \Delta t, \quad (3.3)$$

where $\Delta \epsilon_{ij}$ is the strain, B_{diff} and B_{disl} are the spatially variable diffusion and dislocation parameters respectively, \tilde{q} is the Von Mises stress which is assumed to be 0.1 MPa (Ivins et al., 2021), n is the stress exponent, taken to be 3.5, consistent with Hirth and Kohlstedt (2003), q_{ij} is the deviatoric stress tensor, and Δt is a variable time increment for the numerical integration within the coupling time step. The increments are determined automatically depending on the applied stress and the size of the coupling time step. Detailed explanation of the implementation of the composite rheology in the FE model can be found in Blank et al. (2021).

From Eq. 3.3 it can be derived that the effective viscosity (η_{eff}) for each element of the GIA FE model (van der Wal et al., 2013) becomes:

$$\eta_{eff} = \frac{1}{3B_{diff} + 3B_{disl} q^{n-1}} \quad (3.4)$$

The diffusion and dislocation parameters used in this study are derived from the flow law from Hirth and Kohlstedt (2003) and given by Eq. 3.6a and 3.6b respectively:

$$B_{diff} = A_{diff} d^{-3} f_{H_2O}^1 e^{\frac{E+PV}{RT_{x,y}}} \quad (3.5a)$$

$$B_{disl} = A_{disl} d^0 f_{H_2O}^1 .2 e^{\frac{E+PV}{RT_{x,y}}} \quad (3.5b)$$

where A is experimentally determined ($A_{diff} = 10^6$ MPa, $A_{disl} = 90$ MPa), d is the grain size, f_{H_2O} is the water content, E is the activation energy, P is the depth dependent pressure (Kearey et al., 2009), V is the activation volume, R is the gas constant and $T_{x,y}$ is the spatially variable absolute temperature. A , E and V are different according to the values for wet and dry olivine. All parameters, except temperature, grain size and water content, are taken from Hirth and Kohlstedt (2003). The temperature is derived from an Antarctic seismic model and a global seismic model for each element of the GIA FE model following approach 3 in Ivins et al. (2021) to include a nonlinear rheology. Following this approach, seismic velocity anomalies are converted to temperature, assuming that all seismic velocity anomalies are caused by temperature variations (Goes et al., 2000). Derivatives of seismic velocity anomalies to temperature anomalies are provided as a function of depth in the mantle (Karato et al., 2008). Antarctic seismic velocity anomalies are taken from Lloyd et al. (2020) and global velocity anomalies for regions above -60 degrees latitude are taken from SMEAN2 which is an average of three seismic models (Becker and Boschi, 2002). The models are combined with a smoothing applied at

the boundary at -60 degrees latitude. Mantle melt is assumed to have a relatively small influence on upper mantle viscosity and is therefore not included in this study (van der Wal et al., 2015).

Following Eq. 3.3- 3.6, the mantle viscosity, and thus the deformation, is dependent on the grain size and water content. As little information exists on grain size and water content, these parameters are kept spatially homogeneous (van der Wal et al., 2015). We obtained two different 3D rheologies by choosing a grain size of 4 mm and a water content of 0 (hereafter referred to as 3Ddry) and 500 ppm (hereafter referred to as 3Dwet) to obtain rheologies that can be considered realistic based on other viscosity studies (e.g. Blank et al., 2021; Gomez et al., 2018; Hay et al., 2017). A water content of 500 ppm is within the range of water content found in Antarctic xenoliths (Martin, 2021).

The two rheology models give an idea of some, though not all, variation in 3D mantle viscosity. The viscosity of both 3D rheologies is shown at three depths in the two right columns of Fig. 3.3 (Fig3c-d, g-h, k-l). Increasing the water content lowers the mantle viscosity but the pattern of viscosity variations is maintained (Karato et al., 1986; Blank et al., 2021). This can be seen in Fig. 3.3, where the mantle viscosity of 3Ddry is approximately one order of magnitude higher than the mantle viscosity of 3Dwet. Both 3D rheologies provide an upper mantle viscosity of approximately $10^{18} Pa \cdot s$ in West Antarctica, which is comparable with Barletta et al., (2018), who estimated such low viscosities in West Antarctica by constraining the GIA model using GPS and seismic measurements, and with Blank et al. (2021), who confirmed that a mantle viscosity of $10^{18-19} Pa \cdot s$ is plausible in the Amundsen Sea sector, based on the WINTERC 3.2 temperature model which is constrained by seismic data and satellite gravity data (Fullea et al., 2021). The viscosity pattern of both 3D rheologies used in this study, and the viscosity value of the 3Ddry rheology, are similar to the mantle viscosity used by Gomez et al. (2018) and Hay et al. (2017), who infer mantle viscosity by scaling seismic anomalies to viscosity anomalies and adding them to a background viscosity profile from GIA or geodynamic studies. A background viscosity can be inferred from other GIA or geodynamic studies, however following the method from van der Wal et al. (2015) allows to directly obtain absolute viscosity values from seismic measurements without the need to assume a background viscosity profile.

The results of the coupled model using a 3D rheology can be compared with the results using 1D rheologies. Two experiments are performed using a 1D rheology with two different upper mantle viscosity profiles: 10^{20} (hereafter referred to as 1D20) and $10^{21} Pa \cdot s$ (hereafter referred to as 1D21). These values are consistent with the lower and upper boundaries of the upper mantle viscosity that is generally used in studies for Antarctica (e.g. Albrecht et al., 2020; Gomez et al., 2018; Pollard et al., 2017). The elastic lithospheric thickness is the same for both 1D experiments and is set to 100 km. Fig. 3.13 in the supplementary materials shows the viscosity profile at 4 different locations for the 4 different rheologies. The locations are indicated by the numbers in Fig. 3.3a. At the Thwaites glacier (location I in Fig. 3.3a), the viscosity of the 3D rheologies is between 10^{20} and $10^{22} Pa \cdot s$ between 70 and 100 km depth, whereas the 1D rheologies assume this layer to be elastic. On the other hand, at dome C (location IV in Fig. 3.3a) the viscosity is above 10^{23} between 100 and 170 km depth for the 3D rheologies, whereas the 1D rheologies assume a viscosity of 10^{21} and $10^{20} Pa \cdot s$ between 100 and 170 km depth.

In general, the viscosity of the 3D rheologies are up to 4 orders of magnitude lower in West Antarctica and up to 3 orders of magnitude higher in East Antarctica compared to the 1D21 rheology. It should be noted that the response of the bedrock to changes in ice loading does not solely depend on the local viscosity but on the viscosity of the whole region where the change in ice load occurs.

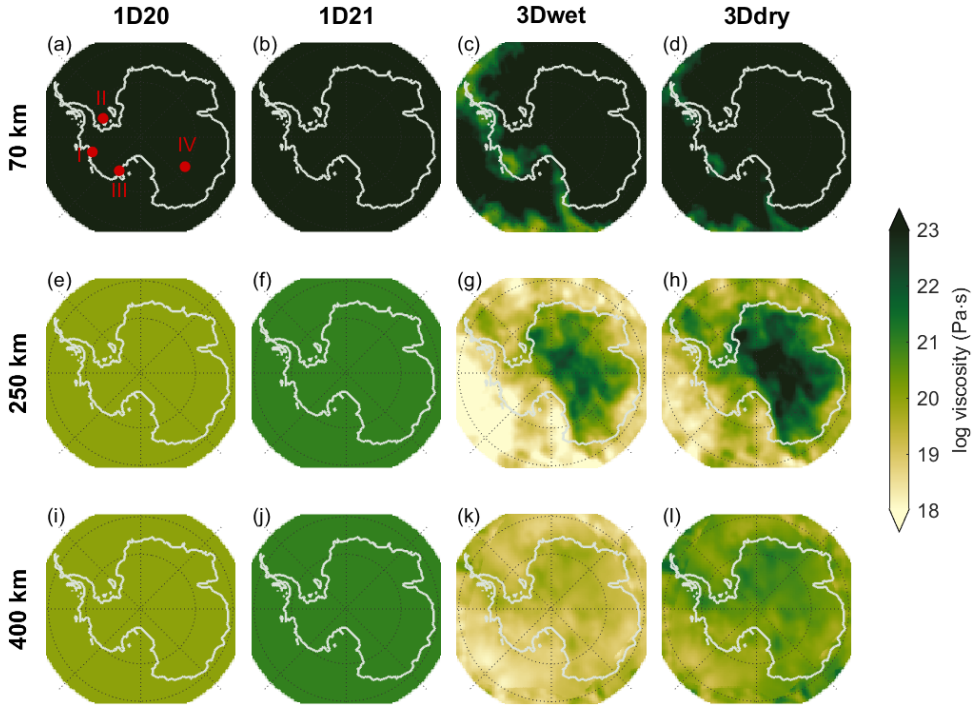


Figure 3.3: Panels a, e and i correspond to the 1D rheology referred to as 1D20. The red dots annotated by roman numbers in panel a correspond to the viscosity profiles shown in Fig. 3.13 in the supplementary material. Panels b, f and j correspond to the 1D rheology referred to as 1D21. Panels a and b show a viscosity of $10^{44} \text{ Pa}\cdot\text{s}$, representing the 100 km thick lithosphere in the 1D rheology. Panels c, g and k correspond to a 3D rheology with a water content of 500 ppm referred to as 3D (wet), and figures d, h and l correspond to a 3D rheology without water content referred to as 3D (dry). Both 3D rheologies assume a grain size of 4 mm. A pressure of 0.1 MPa is used to compute the viscosity from the dislocation and diffusion parameters.

3.2.3. ITERATIVE COUPLING METHOD

The simulation of ice dynamics for a certain coupling time step requires the deformation of the Earth over the coupling time step. On the other hand, the computation of the deformation over this coupling time step, using the GIA FE model, requires the change in ice mass over that coupling time step. For this study, an iterative coupling scheme has been developed that alternates between the models per time step with a varying length of 500 to 5000 yr. The GIA and ice-sheet model outputs (bedrock deformation and change in ice thickness respectively) are generated on different grids and the corresponding interpolation method is described in section 3.5. The iterative scheme is shown

in Fig. 3.4. The ice thickness and deformation at each coupling time step of the coupled model is computed as follows:

1. Simulate the evolution of the AIS for the first coupling time step using ELRA. Use the difference in grounded ice thickness at the end of the coupling time step and the initial grounded ice thickness as input for the GIA FE model which starts initially in isostatic equilibrium.
2. Run the GIA FE model to compute the deformation of the Earth's surface during the first coupling time step. Next, subtract the final bedrock elevation of the coupling time step from the final bedrock elevation of the last time step and interpolate this linearly to obtain deformation at the time steps of the ice-sheet model. Run the ice-sheet model to compute the new ice sheet evolution at the first coupling time step using the updated deformation in linear increases during the coupling time step. The ice-sheet model and the GIA FE model uses its own internal time stepping, as discussed in section 3.2.1 and 3.2.2 respectively.
3. Continue the iterative process described in step 2 until a convergence criterium has been reached. The convergence of the coupled model and the required number of iterations is further described in section 3.2.3.
4. Take the average deformation of the last two iterations as the final deformation to minimize the uncertainties in areas where the coupled model does not converge to zero but alternates between positive and negative values. Pass the average deformation to the ice-sheet model and run the model to calculate the final ice sheet evolution over the first coupling time step.
5. All stresses present at the end of the first coupling time step are saved in the GIA FE model which will be restarted in the second coupling time step. The final configuration of the ice-sheet model at the end of the first coupling time step is also saved and used as starting point for the ice-sheet model simulation at the second coupling time step. The averaged deformation of the last two iterations of the previous coupling time step will be used as initial guess to run the ice-sheet model for the first iteration of the next coupling time step.
6. Once the simulation over the entire glacial cycle has finished, compute the difference between the simulated present day bedrock topography and the observed present day bedrock topography using eq. 6, as will be explained further in section 3.2.3. Then, repeat the simulation of the entire glacial cycle using a corrected initial topography. Repeat the glacial cycle 2 to 4 times to convergence to a simulated present day topography equal to the observed present day topography.

Gomez et al. (2018) create ice loading and bedrock deformation histories of 40 kyr with a temporal resolution of 200 yr and run the ice-sheet model and sea level model alternately at once over the full history. In the method of the present study, the ice-sheet model and GIA FE model run alternately at each dynamic coupling time step, of which the coupling time step can be changed depending on the desired accuracy. However, the GIA FE model used in the present study does not solve the sea level equation, which

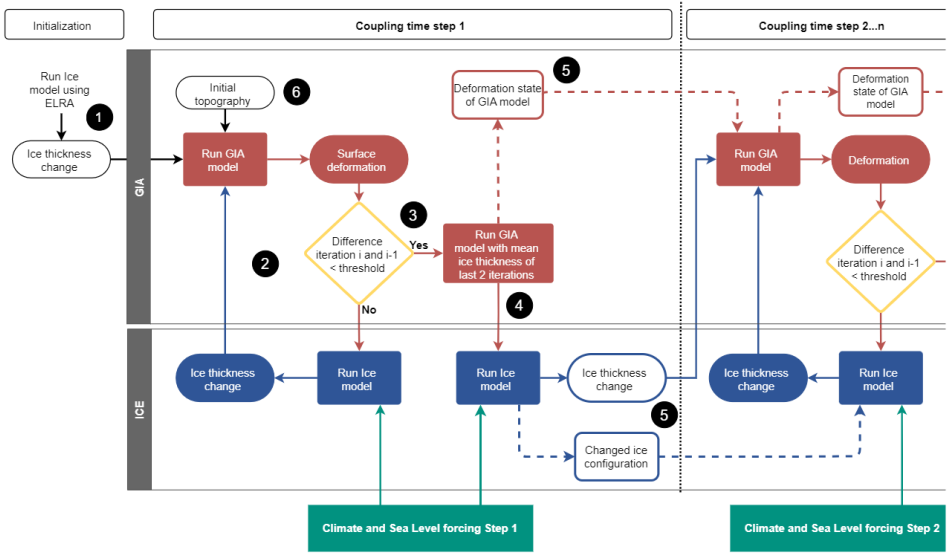


Figure 3.4: Schematic overview of the method for coupling the GIA and ice-sheet model. The numbers 1 to 6 in black circles refer to the steps of the iterative coupling process explained in the main text. The solid lines refer to the flow of input and output. The dashed lines connect the blocks for running the GIA or ice model to show that the saved model of the previous coupling time step is used to restart the model in the next coupling time step.

should be included in the GIA FE model for realistic reconstructions. For the present study, the last glacial cycle is simulated using 51 coupling time steps of 5000, 1000 and 500 yr (section 3.2.3). Tests are performed to determine the required number of iterations per coupling time step (section 3.2.3). After calculating the first glacial cycle there is usually a mismatch between modelled and observed topography at present-day. To solve this mismatch, we use two to four glacial cycle iterations, depending on the rheology, each with 51 coupling time steps to correct for the difference in modelled and observed topography (section 3.2.3) (e.g. Kendall et al., 2005). The method allows to use variable coupling time steps throughout the glacial cycle and between iterations of glacial cycles to decrease the total computation time.

SIZE OF THE COUPLING TIME STEP

A longer coupling time step increases the deformation and change in ice thickness over one coupling time step. Therefore, the coupling time steps need to be chosen sufficiently small, so that deformation and ice thickness change nearly linearly. On the other hand, a large coupling time step is desirable to limit the computation time. The convergence of the coupled model is highly dependent on the length of the coupling time step since the change in ice load, and thus the bedrock deformation, is smaller for smaller time steps, which converges faster.

Table 3.2: Coupling time steps over last glacial cycle.

Period [ka]	Time step size [kyr]	Number of coupling times
120 – 20	5	20
20 – 15	1	5
15 – 5	0.5	20
5 – 1	1	4
1 - 0	0.5	2

The coupled model is tested using different coupling time steps for the 1D21 rheology. Relatively long coupling time steps of 5000 and 1000 yr are tested between 120 ka and 20 ka because the change in GIA signal is small within this period since the ice sheet volume is slowly increasing till Last Glacial Maximum (LGM), and knowledge of the past climate is limited. Using a step size of 1000 yr did not lead to significantly different results than using time steps of 5000 yr and we therefore chose a step size of 5000 yr for the glaciation phase of the last glacial cycle. Because of the fast reduction of ice in a warming climate, smaller coupling time steps are required during the deglaciation. Han et al. (2022) showed that coupling time steps of 200 yr are optimal for the deglaciation phase in their coupled 1D GIA – ice-sheet model. However, their method assumes a constant topography during the coupling time step, which is not the case here, and the topography is updated only at the end of each time step. In our simulation, the topography changes linearly during the coupling time step and is updated every year in the ice-sheet model. In addition we run the ice-sheet model twice per coupling time step, whereas in the method of Han et al., (2022) this is done only once per coupling time step. The method of Han et al. (2022) therefore requires smaller coupling time steps between the GIA and ice-sheet models than the coupling method presented in this study. To determine the length of the coupling time step of the deglaciation phase, we tested a step size of 200 and 500 yr over the period of fast deglaciation between 15 and 5 ka. The results are shown in Fig. 3.14 in the supplementary materials, together with a table showing the exact used step sizes over the glacial cycle (Table 3.3). Difference in bedrock elevation between using a step size of 200 and 500 yr occurs mainly at the Ross embayment and the Princess Astrid Coast of Queen Maud land and bedrock is maximum 20 meter higher at present day when a time step of 200 yr is used. The ice thickness of the Ross Ice Shelf at present day is 70 meter larger when a step size of 200 yr is used and there is no difference in grounding line position. The ice thickness at the Princess Astrid Coast at present day is 680 meter larger and the grounding line lies 80 meter further inland when a step size of 200 yr is used. However, this region with large ice thickness differences is very small and spans only 120 km. The computation time of simulating a time step of 200 yr and 500 yr is similar but the 200 yr time step requires 42 extra time steps. Using time steps of 200 yr between 15 and 5 ka increases the computation time with 56 hours. We therefore chose to use time steps of 500 yr during the deglaciation phase. We used time steps of 1000 yr around LGM and between 5 and 1 ka to create a smooth transition between the glaciation phase, the deglaciation phase and the Late Holocene. The chosen time steps for the entire glacial cycle for this study are shown in Table 3.2.

CONVERGENCE OF THE COUPLED MODEL

The number of iterations needed to converge is dependent on the change in ice load and the Earth's structure. The coupled model requires 3 to 13 iterations per coupling time step to converge to an incremental change in deformation of less than 3 mm per yr in all individual grid cells when using the 1D21 rheology. A different rheology requires a different number of iterations. An example of convergence of a coupling time step using the 1D21 rheology can be seen in Fig. 3.5, which shows the difference in deformation and ice thickness between iterations of one coupling time step from 120 ka till 115 ka. The deformation threshold is set to 15 m for the entire glacial cycle. Panel a of Fig. 3.5 shows the change in ice thickness and panel b shows the change in bedrock elevation over this coupling time step when using the 1D21 rheology. Panels c to f show the difference in ice thickness and bedrock elevation compared to the former iteration. The ice thickness and deformation converge for most of Antarctica, except at the Ross embayment where the shelf thickness still differs between iteration 2 and 3 due to its high sensitivity to grounding line position.

When using the 1D20 rheology, ice thickness and deformation do not converge exactly at multiple locations around the grounding line after iteration 3. A high deformation rate and large changes in ice thickness cause a large shift in the position of the grounding line. Glaciated grid cells of the ice-sheet model are defined as grounded ice or floating ice, depending on their position upstream or downstream of the grounding line. If the grounding line in the ice-sheet model moves with every iteration due to large changes in deformation, the grid cells around the grounding line alternate between an ice shelf and grounded ice status. Since ice thickness can differ with hundreds of meters between adjacent grid cells, the difference in ice thickness at one grid cell between iterations can also differ greatly. In this case, both ice thickness and the change in deformation at these grid cells around the grounding line do not converge to zero but to an alternating value. The bedrock deformation converges better than ice thickness because of the stiffness of the Earth causing a more smooth deformation pattern.

Tests show that the coupled model converges within an acceptable computation time when the convergence criterium is set to 3 mm per yr over the coupling time step. This uncertainty is still below the effect of the uncertainties of the input parameters such as background mantle temperature and seismic velocity (e.g. Blank et al. 2021). Since the grid cells around the grounding line in some cases do not converge to zero, the coupling method introduces an uncertainty. For example, if in one grid cell the change in total deformation over 5000 yr keeps alternating between -2 and +2 meter, the uncertainty range is 4 meter. To decrease this uncertainty, the average deformation of the last two iterations is used as the final deformation to simulate ANICE for the final iteration of the time step. Decreasing the spatial resolution would allow smoother transitions between grounded and floating ice and thus a further improvement of the convergence. However, the ice-sheet model is currently limited to a 40 kilometer resolution.

NUMBER OF ITERATIONS PER COUPLING TIME STEP

Three simulations are conducted to study the effect of the number of iterations on the GIA and the evolution of the AIS using the 1D21 rheology. One simulation is performed with 1 iteration per time step (which means that the ice-sheet model was run twice over

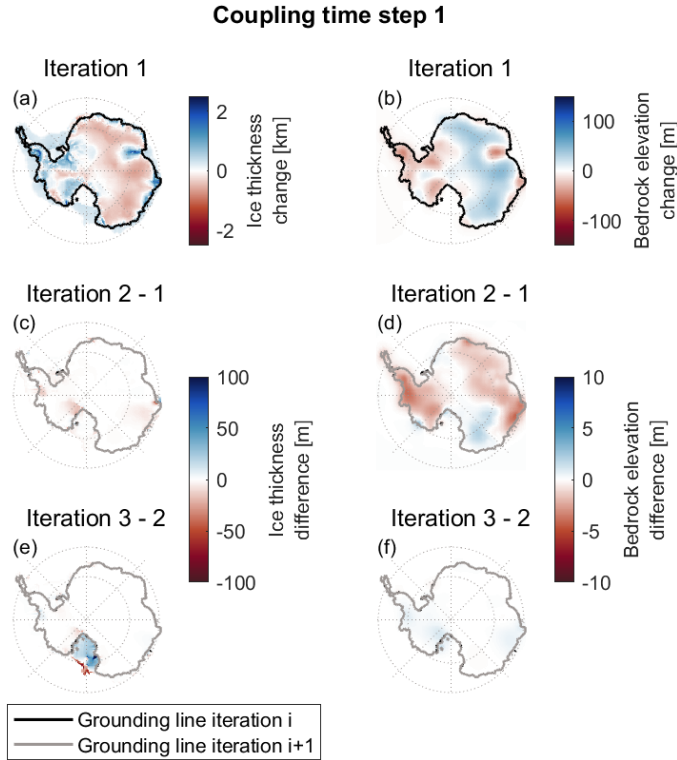


Figure 3.5: Iterations of coupling time step 1 from 120 ka to 115 ka using the 1D21 rheology. (a) Change in ice thickness over this coupling time step. (b) Change in bedrock elevation over this coupling time step. (c-f) Difference in ice thickness and bedrock elevation change compared to the previous iteration. The threshold is set to 10 m over the full coupling time step.

the coupling time step and the GIA FE model was run one time over the coupling time step), one simulation with a varying number of iterations per time step using the convergence threshold as described in section 3.2.3 and one simulation simulates first the full glacial cycle using the ice-sheet model, followed by a full glacial cycle using the GIA FE model, and last another glacial cycle using the ice-sheet model. Differences in deformation and ice thickness between the three simulations are neglectable during the glaciation phase of the last glacial cycle. At present day, the absolute maximum difference between the convergence simulation and the simulation with only 1 iteration is 700 m in ice thickness at the Ross embayment and the grounding line differs by 80 km in this region (Fig. 3.15 in the supplementary materials). The maximum difference in ice thickness at present-day is still 2 times smaller than the maximum difference between using different 1D and 3D rheology's and only occurs over very small regions. The absolute maximum difference between the 1 iteration simulation and simulation where the entire cycle was run at once is much larger with 3500 m in ice thickness at the Ross embayment, and the grounding line differs by approximately 800 km in this region (Fig. 3.16 in the supplementary materials). From this we conclude that the effect of iterating over

the glacial cycle versus iterating per coupling time step is much larger than the effect of the number of iterations over a coupling time step. Furthermore, the effect of decreasing the length of the coupling time step is small.

Reducing the number of iterations significantly reduces the computation time. The coupled model simulations are performed on 16 CPU's of model Intel(R) Xeon(R) Gold 6140 CPU @ 2.30GHz, of which the CPU speed varies between 1085 and 2707 MHz. The GIA FE model takes approximately 20 and 40 minutes to simulate 5000 yr for the 1D rheology and the 3D rheology respectively. The ice-sheet model takes only several minutes so the GIA FE model takes most of the time. A simulation of one glacial cycle using the 1D GIA FE model performing 3 iterations per coupling time step takes 27 days when running on 16 CPU's performing 51 time steps (which is 1 glacial cycle). Performing only one iteration reduces the total running time to 30 hours. Simulating the last glacial cycle using a 3D GIA FE model takes about 5 days when only 1 iteration per time step is performed, and 37 days when in total 293 iterations are performed.

Considering the long computation time if multiple iterations are used, only 1 iteration is used for results in the remainder of this study. This means that for each coupling time step first the ice model is run using the deformation over the former coupling time step, next the GIA FE model is run with the new ice load from the ice model and finally, the ice model is run including the new deformation of the GIA FE model.

ITERATIONS OVER THE ENTIRE GLACIAL CYCLE

The bedrock elevation at last glacial maximum is higher for a larger mantle viscosity since there is less subsidence during the glaciation phase. In that case, the ice sheet in West Antarctica will melt less and less bedrock uplift will occur during the deglaciation phase. Thus, the differences in melt during the deglaciation phase for the various rheologies could be caused not only by the direct effect of the viscosity of the rheology on the uplift, but by the difference in bedrock elevation at last glacial maximum. The direct effect of various rheologies on ice dynamics during the deglaciation phase can be isolated if the model is constrained by ending up at present with the observed bedrock topography. Without iterations, the present-day bedrock topography after a glacial cycle differs per simulation and does not equal the observed bedrock topography. For this reason we apply a commonly used approach in GIA modelling by applying several iterations of the entire last glacial cycle, hereafter called glacial iterations, as described in step 6 of the coupling scheme in Fig. 3.4. They are needed to ensure that modelled and observed present day bedrock topography are in agreement (Peltier, 1994; Kendall et al., 2005). It is assumed here that this difference is solely caused by modelled vertical GIA deformation, neglecting other types of deformation, such as tectonic motion and erosion or restraining assumptions in the ice-sheet model.

The initial bedrock topography at 120 ka of the first glacial iteration is initially assumed to be equal to present-day bedrock topography, taken from ALBMAP (Le Brocq et al., 2010). For the next glacial iterations, the initial bedrock topography is adjusted for the difference in simulated present-day bedrock topography and the observed present-day topography ALBMAP:

$$b_{0,i} = b_{0,i-1} + (b_{ALBMAP} - b_{PD,i-1}), \quad (3.6)$$

where the subscript i refers to the iteration over the glacial cycle, $b_{0,i}$ refers to the bedrock elevation at the beginning of the new glacial iteration, $b_{0,i-1}$ refers to the bedrock elevation at the beginning of the previous glacial iteration, $b_{PD,i-1}$ refers to the present-day bedrock elevation of the last glacial iteration and b_{ALBMAP} refers to the observed present-day bedrock topography based on Le Brocq et al. (2010). Four to five iterations of the entire glacial cycle are typically needed to converge the modelled present-day bedrock topography to the observed present-day bedrock topography, of which the first three iterations are shown in Fig. 3.17 in the supplementary materials.

3.3. RESULTS AND DISCUSSION

3.3.1. TESTING THE COUPLED MODEL USING DIFFERENT 1D RHEOLOGIES

The evolution of the AIS over the entire last glacial cycle shows a similar ice sheet thickness, extent and volume using the 1D coupled model of this study, compared to other studies using coupled 1D GIA – ice-sheet models and coupled ELRA – ice-sheet models (de Boer et al., 2014, 2017; Gomez et al., 2015; Pollard et al., 2017). To further test if the coupled model works as expected, the results for an upper mantle viscosity of $10^{20} Pa \cdot s$ (1D20) are compared to those of $10^{21} Pa \cdot s$ (1D21). The results of both simulations in terms of ice thickness and grounding line position follow a similar pattern as in Pollard et al. (2017). The Filchner-Ronne and Ross embayment (indicated with FR and R respectively in Fig. 3.6a) remain larger during the deglaciation phase for the 1D20 simulation than for the 1D21 simulation because the uplift is faster when using the smaller mantle viscosity of $10^{20} Pa \cdot s$ (Fig. 3.6). Based on the Marine Ice Sheet Instability (MISI) process, increased ice shelf melt and fast grounding line retreat can be expected due to a retrograde bedrock slope and an increasing relative sea level caused by subsidence (Schoof, 2007). At present day, the ice is up to 1 km thinner around the grounding line of the Ross and Filchner-Ronne embayments, and the grounding line is further retreated by approximately 100 km at the Ross embayment in the 1D21 results compared to the 1D20 results, shown in Fig. 3.6h.

3.3.2. STABILIZATION OF THE AIS USING 1D AND 3D RHEOLOGIES.

In a cooling climate between 120 ka and 20 ka, all 1D and 3D coupled simulations show an ice thickness increase mainly at the Ross and the Filchner-Ronne embayments and at the Peninsula, causing the bedrock to subside in these regions. In the 1D simulations, the bedrock subsides 500 m less during this period than in the 3Ddry simulations due to the stiffer 1D rheology compared to the 3Ddry rheology (Fig. 3.7a and 7d). However, the bedrock subsides a similar amount when using the 3Dwet rheology compared to the 1D20 rheology during the glaciation phase. At the Amundsen embayment, the mantle viscosity of the 3Dwet rheology is so low that the bedrock responds quickly to slight changes in ice loading. The ice loading follows a fluctuating pattern due to the atmospheric and sea level forcing (Fig. 3.10 in the supplementary materials) and the bedrock follows the same pattern, although dampened and delayed. The bedrock with the 3Dwet rheology subsides over the full glaciation phase but not as much as the bedrock with the 3Ddry rheology because the 3Dwet rheology can respond fast enough to cause uplift in periods when ice thickness does not grow as much.

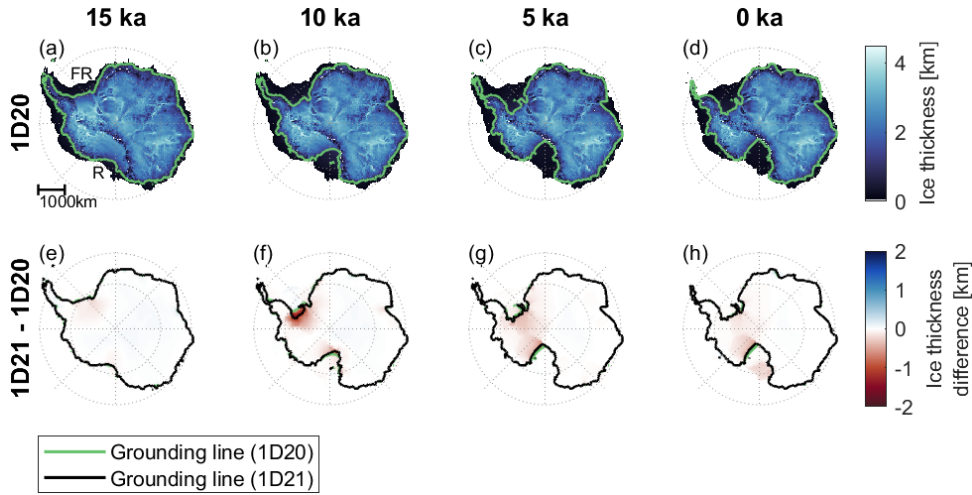


Figure 3.6: Ice thickness of 1D20 (top row) and the difference in ice thickness between 1D20 and 1D21 (bottom row) at four epochs during the deglaciation phase. (a) FR refers to the Filchner-Ronne Ice Shelf and R refers to the Ross embayment. In (e-h), the 1D20 grounding line (green) mostly overlaps with the 1D21 grounding line (black).

At LGM, the ice thickness is several hundreds of meter larger near the Ross and the Filchner-Ronne embayments when using a 1D rheology compared to the 3Ddry rheology (Fig. 3.8bc). During the deglaciation phase, the Ross and Filchner-Ronne embayments retreat fast due to climate warming, similar to what other studies of the AIS evolution suggest (e.g. Albrecht et al., 2020). The 1D mantle viscosity leads to a slower uplift which causes the grounding line near the Ross and Filchner-Ronne embayments to retreat faster in the 1D simulations than in the 3D simulation (Fig. 3.7b-c, e-f), corresponding to results by Pollard et al. (2017) and Gomez et al. (2018). Using a 3Ddry rheology leads to a difference in grounding line position of up to 700 km and a difference in ice thickness of up to 2 km at present-day along the Siple coast (Fig. 3.8c). Using a 3Dwet rheology leads to 600 m thicker ice at present day compared to using the 1D20 rheology and a more advanced grounding line position of 80 km. The ice thickness of the 3Dwet rheology lies closer to the 1D20 ice thickness than the ice thickness of the 3Ddry rheology because the bedrock elevation at LGM is similar for the 1D20 and the 3Dwet rheologies and is 500 m lower for the 3Ddry rheology. Due to the lower bedrock elevation at LGM when the 3Ddry rheology is used, the ice sheet in West Antarctica will melt more and faster bedrock uplift will occur during the deglaciation phase when a stronger rheology is used. The differences in melt during the deglaciation phase between using different rheologies is then not caused by the direct effect of different rheologies on uplift rates, but by the difference in bedrock elevation at last glacial maximum.

In contrast to the changes in West Antarctica, Fig. 3.8 shows that the difference in ice sheet thickness between the 1D and 3Ddry simulations in the interior of the East AIS are not larger than 50 meter, although the mantle viscosity in East Antarctica is several orders of magnitude higher in the 3D rheology than in the 1D rheologies. This is be-

cause the interior of the ice sheet is not as sensitive to the bedrock elevation as the outlet glaciers near the margin, leading to an insignificant effect of mantle viscosity differences. The interior of Antarctica is also less sensitive to changes in the surface temperature and sea level and therefore follows an equilibrium response which is independent of the rheology.

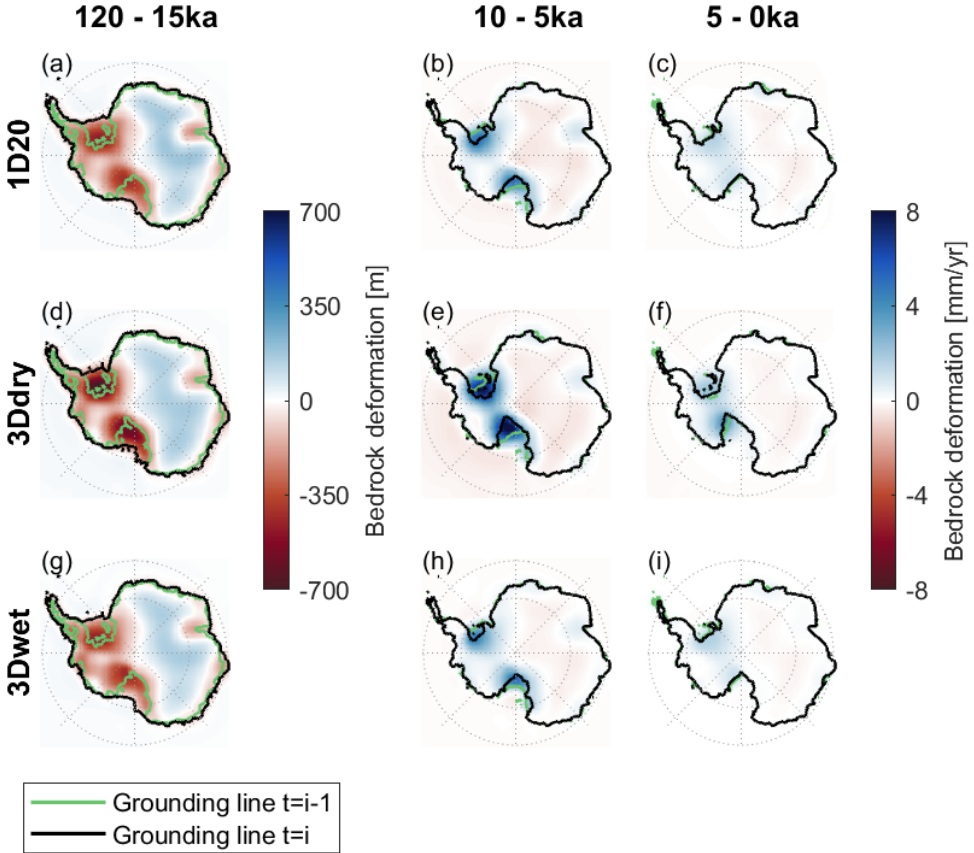


Figure 3.7: Total uplift over the glaciation phase between 120 and 15ka for 1D20 (panel a), 3Ddry (panel d) and 3Dwet (panel g), and average uplift rates between 10ka and present day for the 1D20 (panels b,c), 3Ddry (panels e,f) and 3Dwet (panels h,i) rheologies. The green grounding line shows the grounding line position at the beginning of the period over which the uplift or uplift rate is computed, and the black grounding line shows the position at the end of the period.

As can be seen in Fig. 3.8, Antarctic ice mass variability is dominated by the changes in West Antarctica. Fig. 3.9 shows that 1D21 decreases faster than the 1D20 rheology due to the slower uplift in West Antarctica as shown in Figure S.9 in the supplementary materials. Figure 9 also shows that the present-day ice volume is 0.2-0.6 km³ lower when using 1D rheologies compared to using the 3Dwet rheology. The use of the 3Dwet rheology stabilizes the ice sheet compared to the use of a 1D mantle viscosity (Fig. 3.9) because a lower mantle viscosity at West Antarctica stabilizes the Filchner-Ronne and

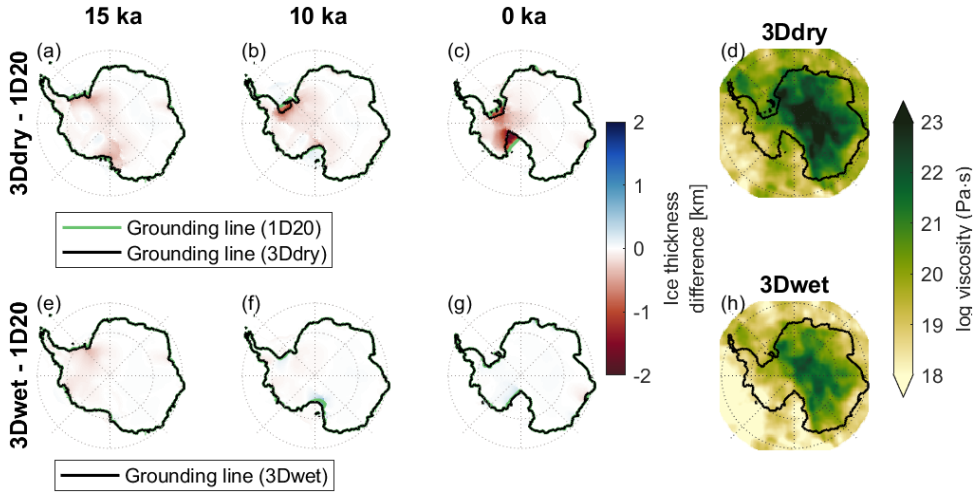


Figure 3.8: 1D vs 3D ice thickness and mantle viscosity at a depth of 250 km. A stress of 0.1 MPa is used to compute the 3D viscosity from dislocation and diffusion parameters. In Fig 3.8, the 1D grounding line (green) mostly overlaps with the 3D grounding lines (black).

Ross embayments (Fig. 3.8). However, the ice volume decreases faster in the deglaciation phase for the 3Ddry rheology compared to the 1D rheologies. The ice volume and ice surface elevation when using the 3Ddry rheology is much lower at LGM than the ice volume when one of the other rheologies is used and the bedrock uplift during the deglaciation phase is not fast enough to prevent the ice sheet from melting more ice compared to the using the other rheologies. The bedrock elevation at LGM plays therefore a very important role to determine the ice sheet evolution during the deglaciation phase.

Gomez et al. (2018) found an insignificant difference in ice volume at present-day for 3D viscosity vs 1D viscosity. Gomez et al. (2018) included the effect of regional sea level in the coupled model. Even though the effect of self-gravitation of the ice sheet on regional sea level is smaller than the effect of bedrock deformation, including the self-gravitation of the ice sheet in our model would decrease ice shelf melt and therefore decrease the ice volume change itself and the difference in ice volume between the 1D and 3D simulations. Differences in terms of ice dynamics formulations, forcings, rheology and resolution could additionally explain the different result of Gomez et al. (2018) and this study.

Overall, it can be concluded that the variations in mantle viscosity between a realistic 3D rheology and commonly used 1D rheology have a significant impact on grounding line position and ice thickness in West Antarctica and an insignificant impact in East Antarctica. Furthermore, during the deglaciation phase the difference in ice thickness of the 3Dwet and the 1D20 simulations is smaller than the difference of the 3Ddry and the 1D20 simulations because the bedrock elevation at LGM is much lower when the 3Ddry is used. The ice thickness is lower for the Ross and Filchner-Ronne embayments when using a 1D rheology compared to the 3Dwet rheology, but much higher compared to the 3Ddry rheology. The stabilizing effect increases when using the 3Dwet rheology com-

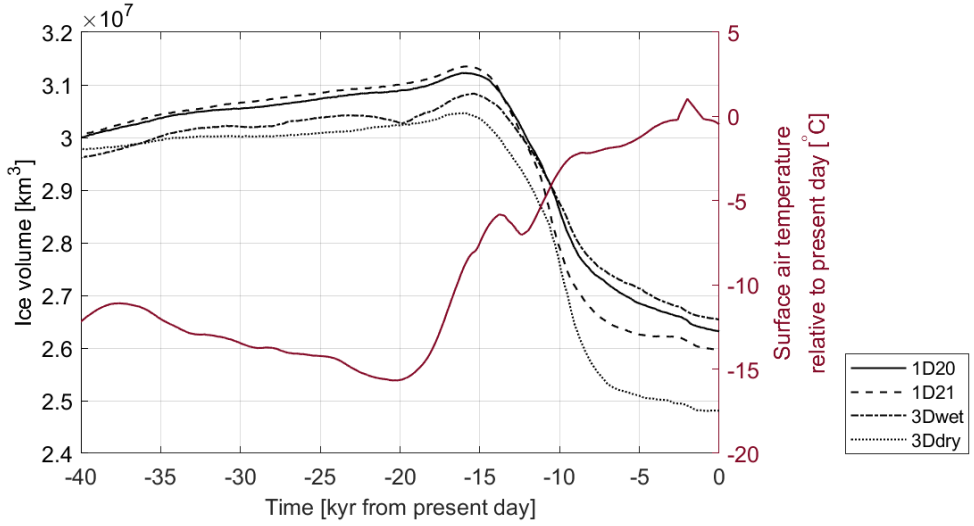


Figure 3.9: The black lines show the AIS volume over time for the 1D simulations and for the two 3D simulations (dry and wet rheology). The red line shows the mean surface temperature.

pared to using the 1D rheologies because the mantle viscosity under West Antarctica is lower and shows fast uplift during the deglaciation phase. Ice-sheet models using a similar 1D rheology with an upper mantle viscosity of 10^{20} Pa-s or higher and a lithospheric thickness of 100 km (e.g. DeConto et al., 2021; Pollard et al., 2017; Konrad et al., 2015), might therefore underestimate the stability for the Ross and Filchner-Ronne embayments.

3.4. CONCLUSIONS AND OUTLOOK

This study presented the first method to study GIA feedback on ice dynamics for laterally varying mantle viscosity on short timescales of hundreds of years using a coupled ice sheet-3D GIA FE model. Each coupling time step needs iterations to include the GIA feedback on short timescales of 500 to 5000 yr. The coupling method is tested for convergence, which is mainly dependent on the size of the time step. We used only one iteration per time step with a variable coupling time step of 500 to 5000 yr. Two to four iterations over the entire cycle are needed to adjust the initial topography to arrive at the present-day topography at the end of the simulation. Experiments where the resolution in near field and far field are varied indicate that a near field resolution of 30 by 30 km and a far field of 200 by 200 km yields an accuracy of 2 mm/yr bedrock deformation and a computation time of 5 days to simulate a single glacial cycle.

We created two 3D Earth rheologies based on an Antarctic-wide seismic model. Using the 3Ddry Earth rheology leads to a difference in grounding line position up to 700 km and a difference in ice thickness of up to 3500 m compared to using a 1D mantle viscosity of 10^{20} Pa-s at present, due to a much lower bedrock elevation at LGM (Fig. 3.8). The bedrock elevation at LGM is similar between using the 3Dwet Earth rheology and a 1D

mantle viscosity of 10^{20} Pa-s because the mantle viscosity at the Amundsen embayment is so low that uplift can occur during short periods of atmospheric temperature decrease in the glaciation phase. Using the 3Dwet Earth rheology leads to a less retreated grounding line position of up to 80 km and thicker ice thickness of up to 600 m compared to using a 1D mantle viscosity of 10^{20} Pa-s at present day (Fig. 3.8). The ice volume at present day increases with 0.5 or 1.8 percent when using the 3Dwet rheology compared to using a 1D mantle viscosity of 10^{20} Pa-s or 10^{21} Pa-s respectively. That is because the low mantle viscosity found in the 3Dwet rheology leads to large uplift rates which stabilize the ice sheet more than the 1D rheologies. An ice-sheet model coupled to a 1D rheology with an upper mantle viscosity of 10^{20} Pa-s or 10^{21} Pa-s and lithospheric thickness of 100 m underestimates the stabilizing effect of GIA. However, when the bedrock elevation at LGM is much lower, such as for the 3Ddry rheology compared to the 1D rheologies, the difference in ice volume is up to 0.2 km^3 between the 3Ddry and the 1D rheologies. In the future it is desired to apply the coupling method presented in this chapter with high resolution models including regional sea level forcing, not only because a higher resolution provides more accurate grounding line simulation, but also because the method will converge better since the grid cell is smaller and thus the ice load on one grid cell as well.

The method developed for this study has several advantages which can be exploited in future work when simulations are performed which are as realistic as possible, rather than focussing on the physical principles as we did in this chapter. First, the time step is variable throughout the glacial cycle and can be adjusted between iterations of the full glacial cycles. This way, computation time can be saved by simulating the first glacial cycle on a low temporal resolution to obtain the first modelled present-day topography, while the second iteration with the adjusted initial topography can be performed with a higher temporal resolution to include the GIA feedback more accurately. Second, the GIA FE model can be restarted at any time step. Therefore, the last glacial cycle can once be simulated on a very high temporal resolution to obtain present-day results and the coupled model can be restarted from present-day to simulate future evolution of the ice sheet under different scenarios or rheologies. Third, the coupling method allows coupling with any ice-sheet model, as long as the model can restart at each coupling time step. Last, the method has potential for a higher temporal resolution than used in this study at designated periods in time. For example, the simulation can be restarted at 500 yr before present and run on a higher temporal resolution such as a coupling time step of 10 yr to simulate recent uplift and future climate change projections.

3.5. SUPPLEMENTAL MATERIALS

FORCING

Fig. 3.10 shows the sea level and temperature forcing for the coupled model simulations. This forcing is in the results of previous simulations of de Boer et al. (2013) where ANICE was used to reconstruct global ice volume and the continental mean temperature at the northern hemisphere over the past 1 Myr. Those simulations used the LR04 benthic $\delta^{18}\text{O}$ stack of 57 deep-sea sediment records as forcing (van de Wal et al., 2011). The results lead to a past surface-air temperature and eustatic sea level.

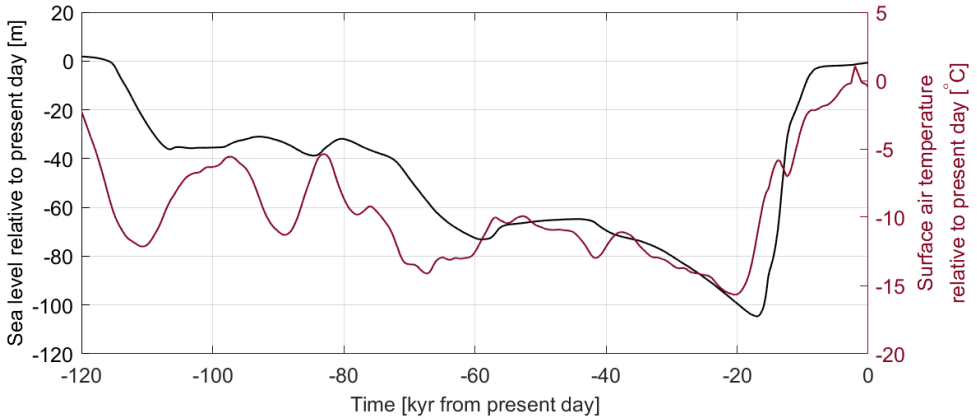


Figure 3.10: Atmospheric temperature (black) and eustatic sea level relative to present-day (red). Both are shown over time, starting 120 kyears before present.

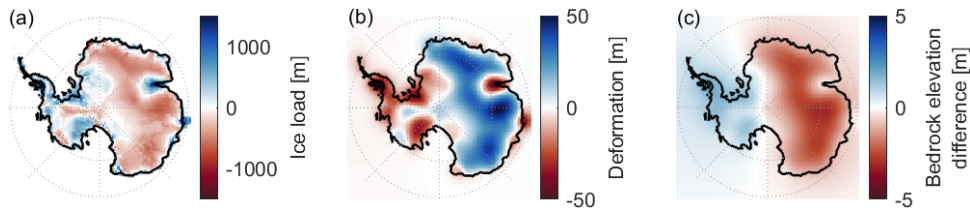


Figure 3.11: Two simulations are performed using the 1D21 GIA model, one with the effect of self-gravity and one without the effect of self-gravity on bedrock deformation. The applied ice load is the change in ice load computed by ANICE using ELRA from 120 ka to 115 ka. Panel a shows the applied ice load over a period of 5000 yr. This change in ice load is the highest change simulated by the 1D21 coupled model over a glacial cycle. Panel b shows the resulting bedrock deformation when the effect of self-gravity is excluded. Panel c shows the bedrock elevation after 5000 yr when the effect of self-gravity is excluded subtracted from the bedrock elevation after 5000 yr when the effect of self-gravity is included.

RESOLUTION AND RUNTIME OF THE GIA MODEL

Fig. 3.12 shows the results of the tests performed to determine the resolution of the GIA model with the best trade-off between accuracy in deformation and the computation time. A 1D viscosity of 1020 Pa-s is used. The tests are performed using ice loading in the shape of a parabolic ice cap of 1500 meter thick with a radius of 1500 meter that is linearly applied to the GIA model from zero thickness to its maximum thickness over a time step of 1000 years. The near field resolution is varied between 15, 30, 55 and 70 km, shown on the horizontal axis, and the far field resolution is varied between 100 and 200 km, shown as dashed and solid lines respectively. For each test, we measured the computation time, shown on the left vertical axis, and we computed the maximum deformation of each simulation, shown on the right vertical axis. As expected, the dashed black line, referring to the runtime of the test with a far field resolution of 100 km, lies much higher than the solid black line, which refers to the runtime of the test with a far field resolution of 200 km. Following the red lines, the maximum difference in deformation with the coarsest resolution (70 km near field-200 km far field resolution) and the finest resolution is 11 cm (15 km near field-100 km far field resolution). However, the computation time is three times as long for the 30 km near field-100 km far field resolution compared to the 30 km near field-200 km far field resolution, while the difference with the higher resolution test is only 5 cm on a total deformation of 171 meter. Also, when considering far field resolution of 200 km, the near field resolution test of 15 km takes twice as long as the near field resolution test of 30 km whereas the difference in deformation is only 2 cm over 1000 years. We therefore chose a far field resolution of 200 km and a near field resolution of 30 km.

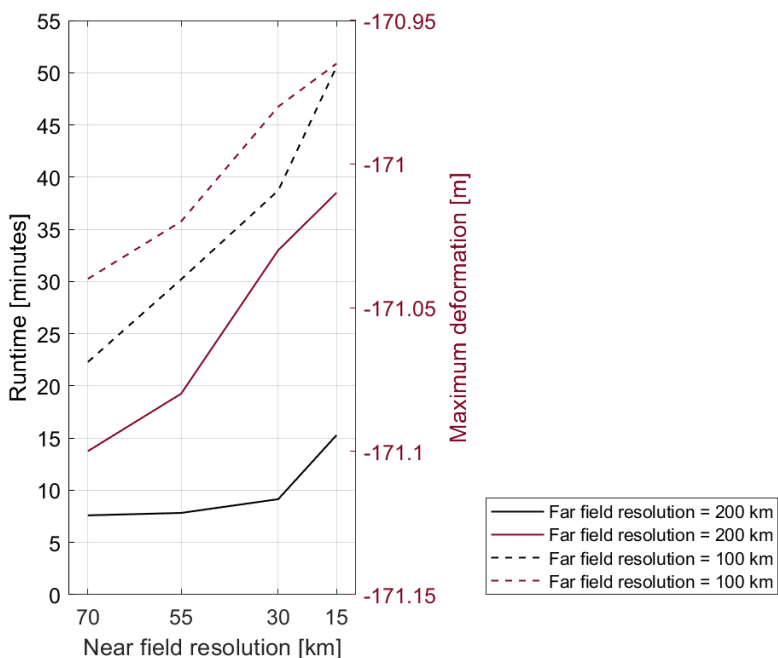


Figure 3.12: The test simulations of 1000 years were conducted using a paraboloid ice load of 1500 meter thick. The x axis shows the near field resolution around Antarctica, the solid lines correspond to a far field resolution of 200 km and the dashed lines to a far field resolution of 100 km.

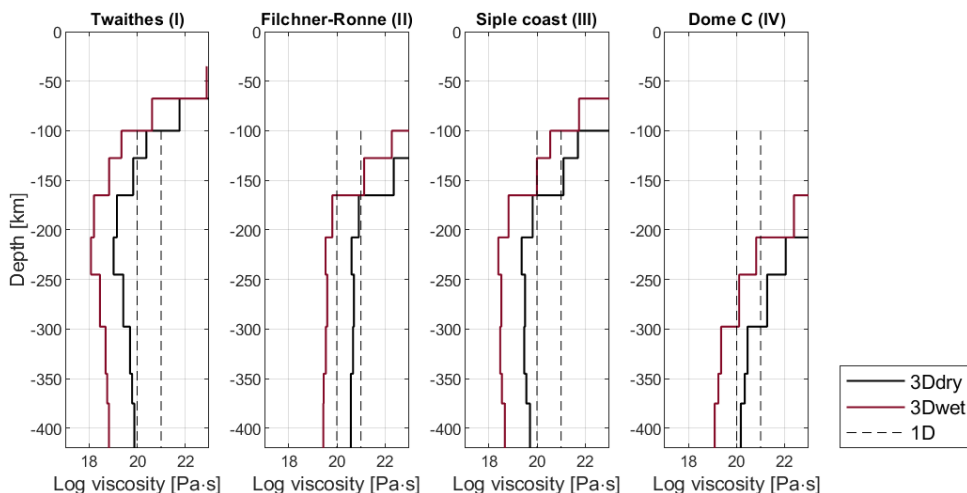


Figure 3.13: Viscosity profile at 4 different locations; Thwaites glacier (-76.5531,-107.4472), Filchner-Ronne embayment (-78.8373,-62.5924), Siple coast (-79.2968,-149.0362), and Dome C (-75.1712,122.9052). The locations with corresponding numbers in the title are indicated in the map in Fig. 3.3a in the main manuscript. The viscosity is computed assuming a stress of 0.1 MPa.

Table 3.3: Two simulations were performed to test the sensitivity of the model to the length of the coupling time step. The length of the time step of the test with 500 yr time steps is shown in Table 3.2 in the main text. Here, we show the time step size of the test with 200 yr time steps during the deglaciation phase.

Period [ka]	Time step size [kyr]
120 – 20	5
20 – 15	0.5
15 – 5	0.2
5 – 1	0.5
1 - 0	0.2

INTERPOLATION OF BEDROCK DEFORMATION AND ICE LOADING

The total deformation computed by the GIA FE model that is used as input for ANICE, is defined on a regular grid of 0.25 by 0.25 degrees, whereas ANICE is defined on a polar stereographic equidistant grid of 40 km. Therefore, interpolation of the ANICE output, the change in ice thickness over the coupling time step, is needed to use the output of the ANICE as input for the GIA FE model. On the other hand, interpolation of the ANICE output is needed to use the output as input for the GIA FE model. For both interpolations we use Oblimap which is suitable for polar projections and takes into consideration conservation of mass (Reerink et al., 2016). The input for the GIA model is defined on a regular grid of 0.25 degrees latitude and longitude. For interpolation from the fine grid size of input of the GIA FE model to a somewhat coarser grid size of ANICE, the so-called radius method is used as this is computationally fast and provides an accurate result (Reerink et al., 2016). All fine grid points within a radius of the order of half the coarse grid size are included by a Shepard distance-weighted averaging interpolation method to obtain a representative value for this coarse grid point (Shepard, 1968). The quadrant method is used for gridding from a coarser ANICE grid to a somewhat finer input grid of the GIA FE model (Reerink et al., 2016). The region around the grid point of the fine grid is divided in four quadrants. For each quadrant, the closest grid point in the coarse grid is selected and Shepard distance-weighted averaging is applied to these coarse grid points using a Shepard’s power parameter of 2 (Shepard, 1968). A lower parameter would result in a smoother output but also less detailed. Furthermore, the ice thickness is linearly interpolated from the regular input grid of 0.25 degrees latitude by 0.25 degrees longitude to the irregular grid of the actual GIA FE sphere.

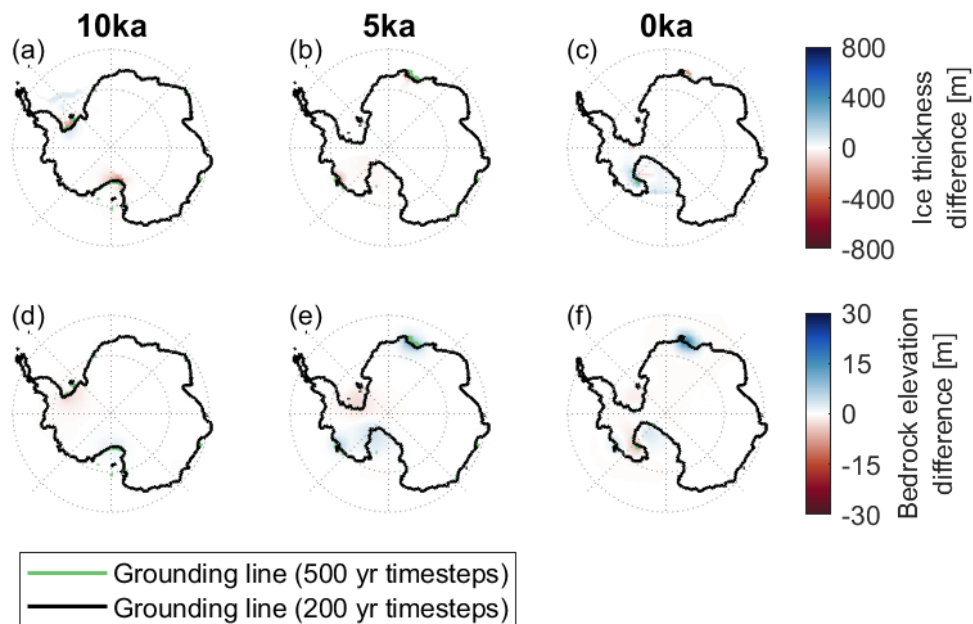


Figure 3.14: Two tests were performed using the 1D21 rheology to test the sensitivity of the model to the length of the coupling time step. Panels a-c show the difference in ice thickness of the 200 yr time step simulation minus the ice thickness of the 500 yr time step simulation at three different moments in time, 10 ka, 5 ka and present day respectively. Panels d-f show the difference in bedrock elevation of the 200 yr time step simulation minus the bedrock elevation of the 500 yr time step simulation at three different moments in time, 10 ka, 5 ka and present day respectively.

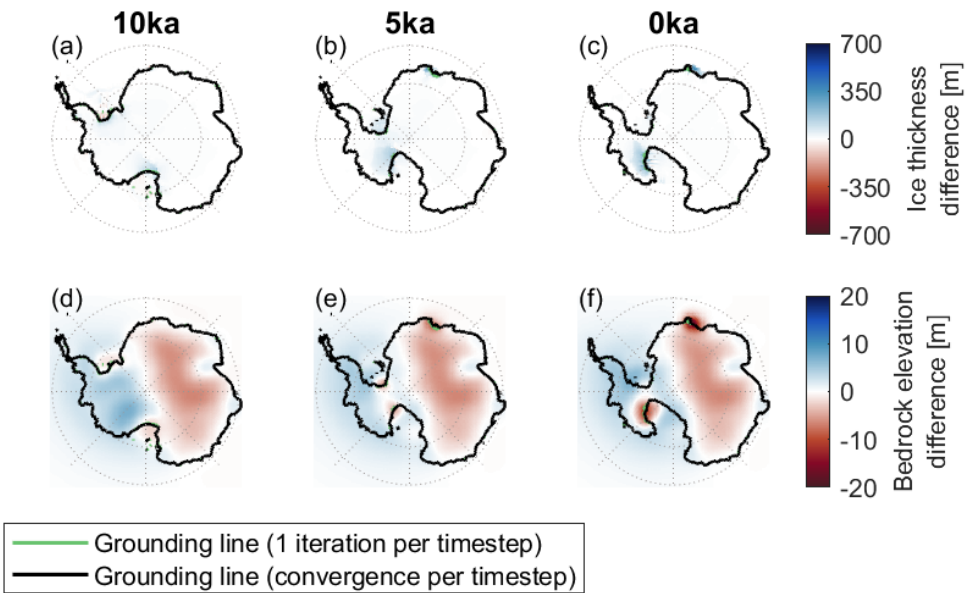


Figure 3.15: The results of two simulations are shown using the 1D21 rheology. One test where the iterations are performed per coupling time step until the convergence threshold of 3mm/yr has been met, and one test where only one iteration is performed. Panels a-c show the difference in ice thickness of the convergence simulation minus the ice thickness of the 1 iteration simulation at three different moments in time, 10 ka, 5 ka and present day respectively. Panels d-f show the difference in bedrock elevation of the convergence simulation minus the bedrock elevation of the 1 iteration simulation at three different moments in time, 10 ka, 5 ka and present day respectively.

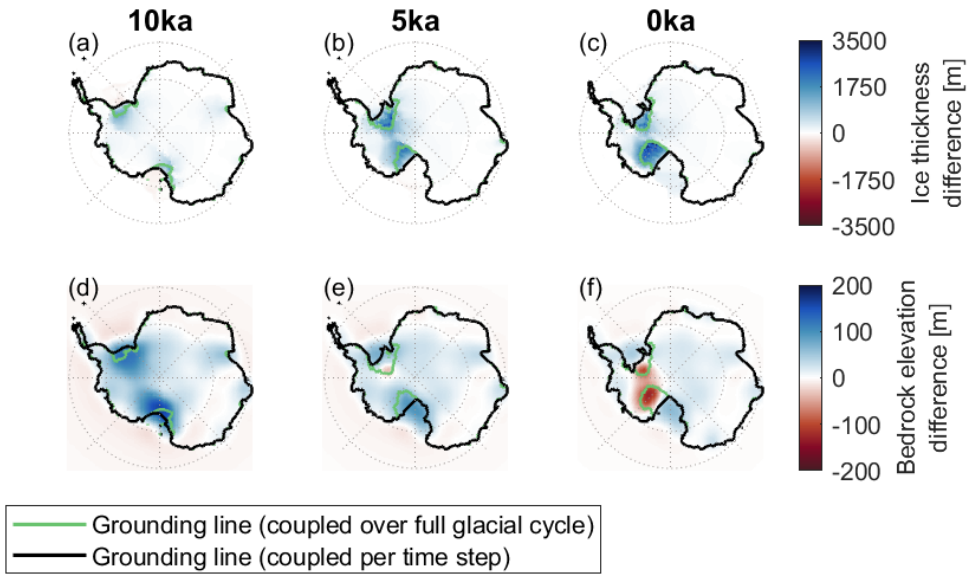


Figure 3.16: The results of two simulations for the 1D21 rheology. One test where only one iteration is performed per coupling time step and one test where there is no iteration performed per coupling time step. Panels a-c show the difference in ice thickness of the convergence simulation minus the ice thickness of the 1 iteration simulation at three different moments in time, 10 ka, 5 ka and present day respectively. Panels d-f show the difference in bedrock elevation of the convergence simulation minus the bedrock elevation of the 1 iteration simulation at three different moments in time, 10 ka, 5 ka and present day respectively.

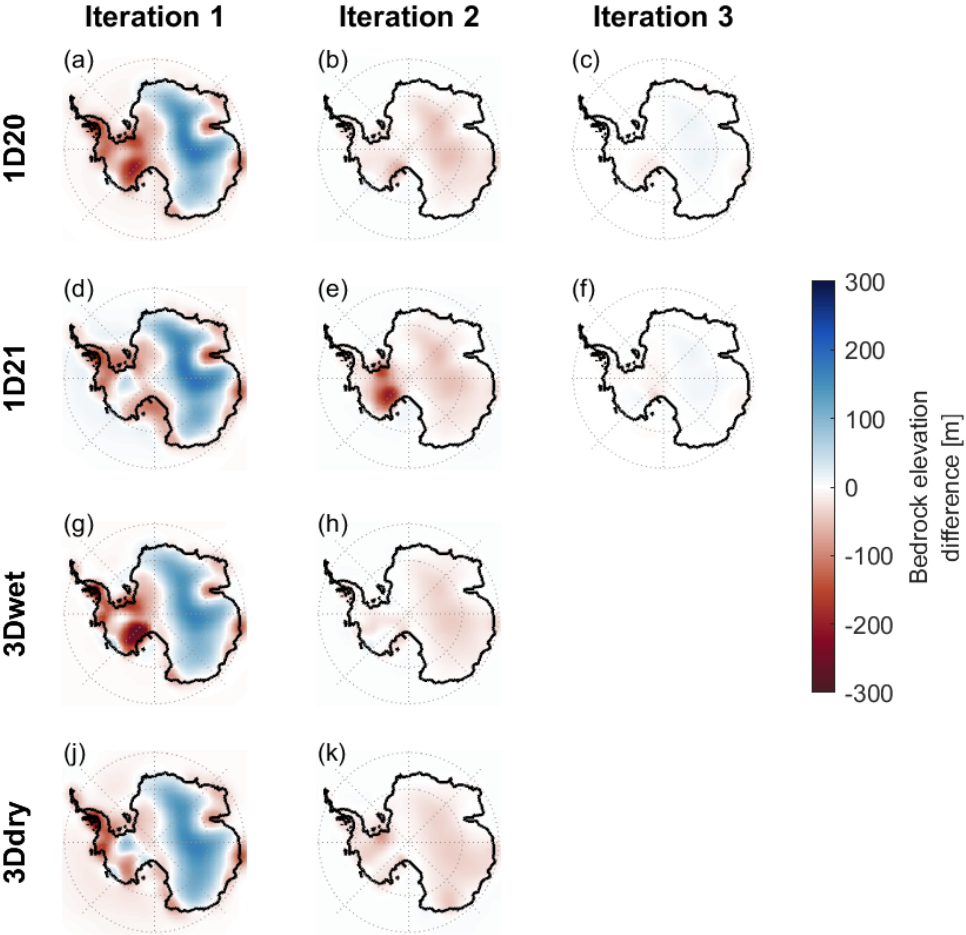


Figure 3.17: Difference in bedrock elevation between topography at the final time step of the simulation and the observed present-day topography for the first three iterations over the glacial cycle using Earth structures 1D20 and 1D21, and two iterations using 3Dwet and 3Ddry.

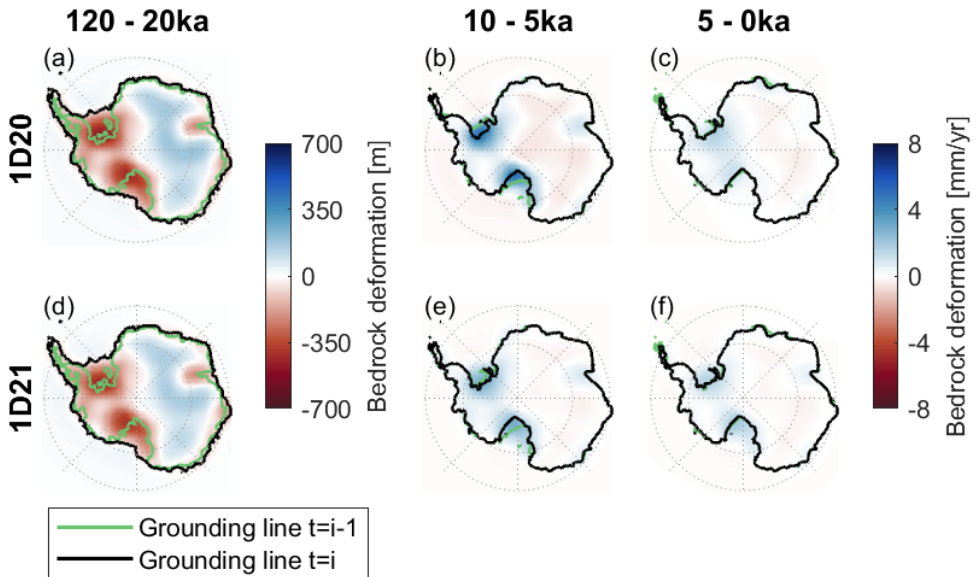


Figure 3.18: Total uplift over the glaciation phase between 120 and 20ka, and average uplift rates between 10ka and present day for the 1D20 (panels a-c) and the 1D21 rheologies (panels d-f). The green grounding line shows the grounding line position at the beginning of the period over which the uplift is computed, and the black grounding line shows the position at the end of the period.



Maxwell bay, Antarctica

4

BEDROCK UPLIFT REDUCES ANTARCTIC SEA-LEVEL CONTRIBUTION OVER NEXT CENTURIES

The contribution of the Antarctic Ice Sheet to global sea-level rise could be as high as eight meters around 2300 but remains deeply uncertain. Retreat of the Antarctic Ice Sheet leads to uplift of the underlying bedrock, which in turn can exert a stabilising effect on the receding grounding line. However, projections of ice mass loss either exclude bedrock adjustment, use simplified Earth structures or do not explore the uncertainty range in lateral variations in Earth structure and the uncertainty from climate models. In our work, we couple an ice sheet model with a bedrock model that includes different realistic radially and laterally varying Earth structure to account for feedbacks between ice loss and bedrock deformation under different shared socio-economic pathways. We show that the grounding line in West Antarctica takes 50 to 130 years longer to retreat when the heterogeneity of the solid Earth is included, leading to a reduction of 9-23% in the Antarctic sea-level contribution by the year 2500. We applied several climate models and 3D Earth structures and found that the effect of the solid Earth feedback in ice sheet projections can be twice as large as the uncertainty due to the climate forcing. Moreover, we show that the use of simplified GIA models lead to systematic overestimates of future sea-level rise. Our results emphasise that radially and laterally varying Earth structures should be considered when projecting the Antarctic contribution to sea-level rise on centennial time scales.

Published as: van Calcar, C.J., Bernales, J., Berends, C.J., van der Wal, W., and van de Wal, R.S.W.: Bedrock uplift reduces Antarctic sea-level contribution over next centuries. Preprint, 2024. Minor corrections are included in this thesis.

4.1. SOLID EARTH AND ICE SHEET STABILITY

The West Antarctic Ice Sheet (WAIS) has been identified as a critical tipping element, with its potential collapse being triggered if certain temperature thresholds are surpassed (Fox-Kemper et al., 2021). The long-term contribution of the Antarctic Ice Sheet to global sea-level rise could be as high as eight meters around 2300 but is deeply uncertain (Fox-Kemper et al., 2021). These uncertainties have been partly attributed to unaccounted feedbacks between ice dynamics and the other components of the Earth system (Gomez et al., 2024). Among these, bedrock deformation due to future ice mass loss has been suggested to exert a stabilising effect on the ice sheet (Barletta et al., 2018) which depends on regional solid Earth properties. This dependence has traditionally not been included in projections of ice sheet evolution (Book et al., 2022; Bulthuis et al., 2019; Coulon et al., 2021, 2024; DeConto et al., 2021; Golledge et al., 2015; Gomez et al., 2015; Kachuck et al., 2020; Konrad et al., 2015; Levermann et al., 2020; Lipscomb et al., 2021; Pollard et al., 2017; Rodehacke et al., 2020). We integrate a heterogeneous solid Earth structure into an ice dynamic model to quantify the impact of the solid Earth effect on Antarctic ice retreat over the next 500 years under different global warming scenarios.

As an ice sheet melts, the load exerted on the underlying bedrock decreases (green lines in Fig. 4.1). Deformation in the Earth's crust and mantle results in the uplift of the bedrock surface (brown lines in Fig. 4.1). This process is called glacial isostatic adjustment (GIA). A critical indicator of ice sheet stability is the retreat of the grounding line, which marks the transition between a grounded ice sheet and its fringing ice shelves (Mercer, 1978; Joughin and Alley, 2011; Schoof, 2007). As shown in Fig. 4.1, a retreat of the grounding line from its initial position purely due to ice shelf melt is partly counteracted by an accompanying bedrock uplift. In this configuration, the solid Earth response has the potential to slow down future grounding line retreat, giving rise to a negative feedback (Book et al., 2022; Bulthuis et al., 2019; Coulon et al., 2021, 2024; DeConto et al., 2021; Golledge et al., 2015; Gomez et al., 2015, 2024; Kachuck et al., 2020; Konrad et al., 2015; Levermann et al., 2020; Lipscomb et al., 2021; Pollard et al., 2017; Rodehacke et al., 2020). In addition, the bedrock uplift can have an impact on ice sheet elevation, bedrock slope and water depth below the ice shelf which control basal melt rates. Finally, a decrease in ice mass leads to a reduction in the self-gravitation effect of the ice sheet, which results in a sea-level drop in its vicinity and a sea-level increase far away from it.

The deformation of the solid Earth depends on changes in ice load and the local mantle viscosity which controls the response time of the bedrock. Several regions in West Antarctica, such as the Amundsen Sea Embayment, overlie relatively weak mantle structures where the mantle relaxes within decades to centuries (Barletta et al., 2018; Lloyd et al., 2019; Nield et al., 2014). Conversely, East Antarctica mostly consists of an old craton underlain by colder mantle, with response times that could reach beyond tens of thousands of years (Lloyd et al., 2019). Thus, there is a large difference to be expected between the dynamical responses of the bedrock in West and East Antarctica to ice load variations. Current long-term projections of the Antarctic Ice Sheet based on ice dynamical models typically do not include the solid Earth response (Levermann et al., 2020; Lipscomb et al., 2021), implement a fixed bedrock response time based on the so-called Elastic Lithosphere Relaxed Asthenosphere (ELRA) model (Bulthuis et al., 2019; Coulon et al., 2021, 2024; DeConto et al., 2021; Levermann et al., 2020), or use a variety of sim-

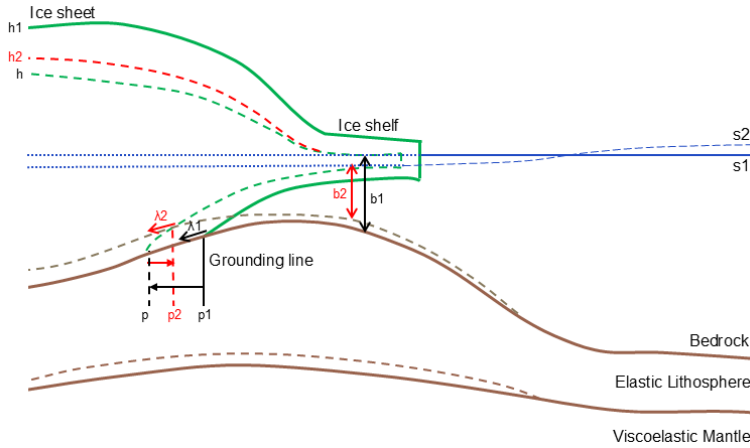


Figure 4.1: Schematic figure of GIA feedback on grounding line migration. The solid green and brown lines represent the initial ice sheet/shelf and lithosphere, respectively. The lower solid brown line separates the elastic lithosphere and the viscoelastic mantle. The solid and dashed blue lines represent local sea level before and after ice sheet melt and GIA, respectively. p_1 is the initial grounding line position. The dashed green line represents the ice sheet/shelf after retreat, while the dashed brown lines are the perturbed mantle elevation and bedrock surface. p is the expected grounding line position after retreat without considering any GIA effects. p_2 is the grounding line position including the GIA response. h_1 is the initial surface elevation, h the surface elevation without GIA effects and h_2 the surface elevation after the GIA response. Bedrock slope, λ , changes from λ_1 to λ_2 due to the bedrock response. b_1 and s_1 are the local water depth and sea level, respectively, before GIA, while b_2 and s_2 are their counterparts after GIA. Modified from van Calcar et al. (2023).

plified representations of the Earth's structure (Golledge et al., 2015; Gomez et al., 2015; Levermann et al., 2020; Rodehacke et al., 2020), or do not explore the uncertainty range of lateral variations in the Earth's structure and climate models (Gomez et al., 2024).

Studies comparing different radially varying Earth structures (hereafter called 1D Earth structures) have shown that ice sheet dynamics are sensitive to the choice of Earth structure, and emphasised the need for including heterogeneity in the Earth's composition (DeConto et al., 2021; Kachuck et al., 2020; Konrad et al., 2015; Pollard et al., 2017). Using a laterally varying relaxation time in an ELRA model resulted in a significant stabilising effect on the WAIS study on multicentennial-to-millennial timescales for varying future emission scenarios (Coulon et al., 2021). However, in Coulon et al. (2021), the relaxation time is prescribed and constant over time, whereas in reality the relaxation time varies as it depends on the evolving size of the ice sheet and the associated mantle viscosity change with depth (Wu and Peltier, 1982; Mitrovica and Peltier, 1991).

Previous research has shown that a radially and laterally varying Earth structure (hereafter 3D Earth structure) might not only lead to a reduction of the global mean sea-level rise (Hay et al., 2017), but also cause an increase in the contribution of the Antarctic Ice Sheet to far-field sea-level due to the water expulsion effect of uplifting regions (Pan et al., 2021; Yousefi et al., 2022). However, in those studies the ice sheet evolution is predefined rather than dynamically modelled, and any stabilising effects on grounding line migration and other ice sheet processes are therefore not accounted for.

Recent work incorporating lateral Earth structure variations on a dynamically modelled ice sheet evolution has demonstrated significant stabilisation of the Antarctic Ice Sheet (Gomez et al., 2024), but this finding is based on only a single climate model and Earth structure. Different climate models exhibit warming patterns in different regions between which the Earth structure varies, yielding a different response as observed in Fig. 4.3 and Fig. 4.7 in section 4.6. Furthermore, the mantle viscosity for the 3D Earth structure is derived from seismic and geologic information on the structure of the Antarctic mantle, which exhibit large uncertainties leading to significantly different bedrock responses (van Calcar et al., 2023). Assuming only a single Earth structure does not take the uncertainties into account. Finally, the mantle rheology is assumed to be linear. However, the Earth's response to mass loss in regions with low upper mantle viscosities, such as the Amundsen Sea Embayment, has shown to be nonlinear (Blank et al., 2021).

Here, we quantify the stabilising effect of the nonlinear response of multiple 3D Earth structures on the Antarctic Ice Sheet. We employ a coupled ice-sheet—GIA model that incorporates 3D mantle viscosities to simulate the Antarctic Ice Sheet evolution up to the year 2500 under two global warming scenarios (Chen et al., 2021): the low emission shared socio-economic pathway SSP1-2.6 and the high emission SSP5-8.5. For both scenarios, we force our simulations with products from two different climate models to be able to compare the uncertainty in the choice of the climate forcing with the uncertainties in the GIA component. We quantify the sensitivity of Antarctic Ice Sheet evolution to different plausible 3D Earth structures and show that they can delay grounding line retreat by 50–130 years and reduce the sea-level contribution in 2500 by 9–23% depending on the choice of climate forcing. Finally, we compare the results of different 3D Earth structures to the 1D and ELRA models, and conclude that these simplified models significantly underestimate the stabilising effect of bedrock deformation. The applied method is discussed in detail in section 4.5.

4.2. SEA-LEVEL RISE REDUCTION THROUGH BEDROCK UPLIFT

The Earth structure can be inferred from seismic measurements when adopting experimental flow laws for mantle rock under the assumption of different parameters, such as water content and grain size in the Earth's mantle. We varied the grain size and water content in the mantle to obtain two different 3D Earth structures, a stronger (hereafter 3D Stronger) and a weaker (hereafter 3D Weaker) structure (Fig. 4.5 in section 4.6). The Earth structures are based on seismic models and mantle flow laws and both result in a local mantle viscosities that are close to those from regional studies of GIA due to past ice sheet variations (Barletta et al., 2018; Blank et al., 2021; Bradley et al., 2015; Wolstencroft et al., 2015, Methods).

Using 3D Weaker leads to a reduction in sea-level rise of 23% in 2500 compared to the rigid Earth that does not deform (Fig. 4.2 and Tab. 4.2 in section 4.6). This corresponds to a sea-level rise reduction of 1 m. 3D Stronger results in less bedrock uplift compared to the 3D Weaker due to its higher mantle viscosity, but still reduces sea-level rise by 14% compared to a rigid Earth (Fig. 4.2 and Tab. 4.2 in section 4.6).

Besides the 3D Earth structures and the rigid Earth, we also applied a commonly used 1D Earth structure with an upper mantle viscosity of $10^{21} \text{ Pa}\cdot\text{s}$, and the ELRA model (see

section 4.5). The 1D and ELRA model exert a less stabilising effect on the ice sheet than both 3D structures (Fig. 4.6 in section 4.6) since the 1D and ELRA models do not take into account the weak zones in the Earth's mantle that deform faster and provide more stability to the ice sheet. In agreement with previous studies, we found negligible differences in sea-level contribution between the ELRA model and the commonly used 1D Earth structure (DeConto et al., 2021; Golledge et al., 2015; Pollard et al., 2017). However, their impact had not been directly compared to that of a 3D Earth structure. Our results show that the 3D Stronger model reduces sea-level rise by 20%, and the 3D Weaker model by 10%, relative to the response from the 1D Earth structure and ELRA (Fig. 4.6 in section 4.6). Current projections using simplified Earth models might therefore overestimate sea-level rise over the next centuries.

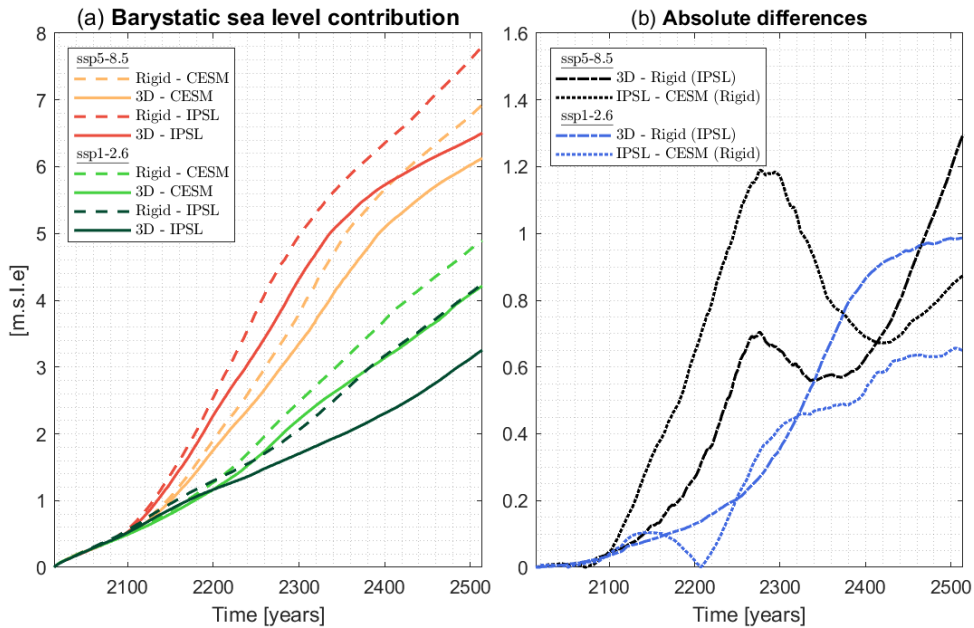


Figure 4.2: The barystatic sea-level contribution using a rigid and the 3D Weaker structure for two different climate models (CESM and IPSL) and two different emission scenarios (SSP1-2.6 and SSP5-8.5, panel a). Dashed lines correspond to using a rigid Earth and solid lines to the use of a 3D Earth structure. Red and orange lines correspond to scenario SSP5-8.5, and light and dark green lines to scenario SSP1-2.6. Panel b shows the absolute difference between the use of a 3D Earth structure and a rigid Earth structure when forcing from IPSL is applied (dashed lines) and the absolute difference between applying forcing from CESM and IPSL using a rigid Earth structure (dotted lines). IPSL contains warming mainly in the Amundsen Sea and CESM contains warming mainly in the Weddell Sea.

4.3. BEDROCK UPLIFT DELAYS ICE SHEET RETREAT

The solid Earth response to ice mass loss differs regionally due to the lateral variability of the Earth's structure in combination with the location of ice sheet retreat. In Antarctica, present trends in ice mass loss are dominated by melt and discharge at the base and

front of ice shelves (Rignot et al., 2013; Depoorter et al., 2013), which in turn can lead to an acceleration of upstream flow through reduced buttressing (Haseloff and Sergienko, 2022; Haseloff and Sergienko, 2018; Dupont and Alley, 2005). In our simulations, mass loss is strongly dependent on regional variations in the ocean temperatures driving sub-shelf melt rates. This forcing is taken from a climate model (see section 4.5) that exhibits particularly strong ocean warming in the Amundsen Sea Embayment (location indicated by AS in Fig. 4.3). The largest retreat therefore initiates from the Thwaites Ice Shelf in the Amundsen Sea Embayment, where the grounding line migrates hundreds of kilometres inland over approximately 350 years (Fig. 4.3). Here, this migration is strongly dependent on the choice of Earth structure, with the rigid Earth model showcasing up to 180 km of further inland grounding line retreat compared to 3D structures by year 2500. The latter provides up to 160 m of bedrock uplift over 500 years, slowing down the retreat. As a result, the grounding line positions reached by the 3D Weaker and Stronger structures in year 2500 have been already reached by the rigid Earth by 2370 and 2420, respectively. Thus, 3D Earth structures delay grounding line retreat by 80-130 years (Tab. 4.3 in section 4.6).

Acknowledging the significant uncertainties in climate projections (Lipscomb et al., 2021), which can include dissimilarities in the regions where ocean warming occurs, we run an experiment employing a different climate model that exhibits a strong warming in the Weddell Sea area instead of the Amundsen Sea (see section 4.5). This choice initiates a retreat of the grounding line of the Ronne Ice Shelf region, leading to a significant mass loss and accompanying solid Earth rebound (Fig. 4.7 in section 4.6). In this region, and compared to a rigid Earth model, the use of 3D structures results in a delay of grounding line retreat by 50-70 years (Tab. 4.3 in section 4.6). This smaller impact and sensitivity of this region relative to the retreat modeled for the Amundsen Sea Embayment can be explained by the mantle viscosity in the Ronne Ice Shelf region, which is up to 2 orders of magnitude higher than that in the Amundsen Sea Embayment. The same holds in other regions with significant grounding line retreat, the Ross Ice Shelf and Wilkes basin (indicated by RS and WB in Fig. 4.8a in section 4.6), where the mantle viscosity is higher in combination with a relatively small amount of ice mass loss compared to the Amundsen Sea Embayment. Even though there are relatively low viscosity regions at the grounding line of the East Antarctic Ice Sheet, the grounding line is stable, because the climate warming is not strong enough to initiate a retreat in those regions on the time scales considered in the framework of the used climate models. The Wilkes region is the exception, as shown in Fig. 4.7 and 4.8 in section 4.6.

Although the uncertainties embedded in climate projections have a significant effect on the resulting sea-level contribution, we found that in certain cases an even greater impact can arise from the choice of the Earth structure model. For example, the difference in modelled sea-level rise between rigid Earth simulations using two different climate models can reach 16% (Fig. 4.2 and Tab. 4.4 in section 4.6). However, when warming occurs in the Amundsen Sea Embayment, the use of a 3D Weaker Earth structure can result in a reduction of 23% in the projected sea-level rise relative to its rigid-Earth counterpart (Fig. 4.2b and Tab. 4.2 and 4.4 in section 4.6) due to delayed grounding line retreat fuelled by a relatively low mantle viscosity and quick bedrock uplift response.

The bedrock adjustment stabilizes the ice sheet and reduces ice mass loss. The peak

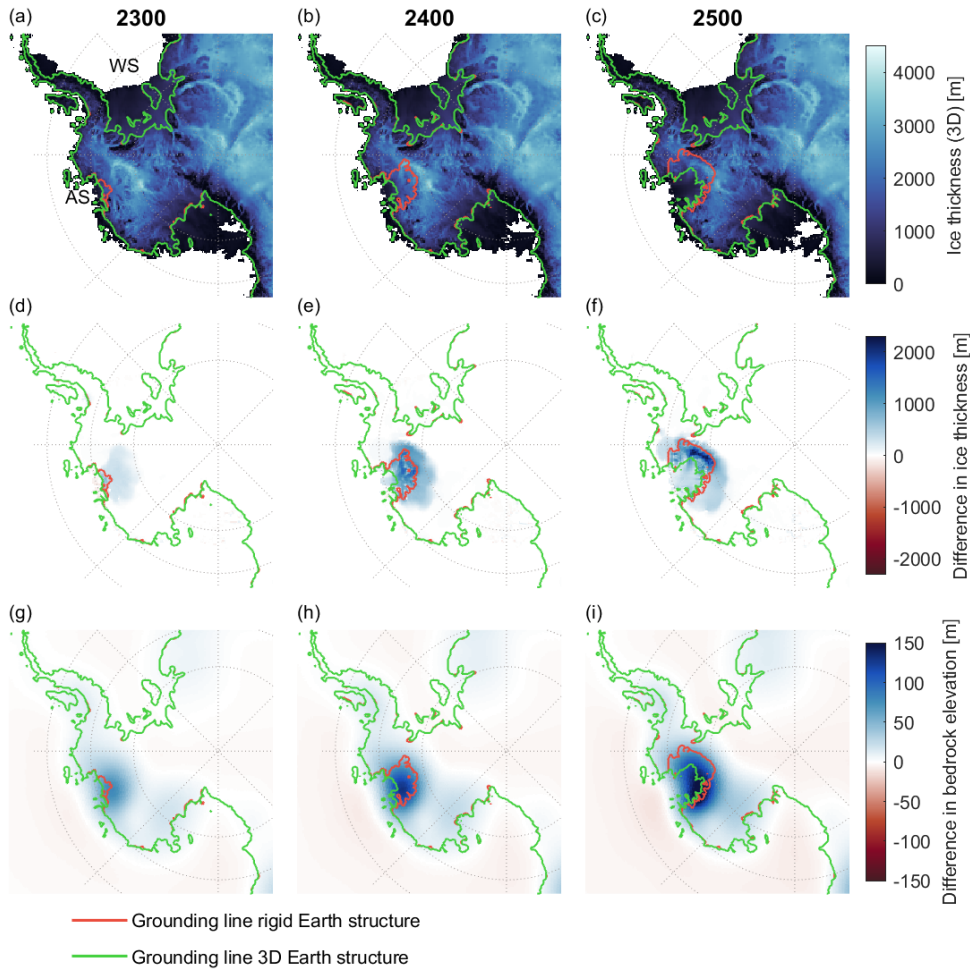


Figure 4.3: The ice thickness of the West Antarctic Ice Sheet in years 2300, 2400 and 2500 using the 3D Weaker Earth structure and IPSL forcing under the low emission scenario SSP1-2.6 (panel a-c). AS in panel a indicates the Amundsen Sea, and WS indicates the Weddell Sea. Panel d-f show the ice thickness difference between using the 3D Weaker structure and the rigid Earth structure. Panel g-i show the difference in bedrock elevation between the application of the 3D Earth structure and the rigid Earth structure. IPSL corresponds to the climate model with main warming in the Amundsen Sea (see section 4.5).

basal mass loss of $2.4 \cdot 10^{13} \text{ m}^3/\text{yr}$ is reached around the years 2100 and 2240, corresponding to periods with the highest sub-shelf ocean temperatures (Fig. 4.4a and c). From 2250, basal melt rates decrease in the 3D Earth structure experiments. The total basal mass loss is determined by the area of the ice shelves and the temperature at the depth of the shelf base. On the one hand, the total ice shelf area is smaller in case of a 3D Earth because of the slower grounding line retreat, which decreases basal mass loss compared to a rigid Earth (Fig. 4.4b). On the other hand, the mean ice shelf thickness being thicker when using the 3D Earth structure results in a draft in contact with warmer water, which

increases basal melt rates (Fig. 4.4c). The effect of the decrease in ice shelf area is larger than the effect of shelf base depth. Hence, the main mechanism behind the stabilising effect is the reduction of ice shelf area growth due to delayed grounding line retreat.

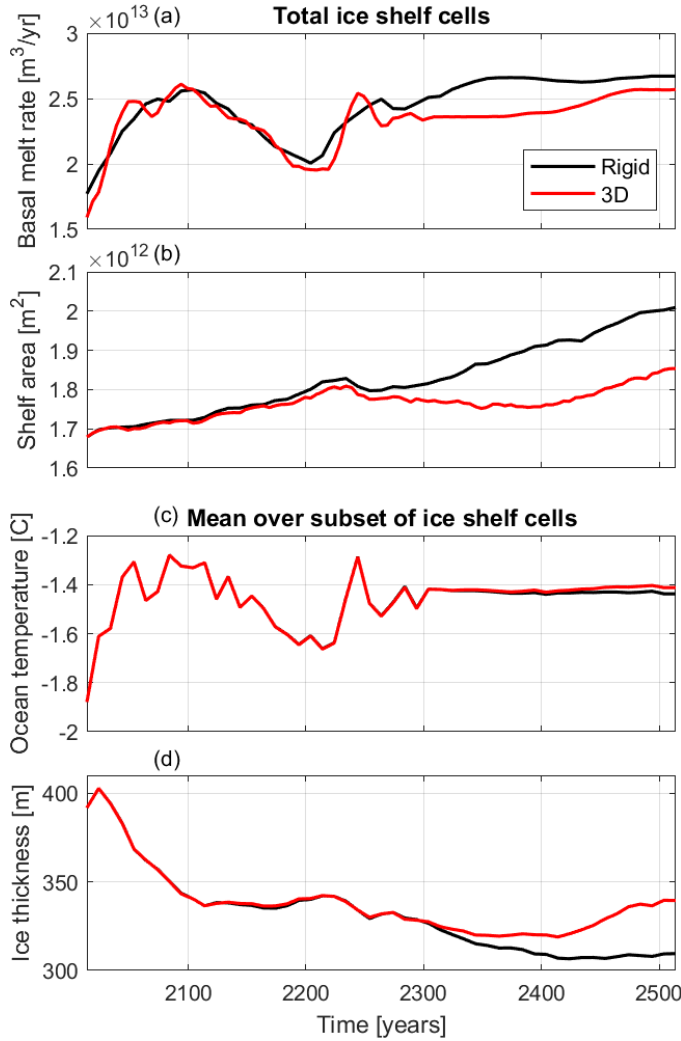


Figure 4.4: The total sub-shelf basal melt rate and total ice shelf area when using a rigid Earth and a 3D Earth structure are shown in panel a and b, respectively. Panel c and d show the mean ocean temperature at shelf base depth and ice thickness over a subset of the ice shelf cells. This subset consists of all cells that are floating, at any given time, in both the rigid-Earth and the 3D-Earth structure simulations. Results are shown only for the experiments driven by IPSL forcing, but they are qualitatively similar under CESM forcing.

4.4. IMPLICATIONS FOR ICE SHEET PROJECTIONS

The timing and magnitude of ice mass loss determine the bedrock response, which in our experiments have been the result of a projected climate warming based on the low-emission SSP1-2.6. In order to account for the uncertainty in projected climate pathways, we also studied the effect of GIA for the high emission SSP5-8.5. We found that the emission scenario is the most important factor determining future sea-level rise, compared to the effect of bedrock deformation and choice of climate model. By year 2500, sea-level rise is reduced by 29-59% under the low emission scenario compared to the high emission scenario, dependent on the combination of chosen climate model and 3D Earth structure (Fig. 4.2a and Tab. 4.5 in section 4.6). Using 3D Weaker instead of a rigid Earth reduces the sea-level contribution from Antarctica by 16-23% (0.7-1 m) under the low-emission scenario, and 12-17% (0.8-1.3 m) under the high emission scenario, dependent on the climate model (Fig. 4.2a and Tab. 4.2 in section 4.6). Some studies (Gomez et al., 2024; Pollard et al., 2017) present a possible stronger reduction of sea level rise by fast bedrock uplift, but such strong reductions in sea level rise are only found when strong East Antarctic Ice Sheet retreat is occurring due to the inclusion of marine ice cliff instability, which is disputed (Morlighem et al., 2024). In addition, we show that the widely used ELRA model and 1D Earth models with a relaxation time of 3000 years and an upper mantle viscosity of $10^{21} \text{ Pa} \cdot \text{s}$, respectively, systematically underestimate the stabilising effect of bedrock uplift. The reduction of sea level rise when using these models is only 2-3% for the low emission scenario, and 3-5% for the high emission scenario, dependent on the climate model and Earth model.

Under the high emission scenario, the grounding line retreat leads to a WAIS collapse for both climate models and the grounding line reaches the same position in 2500, independent from the Earth structure and climate model. The delay in grounding line retreat due to the 3D Earth structure is only 20-30 years, dependent on the Earth structure and climate model, because the bedrock uplift is too slow compared to the fast rate of ice loss under the high emission scenario. This stands in contrast to the results of the low emission scenario presented above, with up to 130 years of delay in grounding line retreat caused by the use of a weak 3D Earth structure. This can be explained by a much slower ice sheet retreat under the lower emission scenario, where the bedrock uplift is fast enough to stabilise the ice sheet. Thus, our results indicate that the impact of a 3D Earth structure is smaller for a high emission scenario than for a low emission one because, under a strong ocean warming, a collapse of WAIS cannot be prevented by bedrock uplift, supporting the findings of other studies using simpler ELRA and 1D Earth structures (Konrad et al., 2015; Coulon et al., 2021), and a 3D Earth structure (Gomez et al., 2024).

To varying degrees, our experiments show that bedrock adjustment provides a stabilising effect in all configurations: the barystatic sea-level contribution using both 3D Earth structures is reduced at any time, relative to using a rigid Earth structure for all scenarios and applied climate models. Overall, we find that the delay in grounding line retreat for the WAIS covers a total range of 50-130 years among all combinations of Earth structure, the climate model and the emission scenario tested in our study.

The negative feedback of GIA on ice dynamics is not only caused by bedrock uplift. The ice mass change in combination with bedrock adjustment affects the gravitational potential surface that the sea level would follow when at rest, called the geoid. An in-

crease of ice mass and bedrock elevation raises the geoid. Previous research that used a 1D Earth model included the self-gravitational effect of the ice sheet on the sea level and found that the near-field sea-level fall is the limiting factor of the retreat (Gomez et al., 2015; Konrad et al., 2015), although these studies did not separate the effect of bedrock uplift and the effect of the self-gravitation of the ice sheet on sea level. Other studies, also including the self-gravitational effect of the ice sheet, have shown the bedrock uplift to be the dominant factor of the stabilising effect of the solid Earth (Coulon et al., 2021; Kachuck et al., 2020). The latter used a lower viscosity, which could lead to faster bedrock uplift for a similar ice mass loss. Apart from the change in gravitational potential, the sea level will be affected by the contribution from the Greenland Ice Sheet, glaciers, land-water storage, and thermal expansion (Fox-Kemper et al., 2021). In our main results, the sea level is assumed to be spatially uniform and constant in time. We investigated the impact of this assumption on ice sheet dynamics by implementing a spatially and temporally varying sea-level where the geoid is computed by the GIA model with the Antarctica forcing using the 1D Earth structure, and the contribution from all other sources is added assuming it is uniform (see section 4.5). We found that grounding line retreat in West Antarctica is delayed even further by about 20 years due a local sea-level drop that peaks at 8 meters. The ice thickness is regionally up to 500 m thicker and the total ice volume loss decreases by 5% in 2500 when regional sea-level variations are included in 2500 compared to keeping sea level fixed at present day (Fig. 4.9 in section 4.6). Hence, our results suggest that the main stabilising effect of GIA on Antarctic Ice Sheet evolution is through bedrock uplift, and local variations in sea-level represent a smaller effect. This is caused by the changes in ice thickness that are highly local.

Since 3D simulations are computationally expensive, simulations in this study share a large set of ice model parameters. This implies that for a complete characterisation of the model spread a wider region of the model parameter space should be explored. Since intercomparison experiments suggest that the uncertainty due to choice of ice sheet model is large, experiments with other ice sheet models are also needed (Seroussi et al., 2020). The modelling setup in this study assumes an Earth in isostatic equilibrium at the start of the simulation and does not take into account already ongoing bedrock uplift at present-day. The bedrock displacement due to past ice mass loss should therefore be added to the projected bedrock displacement, which could potentially increase the stabilization effect on ice dynamics. However, observed present-day uplift rates are, for example at the Amundsen Sea Embayment, in the order of tens of millimeters per year (Barletta et al., 2018), which is considerably lower than projected uplift rates in the order of tens of centimeters per year around 2400 under strong warming, even though GNSS observations of bedrock deformation are sparse and other regions of relatively fast uplift at present-day might be uncovered. Furthermore, the ice sheet model is calibrated to a present-day equilibrium state, which underestimates projected ice mass loss in areas with already ongoing ice loss, such as the Amundsen Sea Embayment (Rignot et al., 2019; van den Akker et al., 2025). Calibrating the ice sheet model to match present-day ice mass loss would advance retreat of the Amundsen Sea Embayment, which might enhance the effect of bedrock deformation on shorter timescales than 300 years. To improve the accuracy, future research on sea level projections should include an ice model that is initialised including ongoing bedrock deformation and ice mass loss.

Finally, dissimilarities between different 3D Earth structures could be constrained if there would be more data on mantle viscosity. Improvements in seismic and geodetic infrastructure, as well as geologic findings, are instrumental in pinning down mantle viscosity. Despite this uncertainty, our results reinforce the notion that the solid Earth feedback cannot stop the fate of WAIS and the associated sea-level rise in case of a high emission scenario, which argues for strong mitigation measures. If a low emission scenario were to be followed, bedrock uplift significantly delays ice sheet retreat.

Our findings confirm that in a high-emission scenario, solid Earth feedback alone cannot prevent the collapse of the West Antarctic Ice Sheet (WAIS) and the resulting sea-level rise, emphasizing the need for strong mitigation efforts. However, under a low-emission scenario, bedrock uplift plays a critical role in significantly slowing the retreat of the ice sheet.

4.5. METHODS

The model developed for this study is a coupled ice sheet – 3D GIA model developed for the last glacial cycle in van Calcar et al. (2023) and adjusted for this study to simulate future ice sheet evolution (van Calcar et al., 2023). We used the ice sheet model IMAU-ICE (Berends et al., 2022) and a GIA finite element (FE) model (van Calcar et al., 2023).

4.5.1. ICE SHEET MODEL

IMAU-ICE combines the shallow ice and the shallow shelf approximations to compute velocities of ice flow (Berends et al., 2022; Morland, 1987; Bueler and Brown, 2009) on a 16 km grid resolution. The present-day geometry for ice and topography is taken from Bedmachine version 3 (Morlighem et al., 2020). The surface mass balance is computed by a temperature and radiation parameterisation (Berends et al., 2022). The basal sliding is determined according to the regularised Coulomb law (Zoet and Iverson, 2020). The geothermal heat flux is taken from Shapiro and Ritzwoller (2004). Basal melt at the ice shelf is computed using the Favier quadratic method (Favier et al., 2019). A detailed model description of IMAU-ICE can be found in Berends et al. (2022).

The barystatic sea level contribution is computed based on the volume above flotation following Equation 1 (Goelzer et al., 2020).

$$V_{af} = \sum_n (H_n + \min(b_n, 0)) \frac{\rho_{ocean}}{\rho_{ice}} A_n \quad (4.1)$$

The volume above flotation is denoted by V_{af} , H is the ice thickness, b is the bedrock elevation, ρ_{ocean} and ρ_{ice} the density of water and ice respectively, A is the area of the gridcell, and n the gridcell number. The sea level equivalent (SLE) is then computed using

$$SLE = \frac{V_{af}}{A_{ocean}} \frac{\rho_{ice}}{\rho_{ocean}} \quad (4.2)$$

The ocean area (A_{ocean}) is assumed to be $3.611 \cdot 10^{14} m^2$ (Goelzer et al., 2020). IMAU-ICE includes a module to compute bedrock surface deformation using the ELRA model. The ELRA model is a simplified representation of Earth's viscoelastic response to surface loading changes (Le Meur and Huybrechts, 1996), commonly used in ice sheet models. It

conceptualizes the lithosphere as an elastic shell and the underlying asthenosphere as a uniform medium with a characteristic relaxation time, capturing the delayed viscous response of the mantle without explicitly solving equations of motion. The bedrock response is described using a relaxation equation for the bedrock elevation h :

$$\frac{dh}{dt} = \frac{h_{eq} - h}{\tau} \quad (4.3)$$

where h_{eq} is the equilibrium bedrock height dictated by isostatic balance, and τ is the relaxation timescale, typically assumed to be 3000 years (Le Meur and Huybrechts, 1996). This approach provides an efficient way to approximate bedrock deformation in ice sheet models while maintaining computational efficiency.

4

4.5.2. CALIBRATION OF THE ICE SHEET MODEL

The Antarctic Ice Sheet is calibrated to an equilibrium state at present day. In there, the difference between observed and modelled ice thickness is minimised by adjusting the basal friction coefficient and ocean temperature over a period of 10,000 years. During this time, there are no vertical displacements of the bedrock such that the ice sheet is in equilibrium with the present-day bedrock topography at the end of the calibration. Present day ocean temperature and salinity from the World Ocean Atlas (Zweng et al., 2019) are extrapolated into the sub-shelf cavities and taken as the initial value for the calibration (Jourdain et al., 2020).

The total ice volume at the end of the calibration deviates 20 mm sea-level equivalent from the present day observed ice volume. The 95th percentile of the absolute difference between the modelled ice thickness at the end of the calibration and the observed ice thickness (Bedmachine version 3) is 50 meters (Fig. 4.10 in section 4.6). The modelled grounding line mostly coincides with the observed grounding line. Where that is not the case, the modelled grounding line lies more towards the ocean and the deviation from the observed grounding line never exceeds 16 km. When run for 2000 years under constant climate and ocean conditions after the calibrated equilibrium state, the model shows a negligible model drift.

4.5.3. FORCING SCENARIOS

The ocean temperature, salinity and atmospheric temperature anomalies, and precipitation ratios result from two climate models: CESM2-WACCM (hereafter CESM) and IPSL-CM6A-LR (hereafter IPSL) for IPCC scenario SSP5-8.5 and SSP1-2.6 (Fig. 4.11 in section 4.6)(as used in Coulon et al., 2024). These two models were selected from the climate model intercomparison project CMIP6 since they are two of the few models providing projections until 2300 (Coulon et al., 2024; Meehl et al., 2020). In the high emission scenario, the ocean temperature anomaly is smaller in CESM than in IPSL, with a maximum difference of 1.2°C at 2300. In the low emission scenario, the ocean temperature anomaly in CESM is smaller than in IPSL until 2100 and larger from 2100 onwards, with a maximum difference of 0.3°C in 2200.

Up to 2300, ocean temperature and salinity anomalies from the climate models are added to the inverted ocean temperature from the calibration and to the extrapolated salinity values from the World Ocean Atlas. Atmospheric temperature anomalies and

precipitation ratios are added to the present day observed climate taken from ERA5 (Upala et al., 2005). Between 2300 and 2500, the forcing is kept constant at the value of 2300 since no data from climate models exist on these time scales (Coulon et al., 2024; Gollledge et al., 2015).

4.5.4. COUPLING TO THE GIA MODEL

The ice sheet model and the GIA model are coupled following the method by van Calcar et al. who applied the coupling method to the last glacial cycle (van Calcar et al., 2023). The ice sheet model IMAU-ICE was adjusted to output ice loading such that it can be used by an external GIA model and to use bedrock deformation provided by an external GIA model.

The total simulation time of 500 years is divided over coupling time steps of 5 years. The coupling time step is the time over which IMAU-ICE is run before the output is passed on to the GIA model and in turn, the time over which the GIA model is run before the output is passed back to IMAU-ICE. The coupling method is based on the following procedure. First, the ice sheet model is run over a period of 5 years using a smaller time step that varies between 1 month and 2 years. The resulting change in ice load is used as input for the GIA model, which is then run for the same period in time as IMAU-ICE. The GIA model uses time steps varying between hours and months to simulate the 5-year period. The GIA model provides the total bedrock deformation over the 5-year period, linearly interpolated to the time steps in IMAU-ICE. This deformation is then used to run the ice sheet model again for the same period. Then, the ice model moves on to the next period.

The coupling timestep can be chosen as short as needed because our method allows to stop the computation, save all important variables, and restart at any time step. We tested the effect of coupling time steps of 20, 10, 5 and 3 years. The effect of the length of the coupling time step and the number of coupling iterations on the total ice volume is in the order of mm sea level equivalent. The difference in ice thickness between a 5 and a 3 yr coupling time step is 120 m on a small scale of approximately 1000 km² (Fig. 4.12 in section 4.6). The shorter the coupling time step, the more time steps need to be performed to simulate 500 years in total. Each coupling time step has approximately the same runtime independent of the length of the coupling time step.

We also tested the impact of running IMAU-ICE twice over the same time step as described above, where the second time includes the deformation computed by the GIA model over that same time step. The difference in ice thickness between iterating or not iterating for a 5 yr coupling time step is 250 m on a small local scale of approximately 1500 km² (Fig. 4.13 in section 4.6). Iterating once over the coupling time step does not increase the computation time much since it only requires an extra simulation of the ice sheet model and not of the GIA model, whereas the GIA model is the main time consuming component. Our final choice is a coupling time step of 5 years with one iteration, which leads to a feasible runtime and acceptable differences with respect to smaller time steps and more iterations.

4.5.5. GIA MODEL

The GIA model is developed by Blank et al. (2021) and adjusted for the coupling to an ice sheet model by van Calcar et al. (2023). The GIA model is a spherical model based on

finite element software ABAQUS that can include self-gravity. For this study, the GIA model contains a total of 9 layers with 1 layer for the core, 7 mantle layers and 1 surface layer. The lithospheric thickness follows from the assigned parameters determining the rheology and therefore varies locally and is not prescribed to follow a certain layer. The model is materially compressible, which includes compressible material but not the effect on buoyancy forces (Klemann et al., 2003). A et al. (2013) showed that present-day Antarctic uplift rates are reduced by about 5% when an incompressible model was used compared to a compressible model. The difference will be smaller for a material compressible model compared to a fully compressible model (Reusen et al., 2023). It is assumed that the Earth is in isostatic equilibrium at present day.

In the main simulations, we exclude the effect of the local sea-level to disentangle the effect between bedrock uplift and local sea-level variations. Due to the decrease in gravitational attraction of the shrinking ice sheet, local sea-level will drop. This will stabilise the ice sheet even further, besides the effect of bedrock uplift. In this study we focus solely on the effect of bedrock uplift. However, we have tested the effect of including local sea-level variations. These are computed for each coupling time step as a result of bedrock deformation and changes in gravitational potential due to the ice load and the deformation using the GIA model. Then, background sea-level change is computed as the combination of projected contribution from thermal expansion and melt from Greenland, glaciers and land-water storage, which is then added to the local sea-level variations (Tab. 4.6 in section 4.6). We assume that this contribution is uniform in space over Antarctica. This underestimates the contribution from Greenland because the actual sea-level contribution in Antarctica is higher due to the self-gravitational effect of the Greenland ice sheet. However, the effect of thermal expansion, Greenland, glaciers and land-water storage on the local sea-level in Antarctica is small compared to the 8 m sea-level drop in Antarctica due to its loss of gravitational attraction (see section 4.4).

The GIA model has a global resolution of 200 km and a higher resolution region of 30 km over Antarctica. Using a resolution of 15 km for Antarctica resulted in negligible difference on ice volume and maximum 6 meter difference in bedrock deformation (Fig. 4.14 in section 4.6), with significant larger computation time than using a resolution of 30 kilometres. The viscoelastic bedrock response to changes in ice loading is a much smoother response than the change in ice loading itself. The resolution of IMAU-ICE is 16 km. Therefore, increasing the resolution of the GIA model without increasing the ice sheet model resolution is not useful. When the sea-level equation would have been solved, the topography should be included at high resolution, separately from the resolution of the FE model, as done in Blank et al. (2021).

Including self-gravitation of the Earth in the GIA model has a negligible effect on ice volume change and results in difference of 100 m in the ice thickness and 3 meters in bedrock deformation on a local scale (Fig. 4.15 in section 4.6). However, including self-gravity doubles the computation time. We therefore decided to not include self-gravitation in the GIA model.

The GIA model used for this study does not include rotational effects. A change in Earth's rotation caused by ice loss affects the equilibrium shape of the ocean surface, and the deformation of the crust directly. This has been shown to be a significant effect in the far field sea level fingerprint of a West Antarctic Ice Sheet collapse (Mitrovica et al., 2009).

In our study, we don't simulate the sea level fingerprint and only compute the barystatic sea level contribution of the Antarctic Ice Sheet. Signals are smaller for Antarctica due to its proximity to the rotational axis, where mass redistributions have a weaker influence on Earth's rotation.

4.5.6. EARTH STRUCTURES

The projections are performed using three different Earth structures, one 1D structure and two 3D structures. The density and Young's modulus are the same for each structure and shown in Table 3.1 (van Calcar et al., 2023). The 1D rheology contains an elastic lithospheric thickness of 100 km and an upper mantle viscosity $10^{21} Pa \cdot s$ (hereafter referred to as 1D), similar other 1D GIA models for Antarctica (Bulthuis et al., 2019; Golledge et al., 2015; Gomez et al., 2015; Levermann et al., 2020; Rodehacke et al., 2020).

The 3D rheology of the mantle is computed using spatially varying seismic velocity anomalies from Lloyd et al. (2019) for Antarctica and from Becker and Boschi (2002) globally. The spatially varying mantle temperature can be derived from the seismic velocity anomalies assuming seismic anomalies are caused by thermal anomalies (Ivins et al., 2023; Karato et al., 2008). The uncertainty rising from the interpretation of the seismic anomaly in terms of temperature and viscosity is taken into account by using different flow law parameters and constraining those with regional viscosity estimates (Ivins et al., 2023). The temperature together with pressure for a hydrostatic Earth is used to compute dislocation and diffusion parameters based on flow law for olivine, as dislocation and diffusion creep are assumed to be the most important mantle deformation mechanisms (van der Wal et al., 2010). The method to obtain dislocation and diffusion parameters from seismic velocities is discussed in van Calcar et al. (2023).

As little information exists on grain size and water content, these parameters are kept spatially homogeneous (van der Wal et al., 2015). To determine the water content and grain size, we consider three regions where significant ice mass loss occurs and for which the mantle viscosity is relatively well known from fitting different GIA models to GPS data, namely the Amundsen Sea Embayment with an upper mantle viscosity of $4 \cdot 10^{18} Pa \cdot s$ (Barletta et al., 2018), and the Weddel Sea Embayment and Palmer Land with a viscosity of $1 - 3 \cdot 10^{20} Pa \cdot s$ (Bradley et al., 2015; Ivins et al., 2023; Wolstencroft et al., 2015). We computed the average mantle viscosity over depth intervals that align with these constraints and are considered sensitive to ice mass loss in each region. For the Amundsen Sea Embayment, Barletta et al. (2018) showed that both the shallow and deeper portions of the upper mantle, with a transition at approximately 200 km depth, respond to changes in ice loading. We therefore computed the average mantle viscosity between 150 and 250 km depth. To ensure the lithosphere was excluded from our calculation, we omitted viscosities above $10^{30} Pa \cdot s$. For the Weddell Sea and Palmer Land, mantle viscosity constraints are defined for the upper mantle between 120 and 660 km depth (Bradley et al., 2015; Wolstencroft et al., 2015). Accordingly, we calculated the average viscosity across the middle part of the upper mantle, from 350 to 450 km depth. All viscosity estimates were computed for a range of water contents from 0 to 800 ppm and grain sizes from 500 μm to 9.5 mm. The best fitted viscosity at the Amundsen Sea Embayment to the data is $5 \cdot 10^{18} Pa \cdot s$ with a water content of 800 ppm and a grain size of 2.5 mm. However, for this combination of parameters, the viscosity is approximately 1 and

Table 4.1: Average mean viscosity for the Weddell Sea Embayment, the Amundsen Sea Embayment and Palmer Land for two different combinations of grain size and water content. 3D Weaker follows from a water content of 400 ppm and a grain size of 2.5 mm, and 3D Stronger follows from a water content of 200 ppm and a grainsize of 4.5 mm.

	3D Weaker Mean viscosity [Pa·s]	3D Stronger Mean viscosity [Pa·s]
Weddel Sea Embayment	$4 \cdot 10^{19}$	$3 \cdot 10^{20}$
Amundsen Sea Embayment	$8 \cdot 10^{18}$	$4 \cdot 10^{19}$
Palmer Land	$1 \cdot 10^{19}$	$1 \cdot 10^{20}$

4

1.5 orders of magnitude too low in the Weddell Sea Embayment and Palmer Land compared to their constraints, respectively. On the other hand, a water content of 400 ppm in combination with a grainsize of 8.5 mm leads to the best fit viscosity of $3 \cdot 10^{20} \text{ Pa} \cdot \text{s}$ for Palmer Land, but this leads to a viscosity in the Amundsen Sea Embayment of 1 and 0.5 orders of magnitude too high at the Amundsen Sea Embayment and the Weddell Sea Embayment respectively. Even though the fit is very good for one of the regions, the combination of parameters leads to a large total misfit for the three regions together. To reduce the total misfit, we chose a combination that fits within half an order of magnitude at the Amundsen Sea Embayment and within one order of magnitude at the other regions, namely a water content of 400 ppm and a grain size of 2.5 mm (referred to as 3D Weaker). Furthermore, we chose a combination that fits within half an order of magnitude at the Weddell Sea and Palmer Land, and within one order of magnitude in the Amundsen Sea Embayment, namely a water content of 200 ppm and a grainsize of 4.5 mm (referred to as 3D Stronger). The average viscosities for each region for 3D Weaker and 3D Stronger are shown in Tab. 4.1. Both rheologies can be considered realistic based on other viscosity estimates and fit with GIA observations (Blank et al., 2021; Barletta et al., 2018). A water content of 400 ppm is within the range of water content found in Antarctic xenoliths (Martin, 2021).

The mantle viscosities of the 3D experiments are shown in Fig. 4.5 in section 4.6 at three depths. The 3D viscosities are up to 4 orders of magnitude lower at certain locations in West Antarctica and up to 3 orders of magnitude higher in East Antarctica compared to the 1D rheology. The viscosity of the 3D Stronger rheology is about 1 order of magnitude higher than the 3D Weaker rheology (Fig. 4.5d-f in section 4.6).

4.6. SUPPLEMENTAL MATERIALS

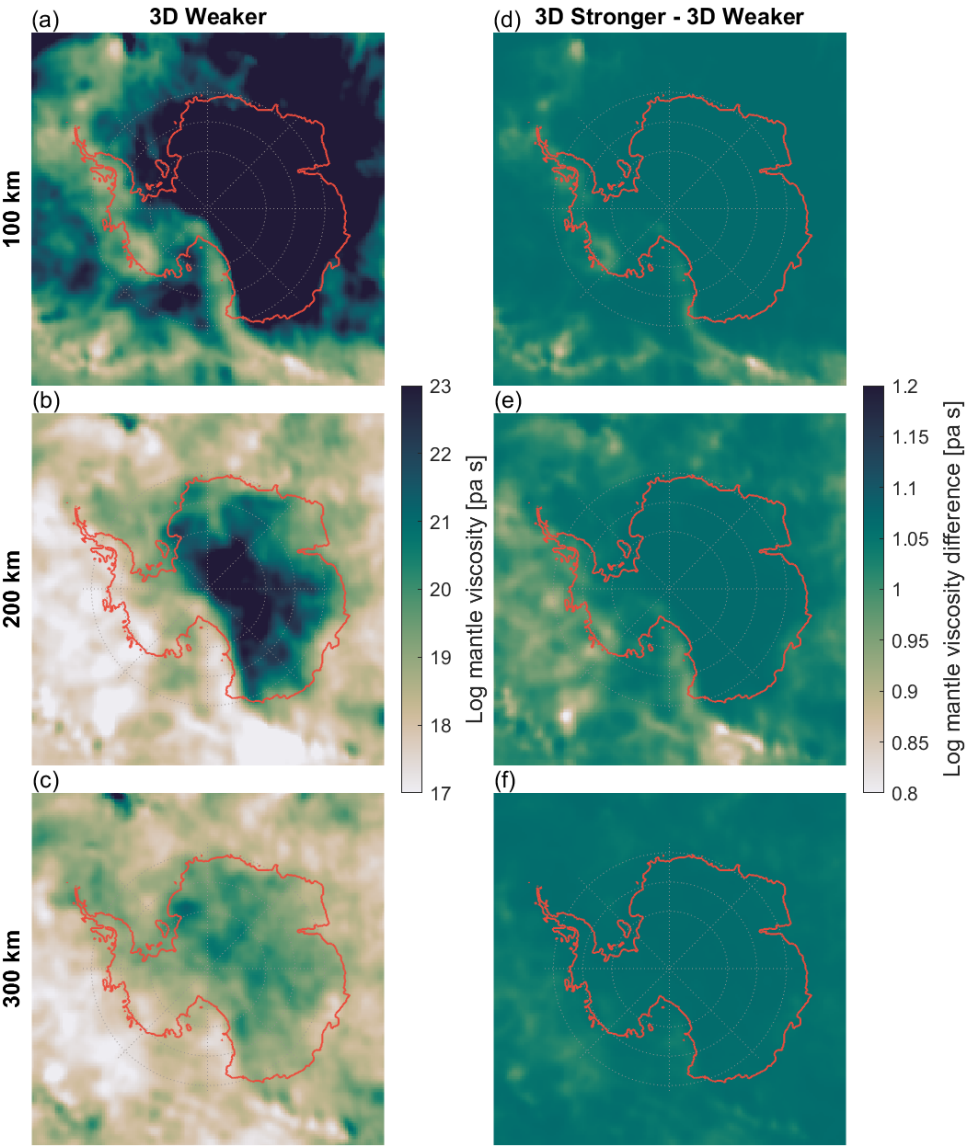


Figure 4.5: Viscosity at the depth of 100, 200 and 300 km of the 3D Weaker rheology (panels a-c) and the difference in viscosity between the 3D Stronger and the 3D Weaker rheologies (panels d-f).

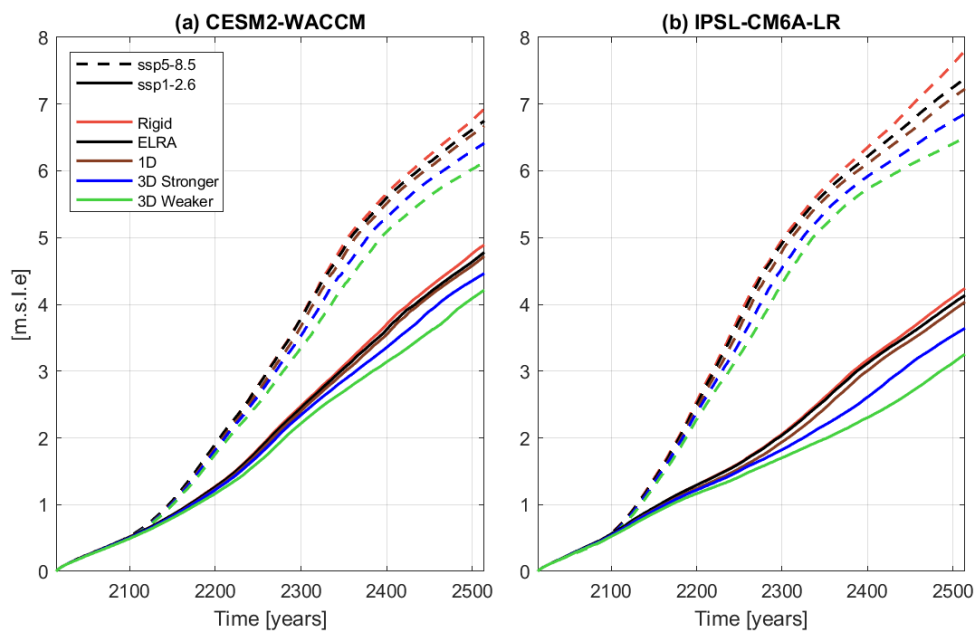


Figure 4.6: Barystatic sea level contribution under two different scenarios, two different global climate models and 5 different Earth structures (see section 4.5).

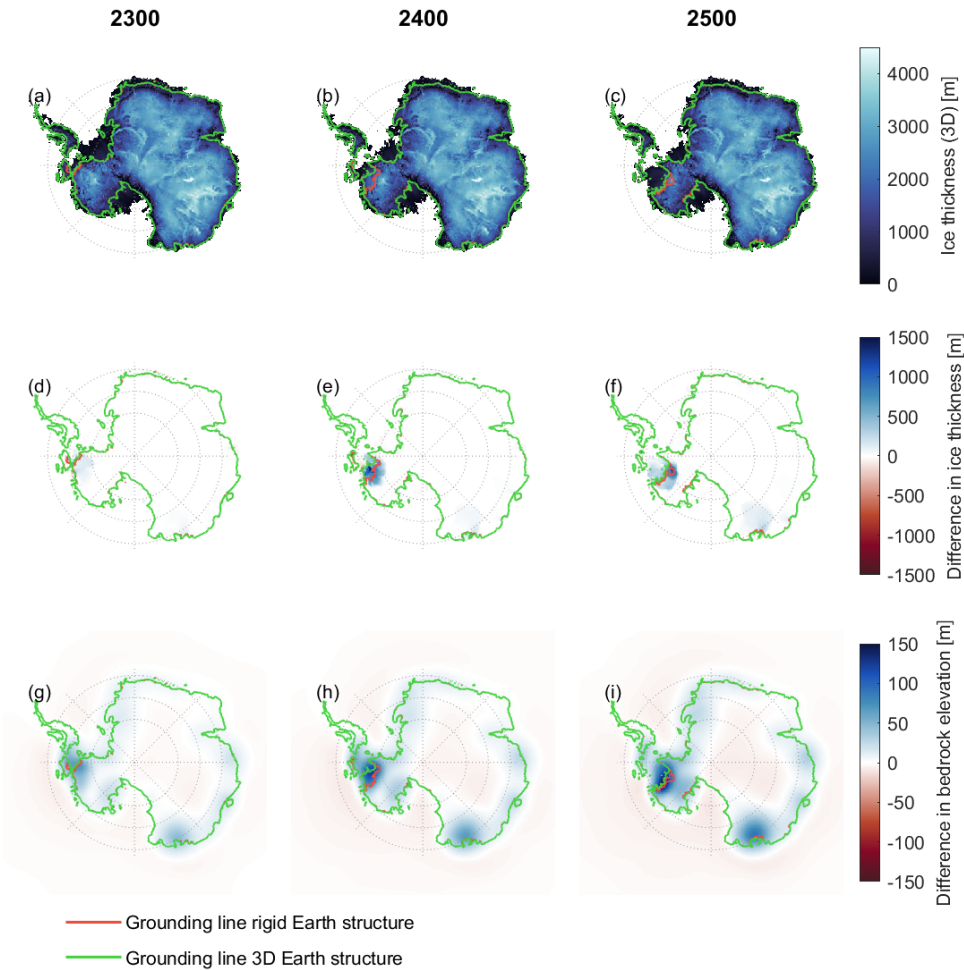


Figure 4.7: The ice thickness of the West Antarctic Ice Sheet at 2300 , 2400 and 2500 using the 3D Earth structure when applying CESM2-WACCM under the low emission scenario ssp1-2.6 (panel a-c). Panel d-f show the ice thickness difference between using the 3D Earth structure and the rigid Earth structure. Panel g-i show the difference in bedrock elevation between using the 3D Earth structure and the rigid Earth structure. CESM2-WACCM corresponds to the climate model with main warming in the Weddel sea (see section 4.5).

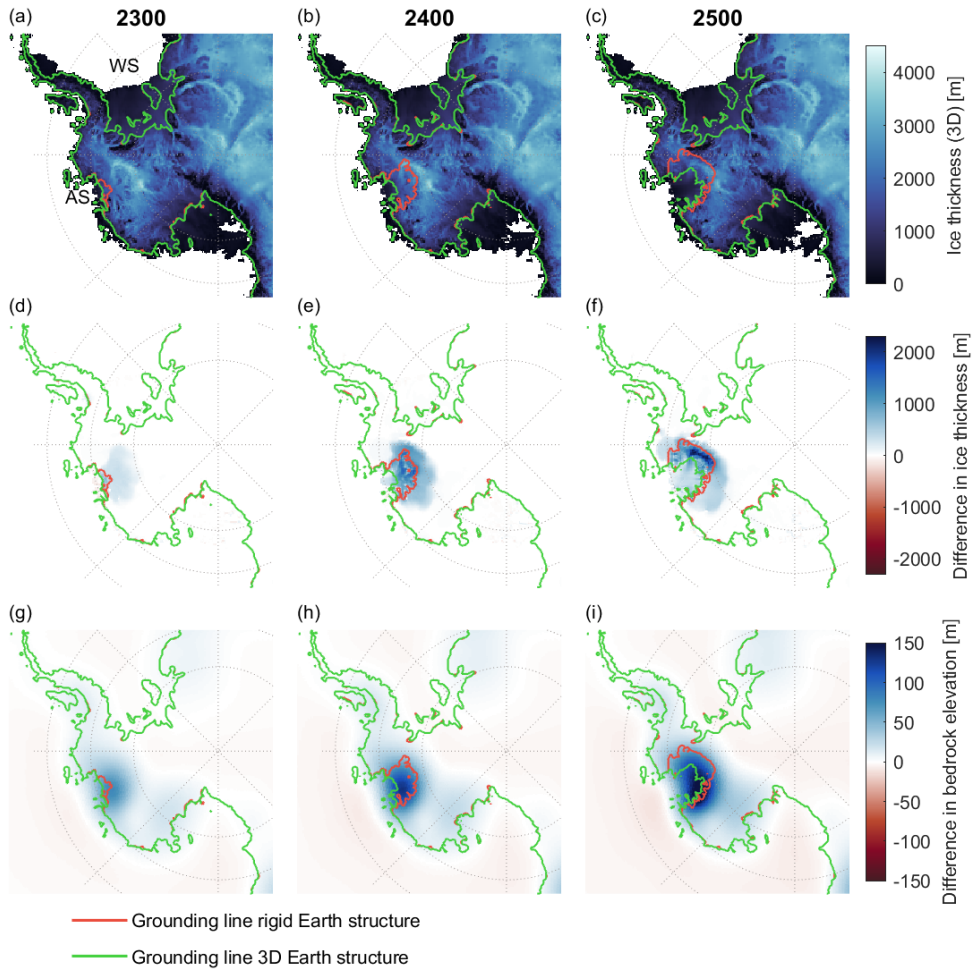


Figure 4.8: The ice thickness of the West Antarctic Ice Sheet at 2300 , 2400 and 2500 using the 3D Earth structure when applying IPSL-CM6A-LR under the low emission scenario ssp1-2.6 (panel a-c). AS in panel a indicates the Amundsen sea, and WS indicates the Weddel sea, and WB indicates Wilkes basin. Panel d-f show the ice thickness difference between using the 3D Earth structure and the rigid Earth structure. Panel g-i show the difference in bedrock elevation between using the 3D Earth structure and the rigid Earth structure. IPSL-CM6A-LR corresponds to the climate model with main warming in the Amundsen sea (see section 4.5).

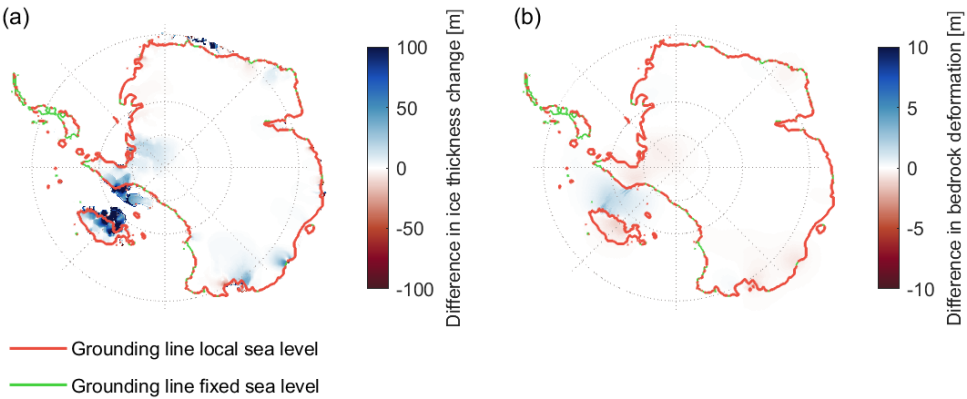


Figure 4.9: Difference in ice thickness change over the 500 year simulation. The left panel shows the difference in ice thickness change when geoid is included vs when geoid is excluded. The right panel shows the difference in bedrock deformation.

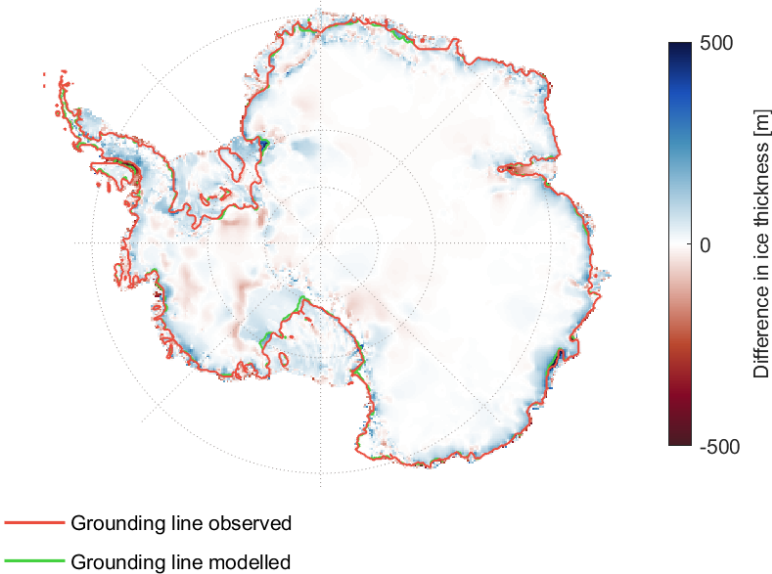


Figure 4.10: Ice thickness at the end of the inversion minus observed ice thickness (Bedmachine version 3).

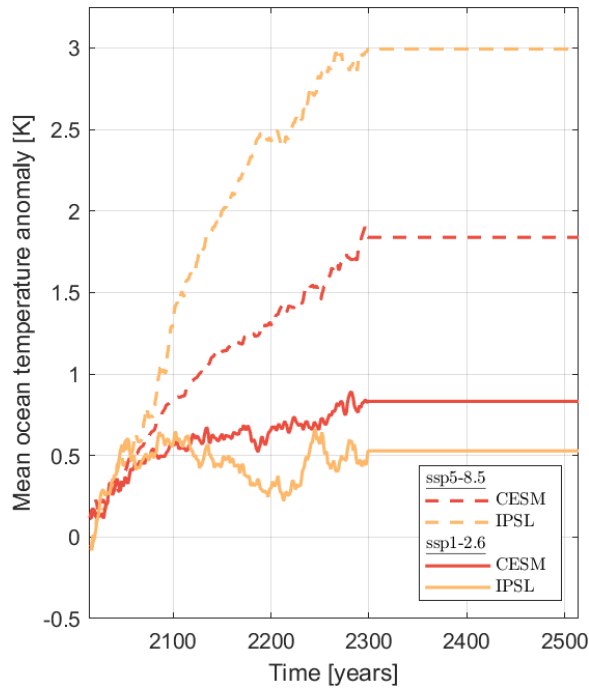


Figure 4.11: The mean ocean temperature anomaly over the present day ice shelf area between 2014 and 2514. The anomalies are taken from Coulon et al.9, whom used ocean temperature anomalies from the global climate models CESM2-WACCM (indicated by CESM) and IPSL-CM6A-LR (indicated by IPSL) for two different IPCC scenario's: SSP5-8.5 and SSP1-2.6. The anomalies are averaged over the present day ice shelf area for each time step.

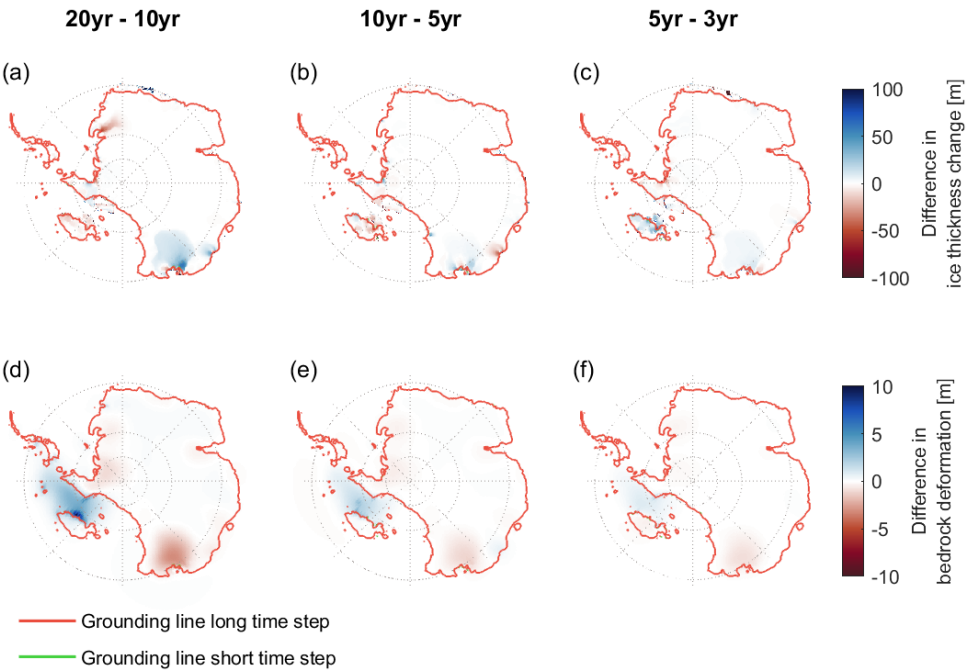


Figure 4.12: Difference in ice thickness (panels a-c) and bedrock deformation (panels d-f) between different coupling time steps. Note that the red line is overlapping the green line. Note that the green line is mostly covered by the red line.

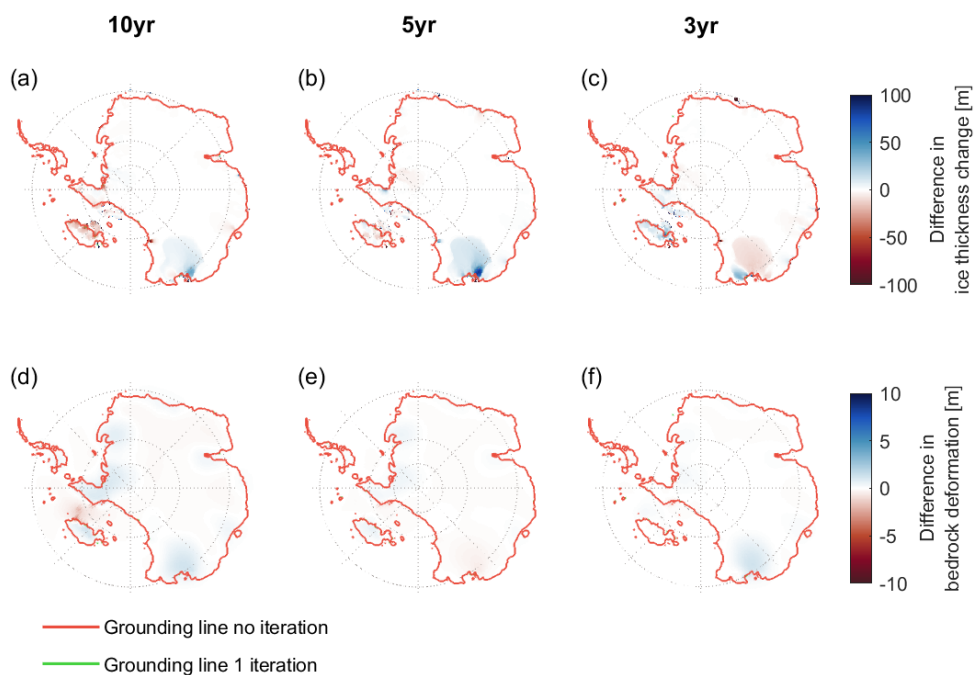


Figure 4.13: Difference in ice thickness and bedrock deformation between applying 1 iteration and applying no iterations for each coupling time step. Note that the red line is overlapping the green line. Note that the green line is mostly covered by the red line.

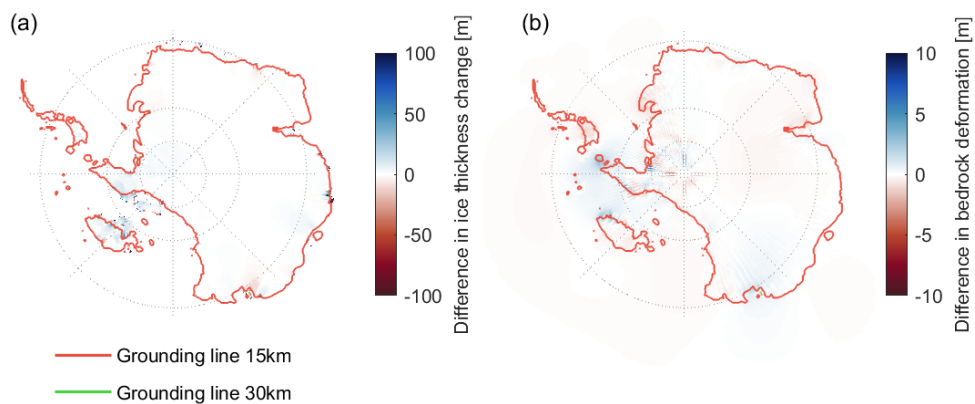


Figure 4.14: The left panel shows the difference in ice thickness change over a 500 year simulation between using a 30 km resolution of the GIA model and 15 km resolution. The right panel shows the difference in bedrock deformation. Note that the red line is overlapping the green line. Note that the green line is mostly covered by the red line.

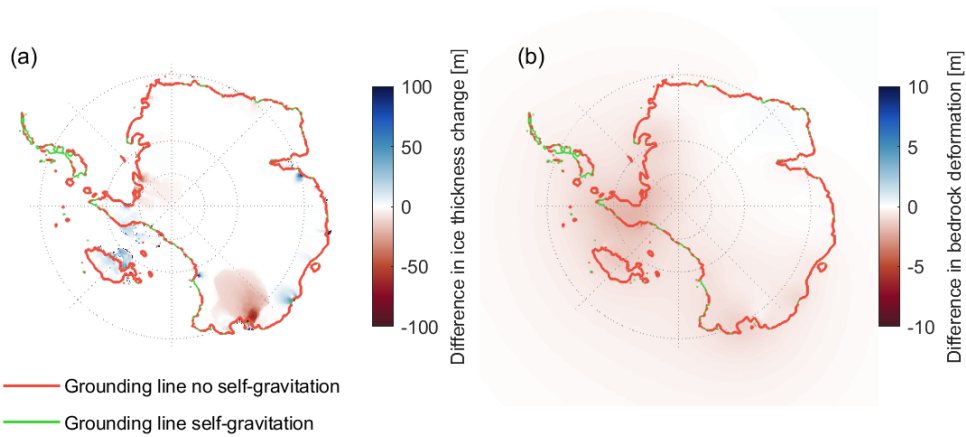


Figure 4.15: The left panel shows the difference in ice thickness change over a 500 year simulation when self-gravity is included vs when self-gravity is excluded. The right panel shows the difference in bedrock deformation. Note that the red line is overlapping the green line. Note that the green line is mostly covered by the red line.

Table 4.2: Maximum reduction in sea level rise of the 3D Earth structures compared to rigid Earth. The climate model IPSL-CM6A-LR is referred to as IPSL and the climate model CESM2-WACCM is referred to as CESM.

Climate model	Emission scenario	Reduction of 3D weaker [%]	Reduction of 3D stronger [%]
CESM	SSP5-8.5	12	7
CESM	SSP1-2.6	16	9
IPSL	SSP5-8.5	17	12
IPSL	SSP1-2.6	23	14

Table 4.3: Maximum delay in grounding line retreat in years under different Earth structures for two climate models.

	IPSL-CM6A-LR	CESM2-WACCM
3D Weaker	130 yr	70 yr
3D Stronger	80 yr	50 yr

4

Table 4.4: Maximum reduction in sea level rise of the climate models IPSL-CM6A-LR compared to CESM2-WACCM.

Emission scenario	Reduction of rigid Earth [%]	Reduction of 3D weaker [%]	Reduction of 3D stronger [%]
SSP5-8.5	26	22	23
SSP1-2.6	16	31	25

Table 4.5: Maximum reduction in sea level rise of the low emission scenario compared to the high emission scenario. The climate model IPSL-CM6A-LR is referred to as IPSL and the climate model CESM2-WACCM is referred to as CESM.

Climate model	Reduction of rigid Earth [%]	Reduction of 3D weaker [%]	Reduction of 3D stronger [%]
CESM	46	36	35
IPSL	29	59	57

Table 4.6: Contribution of all components to global mean sea level rise, except the component of Antarctica (IPCC AR6 chapter 9).

Contribution	SSP1.2-6		SSP5.8-5	
	2100	2300	2100	2300
Thermal expansion	0.14	0.19	0.3	0.92
Greenland	0.06	0.11	0.13	0.32
Glaciers	0.09	0.12	0.18	0.32
Land-water storage	0.03	0.05	0.03	0.05



Antarctic Sound, Antarctica

5

APPROXIMATING ICE SHEET – BEDROCK INTERACTION IN ANTARCTIC ICE SHEET PROJECTIONS

The bedrock response to a melting ice sheet provides a negative feedback on ice mass loss. When modelling the future behaviour of the Antarctic Ice Sheet, accounting for the impact of bedrock deformation on ice dynamics can reduce predictions of future sea level rise by up to 40% in comparison with scenarios that assume a rigid Earth. The rate of the solid Earth response is mainly dependent on the viscosity of the Earth's mantle, which varies laterally and radially with several orders of magnitude across Antarctica. Because modelling the response for a varying viscosity is complex, sea level projections often exclude the Earth's response, or apply a globally constant relaxation time or viscosity. We investigate how accurate such approximations are using an ice sheet model coupled with a glacial isostatic adjustment (GIA) model that simulates the bedrock response to changes in ice loading including lateral and radial variations in viscosity (3D GIA model). Using the 3D model we determined a relation between relaxation time and viscosity which can be used in simpler models. We compare output from an elastic lithosphere relaxed asthenosphere (ELRA) with uniform and laterally varying relaxation times, and a GIA model with a radially varying Earth structure (1D GIA model) and a 3D GIA model. We conducted 500 year projections of the Antarctic Ice Sheet evolution using two different climate models and two emissions scenarios: the high emission scenario SSP5-8.5 and the low emission scenario SSP1-2.6. The results show that using a uniform relaxation time of 300 years in the ELRA model or an upper mantle viscosity of $10^{19} \text{ Pa} \cdot \text{s}$ in the 1D GIA model leads to a total sea

Published as: van Calcar, C.J., Whitehouse, P.L., van de Wal, R.S.W., and van der Wal, W.: Approximating ice sheet – bedrock interaction in Antarctic ice sheet projections. Preprint, 2024. Minor corrections are included in this thesis.

level rise that deviates less than 40 cm from the average of the 3D GIA models. This difference in the sea level rise predicted with 1D and 3D GIA models can be further reduced to 10 cm by using laterally varying relaxation time maps in an ELRA model. Our results show that the effect of 3D viscosity variations on the AIS contribution to sea level rise can be approximated using the ELRA model or a 1D GIA model when the recommended parameters derived from the full 3D GIA model are used.

5.1. INTRODUCTION

The melt of (part of) the Antarctic Ice Sheet might contribute several meters to global mean sea level rise over the next centuries (Fox-Kemper et al., 2021). The rate of ice loss is influenced by many processes such as atmospheric and oceanic feedbacks, ice dynamics, and interactions with the underlying bedrock. Accurately representing these processes in models, along with their associated uncertainties, presents a significant challenge for projecting the ice sheet evolution. To address this, a wide range of parameters in the ice sheet model must be explored, requiring thousands of simulations to produce robust projections of potential sea level rise over the coming centuries (Seroussi et al., 2020).

One of the main uncertainties in projecting the evolution of the Antarctic Ice Sheet over the next centuries is the response of the solid Earth to future changes in ice mass (Fox-Kemper et al., 2021). The bedrock experiences uplift due to the loss of ice mass at the surface, a process known as glacial isostatic adjustment (GIA). The bedrock uplift can delay grounding line retreat and thereby stabilize the ice sheet (Book et al., 2022; Coulon et al., 2021; Gomez et al., 2024; Kachuck et al., 2020; Konrad et al., 2015; Pollard et al., 2017; van Calcar et al., 2024; Whitehouse et al., 2019). The rate of the bedrock uplift depends on the viscosity of the Earth's mantle, which varies both radially and laterally by several orders of magnitude beneath the Antarctic Ice Sheet (Ivins et al., 2023; Kaufmann et al., 2005), as derived from seismic models (e.g. Lloyd et al., 2019). Therefore, bedrock uplift is influenced not only by the amount of ice mass loss but also by the specific region where the loss occurs. Models that include the solid Earth feedback for a realistic Earth structure project a maximum of 23-40% reduction in sea level rise over the coming centuries compared with models that assume a rigid Earth (Gomez et al., 2024; van Calcar et al., 2024), and a delay in grounding line retreat in the Amundsen Sea Embayment by up to 130 years (van Calcar et al., 2024). However, it is currently unfeasible to include a realistic Earth structure in a large ensemble of sea level projections due to the long computation time involved (van Calcar et al., 2023). Therefore, projections of the Antarctic Ice Sheet evolution by ice sheet models either omit bedrock uplift or use simplified Earth models (Levermann et al., 2020).

One such simplified model that is commonly coupled to ice sheet models is the elastic lithosphere relaxed asthenosphere (ELRA) model. ELRA models are computationally cheap and can be used in combination with a range of ice models, allowing large ensembles of sea level projections to be simulated (Bulthuis et al., 2019; Coulon et al., 2024; DeConto et al., 2021). Typically, the ELRA model is used with a uniform relaxation time of 3000 years and a flexural rigidity of $10^{25} \text{ kg m}^2 \text{ s}^2$, which roughly corresponds to a lithospheric thickness of 100 km. The relaxation time of the Earth's mantle, which is a characteristic time scale that expresses how fast the mantle responds to changes in

surface loads, serves as a proxy for mantle viscosity because it also reflects how fast the viscous mantle flows under stress. Flexural rigidity is the resistance of a body, such as the Earth's lithosphere, to bending and is determined, among other, by its stiffness (the Young's modulus) and its thickness.

Alternatively, some sea level projections use ice sheet models coupled with a 1D GIA model. A GIA model can include the bedrock response to changes in ice loading, and can be used in combination with the sea level equation to include changes in ocean loading. In this study, we use the term GIA model for a model that computes deformation based on ice loading only. A 1D GIA model includes an Earth structure where viscosity varies radially and not laterally, equivalent to a self-gravitating viscoelastic Earth (SGVE) model (Le Meur and Huybrechts, 1996). Current existing ice sheet projections use a homogeneous upper mantle viscosity of $10^{21} \text{ Pa} \cdot \text{s}$ (Golledge et al., 2019; Gomez et al., 2015; Konrad et al., 2015; Rodehacke et al., 2020). However, using such a viscosity value, or a relaxation time of 3000 years, does not affect sea level rise projections significantly compared with excluding GIA entirely, and it overestimates sea level rise by up to 20% by the year 2500 compared with projections that use GIA models that consider 3D Earth structure, which we refer to as 3D GIA models (see Chapter 4).

In the Amundsen Sea embayment, mantle viscosity can be as low as $10^{19} \text{ Pa} \cdot \text{s}$ (Barletta et al., 2018). Incorporating a low-viscosity zone in the upper mantle within a 1D GIA model leads to a significant stabilizing effect on the ice sheet over thousands of years (Pollard et al., 2017). However, using different relaxation times for East and West Antarctica did not contribute significantly to the uncertainty in the multi-centennial response of the Antarctic Ice Sheet to climate change. This can be explained by the chosen relaxation times for West Antarctica which were longer than 1000 years, while they might be a lot shorter in this region (Bulthuis et al., 2019). Other research has demonstrated that using a laterally varying relaxation time in the ELRA model (LVELRA) with a shorter relaxation time under West Antarctica results in a significantly reduced sea level contribution from Antarctica on multicentennial-to-millennial timescales for four different warming scenarios of 5000 years (Coulon et al., 2021). While it has long been possible to determine relaxation time spectra for radially varying viscosity profiles (McConnell, 1965), such calculations have not been performed for profiles with both lateral and radial variations in viscosity. Consequently, the variation in mantle relaxation times across Antarctica remains unknown.

A laterally varying relaxation time can be implemented in a straight-forward way in an ELRA model (Coulon et al., 2021; Oude Egbrink, 2018). However, sea level projections generated using coupled ELRA-ice sheet models have not been compared with the output from coupled ice sheet-3D GIA models, leaving it unclear how well different relaxation times and 1D mantle viscosity profiles are able to approximate the behaviour seen in more complex models that include 3D Earth structure. We used the ice sheet model IMAU-ICE coupled to ELRA and a GIA model to answer the following research questions:

1. How well can a coupled ice sheet – ELRA model using uniform relaxation time approximate the ice sheet evolution resulting from a coupled ice sheet - GIA model using a 3D Earth structure?

2. How well can a coupled ice sheet – ELRA model using laterally varying relaxation time approximate the ice sheet evolution resulting from a coupled ice sheet - GIA model using a 3D Earth structure?
3. How well can a coupled ice sheet – GIA model with a 1D Earth structure approximate the ice sheet evolution resulting from this model with a 3D Earth structure?

To address these questions, 3D GIA simulations are conducted using a global spherical finite element model coupled to the ice sheet model IMAU-ICE (see Chapter 4). We use constraints from seismic velocity studies to determine the spatially-varying rheological properties of the mantle (Wu and van der Wal, 2013). Output from models that employ 3D and 1D Earth structures, and maps of different relaxation times are compared in terms of sea level rise, grounding line position, ice thickness and bedrock uplift. As a result, we recommend values for uniform relaxation times in combination with the flexural rigidity that results in a sea level rise close to the average sea level rise resulting from two 3D Earth structures, one based on a viscosity constraint in the Amundsen Sea Embayment, and one based on a constraint in the Weddell Sea Embayment and Palmer Land in the Antarctic Peninsula. Furthermore, we derive a relation between relaxation time and viscosity and recommend a laterally varying relaxation time map in combination with a flexural rigidity. Last, we recommend a 1D viscosity profile to approximate a 3D viscosity profile.

5.2. METHOD

To compare the performance of the ELRA, LVELRA and 1D GIA models with that of a 3D GIA model, we conduct sea level projections using the ice sheet model IMAU-ICE coupled to all three of these GIA models (see Chapter 4). We compare the Antarctic Ice Sheet evolution over the next 500 years under different warming scenarios and climate models using a variety of Earth structures. An overview of the simulations with different Earth models is provided in Table 5.1. We use the low emission scenario SSP1.2-6 and the high emission scenario SSP5.8.5 and the climate models CESM2-WACCM (hereafter CESM), where warming mainly occurs in the Weddell sea, and IPSL-CM6A-LR (hereafter IPSL), with warming mainly in the Amundsen Sea. The climate models provide ocean temperature, salinity and atmospheric temperature anomalies, and precipitation ratios until the year 2300, which are used to force the ice sheet model. The forcing is kept constant between 2300 and 2500. The ice dynamical model IMAU-ICE is based on the shallow ice and shallow shelf approximations (Berends et al., 2022; Bueler and Brown, 2009; Morland, 1985). Ice velocities are computed on a 16 km grid resolution. Basal sliding follows the regularized Coulomb law (Zoet and Iverson, 2020). Basal melt at the ice shelf is computed using the Favier quadratic method and the surface mass balance is computed using a temperature and radiation parameterisation (Berends et al., 2022; Favier et al., 2019). The present-day bedrock and ice surface topography are taken from Bedmachine version 3 (Morlighem et al., 2020).

5.2.1. 1D AND 3D GIA MODELS

To compute the Earth's deformation, a global spherical finite element model based on Abaqus software is used. This GIA model is used for two purposes: (1) To produce re-

Table 5.1: Different Earth structures used in the coupled ice sheet – Earth models. The 3D Stronger and Weaker structures are equal to the 3D structures in Chapter 4.

ELRA	1D GIA	3D GIA
Uniform ($\tau = 3000, 1500, 500, 400, 300, 200, 50$ yr)	1D21	3D Stronger
2D Stronger	1D20	3D Weaker
2D Weaker	1D19	
	1D18	

alistic sea level projections via coupling to the ice sheet model, and (2) to calculate the relaxation time of schematic ice unloading experiments which are used to derive a relation between relaxation time and viscosity. In the GIA model, deformation in the upper mantle is assumed to be governed by diffusion and dislocation creep in olivine (Hirth and Kohlstedt, 2003) as in earlier studies (van der Wal et al., 2013; van der Wal et al., 2015; Blank et al., 2021, van Calcar et al., 2023; van Calcar et al., 2024). We do not specify lithospheric thickness, but instead use seismic velocity perturbations to assign appropriate rheological properties in each element between 35 and 670 km depth. At shallower depths, the layer is defined to be purely elastic. At deeper depths, the lower mantle is assumed to be homogeneous. The effective viscosity, η_{eff} , is a function of the von Mises stress, q , and hence it is an output of the model rather than a property that is assumed a priori:

$$\eta_{eff} = \frac{1}{3B_{diff} + 3B_{disl}q^{n-1}} \quad (5.1)$$

Here, n is the stress exponent, and B_{diff} and B_{disl} are creep parameters for diffusion and dislocation creep as shown in Eq. 5.2a and 5.2b (Hirth and Kohlstedt, 2003).

$$B_{diff} = A_{diff}d^{-3}f_{H_2O}^1e^{-\frac{E+PV}{RT_{x,y}}} \quad (5.2a)$$

$$B_{disl} = A_{disl}d^0f_{H_2O}^{1.2}e^{-\frac{E+PV}{RT_{x,y}}} \quad (5.2b)$$

A is experimentally determined ($A_{diff} = 106$ MPa, $A_{disl} = 90$ MPa), d is the grain size, and f_{H_2O} is the water content. E is the activation energy which is assumed to be $335 \cdot 10^3$ kJ/mol for diffusion creep and $480 \cdot 10^3$ kJ/mol for dislocation creep. P is the depth dependent pressure (Kearey et al., 2009). V is the activation volume which is assumed to be $4 \cdot 10^{-6} m^3/mol$ for diffusion creep and $11 \cdot 10^{-6} m^3/mol$ for dislocation creep. R is the gas constant ($8.314 JK^{-1}mol^{-1}$), and $T_{x,y}$ is the spatially variable absolute temperature. A , E and V have different values for wet and dry olivine (Hirth and Kohlstedt, 2003), and are shown here for wet olivine. All parameters, except temperature, grain size and water content, are taken from Hirth and Kohlstedt (2003). In this study, melt content is neglected as it has a relatively small influence on viscosity in this formulation (van der Wal et al., 2015). $T_{x,y}$ is the spatially varying mantle temperature, which is derived from a high resolution seismic model (Lloyd et al., 2019) in combination with a global seismic model from Becker and Boschi (2002). The mantle temperature variations are determined by converting these global seismic velocity perturbations to temperature perturbations using derivatives from Karato et al. (2008), and then converting these to absolute temperature assuming a standard mantle geotherm (Turcotte and Schubert, 2002). The upper

mantle viscosity can vary greatly depending on the grain size and water content used. To obtain a realistic rheology, two different combinations of grain size and water content are chosen such that the average viscosity values across the Amundsen Sea Embayment and the Weddell Sea Embayment are the same as those constrained by GIA observations (Ivins et al., 2023), resulting in a relatively weaker 3D structure (labelled 3D Weaker) and a relatively stronger 3D Earth structure (labelled 3D Stronger) respectively (see Chapter 4). Since the viscosity is constrained by observations, both structures are considered realistic and not just an upper or lower limit. Background stress that contributes to the variable q in Eq. 5.1 is ignored here. Including background stress from the long-term GIA signal would lower viscosity, which will be compensated by grain size and water content parameters to still match the viscosity constraints.

For the coupling to the ice model, the GIA model is used with 9 vertical layers (0-35 km, 35-100 km, 100-150 km, 150-300 km, 300-420 km, 420-550 km, 550-670 km, 670-1171 km, and 1171-2890 km, and 2890-6371 km). Laterally varying B_{diff} and B_{disl} are assigned to each element between 35 and 670 km depth following Eq. 5.2aa and 5.2bb, respectively. The viscosity according to Eq. 5.1 determines if an element behaves effectively elastic; the lithosphere thickness is not specified explicitly. At shallower depths, the layer is defined to be purely elastic. At deeper depths, the lower mantle is assumed to be homogenous. A high resolution area is defined over Antarctica with a horizontal and vertical grid resolution of 35 km wide and deep between the surface and 670 km depth. The spatial resolution outside the high-resolution area is 200 km.

Different methods can be used to simulate the response due to 1D Earth structures (Peltier, 1974; Wu and Johnston, 1998) but here we use the same GIA model to simulate 1D Earth structures and 3D Earth structures to avoid introducing differences that arise due to model formulation. The relatively high computation time of the GIA model limits the number of cases we can investigate. Four 1D Earth structures are applied in the GIA model: one commonly used structure with an upper mantle viscosity of $10^{21} Pa \cdot s$, two structures with an upper mantle viscosity of 10^{20} and $10^{19} Pa \cdot s$, respectively, to represent the average viscosity under West Antarctica, and one with an upper mantle viscosity between $5 \cdot 10^{18}$ and $3 \cdot 10^{19} Pa \cdot s$ that could represent the Amundsen Sea Embayment (Barletta et al., 2018). These structures are hereafter referred to as 1D21, 1D20, 1D19 and 1DASE, respectively. Fig. 5.1 shows the 1D viscosity variations with depth. To derive a relation between relaxation time and viscosity, we used uplift rates from a schematic experiment using a 3D GIA model. In this case, the spatial resolution is 2 degrees at the surface and includes 8 vertical layers following van der Wal et al., 2013 and van der Wal et al., 2015 (0-35 km, 35-70 km, 70-120 km, 120-170 km, 170-230 km, 230-400 km, 400-670 km, and 670-2890 km), which we label as configuration 2, and the GIA model with variable resolution as 'configuration 1'. This resolution allowed us to run many schematic experiments. We used a global seismic model from Schaeffer and Lebedev (2013) combined with the regional seismic model of Heeszel et al. (2016) derived from Rayleigh wave array analysis over Antarctica to create a global seismic model. Uncertainties in the regional seismic model are used to ensure a smooth transition between values defined by the regional and global seismic models. The mantle temperature is then obtained following the same procedure as described for configuration 1. The dislocation and diffusion parameters are then computed using the mantle temperature, stresses, and a suite of

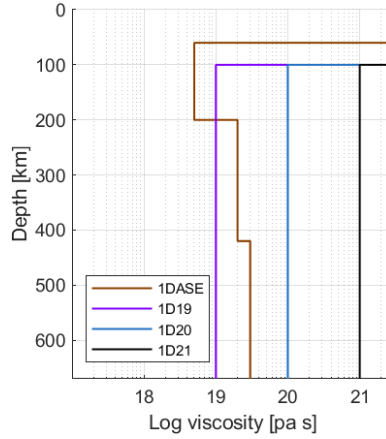


Figure 5.1: Upper mantle viscosity of the 1D Earth structures.

globally-uniform values for grain size (1, 4, and 10 mm) and water content (0 or 1000 ppm H_2O). Below 400 km, uniform creep parameters are adopted, which yield mantle viscosities of $10^{21} - 10^{23} Pa \cdot s$. The 3D GIA model is coupled to a code that solves the sea-level equation (Farrell and Clark, 1976) as implemented by Wang and Wu (2006).

5.2.2. ELRA

In ice sheet modelling, the Earth properties are often simplified to the ELRA approximation as described in detail in Le Meur & Huybrechts (1996). In this approach, bedrock deformation is dependent on a point load, the flexural rigidity and the relaxation time. The flexural rigidity (D) determines, together with the density of the asthenosphere (ρ_a) and the gravity acceleration at the surface (g), the radius of relative stiffness (L_r) as shown in Eq. 5.3.

$$L_r = \left(\frac{D}{\rho_a g} \right)^{\frac{1}{4}} \quad (5.3)$$

First, the equilibrium deflection (w) at a normalized distance (x) from a point load (q) is computed using

$$w(x) = \frac{q L_r^2}{2\pi D} \chi(x), \quad (5.4)$$

where χ is the zeroth order Kelvin function of x . The normalized distance is defined as the real distance (r) from the point load divided by the radius of relative stiffness. The total deflection at each point is the sum of the deflection at all neighboring points within a distance of six times the radius of relative stiffness.

Second, the bedrock deflection can be computed using

$$\frac{db(i, j)}{dt} = \frac{w(i, j) - b(i, j)}{\tau}, \quad (5.5)$$

where $\frac{db}{dt}$ is the bedrock elevation change over time, b the current bedrock elevation, τ the relaxation time and i, j the grid coordinates.

Besides the commonly used relaxation time of 3000 years and flexural rigidity of $10^{25} \text{ N} \cdot \text{m}$, we also applied a relaxation time of 1500, 500, 450, 400, 350, 300, 250, 200 and 50 years in combination with a flexural rigidity of $1.92 \cdot 10^{24} \text{ N} \cdot \text{m}$. The flexural rigidities roughly correspond to lithospheric thicknesses of 100 km and 60 km. This can be derived from the definition of flexural rigidity:

$$D = \frac{Eh^3}{12(1-\nu^2)}, \quad (5.6)$$

with the Young's modulus (E) set to 100 GPa and the Poisson's ratio (ν) set to 0.25. The lithospheric thickness is defined by h .

For the laterally varying ELRA model, we simply made the relaxation time a function of the 2D grid coordinates, as shown in Eq. 5.7.

$$\frac{db(i, j)}{dt} = \frac{w(i, j) - b(i, j)}{\tau(i, j)}, \quad (5.7)$$

5

A laterally varying flexural rigidity is also possible to implement but it is more complex (Coulon et al., 2021), and the effect on bedrock deformation is limited (Coulon et al., 2021; Mitrovica et al., 2011; Zhao et al., 2017). We therefore used uniform flexural rigidity values of $1.536 \cdot 10^{25}$, $1 \cdot 10^{25}$, $4.5511 \cdot 10^{24}$, and $1.92 \cdot 10^{24} \text{ N} \cdot \text{m}$, corresponding roughly to lithospheric thicknesses of 120, 100, 80 and 60 km (Eq. 5.6), in agreement with estimates for lithospheric thickness across West and East Antarctica (Lloyd et al., 2019).

5.3. RELATION BETWEEN 3D VISCOSITY AND RELAXATION TIME

For a GIA model consisting of a viscous half-space with a uniform mantle viscosity, the relaxation time is equal to the Maxwell relaxation time that can be computed directly from the viscosity and shear modulus (e.g. Turcotte and Schubert, 2002). However, in a more realistic Earth structure, there is no longer a simple relation between Maxwell time and viscosity. In GIA models based on the normal mode method (e.g. Wu and Peltier, 1982), each eigenmode has a characteristic relaxation time, but the complete response is controlled by a weighted combination of modes that depends on the spatial scale of the load and the properties of the lithosphere. This implies that the relaxation time depends on the size of the ice sheet and that a single relaxation time cannot be derived. Here, using the 3D GIA model in configuration 2, we determine relaxation times empirically by analysing the solid Earth deformation triggered by the removal of schematic surface loads. These surface loads are chosen to reflect large and small areas of ice mass change for different regions in West Antarctica, such that the resulting empirical relationship between mantle viscosity and relaxation time accounts for the different mantle conditions beneath the regions where the load changes are taking place. The shape of each surface load is controlled by the resolution of the 2-degree finite element mesh that is used in this configuration of the 3D GIA model (Fig. 5.2a). The uniform thickness of each load is taken to be 500 m. Each load is placed on the Earth until equilibrium is reached, and then instantaneously removed. The change in surface load from sea level changes are not taken into account because these experiments encompasses the schematic experiment of instant removal of ice mass.

A total of 40 simulations are conducted, varying the grain size, water content and region of loading. For each simulation, the displacement over time for each surface load/Earth model combination is computed for multiple time steps. From the displacement curve, the uplift rate through time is calculated by time differentiation. The relaxation time is computed as half the time it takes for solid Earth rebound rates to decrease by $\frac{1}{e^2}$ following instantaneous unloading (Table 5.2 in section 5.6). Averaging over two relaxation times reflects more accurately the fact that viscosities at different depths will control the deformation at different stages of the relaxation.

Typically, depth averaged viscosities are computed by taking the average of the log of the viscosity values in a certain layer or area (e.g. Bagge et al., 2021; Paulson et al., 2005; Whitehouse et al., 2006). The filled symbols in Fig. 5.2b show the characteristic relaxation time of each region plotted against the average mantle viscosity, calculated as the volume-weighted mean viscosity of all elements between 120 and 400 km depth beneath each unloaded region indicated in Fig. 5.2a. However, the actual region of the mantle that predominantly influences the response depends on the radial size of the ice loading (Peltier, 1976; Wu, 2006). The sensitivity to the viscosity profile can be taken into account by computing the vertically averaged viscosities weighted by the local strain rate (Christensen, 1984). Such a procedure would result in average viscosity values that are determined more by low viscosity values in sub-surface Antarctica because a low viscosity region experiences the highest strain rates due to the ability to deform more easily under stress. To take that into account, the computed relaxation times are compared to not only the average mantle viscosity value for each region, but also the lowest mantle viscosity derived from the seismic model, which is shown by the open symbols in Fig. 5.2b. A linear fit through the resulting log-log graph provides a relation between relaxation time in years, τ , and viscosity in $Pa \cdot s$ for the average viscosity (Eq. 5.8, solid line in Fig. 5.2) and the lower bound viscosity (Eq. 5.9, dashed line in Fig. 5.2).

$$\tau = 2.3 \cdot 10^{-5} \eta^{0.35} \quad (5.8)$$

$$\tau = 3.9 \cdot 10^{-2} \eta^{0.20} \quad (5.9)$$

Both relations will be used to create 2D relaxation time maps to identify which one is best approximating the sea level rise projections resulting from the coupled 3D GIA – ice sheet model. When the 2D relaxation time maps are used in an ELRA model, either a high-resolution viscosity profile should be used, because this will likely not contain large sharp changes in viscosity, or the relaxation time map should be smoothed, otherwise discontinuities in deformation arise.

Using our empirically derived relationships between viscosity and relaxation time (Eq. 5.8 and 5.9), we derive laterally variable relaxation time maps based on the 3D Weaker and 3D Stronger Earth models described in section 2.1. η_{eff} is taken to be the viscosity of the 3D Earth structure vertically averaged between 120 and 400 km depth (Fig. 5.3a,d). For the ice thickness changes in the projections of the ice sheet evolution by the ice sheet model, the highest sensitivity will be in this relatively shallow layer (Barletta et al., 2018). This results in two relaxation time maps based on the 3D Weaker rheology, hereafter referred to as 2D Weaker Average and 2D Weaker Lower bound (Fig. 5.3 b-c), and two relaxation time maps based on the 3D Stronger rheology, hereafter referred to as 2D Stronger Average and 2D Stronger Lower bound (Fig. 5.3 e-f). Finally, to prevent

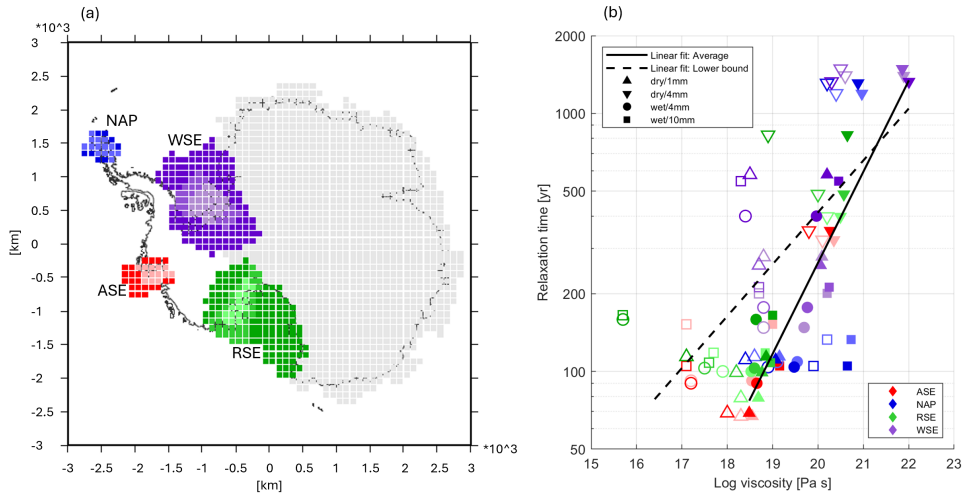


Figure 5.2: The relationship between mean upper mantle viscosity and relaxation time across West Antarctica. (a) Regions from which ice is instantaneously unloaded in order to determine regional relaxation times. Within each of the four main regions, there is a large and a small version of the region, coloured in dark and light colours respectively. The small region overlaps the large region. NAP refers to Northern Antarctic Peninsula, WSE refers to Weddell Sea Embayment, ASE refers to Amundsen Sea Embayment, and RSE refers to Ross Sea Embayment. (b) Log-log plot of relaxation time against mean upper mantle viscosity and the lower bound viscosity. The colours are identical to (a). The symbols reflect the parameters in the 3D GIA model used in each experiment (see Table 1 in supplemental materials of this preprint online). The filled symbols reflect the average viscosity and the open symbols reflect the lower bound viscosity.

the occurrence of unrealistically low relaxation times due to the extrapolation of the linear relation between viscosity and relaxation time, the minimum relaxation time is set to 67 years, which is derived from the minimum viscosity found in the experiments used to derive Eq. 5.8 and 5.9.

5.4. PROJECTIONS USING DIFFERENT APPROACHES TO BEDROCK RESPONSE

The sea level rise is projected for the coming 500 years using two different climate models for a high and a low emissions scenario. The sea level rise projected using simple models that adopt a uniform relaxation time, a laterally variable relaxation time, or a 1D Earth structure is compared to the average sea level rise projected when using the 3D Weaker and 3D Stronger Earth structures within the GIA model in configuration 1 (as described in 5.2.1). The average barystatic sea level rise computed by the ice sheet model using the two different 3D Earth structures is referred to as 3D-Average.

5.4.1. A UNIFORM RELAXATION TIME

The bedrock response is dependent on the climate model because different regions of ocean warming cause different regions of ice retreat, and the mantle viscosity differs in each region. The bedrock response depends on the emission scenario as well, since a

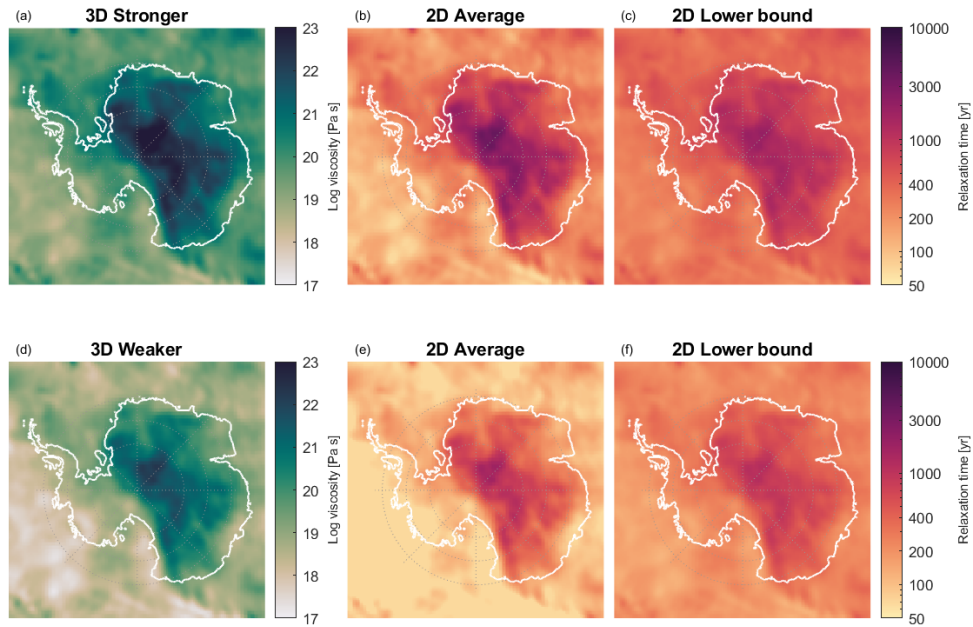


Figure 5.3: Panels a and d show the vertically averaged mantle viscosity between 120 and 400 km depth based on van Calcar et al. (in review). Panels b and e show the relaxation time maps computed using Eq. 5.8, and 3D Stronger and 3D Weaker, respectively. Panels c and f show the relaxation time maps computed using Eq. 5.9, and 3D Stronger and 3D Weaker, respectively.

larger region of ice mass loss will trigger deformation deeper in the mantle where viscosity, and hence relaxation times, will be different to values at shallower depths (Peltier, 1976). The sea level rise resulting from the coupled ice sheet – GIA model using a 3D Earth structure therefore differs from a uniform relaxation time, and this difference in turn varies for different emission scenarios and climate models.

To assess the performance of the ELRA model with a uniform relaxation time, the resulting sea level rise is compared to the sea level rise averaged from the output of the two models that employ 3D Earth structures (3D-Average). The widely used uniform relaxation time of 3000 years (hereafter referred to as ELRA3000) overestimates the contribution from the AIS to sea level rise by 0.44-0.70 m (8-20%) in 2500 compared to the 3D-Average value, with the precise value depending on the emission scenario and the applied climate model (Fig. 5.4b,c,e,f). ELRA3000 overestimates sea level rise because this relaxation time is much longer than the relaxation time associated with the low viscosity values found in the 3D Earth structures (Fig. 5.3), especially when retreat occurs in the Amundsen Sea Embayment (as predicted by climate model IPSL) where the mantle viscosity is relatively low. We therefore search for a better choice of relaxation time, as formulated in research question 1: How well can a uniform relaxation time approximate the ice sheet evolution resulting from 3D Earth structures?

Out of the relaxation times investigated, we find that 300 years yields a reasonable approximation for the 3D results until year 2400, in combination with a flexural rigidity

corresponding to 100 km lithospheric thickness (Fig. 5.4). For longer simulations, a 500 year relaxation time can be recommended. When a smaller lithospheric thickness of 60 km is applied, a longer relaxation should be considered (Fig. 5.8). Since the combination of a higher flexural rigidity and shorter relaxation time yields a similar result to the combination of a lower flexural rigidity and somewhat higher relaxation time we only discuss the results for a flexural rigidity corresponding to a 100 km thick lithosphere in the following.

For the low emission scenario and by using the climate model IPSL, the difference in sea level rise between using a relaxation time of 300 yr (hereafter referred to as ELRA300) and 3D Stronger is negligible until 2400, but increases afterwards, reaching a maximum of 17 cm in 2500 (Fig. 5.4c), which is 5% of the total of 3.6 m of sea level rise using 3D Stronger (Fig. 5.4a). The ice is approximately 50 meter thicker within the Amundsen Sea Embayment using ELRA300 (Fig. 5.5a) due to faster uplift in this region compared to 3D Stronger. On timescales of 400 years and longer, it is not only the local low viscosity, but also the surrounding higher viscosities, which impact bedrock deformation in the 3D model. The rate of uplift predicted by the 3D GIA model therefore slows down on these longer timescales whereas the relaxation time in the ELRA model is constant over time and corresponds only to the low viscosities of the 3D model. As a consequence, the amount of bedrock uplift is about 75 m greater in ELRA300 than 3D Stronger between 2400 and 2500. The impact of the difference in bedrock elevation on ice mass loss and grounding line position is negligible. Contrary to this, the viscosity of 3D Weaker is much lower and the uplift predicted by ELRA300 is too slow compared to 3D Weaker over the full simulation time. The bedrock elevation of ELRA300 is tens of meters lower than 3D Weaker in 2300, causing faster retreat to be predicted by ELRA300 until 2500. In 2500, the grounding line has retreated about 150 km more in ELRA300 compared with 3D Weaker (Fig. 5.5).

For the high emission scenario, ELRA300 underestimates sea level rise by 0.4 m in 2500 compared with 3D-Average (Fig. 5.4a). When there is a larger region of ice mass loss, as is the case in the high emission scenario compared with the low emission scenario, the bedrock response is more sensitive to the rheology of deeper parts of the mantle, where the viscosity can be up to 3 orders of magnitude greater than at shallower depths. This causes the same effect as in the low emission scenario – a slowdown of the uplift projected by the 3D model on longer timescales – but the effect is even stronger. The relaxation time of ELRA300 is therefore too short compared to 3D Stronger and 3D Weaker on the long-term, leading to faster uplift and a higher bedrock elevation by 150 m in 2500 (Fig. 5.9). However, around 2300, uplift in the 3D model has not slowed down much and is faster than the uplift of ELRA300. Therefore, at this moment in time, the ice is about 750 meters thicker in 3D Weaker compared with ELRA300 and the grounding line has retreated about 100 km less in the Amundsen Sea Embayment (Fig. 5.10). The slowdown of bedrock uplift is less strong when retreat is concentrated in the Weddell Sea Embayment (using climate model CESM) due to less vertical variation in mantle viscosity in this region (Fig. 5.4e,f). To conclude, a relaxation time of 300 years fits best until 2400, but a relaxation time of 500 years should be chosen for longer simulations because of the increasing deviation of ELRA300 from 3D-Average over time.

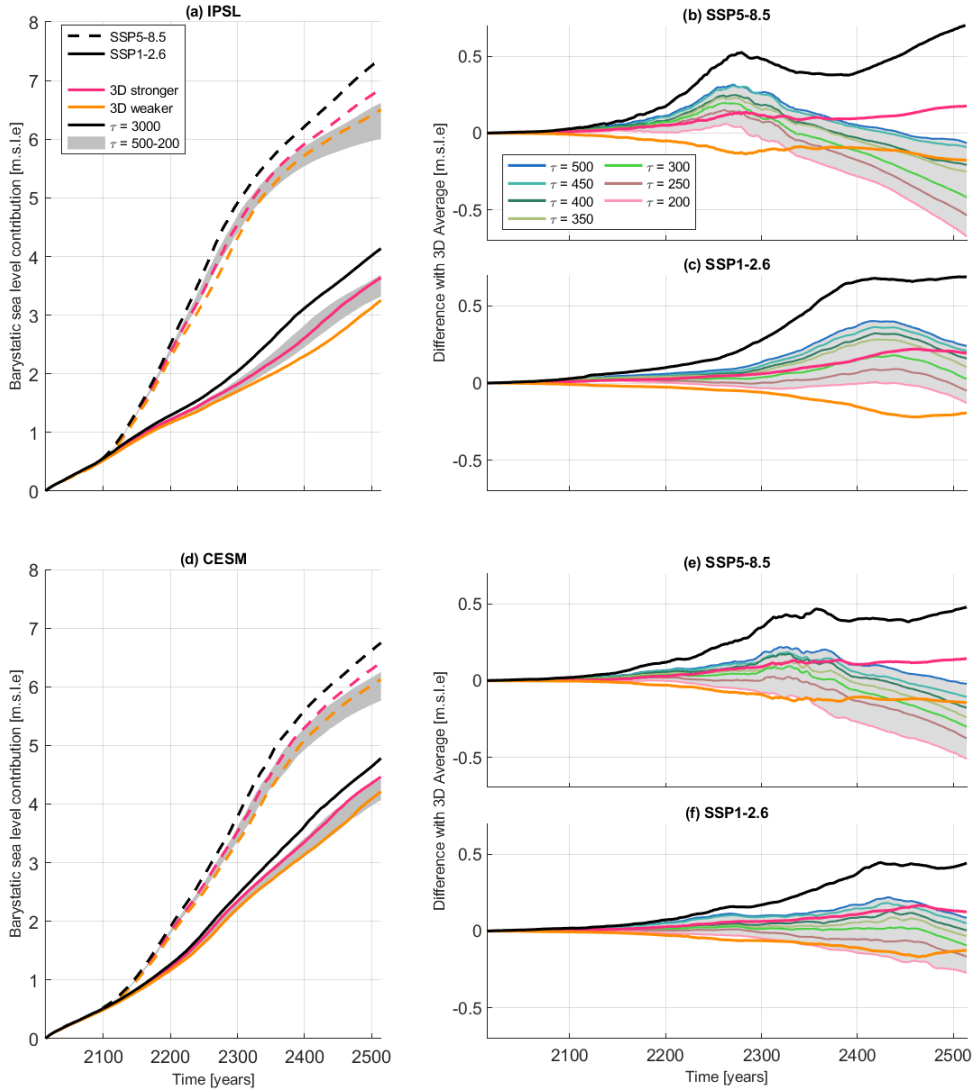


Figure 5.4: The Antarctic Ice Sheet contribution to barystatic sea level rise using the 3D GIA model and the ELRA model for a high and a low emission scenario and two different climate models, IPSL-CM6A-LR (panel a) and CESM2-WACCM (panel d). Two different Earth structures are applied in the 3D GIA model, a stronger Earth structure and a weaker Earth structure. The relaxation time of the ELRA model is varied between 200 and 500 years, and a reference run of 3000 years is used. The flexural rigidity of $10^{25} \text{ km} \cdot \text{m}^2/\text{s}^2$ roughly corresponds to a lithospheric thickness of 100 km. Panels b, c, e, and f show the difference in barystatic sea level contribution between the ELRA model with different relaxation times and the average sea level contribution between the two 3D GIA simulations. The difference between the average sea level contribution between the two 3D GIA simulations and 3D weaker, 3D stronger and ELRA3000 (black solid lines) are also shown.

5.4.2. A Laterally Variable Relaxation Time

Previous studies have shown that a laterally varying Earth structure is needed to accurately simulate AIS evolution (Gomez et al., 2024; van Calcar et al., 2024). As these 3D GIA

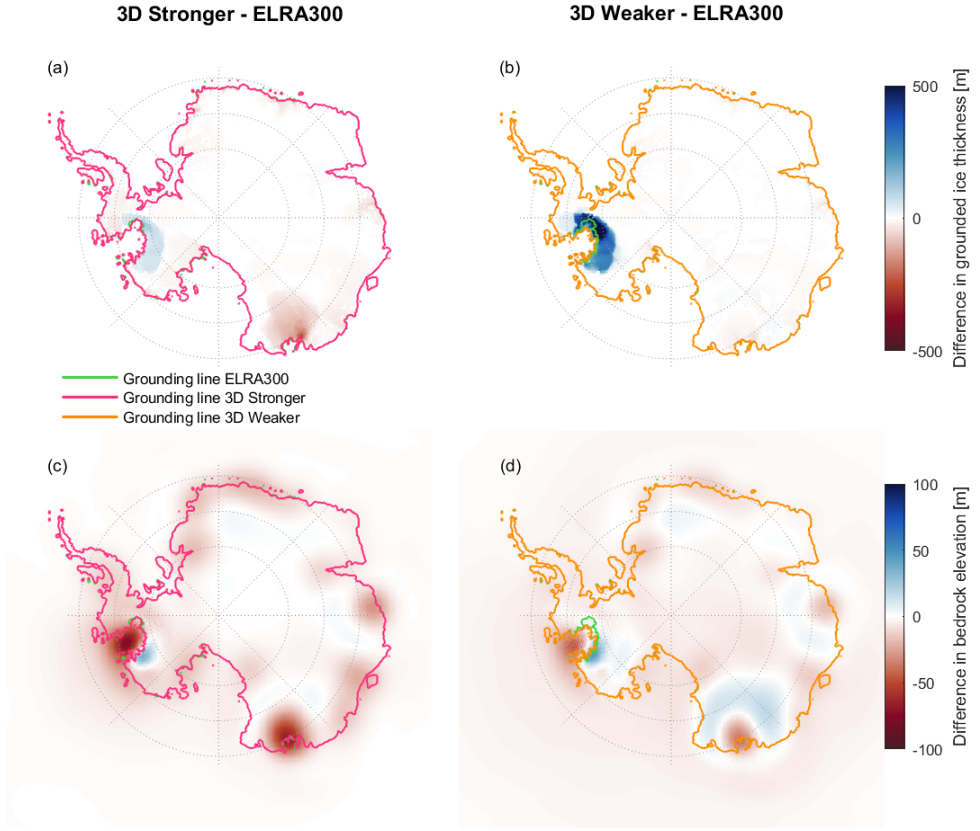


Figure 5.5: Difference in grounded ice thickness above flotation (panel a and b) and bedrock elevation (panel c and d) in 2500 between the ELRA model with a relaxation time of 300 years (referred to as ELRA300) and the two 3D Earth structures. Panels a and c correspond to 3D Stronger and panels b and d to 3D Weaker. The climate model IPSL is applied for the low emission scenario SSP1-2.6.

simulations are very costly, they prohibit large ensemble simulations. We therefore assess the performance of a 2D relaxation time, which is straight forward to implement in an ELRA model, to answer research question 2: How well can a laterally varying relaxation time approximate the ice sheet evolution resulting from 3D Earth structures? We combined 4 different laterally varying relaxation time maps with different uniform flexural rigidities to investigate how well the computationally efficient ELRA model can replicate the results of the 3D models. As there is no a priori reason to select the average or lower bound viscosity equations, or a particular flexural rigidity, we investigate which of the resulting ice sheet evolutions using the 2D maps correspond best to ice sheet evolution using the 3D-Average, and whether the improvement is significant compared to the performance of ELRA300. The different relaxation time maps, in combination with different lithospheric thicknesses, result in a large range of sea level rise projections. The 2D Stronger map, when combined with a flexural rigidity that corresponds to a lithospheric thickness of 120 km and derived from the average viscosity (Eq. 5.8), produces results

which are closest to 3D-Average when considering both emissions scenarios and climate models (Fig. 5.6) and will be considered in the following. For the high emission scenario, the sea level rise is about 30-40 cm closer to 3D-Average at 2500 using 2D Stronger compared to using ELRA300 (Fig. 5.6a-b). The advantage of using 2D Stronger over ELRA300 is particularly great in the Amundsen Sea Embayment projections (IPSL) for scenarios longer than 400 years because the difference between 3D-Average and ELRA300 increases strongly after 2300, whereas the difference between 2D Stronger and 3D-Average is constant over time (Fig. 5.6a). In the high emission scenario driven by the IPSL climate model, the bedrock in the Amundsen Sea Embayment uplifted about 250 meters more by 2500 when using 2D Stronger compared with using the 3D GIA model (Fig. 5.11). However, this uplift occurs mainly in the last 100 years and the effect on grounding line retreat is small due to the fact that the grounding line is already retreating rapidly and the West Antarctic Ice Sheet is in a phase of collapse.

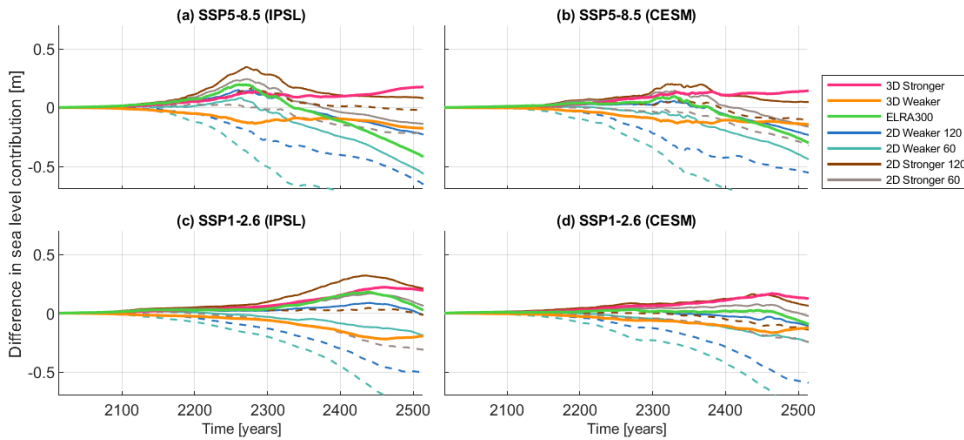


Figure 5.6: The difference in Antarctic Ice Sheet contribution to barystatic sea level rise between the average sea level contribution of the two 3D GIA simulations and the contribution using different 2D relaxation time maps. Results are shown for a high and a low emission scenario and two different climate models, IPSL-CM6A-LR and CESM2-WACCM. The dashed lines refer to the relaxation time calculated from the average viscosity (Eq. 5.8) and the solid lines refer to relaxation times calculated from the lower bound viscosity (Eq. 5.9). The numbers 120 and 60 in the legend refer to the lithospheric thickness.

5.4.3. 1D GIA

Some ice sheet models are coupled with a 1D GIA model to conduct projections (Konrad et al., 2015; Whitehouse et al., 2019; Kachuck et al., 2020). The 1D GIA model is more realistic than the ELRA model because it takes into account the radial depth variation of viscosity, which implies a variable relaxation time as the size of the load determines which part of the radial viscosity profile controls the response. As 1D GIA models can also be considered intermediate in terms of computation time compared to ELRA and 3D GIA, we study whether 1D Earth structures offer an improved accuracy compared to ELRA models to answer research question 3: How well can a 1D Earth structure approximate the ice sheet evolution resulting from 3D Earth structures? A widely used mantle

viscosity for a 1D GIA model is $10^{21} Pa \cdot s$ (hereafter referred to as 1D21) (Gomez et al., 2015; Konrad et al., 2015; Rodehacke et al., 2020; Gollledge et al., 2019). Fig. 5.7 shows that 1D21 overestimates the Antarctic sea level contribution by 0.4-0.55 m, depending on the emission scenario and climate model, because the structure is too stiff in West Antarctica compared to the 3D structures. The viscosity profiles 1DASE and 1D19 produce results similar to each other and to the 3D-Average model for the low emission scenario but, like ELRA300, they still underestimate the sea level contribution by 0.35 m in 2500 for the high emission scenario. The largest improvement of 1D19 compared to ELRA300 and 2D Stronger is in the bedrock uplift. The bedrock elevation of 1D19 in 2500 differs by a maximum of 80 meters from the results of the 3D GIA modelling in the high emission scenario, which is significantly smaller than the difference of 250 m when 2D Stronger is compared with the 3D GIA model output (Fig. 5.12). To replicate not only the sea level contribution from 3D-Average, but also the geometry of the bedrock, it can therefore be recommended to use a 1D GIA model with an upper mantle viscosity of $10^{19} Pa \cdot s$ instead of the ELRA model with a uniform relaxation time of 300 years or the 2D Stronger relaxation time map. Especially for long-term projections under a high emission scenario, the 1D GIA model is preferred over an ELRA model.

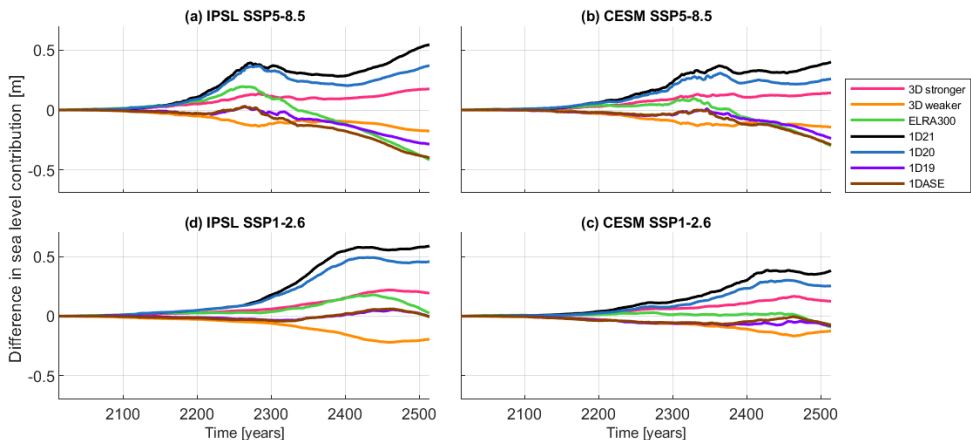


Figure 5.7: The difference in Antarctic Ice Sheet contribution to barystatic sea level rise between the average sea level contribution of the two 3D GIA simulations and the contribution using different 1D Earth structures. Results are shown for a high and a low emission scenario and two different climate models, IPSL-CM6A-LR and CESM2-WACCM. Note that the 1D19 and 1DASE mostly overlap for IPSL SSP1-2.6.

5.5. CONCLUSIONS AND OUTLOOK

We investigated the accuracy of common implementations of bedrock adjustment within an ice model against ice model projections coupled to a GIA model with 3D variations in viscosity, for different emission scenarios and climate models. The ELRA model with a commonly used uniform relaxation time of 3000 years combined with a uniform flexural rigidity overestimates sea level rise by up to 0.70 m (20%) compared with the average barystatic sea level rise predicted using a model that includes 3D Earth structures. A 1D

GIA model with an upper mantle viscosity of $10^{21} \text{ Pa} \cdot \text{s}$ overestimates sea level rise by up to 0.60 m (17%). To replicate the sea level rise of the average of the 3D GIA models (3D Average) better, a relaxation time or mantle viscosity corresponding to the area of ice mass loss should be chosen. We investigated the degree to which different bedrock models, Earth structures and parameterisations can replicate the bedrock uplift predicted by models that include 3D Earth structures.

Research question 1 was: How well can a uniform relaxation time approximate the ice sheet evolution resulting from 3D Earth structures? We recommend to use a uniform relaxation time of 300 years with a lithospheric thickness of 100 km to replicate the sea level rise predicted by a model that includes 3D Earth structure. Using this relaxation time results in a sea level rise that differs from 3D-Average by only 0.05-0.4 m, dependent on the emission scenario and the climate model. Note that using this relaxation time does lead to an increasing underestimation of sea level rise from 2400 onwards. Therefore, for simulations longer than 400 years, a relaxation time of 500 years is recommended. Even though the sea level rise can be similar between ELRA300 and 3D-Average, the ice thickness can locally differ by up to 750 meters, the grounding position may differ by 100 km, and the bedrock elevation may differ by 150 meters between ELRA300 and the different 3D Earth structures. It is therefore recommended to vary the uniform relaxation time between 300 and 500 years to include the same uncertainty range as the 3D Earth structures.

With a small change in the ELRA model, a spatially varying relaxation time can be included. We derived an empirical relation between upper mantle viscosity and relaxation time and computed 2D maps of relaxation times to answer research question 2: How well can a laterally varying relaxation time approximate the ice sheet evolution resulting from 3D Earth structures? Applying the 2D Stronger map, derived using the relation between average viscosity for a strong 3D rheology and relaxation time, and a lithospheric thickness of 120 km, results in a sea level rise projection that differs from the 3D-Average value by only 10 cm in 2500. This difference doesn't increase on the long term in contrast to the ELRA model and it can thus be recommended to use ELRA with spatially varying relaxation time for long term simulations. Still, the bedrock elevation in 2D Stronger is hundreds of meters too high by 2500 compared to the 3D model under a high emission scenario.

For models that are able to use a 1D GIA model, we answer research question 3: How well can a 1D Earth structure approximate the ice sheet evolution resulting from 3D Earth structures? The use of an upper mantle viscosity of $10^{19} \text{ Pa} \cdot \text{s}$ results in sea level rise projections that only differ from 3D-Average by a maximum of 0.3 m. The bedrock elevation in 1D19 differs from 3D-Average by a maximum of 80 meters, thus this model provides the closest resemblance to the 3D Earth structures in terms of geometry, better than the ELRA and LVELRA models. However, the improvement should be traded off against a large increase in computation time. Our recommended values for the relaxation time and 1D viscosity will provide a better approximation of sea level rise than the currently used standard values but should serve to correct the oversimplification of the ELRA model and not as the true relaxation time or viscosity of the Earth's mantle. The simplified Earth models are all compared to the same coupled ice sheet - 3D GIA model and this model did not include the effect of a local sea level drop on ice sheet retreat.

Including the feedback of the sea level drop on the ice sheet dynamics reduces the sea level rise by 5% compared to using a static sea level equal to present day (see Chapter 4). Furthermore, different coupled ice sheet-3D GIA models could lead to different projections of sea level contribution, which might lead to somewhat different recommended values for relaxation time and 1D viscosity.

The laterally varying relaxation time is dependent on the 3D viscosity structure so different 2D relaxation time maps could be produced using the provided relation between relaxation time and viscosity. This allows other modellers to create their own relaxation time maps based on their preferred 3D viscosity profiles. If other regions and time periods are studied, these maps could be derived based on different seismic models, a different time period such as the deglaciation since the last glacial maximum, or for other regions such as Greenland.

5.6. SUPPLEMENTAL MATERIALS

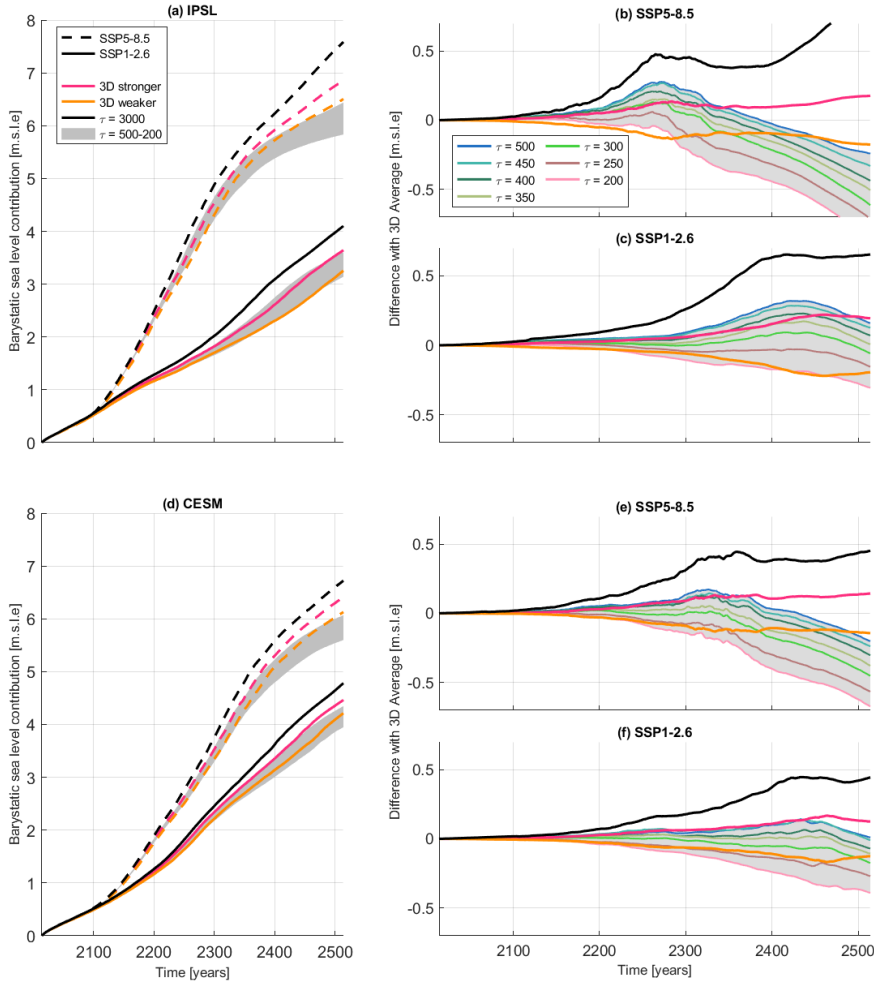
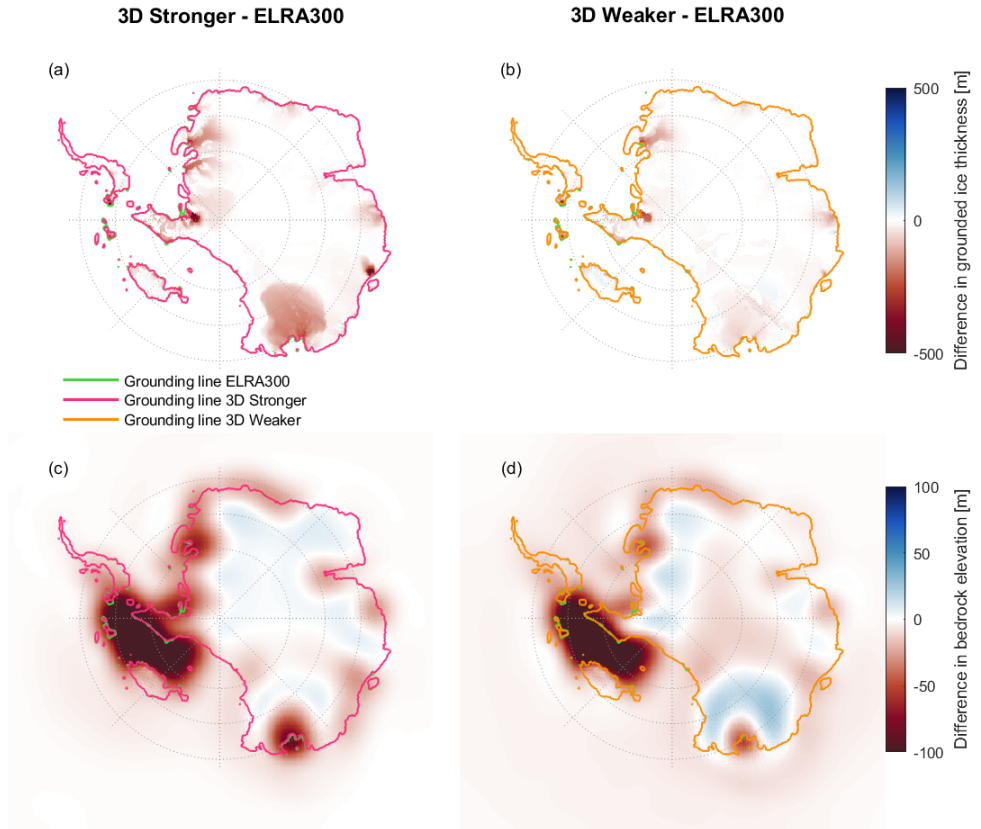


Figure 5.8: The Antarctic Ice Sheet contribution to barystatic sea level rise using the 3D GIA model and the ELRA model for a high and a low emission scenario and two different climate models, IPSL-CM6A-LR (panel a) and CESM2-WACCM (panel d). Two different Earth structures are applied in the 3D GIA model, a stronger Earth structure and a weaker Earth structure. The relaxation time of the ELRA model is varied between 200 and 500 years, and a reference run of 3000 years is used. The flexural rigidity of $1.92 \cdot 10^{24} \text{ km} \cdot \text{m}^2 / \text{s}^2$ roughly corresponds to a lithospheric thickness of 60 km. Panels b, c, e, and f show the difference in barystatic sea level contribution between the ELRA model with different relaxation times and the average sea level contribution of the two 3D GIA simulations.



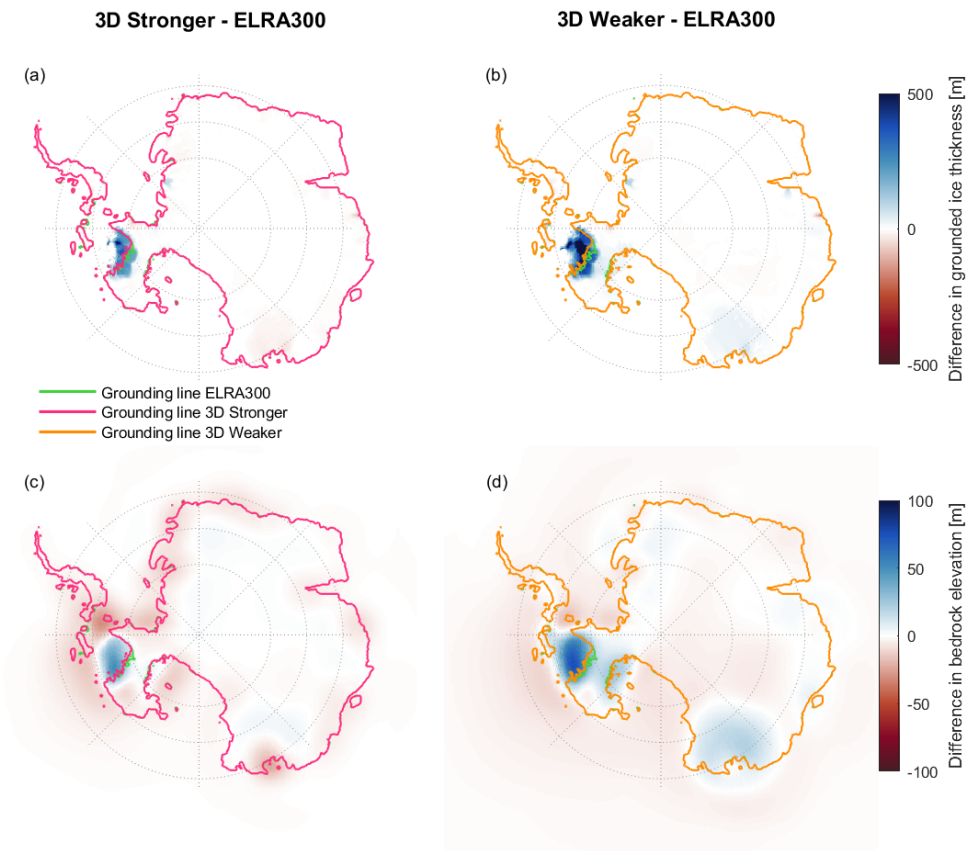
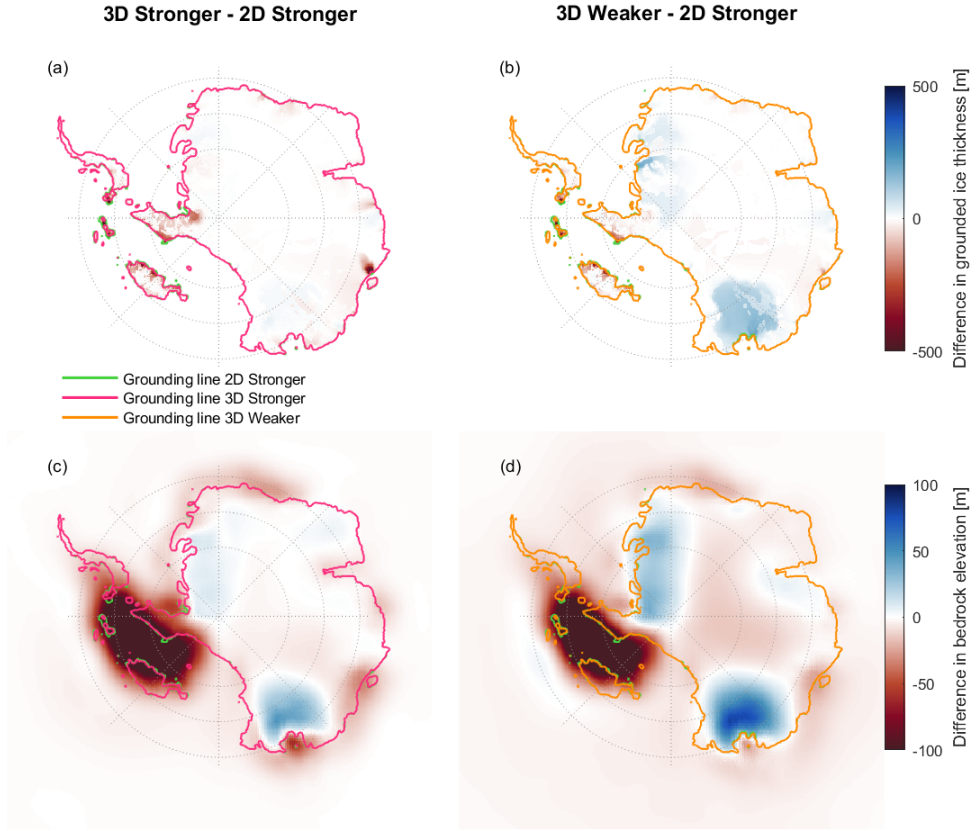


Figure 5.10: Difference in accumulated grounded ice thickness above floatation (panel a and b) and bedrock elevation change (panel c and d) by 2300 between the ELRA model with a relaxation time of 300 years (referred to as ELRA300) and the two 3D Earth structures. Panels a and c correspond to 3D Stronger and panels b and d to 3D Weaker. The climate model IPSL is applied for the high emission scenario SSP5-8.5. Note that the grounding line of the 3D structures overlap the grounding line of ELRA.



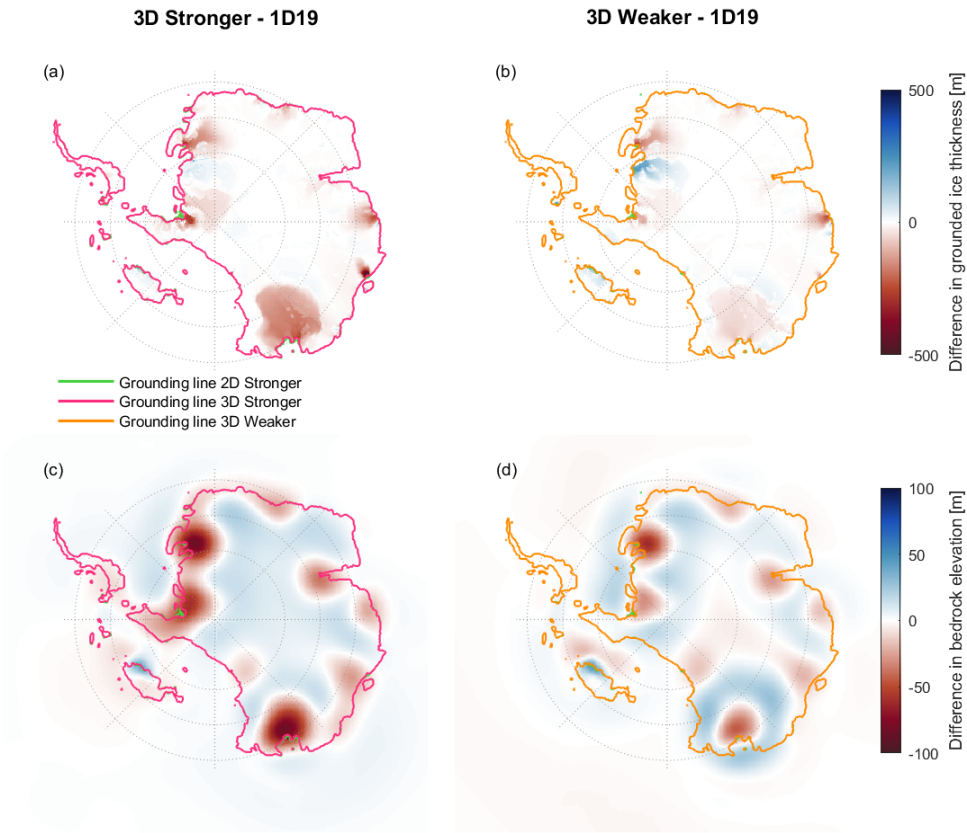


Figure 5.12: Difference in accumulated grounded ice thickness above floatation (panel a and b) and bedrock elevation change (panel c and d) by 2500 between 1D19 and the two 3D Earth structures. Panels a and c correspond to 3D Stronger and panels b and d to 3D Weaker. The climate model IPSL is applied for the high emission scenario SSP5-8.5. Note that the grounding line of the 3D structures overlap the grounding line of 1D19.

Table 5.2: Regional relaxation times. Relaxation times are calculated as half the time taken to decay to $\frac{1}{e^2}$ of the initial rebound rate at the point of unloading. The mean upper mantle viscosity is defined as the volume-weighted mean viscosity of all elements between 120 and 400 km depth beneath each unloaded region. The upper and lower bounds reflect the highest and lowest viscosity beneath each unloaded region between 120 and 400 km depth.

Region name	Mantle water content (ppm)	Mantle grain size (mm)	Relaxation time (yrs)	log (Upper mantle viscosity) (Pa s)		
				Mean	Lower bound	Upper bound
ASE small	0	1	67	18.554	18.3	19.0
ASE small	0	4	323	20.35	20.1	20.8
ASE small	1000	4	92	18.542	17.2	19.1
ASE small	1000	10	152	18.996	17.1	20.0
ASE large	0	1	69	18.484	18.0	19.2
ASE large	0	4	351	20.27	19.8	21.0
ASE large	1000	4	90	18.652	17.2	19.4
ASE large	1000	10	105	19.151	17.1	20.0
NAP small	0	1	114	19.15	18.6	19.7
NAP small	0	4	1194	20.967	20.4	21.6
NAP small	1000	4	109	19.542	19.1	20.0
NAP small	1000	10	133	20.725	20.2	21.2
NAP large	0	1	111	19.067	18.4	19.7
NAP large	0	4	1310	20.883	20.2	21.6
NAP large	1000	4	104	19.475	18.9	20.0
NAP large	1000	10	105	20.65	19.9	21.2
RSE small	0	1	79	18.685	18.3	19.2
RSE small	0	4	398	20.494	20.2	21.0
RSE small	1000	4	100	18.526	17.9	19.1
RSE small	1000	10	118	18.837	17.7	20.3
RSE large	0	1	99	18.764	18.2	19.4
RSE large	0	4	486	20.57	20.0	21.2
RSE large	1000	4	103	18.599	17.5	19.3
RSE large	1000	10	108	18.956	17.6	20.4
RSE LGM	0	1	114	18.856	17.1	22.1
RSE LGM	0	4	825	20.647	18.9	23.8
RSE LGM	1000	4	159	18.635	15.7	20.8
RSE LGM	1000	10	165	18.997	15.7	21.1
WSE small	0	1	278	20.086	18.8	22.0
WSE small	0	4	1399	21.89	20.6	23.8
WSE small	1000	4	148	19.694	18.8	21.5
WSE small	1000	10	201	20.199	18.7	22.4
WSE large	0	1	258	20.054	18.7	22.4
WSE large	0	4	1488	21.859	20.5	24.2
WSE large	1000	4	177	19.766	18.8	21.5
WSE large	1000	10	212	20.243	18.7	22.4
WSE LGM	0	1	579	20.199	18.5	23.0
WSE LGM	0	4	1327	22.004	20.3	24.8
WSE LGM	1000	4	400	19.967	18.4	22.2
WSE LGM	1000	10	547	20.457	18.3	22.5



Errera channel, Antarctica

6

CONCLUSIONS AND RECOMMENDATIONS

6.1. CONCLUSIONS

Results from coupled 3D GIA - ice sheet models demonstrate that Glacial Isostatic Adjustment (GIA) plays a substantial role in shaping ice sheet evolution in Antarctica and its contribution to sea level changes over a glacial cycle and for the coming centuries. By accounting for the spatial variability in Earth's mantle properties, the model shows how GIA affects the stability and dynamics of the ice sheet, and what uncertainty is associated with GIA in sea level rise projections. Furthermore, it is shown how Earth parameters used in simpler Earth models coupled to ice sheet models can be adjusted to prevent a systematic overestimation of sea level rise due to the standard Earth structure that is too stiff. Below, the answers to the research questions presented in Chapter 1 are discussed. The findings of this thesis underscore the importance of integrating spatial variability in Earth's mantle properties in GIA models coupled to ice sheet models to better understand the effect of bedrock deformation on the ice sheet evolution and sea level change.

6.1.1. RESEARCH QUESTION 1

How does a 3D mantle structure affect the Antarctic Ice Sheet over a glacial cycle?

Chapter 3 shows that the bedrock elevation at the Last Glacial Maximum (LGM) primarily determines the ice sheet evolution during the deglaciation phase. Previous studies have either used a fixed ice sheet history for GIA models, employed a coupled 1D GIA - ice sheet model, or started simulations with a coupled 3D GIA-ice sheet model from around 40,000 years ago and not at the start of the glacial cycle. Chapter 3 presents the simulation of an entire glacial cycle using a coupled 3D GIA - ice sheet model. The 3D structure is determined using radially and laterally varying seismic velocity anomalies, from which a mantle temperature is derived. The viscosity of the mantle is computed based on this mantle temperature, the change in pressure from ice loading, and a uni-

form grain size and water content. The two chosen combinations of water content and grain size lead to a stronger and a weaker Earth structure. One Earth structure is relatively weak to fit a mantle viscosity constraint in the Amundsen Sea Embayment, and one structure is relatively strong to fit mantle viscosity constraints in the Weddell Sea Embayment. It concludes that a relatively low mantle viscosity in West Antarctica results in a much higher (i.e. less depressed) bedrock elevation at the LGM compared to a higher mantle viscosity. This is because a weaker Earth structure allows for stabilisation or even uplift during short periods when the ice sheet's growth halts due to warm climate intervals during the glaciation. In contrast, a stronger Earth structure does not respond to changes in ice loading over centuries but only to changes on longer time scales, leading to continued subsidence and a lower bedrock elevation at LGM compared to the weaker Earth structure.

The surface elevation at the LGM that the ice sheet reaches at the end of the glaciation phase depends on the atmospheric temperature and precipitation, and to a significant lesser effect on the bedrock elevation. The surface elevation of the ice sheet at LGM is therefore similar between simulations with different Earth structures. A lower bedrock elevation caused by a stronger Earth structure leads to faster retreat during the deglaciation phase because more ice is floating and thus in contact with the ocean water compared to a higher bedrock elevation caused by a weaker Earth structure. Furthermore, there is more ice to melt because the ice sheet is thicker at the LGM due to a lower bedrock elevation, while the ice surface elevation remains similar for the stronger Earth structure compared to the weaker Earth structure. This results in higher ice mass loss and, counterintuitively, faster uplift than using a weaker Earth structure. The weaker structure would produce more uplift than the stronger structure if the ice mass loss since LGM were the same, but this is not the case due to the different bedrock elevations at the LGM. Still, at present day, the weaker 3D Earth structure leads to a less retreated grounding line position of up to 80 km and a greater ice thickness of up to 600 m compared to using a stronger 3D Earth structure. The stabilising effect of GIA would be stronger if the self-gravitating effect of the ice sheet on sea level, and the effect of ocean loading outside of the ice sheet on bedrock deformation were also to be taken into account.

Thus, the coupling with a 3D earth rheology leads to different ice sheet configurations at present day. Using a prescribed ice history would fail to account for the enhanced stabilizing effect of a weaker Earth structure on ice sheet evolution compared to a stronger Earth structure. Additionally, while a fixed ice mass loss during the deglaciation phase will lead to greater uplift for a weaker Earth structure, a stronger Earth structure results in more uplift because the ice mass loss is greater for the stronger Earth structure.

Due to a lack of mantle viscosity constraints, one cannot determine which of the two used 3D structures is more realistic. If 3D Stronger were the most realistic, a 1D structure with an upper mantle viscosity of $1 \cdot 10^{19} \text{ Pa} \cdot \text{s}$ could also be used to approximate this 3D Earth structure in ice sheet models that can be coupled with 1D GIA models only. However, using this 1D structure results in a significantly different bedrock deformation compared to a weak 3D structure. It is therefore necessary to use multiple 3D Earth structures when simulating the Antarctic Ice Sheet evolution over a glacial cycle to account for the uncertainty in 3D mantle rheology. Other 1D Earth structures could be used, of which at least one structure should have a mantle viscosity in the order of

$1 \cdot 10^{18} Pa \cdot s$ to approximate the effect of a plausible weaker 3D rheology.

In conclusion, the findings emphasize the significant impact of mantle viscosity on ice sheet dynamics. Studying the deglaciation phase of the last glacial cycle provides understanding of the effect of mantle variations on the ice sheet evolution, which is essential to project future ice sheet behavior and sea-level changes.

6.1.2. RESEARCH QUESTION 2

How does a 3D mantle structure affect the Antarctic Ice Sheet over the next centuries?

Previous research has demonstrated the importance of incorporating Glacial Isostatic Adjustment (GIA) in ice sheet projections on centennial timescales. This has typically been done using a 1D GIA model or in one case with an ELRA model with distinct relaxation times for East and West Antarctica (Adhikari et al., 2014; Coulon et al., 2021; Gomez et al., 2012; Konrad et al., 2015; Larour et al., 2019). Alternatively, a 3D GIA model has been used with a prescribed ice sheet evolution (Geruo et al., 2013; Hay et al., 2017; Kaufmann et al., 2005; Powell et al., 2021; van der Wal et al., 2015; Yousefi et al., 2022). The ice sheet evolution is obtained using a standalone ice sheet model coupled to the simple bedrock model ELRA or with no bedrock adjustment at all. However, in Chapter 4, we show that by using a fully coupled 3D GIA-ice sheet model, the barystatic sea level contribution from Antarctica is reduced by 9-23% by the year 2500 compared to using a rigid Earth, depending on the projected greenhouse gas emissions and the climate and ocean conditions. Furthermore, the grounding line retreat between 2300 and 2500 is delayed by 50-130 years by including a 3D Earth structure. Thus, we show that GIA affects the ice sheet evolution on shorter timescales than previously reported, primarily because the lower mantle viscosity in West Antarctica, as represented in the 3D Earth structure, allows for more rapid isostatic adjustment.

General circulation models (GCMs) provide the necessary forcing for the coupled model, including atmospheric and ocean temperatures, precipitation rates, and salinity concentrations. Different GCMs predict varying spatial patterns of warming. When warming is concentrated in the Amundsen Sea, significant ice retreat occurs in the Amundsen Sea Embayment, where the mantle viscosity in the 3D model is relatively low. In a low greenhouse gas emission scenario, using a GCM with warming in the Amundsen Sea leads to 16% more sea level rise compared to using another GCM in which warming mainly occurs in the Weddell Sea. In the same emission scenario, including 3D GIA reduced sea level rise by 23%. In the latter case, the effect of GIA is significantly larger than the uncertainties arising from the choice of GCM.

The impact of GIA is relatively stronger over shorter timescales in a low-emission scenario compared to a high-emission scenario. In the high-emission case, the rapid ice sheet retreat makes the rate of bedrock uplift less significant, allowing GIA to slow the retreat but not to prevent a fast collapse of the West Antarctic Ice Sheet. Conversely, in the low-emission scenario, the slower ice retreat allows more response to the faster bedrock uplift, enabling GIA to slow down the ice sheet retreat more in a relative sense. Significant ice sheet retreat still occurs when including 3D Earth structures, but the grounding line is more advanced towards the ocean by up to hundreds of kilometers compared to excluding GIA. As a result, the influence of GIA is greater under the low-

emission scenario than in the high-emission case around 2400. This advocates for immediate and aggressive mitigation efforts to curb greenhouse gas emissions. This would increase the stabilising effect of GIA relative to other sources of ice sheet mass loss and reduce the extent of ice mass loss and the associated impacts on sea level rise. Continued high emissions will lead to irreversible changes and long-term consequences for coastal infrastructure and ecosystems (IPCC, 2023).

Studying the ice sheet dynamics using a coupled 3D GIA - ice sheet model provided new insights on how GIA exactly impacts ice dynamics. We found that the most important feedback is the effect of GIA on grounding line dynamics. When bedrock rises, more ice stays grounded. Therefore, there is less ice shelf area over which sub-shelf basal melt can occur, causing the grounding line to retreat less. The coupled model is also used to compute the change in regional sea level due to the decrease in gravitational attraction of the ice on the sea level and the Earth's deformation. We conducted a projection for the high emission scenario where we included this change in regional sea level, which leads to a sea level drop of 8 meters. This drop in regional sea level stabilises the ice sheet and thereby reduces the Antarctic contribution to barystatic sea level rise by 5% in 2500. The stabilising effect of the self-gravitation of the ice sheet is a stabilising effect that is significantly smaller than the effect of bedrock deformation on the ice sheet dynamics, which could lead to a reduction of the Antarctic contribution to barystatic sea level rise by 23% in 2500. Taking ocean loading in ice-free regions into account in computing bedrock deformation would further stabilise the ice sheet. Last, we also investigated the effect of depth-dependent ocean temperature on the feedback. When GIA is included, there is less grounding line retreat and therefore the ice shelves are somewhat thicker compared to excluding GIA. The thicker ice shelves have a shelf base in warmer water, leading to an increase in basal melt. However, we found that this effect is negligible.

6.1.3. RESEARCH QUESTION 3

How can the 3D bedrock response be approximated in ice sheet models?

The computational demands of a 3D GIA model are high, making it impractical for ensemble studies that require thousands of ice sheet simulations (Coulon et al., 2024; Seroussi et al., 2020). There is therefore a need to use simpler and hence faster Earth models to approximate the bedrock response of a 3D GIA model, such as the ELRA or 1D GIA models.

The dislocation and diffusion parameters used to simulate mantle deformation in the 3D GIA model depend on seismic velocity anomalies, as well as mantle grain size and water content and other flow law parameters. We assumed uncertainty is represented by grain size and water content and adjusted these parameters to match viscosity constraints for the Amundsen Sea Embayment (Barletta et al., 2018), the Weddel Sea Embayment (Bradley et al., 2015) and Palmer Land (Wolstencroft et al., 2015). However, no single set of parameters can satisfy the viscosity constraints for these three regions simultaneously. To account for this, two Earth structures are used, of which one structure fits best to the Amundsen Sea Embayment constraint, and one structure fits best to constraints of the other two regions.

Chapter 5 demonstrates that, until 2300, the average sea level contribution and ice

sheet evolution resulting from the two 3D Earth structures can be reasonably approximated using an ELRA model with a uniform relaxation time of 300 years. Beyond this, up to 2500, a more refined approach using a laterally varying relaxation time and a 1D GIA model with an upper mantle viscosity of $10^{19} \text{ Pa} \cdot \text{s}$ provides a good approximation. For this conclusion, the 1D GIA and ELRA model results are compared to the average 3D GIA results, but the spread in sea level contribution between the use of the two 3D Earth structures is relatively large. The above mentioned relaxation time and 1D viscosity can be used, but it is always recommended to vary the Earth parameters to approximate the different 3D Earth structures instead of the average of the 3D GIA results, to account for the uncertainty in 3D viscosity.

6.2. RECOMMENDATIONS

The above mentioned conclusions are drawn under the assumptions of prescribed changes in ocean and atmospheric temperature and sea level, and under the assumption of the chosen model parameters. To increase the robustness of the conclusions, more experiments should be done using an uncertainty range of these parameters. For example, the climate forcing could be varied using different general circulation models. The atmospheric and oceanic present-day climatology could be varied by using, for example, RACMO results from van Dalum et al. (2022)) and Jourdain et al. (2020). Furthermore, the atmospheric lapse rate differs regionally and should be varied to include the uncertainty range, and a different sub-shelf melt parameterisation could lead to significant different grounding line retreat.

Besides the exploration of the uncertainties in the current model, several possible extensions of the work done in this thesis are presented in this section. To study the effect of GIA on ice sheet dynamics in more detail, several approaches can be taken. First, the developed coupled 3D GIA - ice sheet model could be further developed and extended in terms of spatial and temporal resolution, parameterisations and by applying the sea level equation (section 6.2.1). Furthermore, the model could make use of more observations and estimates of bedrock surface deformation, ice thickness changes, surface velocities and the geothermal heat flux (section 6.2.2). The model could be included in an Earth system model to study the feedbacks between GIA, ocean and atmosphere (section 6.2.3). Finally, the coupled model can be applied to other ice sheets such as the Greenland, Fennoscandian and Laurentide ice sheets (section 6.2.3).

6.2.1. FURTHER MODEL DEVELOPMENT

Both the ice sheet and GIA models can be improved in several ways. An increased spatial resolution, ideally in the order of a kilometer grid around the grounding line for the ice sheet model and in the order of several kilometers for the elastic layer of the GIA model (Wan et al., 2022), would more accurately simulate the complex interactions between ice dynamics and Earth's viscoelastic response. For the ice sheet model, enhancing spatial resolution is critical for capturing pinning points, which are key to controlling ice flow and grounding line stability. Also, the spatial variations in surface and bedrock elevation is relatively high in the Antarctic Peninsula, which would require a high resolution to solve accurately. Additionally, improving the lateral resolution of the elastic layer in the

GIA model allows for more accurate modeling of localized deformation, which will lead to a better comparison between model results and uplift observations (Wan et al., 2022).

In the GIA model used in this thesis, the Earth is modeled as a Maxwell viscoelastic body including a nonlinear composite rheology. The Maxwell rheology assumes that after an initial elastic response, deformation proceeds at a steady, viscous rate. In contrast, Burgers rheology introduces an additional Kelvin-Voigt component, which allows for a time-dependent response, where the material behaves elastically and viscoelastically in response to varying timescales of applied stress. This transient component is important to capture intermediate timescales. For instance, during events like Meltwater Pulse 1A (the observed rapid change in sea level rise about 15000 years ago), transient deformation significantly affects GIA predictions because of the fast rate of ice melt and corresponding sea-level changes (Lau, 2023). The Burgers model allows the Earth to deform more rapidly in the short term and then return more slowly to its equilibrium state compared to the Maxwell model, which only considers long-term steady-state viscous behavior. This transient deformation is key in explaining the differences in crustal responses, as the Earth's response is not purely elastic or purely viscous but a complex interaction of both and depends on the timescales involved.

Regional variations in sea level affect radial displacements computed by the GIA model due to the extra water load. The changes in ocean loading on ice-free regions are small compared to the changes in ice loading and are therefore not taken into account in this thesis. However, this effect could be taken into account in the GIA model by solving the sea level equation (as done for the GIA model in Blank et al. (2021)). To do so, simultaneous simulations of global ice sheet and glacier variations are needed to solve the sea level equation globally. An intermediate approximation for projections could involve using standalone simulations of Greenland as input for solving the sea level equation, thereby capturing the far-field sea level effect on ice dynamics.

Regional variations in sea level also affect grounding line migration computed by the ice sheet model, which is dependent on the water depth and the ice thickness at grounding zones. Including the effect of regional variations in sea level on ice sheet dynamics leads to a sea level drop of about 8 meters in the year 2500 in the case of a high emission scenario with strong retreat in the Amundsen Sea Embayment. In this thesis, this test is performed by computing the geoid change due to the Antarctic ice mass changes using the GIA model. The geoid is the equipotential surface of the Earth's gravity field that best approximates regional sea level. The contributions from glaciers, Greenland, steric effects and the decreased gravitational attraction of the Antarctic Ice Sheet on sea level were assumed to be spatially uniform in Antarctica and were added to the geoid change. Using the regional sea level computed with the sea level equation for global contributions instead of only the geoid contributions from the Antarctic Ice Sheet would provide insight on the main factors determining regional sea level and its effect on ice sheet dynamics.

6.2.2. IMPROVEMENT THROUGH INCORPORATING ADDITIONAL OBSERVATIONS

The models can be better constrained by including additional datasets. First we focus on datasets on the solid Earth, then on the improvement in modeling the present-day

state of the ice sheet by observations of bedrock uplift, ice thickness change, ice surface velocities, and sea level followed by observations of the geothermal heat flux to improve basal hydrology of grounded ice.

SOLID EARTH

Deriving a 3D rheology is subject to uncertainty and could be improved in several ways. For example, seismic stations are scarce in Antarctica, mainly around the East Antarctic coastline and the peninsula, whereas these are interesting areas where the viscosity varies laterally and radially on short spatial scales (Lloyd et al., 2019). Furthermore, most of the stations are temporary and not permanent whereas long-term records are needed to measure seismic wave velocities induced by earthquakes. Improving the spatial resolution of permanent seismic stations would reduce the uncertainty in the conversion from seismic wave velocity to mantle temperature.

Furthermore, the conversion from seismic velocity anomalies to mantle temperature could be better constrained by using another dataset such as gravity field observations to derive the mantle temperature and composition (e.g. Fullea et al., 2021). The mantle temperature determines the spatial pattern of the viscosity and using another dataset as input in the seismic model could reveal new regions with a relatively low viscosity which would lead to increased deformation, or change a currently indicated low-viscosity region to a higher viscosity region.

In the 3D GIA model, the lateral variations in the mantle viscosity are now only applied to the upper mantle, whereas data exists for the transition zone and the deeper mantle, although interpretation in terms of rheology is subject to larger uncertainty. The further the grounding line retreats, the larger the area of ice loss, and the deeper the deformation of the solid Earth occurs. Although lateral variability is smaller for the deeper mantle, it might be important to include it in periods with ice retreat in large regions such as the Laurentide and the Antarctic Ice Sheet retreat over glacial time scales.

The 3D GIA model uses a flow law to compute the strain rate of the material based on material-dependent parameters such as the temperature (Hirth and Kohlstedt, 2003). Flow laws are often derived from laboratory experiments. In these experiments, conditions such as temperature, pressure, and grain size are controlled to simulate the environment within the Earth's mantle. The results of these experiments are analyzed to establish the dependence of strain rate on differential stress, temperature, grain size, and other factors. These empirical data are then used to formulate constitutive equations, or flow laws, that describe how rocks will deform under specific conditions (Hansen and Kohlstedt, 2015). Further lab experiments of rock behaviour, and including different flow laws in the 3D GIA model used in this thesis, would improve the understanding of the effect of the flow law on rock deformation.

THE PRESENT DAY STATE OF THE EARTH AND THE ICE SHEET

A critical step in improving the accuracy of future ice sheet projections is to identify a 3D Earth structure in combination with ice sheet model parameters that results in the observed present-day state and dynamics. For this we can calculate present-day uplift rates by simulating the last glacial cycle. Tuning the Earth model in the simulation of the glacial cycle to match sea level observations, based on sea level indicators, satellite altimetry and tide gauges, and current uplift observations better constrains variations in

mantle viscosity, lithospheric thickness, and other geophysical properties, leading to a more accurate representation of the bedrock response for the glacial cycle itself as well as for projections. This has been done using prescribed ice sheet histories (e.g. Barletta et al., 2018; Bradley et al., 2015; Nield et al., 2014; Wolstencroft et al., 2015; Zhao et al., 2017), but not using a coupled GIA - ice sheet model. It might be necessary to increase the spatial resolution of the models to fit bedrock deformation to Global Navigation Satellite System (GNSS) measurements and tide gauge data. The continuation of GNSS measurements in Antarctica is crucial to constrain the models.

Furthermore, it has been shown that present-day mass loss rates can be used as constraints on the ice sheet initialisation when projecting the Antarctic Ice Sheet evolution (van den Akker et al., 2025). The simulation of the last glacial cycle as described above should therefore not only result in the observed present day uplift rates of the bedrock, but also in the observed surface velocities, ice thickness (change) and surface mass balance. Current satellite measurements based on for example gravimetry and altimetry offer detailed information on the rates and spatial patterns of ice loss (Rignot et al., 2019). By adjusting the model's parameters, such as initial ocean temperature, basal melt rates and the friction coefficient, to match these observations, the simulation will more accurately capture the interplay between ice dynamics and GIA, leading to more reliable predictions of future ice mass loss and sea level rise. The residual stresses resulting from past ice load fluctuations play a crucial role in controlling the ongoing deformation of the bedrock for a mantle which partly responds non-linearly to stress changes (e.g. Blank et al., 2021). By incorporating these stress fields in the mantle into future simulations, the model will provide a more realistic present day stress field of the Earth. This can be used as starting point to project how the ice sheet will evolve under different climate scenarios.

THE GEOTHERMAL HEAT FLUX

In this thesis, the geothermal heat flux (GHF) is based on the model provided by Shapiro and Ritzwoller (2004). While this model has been widely used, it is now surpassed by advances in geophysical research and technology. A straightforward improvement to the current model would involve replacing the GHF data with a more recent and refined GHF map. Modern geothermal heat flux models incorporate updated data from various sources, such as improved seismic tomography and increased local heat flow measurements (Fisher et al., 2015; Morin et al., 2010), combined with advanced techniques, which provide a more accurate representation of geothermal gradients and variations, such as Lösing et al. (2020)). New GHF estimates are higher than previous models due to inclusion of new data, improved models and by using a combination of geological information and geophysical data analysis, which could lead to increased basal melt, reduced friction at the base of the ice sheet and therefore, increased ice flow. Incorporating geological constraints improves GHF modeling, and future work should combine sparse data with tectonic context to refine these estimates. Ideally, the geothermal heat flux model should be consistent with the mantle temperature used in the GIA model to ensure full consistency between the coupled ice sheet-GIA simulations.

6.2.3. COUPLING TO AN EARTH SYSTEM MODEL

Earth System Models (ESMs) are advanced computational tools designed to simulate and understand the complex interactions within the Earth's climate system (Bonan and Doney, 2018). These models integrate various components to provide a comprehensive view of how these components interact and change over time. ESMs combine atmospheric models, which simulate climate processes such as temperature and precipitation, with ocean models that address ocean currents, sea surface temperatures, and their interactions with the atmosphere. They can also include land surface models that focus on processes like vegetation dynamics, soil moisture, and heat fluxes.

Recently, ESMs started to include ice sheet models to simulate the behavior of glaciers and ice sheets, including their growth, melt, and interactions with the climate and ocean (Siahaan et al., 2022). However, these ESMs currently do not include 3D GIA models when calculating global sea level. As a result, when ice sheet models are included, the ESMs overestimate grounding line retreat rates and, consequently, sea level rise. To address this issue and improve the accuracy of sea level projections, it is recommended that ESMs integrate 3D GIA models or different Earth parameters for simpler models as suggested in Chapter 5. Furthermore, bathymetry of the continental shelf plays a crucial role in modulating sub-shelf melt rates as they influence the access of Circumpolar Deep Water to ice-shelf cavities (Goldberg et al., 2020). A change in bedrock deformation might affect this access of deep water to ice-shelf cavities (Kreuzer et al., 2023). This effect could be quantified by coupling a 3D GIA model with an Earth system model. A large uncertainty of this model is the bathymetry itself, which should be improved by increased measurements.

6.2.4. OTHER REGIONS OF INTEREST

The coupled 3D GIA - ice sheet model is suitable for large scale ice sheets on different time scales. The model could therefore also be applied to the Northern Hemisphere ice sheets of the past (i.e. the Fennoscandian, Laurentide, and the Greenland ice sheet). In these areas, ice sheets cover such a wide region that the mantle viscosity also varies significantly laterally underneath or near the ice sheets. The assumptions made in this thesis on the effect of self-gravitation of the ice sheet and the solid Earth might not be valid for these regions and should thus be explored if the model were to be applied to new regions.

The Laurentide ice sheet was partly marine-based after the inflow of water in the Hudson Bay. GIA also allowed the formation of proglacial lakes due to a depression in the landscape formed in a glaciation phase which can fill up with meltwater in a deglaciation phase (Scherrenberg et al., 2024). These proglacial lakes enhance ice mass loss. This effect has not been studied using a coupled GIA - ice sheet model and doing so might lead to new insights on the dynamics of the Laurentide ice sheet.

Greenland exhibits lateral variations in mantle viscosity and lithospheric thickness (Steffen et al., 2018; Pourpoint et al., 2018; Darbyshire et al., 2018), though these differences are less pronounced than those observed beneath Antarctica. In southern Greenland, where the lithosphere is thinner and the mantle is hotter, the upper mantle viscosity is relatively low. Conversely, northern Greenland features a thicker, colder lithosphere with a higher mantle viscosity, differing by about two orders of magnitude.

Contrary to Antarctica, the main effect of GIA on the Greenland ice sheet is not via the grounding line but via the melt-elevation feedback. Using the coupled 3D GIA-ice sheet model from Chapter 3, applied at high resolution over Greenland throughout a glacial cycle, it is shown that the ice surface elevation at the Last Glacial Maximum can be up to 900 meters higher in northern Greenland when a 3D Earth structure is employed compared to a 1D model (Kempenaar, 2022). This elevation increase is attributed to the higher viscosity in the 3D model. Consequently, this elevation delay shifts the onset of ablation during the deglaciation phase, as the ice surface remains longer at higher elevation in a cooler atmosphere.

The study from Kempenaar (2022) did not include ice shelves but including shelves could lead to a different grounding line retreat and therefore also a different effect of GIA on the grounding line. To further explore the sensitivity of the Greenland ice sheet to GIA and the melt-elevation feedback, it is recommended to repeat the study using the updated coupled model from Chapters 4 and 5. Compared to ANICE used in Kempenaar (2022), the ice sheet model IMAU-ICE allows the Greenland ice sheet to grow and melt shelves. Furthermore, it has an updated grounding line approximation and method to compute ice velocities, and simulates refreezing more accurately.

BIBLIOGRAPHY

- A, G., Wahr, J., & Zhong, S. (2013). Computations of the viscoelastic response of a 3-d compressible earth to surface loading: An application to glacial isostatic adjustment in antarctica and canada. *Geophysical Journal International*, 192(2), 557–572.
- Abe-Ouchi, A., Saito, F., Kawamura, K., Raymo, M. E., Okuno, J., Takahashi, K., & Blatter, H. (2013). Insolation-driven 100,000-year glacial cycles and hysteresis of ice-sheet volume. *Nature*, 500(7461), 190–193.
- Adhikari, S., Ivins, E. R., Larour, E., Seroussi, H., Morlighem, M., & Nowicki, S. (2014). Future antarctic bed topography and its implications for ice sheet dynamics. *Solid Earth*, 5, 569–584. <https://doi.org/10.5194/se-5-569-2014>
- Albrecht, T., Winkelmann, R., & Levermann, A. (2020). Glacial-cycle simulations of the antarctic ice sheet with the parallel ice sheet model (pism) – part 1: Boundary conditions and climatic forcing. *The Cryosphere*, 14, 599–632. <https://doi.org/10.5194/tc-14-599-2020>
- Albrecht, T., Bagge, M., & Klemann, V. (2024). Feedback mechanisms controlling antarctic glacial-cycle dynamics simulated with a coupled ice sheet–solid earth model. *The Cryosphere*, 18(9), 4233–4255.
- Annan, J. D., Hargreaves, J. C., & Mauritsen, T. (2022). A new global surface temperature reconstruction for the last glacial maximum. *Climate of the Past*, 18, 1883–1896. <https://doi.org/10.5194/cp-18-1883-2022>
- Bagge, M., Klemann, V., Steinberger, B., Latinović, M., & Thomas, M. (2021). Glacial-isostatic adjustment models using geodynamically constrained 3d earth structures. *Geochemistry, Geophysics, Geosystems*, 22(11), e2021GC009853. <https://doi.org/10.1029/2021GC009853>
- Barletta, V., Bevis, M., Smith, B., Wilson, T., Brown, A., Bordoni, A., Willis, M., Khan, S., Rovira-Navarro, M., Dalziel, I., Smalley, R., Kendrick, E., Konfal, S., Caccamise, D., Aster, R., Nyblade, A., & Wiens, D. (2018). Observed rapid bedrock uplift in amundsen sea embayment promotes ice-sheet stability. *Science*, 360, 1335–1339. <https://doi.org/10.1126/science.aao1447>
- Becker, T., & Boschi, L. (2002). A comparison of tomographic and geodynamic mantle models. *Geochemistry, Geophysics, Geosystems*, 3. <https://doi.org/10.1029/2001GC000168>
- Berends, C. J., de Boer, B., Dolan, A. M., Hill, D. J., & van de Wal, R. S. W. (2019). Modelling ice sheet evolution and atmospheric co₂ during the late pliocene. *Climate of the Past*, 15, 1603–1619. <https://doi.org/10.5194/cp-15-1603-2019>
- Berends, C. J., de Boer, B., & van de Wal, R. S. W. (2018). Application of hadcm3@bristolv1.0 simulations of paleoclimate as forcing for an ice-sheet model, anice2.1: Set-up and benchmark experiments. *Geoscientific Model Development*, 11, 4657–4675. <https://doi.org/10.5194/gmd-11-4657-2018>

- Berends, C. J., Goelzer, H., & van de Wal, R. S. W. (2021). The utrecht finite volume ice-sheet model: Ufemism (version 1.0). *Geoscientific Model Development*, 14(5), 2443–2470. <https://doi.org/10.5194/gmd-14-2443-2021>
- Berends, C., Goelzer, H., Reerink, T., Stap, L., & van de Wal, R. (2022). Benchmarking the vertically integrated ice-sheet model imau-ice (version 2.0). *Geoscientific Model Development*, 15, 5667–5688. <https://doi.org/10.5194/gmd-15-5667-2022>
- Bintanja, R., & van de Wal, R. (2008). North american ice-sheet dynamics and the onset of 100 000 year glacial cycles. *Nature*, 454, 869–872. <https://doi.org/10.1038/nature07158>
- Bintanja, R., van de Wal, R., & Oerlemans, J. (2005). Modelled atmospheric temperatures and global sea levels over the past million years. *Nature*, 437, 125–128. <https://doi.org/10.1038/nature03975>
- Bintanja, R., Van de Wal, R., & Oerlemans, J. (2002). Global ice volume variations through the last glacial cycle simulated by a 3-d ice-dynamical model. *Quaternary International*, 95, 11–23.
- Blank, B., Barletta, V., Hu, H., Pappa, F., & van der Wal, W. (2021). Effect of lateral and stress-dependent viscosity variations on gia induced uplift rates in the amundsen sea embayment. *Geochemistry, Geophysics, Geosystems*, 22(9). <https://doi.org/10.1029/2021GC009807>
- Bonan, G. B., & Doney, S. C. (2018). Climate, ecosystems, and planetary futures: The challenge to predict life in earth system models. *Science*, 359(6375), eaam8328.
- Book, C., Hoffman, M., Kachuck, S., Hillebrand, T., Price, S., Perego, M., & Bassis, J. (2022). Stabilizing effect of bedrock uplift on retreat of thwaites glacier, antarctica, at centennial timescales. *Earth and Planetary Science Letters*, 597, 117798. <https://doi.org/10.1016/j.epsl.2022.117798>
- Bradley, S. L., Reerink, T. J., van de Wal, R. S. W., & Helsen, M. M. (2018). Simulation of the greenland ice sheet over two glacial–interglacial cycles: Investigating a sub-ice-shelf melt parameterization and relative sea level forcing in an ice-sheet–ice-shelf model. *Climate of the Past*, 14, 619–635. <https://doi.org/10.5194/cp-14-619-2018>
- Bradley, S. L., et al. (2015). Low post-glacial rebound rates in the weddell sea due to late holocene ice-sheet readvance. *Earth and Planetary Science Letters*, 413, 79–89.
- Bronselaer, B., Winton, M., Griffies, S. M., Hurlin, W. J., Rodgers, K. B., Sergienko, O. V., Stouffer, R. J., & Russell, J. L. (2018). Change in future climate due to antarctic meltwater. *Nature*, 564(7734), 53–58.
- Bueler, E., & Brown, J. (2009). Shallow shelf approximation as a “sliding law” in a thermo-mechanically coupled ice sheet model. *Journal of Geophysical Research-Earth*, 114(F03008). <https://doi.org/10.1029/2008JF001179>
- Bueler, E., Lingle, C. S., & Brown, J. (2007). Fast computation of a viscoelastic deformable earth model for ice-sheet simulations. *Annals of Glaciology*, 46, 97–105. <https://doi.org/10.3189/172756407782871567>
- Bulthuis, K., Arnst, M., Sun, S., & Pattyn, F. (2019). Uncertainty quantification of the multi-centennial response of the antarctic ice sheet to climate change. *The Cryosphere*, 13, 1349–1380. <https://doi.org/10.5194/tc-13-1349-2019>

- Chen, D., et al. (2021). Framing, context, and methods. In V. Masson-Delmotte, P. Zhai, A. Pirani, S. Connors, C. Pean, S. Berger, N. Caud, Y. Chen, L. Goldfarb, M. Gomis, M. Huang, K. Leitzell, E. Lonnoy, J. Matthews, T. Maycock, T. Waterfield, O. Yelekci, R. Yu, & B. Zhou (Eds.), *Climate change 2021: The physical science basis. contribution of working group i to the sixth assessment report of the intergovernmental panel on climate change* (pp. 147–286). Cambridge University Press.
- Cheng, C.-A., Yan, X., Ratliff, N., & Boots, B. (2019). Predictor-corrector policy optimization. *International Conference on Machine Learning*, 1151–1161.
- Coulon, V., Bulthuis, K., Whitehouse, P. L., Sun, S., Haubner, K., Zipf, L., & Pattyn, F. (2021). Contrasting response of west and east antarctic ice sheets to glacial isostatic adjustment. *Journal of Geophysical Research-Earth*, 126(e2020JF006003). <https://doi.org/10.1029/2020JF006003>
- Coulon, V., Klose, A., Kittel, C., Edwards, T., Turner, F., Winkelmann, R., & Pattyn, F. (2024). Disentangling the drivers of future antarctic ice loss with a historically calibrated ice-sheet model. *The Cryosphere*, 18, 653–681. <https://doi.org/10.5194/tc-18-653-2024>
- Darbyshire, F. A., Dahl-Jensen, T., Larsen, T. B., Voss, P. H., & Joyal, G. (2018). Crust and uppermost-mantle structure of greenland and the northwest atlantic from rayleigh wave group velocity tomography. *Geophysical Journal International*, 212(3), 1546–1569.
- De Boer, B., Stocchi, P., & van de Wal, R. S. W. (2014). A fully coupled 3-d ice-sheet–sea-level model: Algorithm and applications. *Geoscientific Model Development*, 7, 2141–2156. <https://doi.org/10.5194/gmd-7-2141-2014>
- De Boer, B., Stocchi, P., Whitehouse, P. L., & Van De Wal, R. S. W. (2017). Current state and future perspectives on coupled ice-sheet–sea-level modelling. *Quaternary Science Reviews*, 169, 13–28. <https://doi.org/10.1016/j.quascirev>
- De Boer, B., Van De Wal, R. S. W., Lourens, L. J., Bintanja, R., & Reerink, T. J. (2013). A continuous simulation of global ice volume over the past 1 million years with 3-d ice-sheet models. *limate Dynamics*, 41, 1365–1384. <https://doi.org/10.1007/s00382-012-1562-2>
- DeConto, R., Pollard, D., Alley, R., Velicogna, I., Gasson, E., Gomez, N., Sadai, S., Condrón, A., Gilford, D., Ashe, E., Kopp, R., Li, D., & Dutton, A. (2021). The paris climate agreement and future sea-level rise from antarctica. *Nature*, 593, 83–89. <https://doi.org/10.1038/s41586-021-03427-0>
- Depoorter, M., Bamber, J., Griggs, J., et al. (2013). Calving fluxes and basal melt rates of antarctic ice shelves. *Nature*, 502, 89–92.
- Dupont, T., & Alley, R. (2005). Assessment of the importance of ice-shelf buttressing to ice-sheet flow. *Geophysical Research Letters*, 32, L04503.
- Farrell, W., & Clark, J. (1976). On postglacial sea level. *Geophysical Journal of the Royal Astronomical Society*, 46, 647–667. <https://doi.org/10.1111/j.1365-246X.1976.tb01252.x>
- Favier, L., Jourdain, N., Jenkins, A., Merino, N., Durand, G., Gagliardini, O., Gillet-Chaulet, F., & Mathiot, P. (2019). Assessment of sub-shelf melting parameterisations using the ocean–ice-sheet coupled model nemo(v3.6)–elmer/ice(v8.3). *Geoscientific*

- tific Model Development*, 12, 2255–2283. <https://doi.org/10.5194/gmd-12-2255-2019>
- Fettweis, X., Hofer, S., Krebs-Kanzow, U., Amory, C., Aoki, T., Berends, C. J., Born, A., Box, J. E., Delhasse, A., Fujita, K., Gierz, P., Goelzer, H., Hanna, E., Hashimoto, A., Huybrechts, P., Kapsch, M.-L., King, M. D., Kittel, C., Lang, C., ... Zolles, T. (2020). Grsmbmip: Intercomparison of the modelled 1980–2012 surface mass balance over the greenland ice sheet. *The Cryosphere*, 14(11), 3935–3958. <https://doi.org/10.5194/tc-14-3935-2020>
- Fisher, A. T., Mankoff, K. D., Tulaczyk, S. M., Tyler, S. W., Foley, N., & Team, W. S. (2015). High geothermal heat flux measured below the west antarctic ice sheet. *Science Advances*, 1(6), e1500093.
- Fox-Kemper, B., Hewitt, H., & Xiao, C. (2021). Ocean, cryosphere and sea level change, 1211–1362. <https://doi.org/10.1017/9781009157896.011>
- Fullea, J., Lebedev, S., Martinec, Z., & Celli, N. L. (2021). Winterc-g: Mapping the upper mantle thermochemical heterogeneity from coupled geophysical–petrological inversion of seismic waveforms, heat flow, surface elevation and gravity satellite data. *Geophysical Journal International*, 226, 146–191. <https://doi.org/10.1093/gji/ggab094>
- Geruo, A., Wahr, J., & Zhong, S. (2013). Computations of the viscoelastic response of a 3-d compressible earth to surface loading: An application to glacial isostatic adjustment in antarctica and canada. *Geophysical Journal International*, 192, 557–572. <https://doi.org/10.1093/gji/ggs030>
- Goelzer, H., Nowicki, S., Payne, A., Larour, E., Seroussi, H., Lipscomb, W. H., Gregory, J., Abe-Ouchi, A., Shepherd, A., Simon, E., et al. (2020). The future sea-level contribution of the greenland ice sheet: A multi-model ensemble study of ismip6. *The cryosphere*, 14(9), 3071–3096.
- Goes, S., Govers, R., & Vacher, A. P. (2000). Shallow mantle temperatures under europe from p and s wave tomography. *Journal of Geophysical Research: Solid Earth*, 105, 11153–11169. <https://doi.org/10.1029/1999JB900300>
- Goldberg, D. N., Smith, T. A., Narayanan, S. H., Heimbach, P., & Morlighem, M. (2020). Bathymetric influences on antarctic ice-shelf melt rates. *Journal of Geophysical Research: Oceans*, 125(11), e2020JC016370.
- Golledge, N., et al. (2015). The multi-millennial antarctic commitment to future sea-level rise. *Nature*, 526, 421–425.
- Golledge, N., Keller, E., Gomez, N., Naughten, K., Bernalles, J., Trusel, L., & Edwards, T. (2019). Global environmental consequences of twenty-first-century ice-sheet melt. *Nature*, 566, 65–72. <https://doi.org/10.1038/s41586-019-0889-9>
- Gomez, N., Latychev, K., & Pollard, D. (2018). A coupled ice sheet–sea level model incorporating 3d earth structure: Variations in antarctica during the last deglacial retreat. *Journal of Climate*, 31, 4041–4054. <https://doi.org/10.1175/JCLI-D-17-0352.1>
- Gomez, N., Mitrovica, J. X., Tamisiea, M. E., & Clark, P. U. (2010). A new projection of sea level change in response to collapse of marine sectors of the antarctic ice sheet. *Geophysical Journal International*, 180, 623–634. <https://doi.org/10.1111/j.1365-246X.2009.04419.x>

- Gomez, N., Pollard, D., & Holland, D. (2015). Sea-level feedback lowers projections of future antarctic ice-sheet mass loss. *Nature Communications*, 6, 8798. <https://doi.org/10.1038/ncomms9798>
- Gomez, N., Pollard, D., & Mitrovica, J. X. (2013). A 3-d coupled ice sheet – sea level model applied to antarctica through the last 40 ky. *Earth and Planetary Science Letters*, 384, 88–99. <https://doi.org/10.1016/j.epsl.2013.09.042>
- Gomez, N., Pollard, D., Mitrovica, J. X., Huybers, P., & Clark, P. U. (2012). Evolution of a coupled marine ice sheet–sea level model. *Journal of Geophysical Research-Earth*, 117, 850–853. <https://doi.org/10.1029/2011JF002076>
- Gomez, N., Weber, M. E., Clark, P. U., Mitrovica, J. X., & Han, H. K. (2020). Antarctic ice dynamics amplified by northern hemisphere sea-level forcing. *Nature*, 587, 600–604. <https://doi.org/10.1038/s41586-020-2916-2>
- Gomez, N., Yousefi, M., Pollard, D., DeConto, R., Sadai, S., Lloyd, A., Nyblade, A., Wiens, D., Aster, R., & Wilson, T. (2024). The influence of realistic 3d mantle viscosity on antarctica's contribution to future global sea levels. *Science Advances*, 10(31), eadn1470. <https://doi.org/10.1126/sciadv.adn1470>
- Goosse, H., & Fichefet, T. (1999). Importance of ice-ocean interactions for the global ocean circulation: A model study. *Journal of Geophysical Research: Oceans*, 104(C10), 23337–23355.
- Gowan, E. J., Zhang, X., Khosravi, S., Rovere, A., Stocchi, P., Hughes, A. L. C., Gyllencreutz, R., Mangerud, J., Svendsen, J.-I., & Lohmann, G. (2021). A new global ice sheet reconstruction for the past 80,000 years. *Nature Communications*, 12, 1199. <https://doi.org/10.1038/s41467-021-21469-w>
- Hahn, L. C., Armour, K. C., Battisti, D. S., Donohoe, A., Pauling, A., & Bitz, C. M. (2020). Antarctic elevation drives hemispheric asymmetry in polar lapse rate climatology and feedback. *Geophysical Research Letters*, 47(16), e2020GL088965.
- Han, H. K., Gomez, N., Pollard, D., & DeConto, R. (2021). Modeling northern hemispheric ice sheet dynamics, sea level change, and solid earth deformation through the last glacial cycle. *Journal of Geophysical Research-Earth*, 126. <https://doi.org/10.1029/2020JF006040>
- Han, H. K., Gomez, N., & Wan, J. X. W. (2022). Capturing the interactions between ice sheets, sea level and the solid earth on a range of timescales: A new “time window” algorithm. *Geoscientific Model Development*, 15, 1355–1373. <https://doi.org/10.5194/gmd-15-1355-2022>
- Hansen, L., & Kohlstedt, D. (2015). 2.18 constitutive equations, rheological behavior, and viscosity of rocks. *Treatise on Geophysics*, 2, 441–472.
- Haseloff, M., & Sergienko, O. (2018). The effect of buttressing on grounding line dynamics. *Journal of Glaciology*, 64, 417–431.
- Haseloff, M., & Sergienko, O. (2022). Effects of calving and submarine melting on steady states and stability of buttressed marine ice sheets. *Journal of Glaciology*, 68, 1149–1166.
- Hay, C. C., Lau, H. C., Gomez, N., Austermann, J., Powell, E., Mitrovica, J. X., Latychev, K., & Wiens, D. A. (2017). Sea level fingerprints in a region of complex earth structure: The case of wais. *Journal of Climate*, 30, 1881–1892. <https://doi.org/10.1175/JCLI-D-16-0388.1>

- Heeszel, D., Wiens, D., Anandakrishnan, S., Aster, R., Dalziel, I., Hierta, A., Nyblade, A., Wilson, T., & Winberry, J. (2016). Upper mantle structure of central and west antarctica from array analysis of rayleigh wave phase velocities. *Journal of Geophysical Research: Solid Earth*, 121, 1758–1775. <https://doi.org/10.1002/2015JB012616>
- Hirth, G., & Kohlstedt, D. L. (2003). Rheology of the upper mantle and the mantle wedge: A view from the experimentalists. In J. Eiler (Ed.), *Inside the subduction factory* (pp. 83–105). American Geophysical Union. <https://doi.org/10.1029/138GM06>
- Hu, H., van der Wal, W., & Vermeersen, L. L. A. (2017). A numerical method for reorientation of rotating tidally deformed viscoelastic bodies. *Journal of Geophysical Research-Planets*, 122, 228–248. <https://doi.org/10.1002/2016JE005114>
- Huang, P., Steffen, R., Steffen, H., Klemann, V., Wu, P., van der Wal, W., Martinec, Z., & Tanaka, Y. (2023). A commercial finite element approach to modelling Glacial Isostatic Adjustment on spherical self-gravitating compressible earth models. *Geophysical Journal International*, 235(3), 2231–2256. <https://doi.org/10.1093/gji/ggad354>
- Huybrechts, P. (1996). Basal temperature conditions of the greenland ice sheet during the glacial cycles. *Annals of Glaciology*, 23, 226–236.
- Huybrechts, P., & De Wolde, J. (1999). The dynamic response of the greenland and antarctic ice sheets to multiple-century climatic warming. *Journal of Climate*, 12(8), 2169–2188.
- IPCC. (2023). *Climate change 2022 – impacts, adaptation and vulnerability: Working group ii contribution to the sixth assessment report of the intergovernmental panel on climate change*. Cambridge University Press.
- Ivins, E. R., van der Wal, W., Wiens, D. A., Lloyd, A. J., & Caron, L. (2023). Antarctic upper mantle rheology. In A. P. Martin & W. van der Wal (Eds.), *The geochemistry and geophysics of the antarctic mantle*. Geological Society, London. <https://doi.org/10.1144/M56-2020-19>
- Jakobs, C., Reijmer, C., Van den Broeke, M., Van de Berg, W., & Van Wessem, J. (2021). Spatial variability of the snowmelt-albedo feedback in antarctica. *Journal of Geophysical Research: Earth Surface*, 126(2), e2020JF005696.
- Jenkins, A., Shoosmith, D., Dutrieux, P., et al. (2018). West antarctic ice sheet retreat in the amundsen sea driven by decadal oceanic variability. *Nature Geoscience*, 11, 733–738. <https://doi.org/10.1038/s41561-018-0207-4>
- Joughin, I., & Alley, R. (2011). Stability of the west antarctic ice sheet in a warming world. *Nature Geoscience*, 4, 506–513.
- Joughin, I., Smith, B. E., & Schoof, C. G. (2019). Regularized coulomb friction laws for ice sheet sliding: Application to pine island glacier, antarctica. *Geophysical research letters*, 46(9), 4764–4771.
- Jourdain, N. C., et al. (2020). A protocol for calculating basal melt rates in the ismip6 antarctic ice sheet projections. *The Cryosphere*, 14, 3111–3134.
- Kachuck, S. B., Martin, D. F., Bassis, J. N., & Price, S. F. (2020). Rapid viscoelastic deformation slows marine ice sheet instability at pine island glacier. *Geophysical Research Letters*, 47, e2019GL086446. <https://doi.org/10.1029/2019GL086446>
- Karato, S. I., Jung, H., Katayama, I., & Skemer, P. (2008). Geodynamic significance of seismic anisotropy of the upper mantle: New insights from laboratory studies. *An-*

- nual Review of Earth and Planetary Sciences*, 36, 59–95. <https://doi.org/10.1146/annurev.Earth.36.031207.124120>
- Kaufmann, G., Wu, P., & Ivins, E. R. (2005). Lateral viscosity variations beneath antarctica and their implications on regional rebound motions and seismotectonics. *Journal of Geodynamics*, 39(2), 165–181. <https://doi.org/10.1016/j.jog.2004.08.009>
- Kearey, P., Klepeis, K. A., & Vine, F. J. (2009). *Global tectonics*, 3rd edn. Wiley–Blackwell.
- Kempenaar, G. (2022). *Modelling the greenland ice sheet following the mid-eemian*. [Master thesis available at <http://resolver.tudelft.nl/uuid:ce098ccc-4967-4c3b-a84c-d0a9a12a2212>].
- Kendall, R. A., Mitrovica, J. X., & Milne, G. A. (2005). On post-glacial sea level–ii. numerical formulation and comparative results on spherically symmetric models. *Geophysical Journal International*, 161, 679–706. <https://doi.org/10.1111/j.1365-246X.2005.02553.x>
- Khazendar, A., Borstad, C. P., Scheuchl, B., Rignot, E., & Seroussi, H. (2015). The evolving instability of the remnant larsen b ice shelf and its tributary glaciers. *Earth and Planetary Science Letters*, 419, 199–210. <https://doi.org/10.1016/j.epsl.2015.03.014>
- Kittel, C., Amory, C., Agosta, C., Jourdain, N. C., Hofer, S., Delhasse, A., Doutreloup, S., Huot, P.-V., Lang, C., Fichet, T., et al. (2021). Diverging future surface mass balance between the antarctic ice shelves and grounded ice sheet. *The Cryosphere*, 15(3), 1215–1236.
- Klemann, V., Wu, P., & Wolf, D. (2003). Compressible viscoelasticity: Stability of solutions for homogeneous plane-earth models. *Geophysical Journal International*, 153(3), 569–585.
- Konrad, H., Sasgen, I., Pollard, D., & Klemann, V. (2015). Potential of the solid-earth response for limiting long-term west antarctic ice sheet retreat in a warming climate. *Earth and Planetary Science Letters*, 432, 254–264. <https://doi.org/10.1016/j.epsl.2015.10.008>
- Kreuzer, M., Albrecht, T., Nicola, L., Reese, R., & Winkelmann, R. (2023). Oceanic gateways in antarctica – impact of relative sea-level change on sub-shelf melt. *EGU-sphere [preprint]*. <https://doi.org/10.5194/egusphere-2023-2737>
- Lambeck, K., Rouby, H., Purcell, A., Sun, Y., & Sambridge, M. (2014). Sea level and global ice volumes from the last glacial maximum to the holocene. *Proceedings of the National Academy of Sciences*, 111, 15296–15303. <https://doi.org/10.1073/ProceedingsoftheNationalAcademyofSciences.1411762111>
- Larour, E., Seroussi, H., Adhikari, S., Ivins, E., Caron, L., Morlighem, M., & Schlegel, N. (2019). Slowdown in antarctic mass loss from solid earth and sea-level feedbacks. *Science*, 364(6444). <https://doi.org/10.1126/science.aav7908>
- Laskar, J., Robutel, P., Joutel, F., Gastineau, M., Correia, A. C. M., & Levrard, B. (2004). A long-term numerical solution for the insolation quantities of the earth. *Astronomy & Astrophysics*, 428, 261–285. <https://doi.org/10.1051/0004-6361:20041335>
- Lau, H. C., Mitrovica, J. X., Austermann, J., Crawford, O., Al-Attar, D., & Latychev, K. (2016). Inferences of mantle viscosity based on ice age data sets: Radial structure. *Journal of Geophysical Research: Solid Earth*, 121, 6991–7012. <https://doi.org/10.1111/j.1365-246X.2005.02536.x>

- Lau, H. C. (2023). Transient rheology in sea level change: Implications for meltwater pulse 1a. *Earth and Planetary Science Letters*, 609, 118106. <https://doi.org/https://doi.org/10.1016/j.epsl.2023.118106>
- Le Brocq, A. M., Payne, A. J., & Vieli, A. (2010). An improved antarctic dataset for high resolution numerical ice sheet models (albmap v1). *Earth System Science Data*, 2, 247–260. <https://doi.org/10.5194/essd-2-247-2010>
- Le Meur, E., & Huybrechts, P. (1996). A comparison of different ways of dealing with isostasy: Examples from modelling the antarctic ice sheet during the last glacial cycle. *Annals of glaciology*, 23, 309–317.
- Leguy, G. R., Lipscomb, W. H., & Asay-Davis, X. S. (2021). Marine ice sheet experiments with the community ice sheet model. *The Cryosphere*, 15(7), 3229–3253. <https://doi.org/10.5194/tc-15-3229-2021>
- Levermann, A., Winkelmann, R., Albrecht, T., Goelzer, H., Golledge, N. R., Greve, R., Huybrechts, P., Jordan, J., Leguy, G., Martin, D., Morlighem, M., Pattyn, F., Pollard, D., Quiquet, A., Rodehacke, C., Seroussi, H., Sutter, J., Zhang, T., Van Breedam, J., ... van de Wal, R. S. W. (2020). Projecting antarctica's contribution to future sea-level rise from basal ice shelf melt using linear response functions of 16 ice sheet models (larmip-2). *Earth System Dynamics*, 11(1), 35–76. <https://doi.org/10.5194/esd-11-35-2020>
- Lipscomb, W., et al. (2021). Ismip6-based projections of ocean-forced antarctic ice sheet evolution using the community ice sheet model. *The Cryosphere*, 15, 633–661.
- Lipscomb, W. H., Price, S. F., Hoffman, M. J., Leguy, G. R., Bennett, A. R., Bradley, S. L., Evans, K. J., Fyke, J. G., Kennedy, J. H., Perego, M., et al. (2019). Description and evaluation of the community ice sheet model (cism) v2. 1. *Geoscientific Model Development*, 12(1), 387–424.
- Livingstone, S. J., Ó Cofaigh, C., Stokes, C. R., Hillenbrand, C. D., Vieli, A., & Jamieson, S. S. R. (2012). Antarctic palaeo-ice streams. *Earth-Science Reviews*, 111(1–2), 90–128. <https://doi.org/10.1016/j.earscirev.2011.10.003>
- Lloyd, A., Wiens, D., Zhu, H., Tromp, J., Nyblade, A., Aster, R., Hansen, S., Dalziel, I., Wilson, T., Ivins, E., & O'Donnell, J. (2019). Seismic structure of the antarctic upper mantle imaged with adjoint tomography. *Journal of Geophysical Research: Solid Earth*, 124, 1115–1130. <https://doi.org/10.1029/2019JB017823>
- Löfverström, M., Caballero, R., Nilsson, J., & Kleman, J. (2014). Evolution of the large-scale atmospheric circulation in response to changing ice sheets over the last glacial cycle. *Climate of the Past*, 10(4), 1453–1471. <https://doi.org/10.5194/cp-10-1453-2014>
- Lösing, M., Ebbing, J., & Szwillus, W. (2020). Geothermal heat flux in antarctica: Assessing models and observations by bayesian inversion. *Frontiers in Earth Science*, 8, 105.
- Maris, M. N. A., de Boer, B., Ligtenberg, S. R. M., Crucifix, M., van de Berg, W. J., & Oerlemans, J. (2014). Modelling the evolution of the antarctic ice sheet since the last interglacial. *The Cryosphere*, 8, 1347–1360. <https://doi.org/10.5194/tc-8-1347-2014>
- Martin, A. P. (2021). A review of the composition and chemistry of peridotite mantle xenoliths in volcanic rocks from antarctica and their relevance to petrological

- and geophysical models for the lithospheric mantle. In *The geological society of london - memoirs* (pp. 343–354, Vol. 56). <https://doi.org/10.1144/M56-2021-26>
- Martin, A., & van der Wal, W. (2023). *The geochemistry and geophysics of the antarctic mantle*. Geological Society of London.
- Martin, M. A., Winkelmann, R., Haseloff, M., Albrecht, T., Bueler, E., Khroulev, C., & Levermann, A. (2011). The potsdam parallel ice sheet model (pism-pik) – part 2: Dynamic equilibrium simulation of the antarctic ice sheet. *The Cryosphere*, 5, 727–740. <https://doi.org/10.5194/tc-5-727-2011>
- Martinec, Z., & Hagedoorn, J. (2014). The rotational feedback on linear-momentum balance in glacial isostatic adjustment. *Geophysical Journal International*, 199(3), 1823–1846.
- McConnell, R. (1965). Viscosity of the mantle from relaxation time spectra of isostatic adjustment. *Journal of Geophysical Research*, 70, 5171–5188. <https://doi.org/10.1029/JZ070i020p05171>
- Meehl, G. A., et al. (2020). Context for interpreting equilibrium climate sensitivity and transient climate response from the cmip6 earth system models. *Science Advances*, 6(1981).
- Mercer, J. (1978). West antarctic ice sheet and co2 greenhouse effect: A threat of disaster. *Nature*, 271, 321–325.
- Meredith, M., Sommerkorn, M., Cassotta, S., Derksen, C., Ekaykin, A., Hollowed, A., Kofinas, G., Mackintosh, A., Melbourne-Thomas, J., Muelbert, M. M. C., Ottersen, G., Pritchard, H., & Schuur, E. A. G. (2019). *Polar regions*. Cambridge University Press. <https://doi.org/10.1017/9781009157964.005>
- Miles, B., Stokes, C., Jamieson, S., et al. (2022). High spatial and temporal variability in antarctic ice discharge linked to ice shelf buttressing and bed geometry. *Scientific Reports*, 12, 10968. <https://doi.org/10.1038/s41598-022-13517-2>
- Milillo, P., Rignot, E., Rizzoli, P., Scheuchl, B., Mougnot, J., Bueso-Bello, J., & Prats-Iraola, P. (2019). Heterogeneous retreat and ice melt of thwaites glacier, west antarctica. *Science advances*, 5(1), eaau3433.
- Milne, G. A., & Mitrovica, J. X. (2008). Searching for eustasy in deglacial sea-level histories. *Quaternary Science Reviews*, 27(25–26), 2292–2302.
- Mitrovica, J. X., Gomez, N., & Clark, P. U. (2009). The sea-level fingerprint of west antarctic collapse. *Science*, 323(5915), 753–753.
- Mitrovica, J. X., & Milne, G. A. (2003). On post-glacial sea level: I. General theory. *Geophysical Journal International*, 154(2), 253–267. <https://doi.org/10.1046/j.1365-246X.2003.01942.x>
- Mitrovica, J., Gomez, N., Morrow, E., Hay, C., Latychev, K., & Tamisiea, M. (2011). On the robustness of predictions of sea level fingerprints. *Geophysical Journal International*, 187, 729–742. <https://doi.org/10.1111/j.1365-246X.2011.05090.x>
- Mitrovica, J., & Peltier, W. (1991). A complete formalism for the inversion of post glacial rebound data: Resolving power analysis. *Geophysical Journal International*, 104, 267–288.
- Morin, R. H., Williams, T., Henrys, S. A., Magens, D., Niessen, F., & Hansaraj, D. (2010). Heat Flow and Hydrologic Characteristics at the AND-1B borehole, ANDRILL

- McMurdo Ice Shelf Project, Antarctica. *Geosphere*, 6(4), 370–378. <https://doi.org/10.1130/GES00512.1>
- Morland, L. W. (1987). Unconfined ice-shelf flow. In C. J. Van der Veen & J. Oerlemans (Eds.), *Dynamics of the west antarctic ice sheet. glac. quat. g., vol. 4* (pp. 109–126). Springer. https://doi.org/10.1007/978-94-009-3745-1_6
- Morland, L. W., & Johnson, I. R. (1980). Steady motion of ice sheets. *Journal of Glaciology*, 25, 229–246. <https://doi.org/10.3189/S0022143000010467>
- Morland, L. (1985). Unconfined ice-shelf flow. In C. J. Van der Veen & J. Oerlemans (Eds.), *Dynamics of the west antarctic ice sheet* (pp. 99–116). D. Reidel Publishing Company. <https://doi.org/10.1007/978-94-009-3745-1>
- Morlighem, M., Goldberg, D., Barnes, J. M., Bassis, J. N., Benn, D. I., Crawford, A. J., Gudmundsson, G. H., & Seroussi, H. (2024). The west antarctic ice sheet may not be vulnerable to marine ice cliff instability during the 21st century. *Science Advances*, 10(34), eado7794.
- Morlighem, M., Rignot, E., Binder, T., Blankenship, D. D., Drews, R., Eagles, G., Eisen, O., Ferraccioli, F., Forsberg, R., Fretwell, P., Goel, V., Greenbaum, J. S., Gudmundsson, H., Guo, J., Helm, V., Hofstede, C., Howat, I., Humbert, A., Jokat, W., ... Young, D. A. (2020). Deep glacial troughs and stabilizing ridges unveiled beneath the margins of the antarctic ice sheet. *Nature Geoscience*, 13. <https://doi.org/10.1038/s41561-019-0510-8>
- Mouginot, J., Rignot, E., Scheuchl, B., & Millan, R. (2017). Comprehensive annual ice sheet velocity mapping using landsat-8, sentinel-1, and radarsat-2 data. *Remote Sensing*, 9(4), 364.
- Nicola, L., Notz, D., & Winkelmann, R. (2023). Revisiting temperature sensitivity: How does antarctic precipitation change with temperature? *The Cryosphere*, 17(7), 2563–2583. <https://doi.org/10.5194/tc-17-2563-2023>
- Nield, G. A., Barletta, V. R., Bordon, A., King, M. A., Whitehouse, P. L., Clarke, P. J., Domack, E., Scambos, T. A., & Berthier, E. (2014). Rapid bedrock uplift in the antarctic peninsula explained by viscoelastic response to recent ice unloading. *Earth and Planetary Science Letters*, 397, 32–41. <https://doi.org/10.1016/j.epsl.2014.04.019>
- Nield, G. A., Whitehouse, P. L., van der Wal, W., Blank, B., O'Donnell, J. P., & Stuart, G. W. (2018). The impact of lateral variations in lithospheric thickness on glacial isostatic adjustment in west antarctica. *Geophysical Journal International*, 214, 811–824. <https://doi.org/10.1093/gji/ggy158>
- Noble, T. L., Rohling, E. J., Aitken, A. R. A., Bostock, H. C., Chase, Z., Gomez, N., et al. (2020). The sensitivity of the antarctic ice sheet to a changing climate: Past, present, and future. *Reviews of Geophysics*, 58, e2019RG000663. <https://doi.org/10.1029/2019RG000663>
- Oerlemans, J. (1980). Model experiments on the 100,000-yr glacial cycle. *Nature*, 287(5781), 430–432.
- Ohmura, R., Shigetomi, T., & Mori, Y. H. (1999). Formation, growth and dissociation of clathrate hydrate crystals in liquid water in contact with a hydrophobic hydrate-forming liquid. *Journal of crystal growth*, 196(1), 164–173.

- Oude Egbrink, D. (2018). *Modelling the last glacial ice sheet on antarctica with laterally varying relaxation time*.
- Pan, L., Powell, E. M., Latychev, K., Mitrovica, J. X., Creveling, J. R., Gomez, N., Hoggard, M. J., & Clark, P. U. (2021). Rapid postglacial rebound amplifies global sea level rise following west antarctic ice sheet collapse. *Science Advances*, 7(eabf7787). <https://doi.org/10.1126/sciadv.abf7787>
- Pappa, F., Ebbing, J., Ferraccioli, F., & van der Wal, W. (2019). Modeling satellite gravity gradient data to derive density, temperature, and viscosity structure of the antarctic lithosphere. *Journal of Geophysical Research: Solid Earth*, 124, 12053–12076. <https://doi.org/10.1029/2019JB017997>
- Pattyn, F. (2017). Sea-level response to melting of antarctic ice shelves on multi-centennial timescales with the fast elementary thermomechanical ice sheet model (f.etish v1.0). *The Cryosphere*, 11, 1851–1878. <https://doi.org/10.5194/tc-11-1851-2017>
- Pattyn, F., & Morlighem, M. (2020). The uncertain future of the antarctic ice sheet. *Science*, 367, 1331–1335. <https://doi.org/10.1126/science.aaz5487>
- Paulson, A., Zhong, S., & Wahr, J. (2005). Modelling post-glacial rebound with lateral viscosity variations. *Geophysical Journal International*, 163, 357–371. <https://doi.org/10.1111/j.1365-246X.2005.02645.x>
- Pelletier, C., Fichefet, T., Goosse, H., Haubner, K., Helsen, S., Huot, P.-V., Kittel, C., Klein, E., Le clec'h, S., van Lipzig, N. P. M., Marchi, S., Massonnet, F., Mathiot, P., Moravveji, E., Moreno-Chamarro, E., Ortega, P., Pattyn, F., Souverijns, N., Van Achter, G., ... Zipf, L. (2022). Paraso, a circum-antarctic fully coupled ice-sheet–ocean–sea-ice–atmosphere–land model involving f.etish1.7, nemo3.6, lim3.6, cosmo5.0 and clm4.5. *Geoscientific Model Development*, 15, 553–594. <https://doi.org/10.5194/gmd-15-553-2022>
- Peltier, W. (1974). The impulse response of a maxwell earth. *Reviews of Geophysics*, 12(4), 649–669.
- Peltier, W. (1976). Glacial-isostatic adjustment—ii. the inverse problem. *Geophysical Journal International*, 46, 669–705. <https://doi.org/10.1111/j.1365-246X.1976.tb01253.x>
- Pollard, D., & DeConto, R. (2009). Modelling west antarctic ice sheet growth and collapse through the past five million years. *Nature*, 458, 329–332. <https://doi.org/10.1038/nature07809>
- Pollard, D., Gomez, N., & DeConto, R. (2017). Variations of the antarctic ice sheet in a coupled ice sheet-earth-sea level model: Sensitivity to viscoelastic earth properties. *Journal of Geophysical Research-Earth Surf.*, 122(11), 2124–2138. <https://doi.org/10.1002/2017JF004371>
- Pourpoint, M., Anandakrishnan, S., Ammon, C. J., & Alley, R. B. (2018). Lithospheric structure of greenland from ambient noise and earthquake surface wave tomography. *Journal of Geophysical Research: Solid Earth*, 123(9), 7850–7876.
- Powell, E. M., Pan, L., Hoggard, M. J., Latychev, K., Gomez, N., Austermann, J., & Mitrovica, J. X. (2021). The impact of 3-d earth structure on far-field sea level following interglacial west antarctic ice sheet collapse. *Quaternary Science Reviews*, 273, 107256. <https://doi.org/10.1016/j.quascirev.2021.107256>

- Reading, A. M., Stål, T., Halpin, J. A., et al. (2022). Antarctic geothermal heat flow and its implications for tectonics and ice sheets. *Nature Reviews Earth & Environment*, 3, 814–831. <https://doi.org/10.1038/s43017-022-00348-y>
- Reerink, T. J., van de Berg, W. J., & van de Wal, R. S. W. (2016). Oblimap 2.0: A fast climate model–ice sheet model coupler including online embeddable mapping routines. *Geoscientific Model Development*, 9, 4111–4132. <https://doi.org/10.5194/gmd-9-4111-2016>
- Reusen, J. M., Steffen, R., Steffen, H., Root, B. C., & van der Wal, W. (2023). Simulating horizontal crustal motions of glacial isostatic adjustment using compressible Cartesian models. *Geophysical Journal International*, 235(1), 542–553. <https://doi.org/10.1093/gji/ggad232>
- Rignot, E., et al. (2013). Ice-shelf melting around antarctica. *Science*, 341, 266–270.
- Rignot, E., et al. (2019). Four decades of antarctic ice sheet mass balance from 1979–2017. *Proceedings of the National Academy of Sciences*, 116, 1095–1103.
- Rignot, E., Casassa, G., Gogineni, P., Krabill, W., Rivera, A., & Thomas, R. (2004). Accelerated ice discharge from the antarctic peninsula following the collapse of larsen b ice shelf. *Geophysical research letters*, 31(18).
- Robinson, A., Alvarez-Solas, J., Montoya, M., Goelzer, H., Greve, R., & Ritz, C. (2020). Description and validation of the ice-sheet model yelmo (version 1.0). *Geoscientific Model Development*, 13(6), 2805–2823.
- Rodehacke, C., Pfeiffer, M., Semmler, T., Gurses, O., & Kleiner, T. (2020). Future sea level contribution from antarctica inferred from cmip5 model forcing and its dependence on precipitation ansatz. *Earth System Dynamics*, 11(4), 1153–1194. <https://doi.org/10.5194/esd-11-1153-2020>
- Sabadini, R., Vermeersen, B., & Cambiotti, G. (2016). *Global dynamics of the earth*. Springer.
- Schaeffer, A., & Lebedev, S. (2013). Global shear speed structure of the upper mantle and transition zone. *Geophysical Journal International*, 194, 417–449. <https://doi.org/10.1093/gji/ggt095>
- Scheinert, M., Engels, O., Schrama, E. J., van der Wal, W., & Horwath, M. (2021). Geodetic observations for constraining mantle processes in antarctica. In *The geological society of london - memoirs* (pp. 295–313, Vol. 56). <https://doi.org/10.1144/M56-2021-22>
- Scherrenberg, M. D. W., Berends, C. J., & van de Wal, R. S. W. (2024). Late pleistocene glacial terminations accelerated by proglacial lakes. *Climate of the Past*, 20(8), 1761–1784. <https://doi.org/10.5194/cp-20-1761-2024>
- Schoof, C. (2007). Ice sheet grounding line dynamics: Steady states, stability, and hysteresis. *Journal of Geophysical Research-Earth*, 112(F03S28). <https://doi.org/10.1029/2006JF000664>
- Seroussi, H., Nowicki, S., Payne, A., Goelzer, H., & et al. (2020). Ismip6 antarctica: A multi-model ensemble of the antarctic ice sheet evolution over the 21st century. *The Cryosphere Discussions*. <https://doi.org/10.5194/tc-2019-324>
- Shapiro, N. M., & Ritzwoller, M. H. (2004). Inferring surface heat flux distributions guided by a global seismic model: Particular application to antarctica. *Earth and Planetary Science Letters*, 223, 213–224.

- Siahaan, A., Smith, R. S., Holland, P. R., Jenkins, A., Gregory, J. M., Lee, V., Mathiot, P., Payne, A. J., Ridley, J. K., & Jones, C. G. (2022). The antarctic contribution to 21st-century sea-level rise predicted by the uk earth system model with an interactive ice sheet. *The Cryosphere*, 16(10), 4053–4086. <https://doi.org/10.5194/tc-16-4053-2022>
- Simms, A. R., Lisiecki, L., Gebbie, G., Whitehouse, P. L., & Clark, J. F. (2019). Balancing the last glacial maximum (lgm) sea-level budget. *Quaternary Science Reviews*, 205, 143–153. <https://doi.org/10.1016/j.quascirev.2018.12.018>
- Spada, G., Barletta, V. R., Klemann, V., Riva, R. E. M., Martinec, Z., Gasperini, P., Lund, B., Wolf, D., Vermeersen, L. L. A., & King, M. A. (2011). A benchmark study for glacial isostatic adjustment codes. *Geophysical Journal International*, 185, 106–132. <https://doi.org/10.1111/j.1365-246x.2011.04952.x>
- Spada, G., & Melini, D. (2019). Selen 4 (selen version 4.0): A fortran program for solving the gravitationally and topographically self-consistent sea-level equation in glacial isostatic adjustment modeling. *Geoscientific Model Development*, 12(12), 5055–5075.
- Stammerjohn, S., & Scambos, T. (2020). Warming reaches the south pole. *Nature Climate Change*, 10, 710–711. <https://doi.org/10.1038/s41558-020-0827-8>
- Stap, L. B., Van De Wal, R. S., De Boer, B., Bintanja, R., & Lourens, L. J. (2017). The influence of ice sheets on temperature during the past 38 million years inferred from a one-dimensional ice sheet–climate model. *Climate of the Past*, 13(9), 1243–1257.
- Steffen, R., Audet, P., & Lund, B. (2018). Weakened lithosphere beneath greenland inferred from effective elastic thickness: A hot spot effect? *Geophysical Research Letters*, 45(10), 4733–4742.
- Stocker, T., Qin, D., Plattner, G.-K., Tignor, M., Allen, S., Boschung, J., Nauels, A., Xia, Y., Bex, V., & Midgley, P. (2013). *Climate change 2013: The physical science basis* (T. Stocker, D. Qin, G.-K. Plattner, M. Tignor, S. Allen, J. Boschung, A. Nauels, Y. Xia, V. Bex, & P. Midgley, Eds.) [Contribution of working group i to the fifth assessment report of the intergovernmental panel on climate change]. Cambridge University Press.
- Tanaka, Y., Klemann, V., Martinec, Z., & Riva, R. E. M. (2011). Spectral-finite element approach to viscoelastic relaxation in a spherical compressible Earth: application to GIA modelling. *Geophysical Journal International*, 184(1), 220–234. <https://doi.org/10.1111/j.1365-246X.2010.04854.x>
- team, T. I. (2018). Mass balance of the antarctic ice sheet from 1992 to 2017. *Nature*, 558, 219–222. <https://doi.org/10.1038/s41586-018-0179-y>
- Tewari, K., Mishra, S. K., Dewan, A., Dogra, G., & Ozawa, H. (2021). Influence of the height of antarctic ice sheet on its climate [SuperDARN / Studies of Geospace Dynamics - Today and Future]. *Polar Science*, 28, 100642. <https://doi.org/https://doi.org/10.1016/j.polar.2021.100642>
- Tierney, J. E., Zhu, J., King, J., Malevich, S. B., Hakim, G. J., & Poulsen, C. J. (2020). Glacial cooling and climate sensitivity revisited. *Nature*, 584, 569–573. <https://doi.org/10.1038/s41586-020-2617-x>
- Turcotte, D., & Schubert, G. (2002). *Geodynamics* (2nd). Cambridge University Press.

- Uppala, S. M., et al. (2005). The era-40 re-analysis. *Quarterly Journal of the Royal Meteorological Society*, 131, 2961–3012.
- van Calcar, C. J., Bernales, J., Berends, C., van de Wal, R., & van der Wal, W. (2024). Assessing the interaction between ice dynamics, sub-shelf melt and GIA over a glacial cycle using a fully coupled GIA-ice sheet model. *Preprint*.
- van Calcar, C., van de Wal, R., Blank, B., de Boer, B., & van der Wal, W. (2023). Simulation of a fully coupled 3d glacial isostatic adjustment – ice sheet model for the antarctic ice sheet over a glacial cycle. *Geoscientific Model Development*, 16, 5473–5492. <https://doi.org/10.5194/gmd-16-5473-2023>
- van Dalum, C. T., van de Berg, W. J., & van den Broeke, M. R. (2022). Sensitivity of antarctic surface climate to a new spectral snow albedo and radiative transfer scheme in racmo2. 3p3. *The Cryosphere*, 16(3), 1071–1089.
- Van Den Berg, J., Van De Wal, R. S. W., & Oerlemans, J. (2008). A mass balance model for the eurasian ice sheet for the last 120,000 years. *Global and Planetary Change*, 61, 194–208. <https://doi.org/10.1029/2007JB004994>
- van den Akker, T., Lipscomb, W. H., Leguy, G. R., Bernales, J., Berends, C. J., van de Berg, W. J., & van de Wal, R. S. (2025). Present-day mass loss rates are a precursor for west antarctic ice sheet collapse. *The Cryosphere*, 19(1), 283–301.
- van der Wal, W., Barnhoorn, A., Stocchi, P., Gradmann, S., Wu, P., Drury, M., & Vermeersen, B. (2013). Glacial isostatic adjustment model with composite 3-d earth rheology for fennoscandia. *Geophysical Journal International*, 194, 61–77. <https://doi.org/10.1093/gji/ggt099>
- van der Wal, W., Whitehouse, P. L., & Schrama, E. J. O. (2015). Effect of GIA models with 3d composite mantle viscosity on grace mass balance estimates for antarctica. *Earth and Planetary Science Letters*, 414, 134–143. <https://doi.org/10.1016/j.epsl.2015.01.001>
- van der Wal, W., Wu, P., Wang, H., & Sideris, M. G. (2010). Sea levels and uplift rate from composite rheology in glacial isostatic adjustment modeling. *Journal of Geodynamics*, 50, 38–48. <https://doi.org/10.1016/j.jog.2010.01.006>
- van der Wal, W., Barletta, V., Nield, G., & van Calcar, C. (2023, February). Glacial isostatic adjustment and post-seismic deformation in Antarctica. In *The Geochemistry and Geophysics of the Antarctic Mantle*. Geological Society of London. <https://doi.org/10.1144/M56-2022-13>
- Wan, J. X. W., Gomez, N., Latychev, K., & Han, H. K. (2022). Resolving glacial isostatic adjustment (GIA) in response to modern and future ice loss at marine grounding lines in west antarctica. *The Cryosphere*, 16(6), 2203–2223. <https://doi.org/10.5194/tc-16-2203-2022>
- Wang, H., & Wu, P. (2006). Effects of lateral variations in lithospheric thickness and mantle viscosity on glacially induced relative sea levels and long wavelength gravity field in a spherical, self-gravitating maxwell earth. *Earth and Planetary Science Letters*, 249(3–4), 368–383. <https://doi.org/10.1016/j.epsl.2006.07.011>
- Weerdesteijn, M., Hu, H., van der Wal, W., & Riva, R. (2019). The potential of numerical modelling for glaciation-induced true polar wander of the earth [ISSN 1029-7006].

- Whitehouse, P., Gomez, N., King, M. A., & Wiens, D. A. (2019). Solid earth change and the evolution of the antarctic ice sheet. *Nature Communications*, 10, 503. <https://doi.org/10.1038/s41467-018-08068-y>
- Whitehouse, P. L. (2018). Glacial isostatic adjustment modelling: Historical perspectives, recent advances, and future directions. *Earth Surface Dynamics*, 6, 401–429. <https://doi.org/10.5194/esurf-6-401-2018>
- Whitehouse, P. L., Bentley, M. J., Milne, G. A., King, M. A., & Thomas, I. D. (2012). A new glacial isostatic adjustment model for antarctica: Calibrated and tested using observations of relative sea-level change and present-day uplift rates. *Geophysical Journal International*, 190, 1464–1482. <https://doi.org/10.1111/j.1365-246X.2012.05557.x>
- Whitehouse, P. L., Latychev, K., Milne, G. A., Mitrovica, J. X., & Kendall, R. (2006). Impact of 3-d earth structure on fennoscandian glacial isostatic adjustment: Implications for space-geodetic estimates of present-day crustal deformations. *Geophysical Research Letters*, 33(13), L13502. <https://doi.org/10.1029/2006GL026568>
- Wilner, J. A., Morlighem, M., & Cheng, G. (2023). Evaluation of four calving laws for antarctic ice shelves. *The Cryosphere Discussions*, 2023, 1–19.
- Wolstencroft, M., et al. (2015). Uplift rates from a new high-density gps network in palmer land indicate significant late holocene ice loss in the southwestern weddell sea. *Geophysical Journal International*, 203, 737–754.
- Wu, P. (2004). Using commercial finite element packages for the study of earth deformations, sea levels and the state of stress. *Geophysical Journal International*, 158, 401–408. <https://doi.org/10.1111/j.1365-246X.2004.02338.x>
- Wu, P. (2006). Sensitivity of relative sea levels and crustal velocities in laurentide to radial and lateral viscosity variations in the mantle. *Geophysical Journal International*, 165, 401–413. <https://doi.org/10.1111/j.1365-246X.2006.02960.x>
- Wu, P., & Peltier, W. R. (1982). Viscous gravitational relaxation. *Geophysical Journal International*, 70, 435–485. <https://doi.org/10.1111/j.1365-246X.1982.tb04976.x>
- Wu, P., & van der Wal, W. (2013). Postglacial sealevels on a spherical, self-gravitating viscoelastic earth: Effects of lateral viscosity variations in the upper mantle on the inference of viscosity contrasts in the lower mantle. *Geophysical Journal International*, 192, 7–17. [https://doi.org/10.1016/S0012-821X\(03\)00199-7](https://doi.org/10.1016/S0012-821X(03)00199-7)
- Wu, P., & Johnston, P. (1998). Validity of using flat-earth finite element models in the study of postglacial rebound. *Dynamics of the ice age earth: A modern perspective*, 191–202.
- Wu, P., & Peltier, W. (1984). Pleistocene deglaciation and the earth's rotation: A new analysis. *Geophysical Journal International*, 76(3), 753–791.
- Yousefi, M., Wan, J., Pan, L., Gomez, N., Latychev, K., Mitrovica, J. X., Pollard, D., & DeConto, R. M. (2022). The influence of the solid earth on the contribution of marine sections of the antarctic ice sheet to future sea-level change. *Geophysical Research Letters*, 49(e2021GL097525). <https://doi.org/10.1029/2021GL097525>
- Zhao, C., King, M. A., Watson, C. S., Barletta, V. R., Bordoni, A., Dell, M., & Whitehouse, P. L. (2017). Rapid ice unloading in the fleming glacier region, southern antarctic peninsula, and its effect on bedrock uplift rates. *Earth and Planetary Science Letters*, 473, 164–176. <https://doi.org/10.1016/j.epsl.2017.06.002>

- Zoet, L. K., & Iverson, N. R. (2020). A slip law for glaciers on deformable beds. *Science*, 368(6486), 76–78. <https://doi.org/10.1126/science.aaz1183>
- Zweng, M., et al. (2019). *World ocean atlas 2018, volume 2: Salinity* (A. Mishonov, Ed.; tech. rep. No. 82). NOAA Atlas NESDIS.

DATA STATEMENTS

CHAPTER 3

The model, the data, and the MATLAB scripts to generate the figures included in this work are freely available with DOI 10.4121/19765816.v2 (van Calcar et al., 2023) for the model and with DOI 10.4121/19772815.v2 (van Calcar, 2023) for the data.

CHAPTER 4

The source code of IMAU-ICE can be found on Github: <https://github.com/IMAU-paleo/IMAU-ICE>. The GIA model code has been made publicly available by van Calcar et al. (2023) with DOI 10.4121/19765816.v2. The data produced for this manuscript is freely available at <https://doi.org/10.6084/m9.figshare.26767534>.

CHAPTER 5

The supplemental data, i.e. Table 1 and the laterally varying relaxation time maps, are publicly available with DOI 10.4121/a7215d4c-767f-49f1-a8bb-da40d0d2b01d. The data produced for this publication is available with DOI 10.4121/b5548aaa-4c05-45f7-b0ce-775b83f13e5d. The source code of IMAU-ICE is included in this DOI and can be found at Github: <https://github.com/IMAU-paleo/IMAU-ICE>. The GIA model code and coupling script have been made publicly available by van Calcar et al. (2023) with DOI 10.4121/19765816.v2.



Errera channel, Antarctica

ACKNOWLEDGEMENTS

My PhD studies has been a truly special chapter of my life — one filled with curiosity and challenge. I threw myself into learning as much as I could, not just about the physics of ice and rocks, but also how to critically read papers, find the unknowns in literature, develop and link models written in different languages, analyse large datasets, and tell the whole story in a way that's both concise and reproducible. Being able to break down a complex scientific problem and communicate a solution is what I'm most proud of learning.

My promotors, Wouter van der Wal and Roderik van de Wal, taught me these skills over the years, and I couldn't be more grateful for the time and energy they invested in me. Our weekly meetings always motivated me to keep going, even when I was completely stuck trying to fix (yet another) bug in the model. You both taught me that there's always a way forward. And Bert Vermeersen, thank you for your valuable insights, for checking in regularly, and helping me improve this thesis.

Speaking of model bugs: Jorjo and Tijn, thank you for solving tons of them with me until I could finally fly solo and actually enjoy debugging. You turned debugging from a soul-draining panic into a puzzle I actually enjoy solving. Franka, you too deserve credit here - thanks for joining me into the crotches of IMAU-ICE. I'm really happy you'll be sitting next to me as my paranymph. Bas, thanks for generously sharing your GIA model and explaining it to me (again and again) when I was still figuring everything out as a master's student.

My PhD was funded by EU's Horizon2020 project PROTECT and by ESA's 3D Earth project. These projects not only allowed me to do this PhD, but also made it possible to travel and meet scientists from all over the world. I got to attend conferences in Austria, France, Belgium, Italy, Denmark, the US, and Singapore. Furthermore, I attended two fantastic summer schools in Karthaus (Italy) and Gävle (Sweden). One of the absolute highlights was being part of the expedition team on a cruise to Antarctica, where I got to share Antarctic science with the public. I want to thank the amazing people I met during these trips - you were truly motivational, supportive, and inspirational.

Back home, my fellow PhD students at IMAU and Aerospace Engineering made everything a lot more fun and a lot less lonely—especially during the Covid years. Even when we were stuck behind our screens for the first two years of my PhD, the online HOEMBA meetings helped keeping me motivated. A special thanks to Clara Burgard, with whom I started the PROTECT early career researchers community—we had many valuable online chats! Even though I spent most of my free time horse riding and missed many social activities, I always felt connected thanks to the great people at IMAU and the Planetary Exploration group. Too many to name, but I'd especially like to thank Al-lard, Riva, Sam, Linh, Fernando, Livio, Rania, Andrea, Yael, Natalia, Tim, and the entire HOEMBA group for making these years so enjoyable.

Outside of work, I owe a big thank-you to my friends, who made sure I didn't disappear entirely into science and stables. When I was buried in deadlines or too busy training, you kept pulling me out to do fun stuff and kept calling me regularly. I want to especially thank my dear friends Fay, Patty, Fokke, Maud, Nienke, Maaïke, Hilde, Berna, Fieke and Dyonne. And of course all my lovely friends from Club Link, my student houses, and my high school group—this year we're celebrating 20 years of friendship. Special thanks to Renato for encouraging me to start this PhD and for listening to more bug-related rants than anyone ever should.

To my family: thank you for always being excited to hear about my research, your encouragement means the world. Thank you for being there for me. Special thanks to my dad for all the fruitful discussions and for carefully proofreading my whole thesis, to my mom for taking some of the beautiful pictures shown in this thesis, and to Arnd for helping me with the layout of the thesis and editing the pictures. Irene, despite living in Spain, you've always been there for me with an open ear and open heart. A special thanks to my sister for helping me organise the defense. We've grown closer over the years, and I'm proud to have you beside me as my paranymp.

Last but definitely not least, a heartfelt thank you to the owners of the incredible horses I had the privilege to train every single day. Odile, Jo, and Linda—thank you for trusting me with your amazing horses. Riding has been my daily reset, my source of peace, and, honestly, my therapy. No matter how chaotic or stressful things got, time in the saddle always brought me back to myself.

I've experienced the PhD as an amazing job where I could genuinely contribute to society by improving sea-level projections. At the same time, I got to develop skills and learn as much as I possibly could—that's what made this PhD so special to me. I'm really happy that Taco Broerse gave me the opportunity to continue in academia—thank you!

Writing these acknowledgements was honestly one of the hardest parts of the PhD, and I postponed it until the printing house was desperately waiting for me to submit (one thing I definitely did not learn: I still leave things until the last minute and then pull all-nighters). It wasn't hard because I'm not thankful — it's hard because it's so difficult to put into words how much your support has meant to me. There's not enough space to mention everyone personally, but please know that I'm deeply thankful to all of you.

CURRICULUM VITÆ

Caroline van Calcar

Date of birth: 4 March 1993

Place of birth: Ermelo, The Netherlands



EDUCATION

2005–2011	Grammar School Christelijk College Nassau Veluwe, Harderwijk
2012–2016	Bachelor of Science in Systems Engineering, Policy Analysis and Management Technical University of Delft
2017–2020	Master of Science in Geoscience and Remote Sensing Technical University of Delft
ORCID-ID:	0000-0003-4659-0678

AWARDS

2022	Outstanding student presentation award, PALSEA meeting, Singapore
2023	Outstanding student presentation award, AGU meeting, San Fransisco, US

LIST OF PUBLICATIONS

- **van Calcar, C.J.**, Whitehouse, P.L., van de Wal, R.S.W. & van der Wal, W. *Approaching Antarctic ice sheet evolution over the next centuries from a coupled 3D GIA – ice sheet model using ELRA and 1D GIA*. Preprint (2024).
- **van Calcar, C.J.**, Bernales, J., Berends, C.J., van der Wal, W., & van de Wal, R.S.W. *Bedrock uplift reduces Antarctic sea-level contribution over next centuries*. Preprint, (2024).
- **van Calcar, C. J.**, van de Wal, R. S. W., Blank, B., de Boer, B., & van der Wal, W. *Simulation of a fully coupled 3D glacial isostatic adjustment – ice sheet model for the Antarctic ice sheet over a glacial cycle*. Geoscientific Model Development, 16, 5473–5492 (2023).
- van der Wal, W., Barletta, V., Nield, G. & **van Calcar, C. J.** *Glacial isostatic adjustment and post-seismic deformation in Antarctica*. The Geochemistry and Geophysics of the Antarctic Mantle, A. P. Martin, W. van der Wal (2023).
- Durand, G., van den Broeke, M.R., Le Cozannet, G., Edwards, T.L., Holland, P.R., Jourdain, N.C., Marzeion, B., Mottram, R., Nicholls, R.J., Pattyn, F., Paul, F., Slangen, A.B.A., Winkelmann, R., Burgard, C., **van Calcar, C. J.**, Barre, J., Bataille, A. & Chapuis, A. *Sea-Level Rise: From Global Perspectives to Local Services*. Frontiers in Marine Science, 8 (2021).
- Klose, A., Turner, F., Berends, T., Bradley, A., Chapuis, A., Coulon V., Edwards, T., Goelzer, H., Hermans, T.H.J., Holland, P.R., Jourdain, N.C., Lambert, E., Mottram, R., Philippenko, X., Simonsen, S.B., Slangen, A.B.A., **van Calcar, C.J.**, van den Broeke, M., Volz, V., Wouters, B., Bataille, A., Bett, D., Champollion, N., Durand, G., Foucher, C., Gomez Valdivia, F., Hansen, N., Heslop, F., Huybrechts, P., Jenkins, A., Le Bars, D., Le Cozannet, G., Lincke, D., Malagon Santos, V., Mosbeux, C., Mugford, R., Nicholls, R., Olesen, M., Pattyn, F., Rahlves, C., Ravinder, N., Richter, O., Rohmer, J., Thrivikraman Pillai, J., & van de Wal, R.S.W. *Improving the inclusion and role of early career scientists in EU-funded projects and beyond*. Open Research Europe, in prep.

